Using Micro-CT scanning to identify structural changes in Craniofacial, Neural, and Cardiovascular systems of spotting-lethal rat, a model of Hirschsprung disease

A thesis submitted in fulfillment of the requirements for the degree of Doctor of Philosophy, Australian National University.

JUNE 20, 2021

KO-CHIN CHEN
BSc MBBS (ANU) FACRRM

Using Micro-CT scanning to identify structural changes in Craniofacial, Neural, and Cardiovascular systems of spotting-lethal rat, a model of Hirschsprung disease

Ko-Chin Chen
MB BS (ANU), FACRRM

A thesis submitted in fulfillment of the requirements for the degree of Doctor of Philosophy, Australian National University.

Declaration

I hereby certify that the work presented herein is the result of original research and is not being submitted for a higher degree to any other university or institution. All laboratory work was principally carried out by the author, with some assistance, as noted in the acknowledgments on page 4.

…….……. …….

Ko-Chin Chen Date

Ethics Clearance

The studies described in this thesis were approved by the ACT Health Human Research Ethics Committee (ACTH-HREC) and Australian National University Animal Experimentation Ethics Committee (ANU-AEEC), project number A2011/67. All tissues and animals used were handled with strict adherence to the ethical requirements.

Dedications and Acknowledgements

Dedications

To my family, who was patient with me for my preoccupation and absences.

And to all the friends and mentors who gave me the supports and encouragement to pursue my interests.

Acknowledgments

The author wishes to thank:
John Curtin School of Medical Research and Australian National University for laboratory support and animal facility.
The Applied Mathematics Department of Australian National University for their technical supports on Micro-CT operation. I am especially grateful to Dr. Michael Turner for micro-CT operation and Prof. Timothy Senden for technical advice on micro-CT principles and protocols.
The members of Paediatric Surgical Lab and Animal Care Facility at the Canberra Hospital, Woden for their ongoing animal care and laboratory supports.
Prof. Alon Arad of University of Houston for mathematical background and principles of image processing and analysis.
Dr. Zan-Min Song of John Curtin School of Medical Research for technical supports on genotyping, background of spotting-lethal rat and Hirschsprung disease.
Dr. Lavinia Hallam of Pathology department at the Canberra Hospital for microscopy supports and tissue processing.
Ms. Ko-Chien Chen of University of Texas MD Anderson Cancer Centre for manuscript editing, experimental inputs, and statistical supports.
Mr. Timothy Harris of Automated Analytics for technical implementations of image processing protocols.
Ms. Allison Gee of Australian National University Medical School for inputs on morphological analysis.

And lastly and importantly, Prof. David Croaker of Australian National University and the Canberra Hospital, for his ongoing inspiration, guidance, and patient supports over past number of years.

List of abbreviations:

AA: aortic arch

a.a.: amino acid

ABCD syndrome: albinism, black lock, cell migration disorder of enteric nervous system, and deafness.

AChE: acetylcholinesterase

ACTH: adrenocorticotrophic hormone

Ang II: angiotensin II

ANP: atrial natriuretic peptides

ANU-AEEC: Australian National University Animal Experimentation Ethics Committee

ACTH-HREC: ACT Health Human Research Ethics Committee

AGWN: Additive Gaussian White Noise

AP-1: activator protein-1

ASD: atrial septal defect

ATP: adenosine triphosphate

AV node: atrioventricular node

AVP: arginine vasopressin

BBS: Barder-Biedl syndrome

big-ET: big-endothelin

BM3D: block-matching 3-dimensional

BNP: brain natriuretic peptides

BP: blood pressure

BrdU: 5-bromo-2'-deoxyuridine

CaNCC: cardiac neural crest cell

cAMP: cyclic adenosine monophosphate

CA1: CA1 field of hippocampus

CA3: CA3 field of hippocampus

CAS: cardiovascular system

CATCH 22 syndrome: cardiac defects, abnormal facial features, thymic hypoplasia, cleft palate, and hypocalcaemia syndrome

cc: corpus callosum

CCD: X-ray coupled-charged device

cDNA: complementary DNA

Cer: cerebellum

Cg: cingulate gyrus

CHD: congenital heart disease

CLSM: confocal laser scanning microscopy

CNCC: cephalic neural crest cell

CNS: central nervous system

CNTF: ciliary neurotrophic factor

Coch: cochlea

CPU: computational-processing-unit

CRH: corticotrophin-releasing hormone

CSF: cerebrospinal fluid

CX32: connexin-32

DAG: 1,2-diacylglycerol

DICOM: digital imaging and communications in medicine

dNTP: deoxyribonucleotide triphosphate

DS: Down syndrome

DSD: detector-sample distance

ECE: endothelin converting enzyme

ECE-1: endothelin converting enzyme-1

ECE-2: endothelin converting enzyme-2

ECG: electrocardiography

EDN1: endothelin-1 gene

EDN2: endothelin-2 gene

EDN3: endothelin-3 gene

EDNRA: endothelin A receptor gene

EDNRB: endothelin B receptor gene

EDRF: endothelium-relaxing factor

EGF: epidermal growth factor

ELISA: enzyme-linked immunosorbent assay

ENaC: epithelial sodium channel

ENCC: enteric neural crest cell

End: endopiriform nucleus

ENS: enteric nervous system

ER: endoplasmic reticulum

ERK: extracellular signal-regulated kinase

ET_A: endothelin A receptor

ET_B: endothelin B receptor

ET_C: endothelin C receptor

ET_R: endothelin receptor

ET: endothelin

ET-1: endothelin-1

ET-2: endothelin-2

ET-3: endothelin-3

EtOH: ethanol

Epi: epiglottis

4D: 4-dimensional

5-HT$_{1B}$: 5-hydroxytryptamine receptor

FGF-2: fibroblast growth factor-2

Flk: foetal liver kinase

Flt: *fms*-like tyrosine kinase

FMTC: familial medullary carcinoma

FOV: field of view

FSH: follicle-stimulating hormone

GDNF: glial cell line derived neurotrophic factor

GFR: glomerular filtration rate

GFRα1: glycosyl phosphatidylinositol (GPI)-anchored cell surface protein

GI: gastrointestinal

GPCR: G-protein coupled receptors

GPGPU: general-purpose graphic processing unit

GPI: glycosyl phosphatidylinositol

GPU: graphics-processing-unit

GRK: G protein-coupled receptor kinase

GSS: Goldberg-Shprintzen syndrome

gsv: grey scale value

HAEC: Hirschsprung's disease-associated enterocolitis

H.b: hyoid bone

HCAD: Hirschsprung disease, cardiac defects, and autonomic dysfunction

H&E: hematoxylin and eosin stain

HMG: high-mobility-group

H. palate: hard palate

HSCR: Hirschsprung disease

ic: internal capsule

ICC: interstitial cells of Cajal

ICU: intensive care unit

IC50: half maximal inhibitory concentration

IDC: infiltrating ductal carcinoma

IL-6: interleukin-6

IL-8: interleukin-8

INC: interkinetic nuclear migration

IP_3: inositol 1,4,5-trisphostate

ir-ET-3: immunoreactive ET-3

IUPHAR: International Union of Pharmacology

Lat rid: lateral ridge of skull

LA: left atrium

LAD: left anterior descending artery

LDL: low-density-lipoproteins

LH: luteinizing hormone

L. Inc: lower incisor

LT: lateral thalamus

LV: left ventricle

M: mandible

MAF: moving average filter

MAP: mean arterial pressure

MAPK: mitogen-activated-protein kinase

Mandi: mandibular gland

Med: medulla

MENIIA: multiple endocrine neoplasia IIA

MEK: mitogen-activated protein kinase

MITF: microphthalmia-associated transcription factor

MitA: mithramycin A

Micro-CT: micro-computed tomography

Micro-MRI: micro-magnetic resonance imaging

MKKS: McKusick-Kauffman syndrome

mRNA: messenger RNA

MWS: Mowat-Wilson syndrome

NasCa: nasal cavity

Nasop: nasopharynx

NCC: neural crest cell

NCI: National Computational Infrastructure

NetCDF: network Common Data Form

NGF: nerve growth factor

NID A: neuronal intestinal dysplasia type A

NID B: neuronal intestinal dysplasia type B

NLM: non-local-means processing

NMR: nuclear magnetic resonance

NO: nitric oxides

NPC: neural progenitor cell

NTN: neurturin

OB: olfactory bulb

OFT: cardiac outflow tract

OPT: optical projection tomography

Orb: orbital cortex

PAA: pharyngeal arch arteries

PAH: pulmonary arterial hypertension

PAX3: paired box gene 3

$PaCO_2$: arterial partial pressure of carbon dioxide

PaO_2: arterial partial pressure of oxygen

Parot: parotid gland

PBS: phosphate-buffered saline

PDGF: platelet-derived growth factor

PET: positron emission tomography

PGI_2: prostacyclin

Pir: piriform cortex

Pit: pituitary gland

PLC: phospholipase C

PMN: polymorphonuclear cell

PNS: peripheral nervous systems

prepro-ET: preproendothelin

PS: pixel size

PSNR: peak signal to noise ratio

PTA: phosphotungstic acid

RA: right atrium

RET: receptor tyrosine kinase

ROS: rostral ridge of skull

RP-HPLC: reverse-phase high-performance liquid chromatography

RT-PCR: reverse transcription polymerase chain reaction

RV: right ventricle

S1BF: Somatosensory 1 Barrel Field

SAH: subarachnoid haemorrhage

Sal. Gland: salivary gland

S&I Col: superior and inferior colliculus

sl/sl: spotting-lethal

S. palate: soft palate

STEP: serial transverse enteroplasty procedure

Sterno: sternomastoideus

SDD: source-detector distance

SEM: scanning electron microscopy

sem: standard error of the mean

SIP1: Smad interacting protein 1

SLO: Smith-Lemli-Opitz syndrome

SOX10: SRY-related high-mobility-group box transcription factor

SS: spot size

SSD: sample-source distance

ssd: sum of squared differences

2D: 2-dimensional

3V: 3rd ventricle

3D: 3-dimensional

TAB: transabdominal

TBr: total brain

T-CC: total cerebral cortex

T-CP: total caudate putamen

TER: transanal endorectal

Temp: temporalis

TGF- β: transforming growth factor β

TMeAVP: l-(β-mercapto-β, β-cyclopentamethylenepropionic acid), 2-(O-methyl)-tyrosine]

AVP

tmENCC: trans-mesenteric enteric neural crest cell

Tong: tongue

Trac: trachea

TSH: thyroid stimulating hormone

TYRP1: tyrosine-related protein 1

$T_{1/2}$: half-life

U. Inc: upper incisor

VIC: vasoactive intestinal contractor

VEGF: vascular endothelial growth factors

VSD: ventricular septal defect

VSMC: vascular smooth muscle cell

VT: ventral thalamus

vt: ventricular tachycardia

WS: Waardenburg syndrome

WS IV: Waardenburg syndrome type IV or Shah-Waardenburg syndrome

Thesis Abstract:

HSCR has long been regarded as an enteric disease for its well-known colonic aganglionosis. However, the fact of it being a polygenic neurocristopathy begs the question: is structural growth retardation a more general feature in HSCR individuals? To clarify, we examine the multi-organ changes within the *sl/sl* rat, which is an autosomal recessive HSCR model with high genetic penetrance that arises from ET_B knockout mutation.

This thesis contributes to improving our understanding in modified soft tissue imaging workflow and multi-systemic changes associated with HSCR using an animal model.

A. Imaging methodology:

1. Micro-CT scanning can be a useful structural-preserving visualization tool for studying external morphology, neuroanatomy, and cardiovascular anatomy in small animals.
2. Successful micro-CT scanning of soft tissue requires contrast staining, which can be achieved with iodine or PTA. Iodine is a more effective and safer choice among the two.
3. *Ex vivo* micro-CT scans can offer structural details comparable to those of 4x H&E light micrographs.
4. Image degradation of *in vivo* micro-CT scan can be improved by raising the voltage and/or current of X-ray source.
5. Post-acquisition NLM filtering is an effective enhancement technique for *in vivo* micro-CT scans.

B. Global structural changes associated with HSCR model:

1. The HSCR model, *sl/sl* rat, is associated with subtle body growth impairment during

early life; this impairment may progressively worsen with age.

2. The craniofacial changes in *sl/sl* rat share some resemblances to those seen in domestication syndrome, including a flatter cranium, a smaller maxilla, a larger mandible, a disproportionally shorter but wider nose, a shrunken molar bed and reduced superior incisor dimensions. It may therefore be prudent to suspect that HSCR patients may have similar dysmorphology and thus increased risks for obstructive sleep apnoea and dental malocclusion.
3. *sl/sl* rat has a grossly normal neural morphology with intact constituents; however, significant structural reductions of 20.33% in brain volume and 7.35% in brain growth rate are detected. Similar reductions are seen in cerebral cortex, caudate putamen, olfactory bulb, medulla, and pituitary gland. These findings suggest that HSCR patients may exhibit varying degrees of brain reductions and subsequent neurological dysfunction, either subtle or overt.
4. Despite having an impaired endothelin signalling, congenital conotruncal cardiac malformations are not detected in *sl/sl* rat.
5. Cardiac morphology is grossly normal in *sl/sl* rat; however, marked reductions are detected in heart volume (40%), growth rate (20%), and organ volume/bodyweight index (25%). Measurements of LA, LV, RA, and RV share similar reducing trends. Our findings are not only consistent with prior notions that HSCR patients have elevated risks for congenital heart diseases, but also suggest that structural cardiac anomaly may be a more general feature. Thus, long-term follow-up and systematic assessments may be recommended clinically.

The above findings support the concept that HSCR, at least with the $ET_B^{-/-}$ subtype, is likely a

multi-organ condition, with significant changes to craniofacial, neurological, and cardiovascular systems.

Publications and presentations directly arising from the thesis

Publications:

Chen KC, Arad A, Song ZM, Croaker GD. High-definition neural visualization of rodent brain using micro-CT scanning and non-local-means processing. *BMC Med Imaging* 18, 38 (2018). https://doi.org/10.1186/s12880-018-0280-6

Chen KC, Arad A, Song ZM, Croaker GD. High-Definition Heart Visualization using Micro-CT Scanning on Experimental Rats. *J Clin Exp Cardiolog* 2018;9(606). DOI: 10.4172/2155-9880.100

Chen KC, Song ZM, Croaker GD. Brain size reductions associated with endothelin B receptor mutation, a cause of Hirschsprung's disease. *BMC Neurosci* 22, 42 (2021). https://doi.org/10.1186/s12868-021-00646-z

Chen KC, Chen KC, Song ZM, Croaker GD. Structural heart defects associated with ET_B mutation, a cause of Hirschsprung disease. *BMC Cardiovasc Disord* 21, 475 (2021). https://doi.org/10.1186/s12872-021-02281-2

Presentations:

"Investigating the Domesticated Human – Obscure Associations of Hirschsprung Disease."- 23rd International Meeting of the Paediatric Colorectal Club (2016), Prague, Czech Republic.

"Intracranial imaging of the spotting lethal rat using Micro-CT scanning" accepted for 26th International Symposium of Paediatric Surgical Research, Cape Town, South Africa.

"A new method for the investigation of the CNS of the lethal spotting rat" accepted for 4th World Congress of Paediatric Surgery (WOFAPS 2013) Organizing Committee in October 2013, Berlin, Germany.

Table of Contents

List of Tables:

Chapter 2:

Chapter 3:

Chapter 3.2:

Chapter 4:

List of Figures

Chapter 2:

Chapter 3:

Chapter 3.1:

Chapter 3.2:

Chapter 4:

Chapter 5:

Chapter 6:

<u>Supplementary Tables:</u>

Chapter 3.1:

Chapter 4:

Chapter 5:

Chapter 6:

<u>Supplementary Figures:</u>

Chapter 3.1:

Chapter 6:

Chapter 1: Aim of the thesis

To investigate multi-systemic changes associated with Hirschsprung disease through quantitative imaging analyses on the structural variations in an $ET_B^{-/-}$ genetic model, spotting-lethal rat.

1.1. Definition

1.2. Hypothesis

1.3. Specific predictions

1.1. Definition

Hirschsprung disease (HSCR) is a polygenic neurocristopathy, traditionally known for its segmental colonic aganglionosis. It arises from the migration failure of neural crest cells during embryonic development. One of the significant genetic causes is the homozygous knock-out mutations in endothelin B receptor (ET_B) gene, which results in HSCR-associated type IV Waardenburg syndrome (WS-IV). For this thesis, we adopted spotting-lethal *(sl/sl*) rat as the HSCR model for studying the disease's multi-organ associations.

1.2. Hypotheses

While organ dysfunctions in various clinical syndromes have been suggested to associate with HSCR, little is known about the structural changes in non-syndromic patients. ET_B, a major cause of HSCR and a pivotal receptor in the endothelin regulatory system, has been implicated in mediating multiple key organ developments. Given the neurocristopathy nature of HSCR and ET_B's regulatory roles, I propose that HSCR animals with $ET_B^{-/-}$ subtype will not only suffers the aganglionic disease but also structural and growth changes in craniofacial morphology, central nervous system, and cardiac system.

This thesis seeks to support multi-organ involvements in HSCR model by:

A. Devise a high-resolution imaging workflow with adequate soft-tissue contrast for anatomical visualization and quantitative measurements.
B. Define the potential craniofacial changes associated with $ET_B^{-/-}$ HSCR model; these changes associated with ET_B mutation may resemble features of domestication syndrome.
C. Define the structural changes and growth impairments in the central nervous system

of $ET_B^{-/-}$ HSCR model.

D. Define the cardiovascular structural changes associated with $ET_B^{-/-}$ HSCR.

1.3. Specific predictions are that

A. Micro-CT scanning with modified iodine or PTA staining protocols can provide detailed anatomical visualizations for quantitative analysis.

B. The signal-to-noise ratio of micro-CT images can be maximized through contrast staining, x-ray source adjustments, and post-acquisition image filtering.

C. Subtle body growth impairment may be presented in HSCR model during the early stage of life; this impairment may grow increasingly apparent with animal age.

D. Loss-of-function mutation of ET_B may result in subtle morphological changes like features of domestication syndrome.

E. HSCR model of homozygous ET_B knockout mutation may exhibit multiple intracranial structural changes and growth impairments; these impairments are likely to be disproportionally larger than those observed in respective body growth.

F. HSCR model of homozygous ET_B knockout mutation may exhibit significant size impairments in its cardiovascular system despite having a grossly normal morphology.

Chapter 2: Literature review

1. Hirschsprung Disease Background

Hirschsprung disease (HSCR) is a high morbidity and mortality disease deserving more medical and research attention. It has a relatively high global incidence with an average incident of 1/5000 births, comparable to other more publicized diseases, such as acute myeloid leukemia with an incidence of 1/7245 (1).

HSCR is commonly known for its colonic manifestation. However, its multi-genetic pathogenesis and multi-signalling involvements imply multiple organs are likely affected. Indeed, one of the major causes of HSCR is through disruptions in the endothelin system. Disruptions have wide pathological implications, including vasodysregulation, cerebrovascular and cardiovascular diseases, and impaired neurogenesis and angiogenesis. Currently, over 28,000 scientific publications have been completed on endothelin systems. We aim to complement prior findings by studying morphological and anatomical changes associated with endothelin B receptor (ET_B) mutation. Analyses of foetal anatomy is achieved through analyses on the micro-CT scans of spotting-lethal (*sl/sl*) rat, an $ET_B^{-/-}$ HSCR animal model. In this chapter, we will establish the basis and logics behind this series of studies by providing a brief description on the clinical understanding and impacts of HSCR followed by a summary on the endothelin system.

2. History of Hirschsprung disease

Hirschsprung disease (HSCR) is known as congenital megacolon or intestinal aganglionosis. Anatomist Frederick Ruysch first describes the condition in 1691 (2).

Subsequently, the concept of “dilatation and hypertrophy of colon” is popularized by Dr. Harald Hirschsprung in 1886 and formally named Hirschsprung’s disease (3). However, a causative link between aganglionosis and the spastic contraction of the aganglionic segment only became apparent after Whitehouse and Kernohan (1948) and Swenson (1948) demonstrated histological aganglionic distal colon (4-7). Bodian et al (1949) later also confirmed this finding (8).

3. Epidemiology of Hirschsprung disease and associated syndromes

HSCR is a paediatric intestinal aganglionic disease affecting approximately 1/5000 births globally (9). However, regional incidences can range from 1/1370 to 1/7165 births, suggesting ethnicity may be an important determining factor for occurrence (8, 10-12). Up to 80-90% of HSCR cases are syndromic and diagnosed in the neonatal stage (13). 75-80% of these patients have short-segment disease with aganglionosis restricting to rectosigmoid and descending colon. Conversely, up to 15% of these patients have long-segment disease extending to transverse colon and 3-8% of whom have total colonic aganglionosis (14, 15). Lastly, 5% of HSCR are ultrashort-segment disease limiting to distal rectum. (16). Aganglionic colons are bordered proximally by a transition zone, which is formed by reduced enteric neuron and thus hypoganglionosis (17-19).

As a side note, colonic histochemical biopsies of 358 classifiable congenital colorectal innervation defects demonstrate the following disease distribution: aganglionosis (52.2%), hypoganglionosis (5%), neuronal intestinal dysplasia type A (NID A; 2.2%), and neuronal intestinal dysplasia type B (NID B; 40.6%). Among which, NID A is characterized by hypoplastic/aplastic sympathetic innervation in myenteric plexus, submucosal arteries, and

mucosa, whereas NID B is characterized by malformations of the parasympathetic plexus (20). Colonic aganglionosis is further classified into isolated HSCR (22.9%), HSCR with proximal NID B (17.9%), total colonic aganglionosis (2.5%), ultra-short HSCR (5.0%), and neurogenic achalasia of anal sphincter (9.0%). Interestingly, up to half of HSCR cases are associated with NID B and up to one-third NID B cases have HSCR, suggesting both may share common pathogenesis.

HSCR has an overall of 3.5-4.5:1 male predominance (9, 10, 21, 22). The male-to-female incidence ratio is slightly elevated in short-segment disease to 4.2-4.4:1; long-segment disease, on the other hand, has only 1.2-1.9:1 male predominance (14, 21). Siblings of the affected individual have up to 200 times higher risks for developing HSCR than the general population, 4% vs 0.02% (23).

Due to the pleomorphic effects of multi-genetic involvement in HSCR aetiology, up to 30% of patients exhibit various associated abnormalities in central nervous system (CNS; e.g. Down syndrome-DS, congenital central hypoventilation syndrome, Smith-Lemli-Opitz syndrome-SLO, spinal bifida), cardiovascular (e.g. Di George syndrome, velocardiofacial syndrome), endocrine (e.g. Multiple Endocrine Neoplasia IIA-MENIIA), gastrointestinal (GI), genitourinary (e.g. Barder-Biedl syndrome-BBS), craniofacial (e.g. Goldberg-Shprintzen syndrome-GSS), sensorineural (e.g. Shah-Waardenburg syndrome - WS IV), and musculoskeletal systems (e.g. cartilage-hair hypoplasia syndrome) (23-32). Among the HSCR-associated anomalies, Down syndrome is the most common, presented in up to 2-10% of HSCR cases (23, 33).

4. Clinical presentation of Hirschsprung disease

HSCR is commonly known for its clinical manifestations of pseudo-obstruction and associated complications, including death if left untreated. Clinical presentations of HSCR may range from intestinal obstruction in neonates to progressive chronic constipation in older patients (34). Typically, 80% of the affected children exhibit irregular bowel movements, reduced feeding, and worsening abdominal distension within the first few months of life (35).

In infants with HSCR, typical presentations may include, enterocolitis, chronic constipation, poor feeding, bilious vomiting, and jaundice (34, 35). In HSCR children older than 1 month, constipation is the most common, along with other symptoms including progressive abdominal distension, failure to thrive, malnutrition, and faecal loading (14, 35). Counterintuitively, up to one-third of HSCR patients may present with diarrhea, which is secondary to enterocolitis and has a mortality rate as high as 30% (35, 36). failure to pass meconium within the first twenty-four hours of life, acute intestinal obstruction

5. Diagnosis of Hirschsprung disease

Diagnostic workups for HSCR often involve imaging investigations and colonic manometry. Imaging modalities generally have a sensitivity of 80-90% (37). Plain abdominal radiographs can detect proximal bowel dilatation with air-fluid levels to suggest complete or partial bowel obstruction with respective sensitivity of 46% and 30%; however, these are generally late findings of HSCR (38). Barium enema has a sensitivity up to 90% in detecting the transition zone, a hallmark of HSCR. Concurrently, rectosigmoid index (diameter of rectum/diameter of sigmoid colon; ratio < 1 suggests short-segment HSCR) can also be

calculated with barium enema scan and has a sensitivity of 76.7% in diagnosing HSCR (14, 39). The disadvantages of barium enema, however, are that transition zone may be absent in up to 25% of neonates (age < 1-month-old) and contrast administration may be contraindicated in patients with acute enteritis (40, 41). Moreover, anorectal manometry has been used to detect the absence of inhibitory reflex in internal sphincter relaxation following rectal distension in HSCR. This technique has a sensitivity ranging between 79% and 95%; however, it is only useful in neonates aged 12 days or older when rectoenteric reflex has developed (42, 43). Furthermore, anorectal manometry is also a reliable measure for functional outcomes post-therapy (e.g. Swenson's operation) and surgical planning for HSCR (44-46).

The gold standard for the diagnosis of HSCR involves rectal suction biopsy or full-thickness rectal biopsy followed by hematoxylin and eosin (H&E) stain, acetylcholinesterase staining, and/or calretinin immunohistochemistry (47-50). Due to the presence of normal hypoganglionic zone, the biopsy should be taken at > 1.5 cm above the dentate line for sufficient ganglion cells in the submucosal plexus (51). Bedside rectal suction biopsy is simple and can be performed without anaesthesia. Hence, it is currently the method of choice, although its sampling is limited to surface submucosal nerve plexus, reducing its diagnostic value (47, 48). Full-thickness biopsy with intramuscular nerve plexus sampling is recommended for patient with more than one inconclusive suction biopsy (52).

Tissue preparations following biopsy are tailored for different procedures. Typical H&E requires tissue-fixation in formalin and followed by standard staining protocols (53). Although H&E staining remains to be the method of choices for identifying the ganglion cells

in mucosa and submucosa, it is time consuming. Furthermore, to ensure adequate specificity, analysis on hundreds of histological sections is often required. To complicate things further, the identification of ganglionic cells in neonate can be challenging with H&E technique. To improve diagnostic accuracy, histochemical staining such as acetylcholinesterase (AChE) and calretinin are often adopted.

Current AChE histochemical staining protocols are developed from techniques originally described by Karnowsky and Roots in 1964 (54). Detections of increased AChE activity in lamina propria and muscularis mucosa in aganglionic segment is pathognomonic of HSCR. Additionally, various modifications and interpretation criteria on AChE staining have been made to improve diagnostic accuracy of aganglionosis, up to 99-100% (47, 55, 56). However, false negative result has been reported in infants under three-months-old presenting with HSCR, up to 15%; hence, the absence of abnormal AChE activity in neonates under the age of 3 weeks does not exclude HSCR based on current diagnostic criteria (57, 58).

To improve the sensitivity of HSCR detection, calretinin immunohistochemistry is first suggested by Barshack et al (2004) (59). Calretinin is a calcium-binding protein mediating calcium signalling pathway thus the development of central nervous system (60). Calretinin immunostaining can be carried out on a formalin-fixed superficial biopsy. Its interpretation is unambiguous: absence of calretinin reaction in nerve fibres correlates with aganglionosis in HSCR. This method has a sensitivity up to 98% (50, 59, 61); however, its utility for ultra-short HSCR remain to be determined.

6. Current treatments options for Hirschsprung disease

The aims of current HSCR managements are to maintain or restore colonic functions, prevent bowel obstruction or perforations, and treat potential complications including electrolyte and nutritional deficiencies.

Surgical resection of diseased colon is currently the definitive treatment for HSCR. Traditionally, resection is completed by an abdominoperineal pull-through operation in three-stages. The initial reversible colostomy at the time of diagnosis aims to decompress the dilated bowel. This is followed by a delayed transabdominal pull-through surgery after optimising the patient's physical conditions, usually when the child grows to a weight of 8-10kgs. Finally, the colostomy is closed after anastomosis of ganglionic colon to the anal canal (62). The theory behind diverting colostomy prior to definitive pull-through procedures offers maximal protection against wound dehiscence and reduces post-operative complications. However, single-staged pull-through procedures have become progressively more favourable with evidences showing no increases in complication rates (62-64). Currently, several standard single-staged pull-through procedures have been performed: Swenson, Duhamel, and Soave and Boley procedures (65-68).

6.1. Swenson Procedure

Swenson's procedure is first performed in 1948 by Swenson and Billah (65). It serves as the fundamental basis of all HSCR operative variants. Its principle involves an end-to-end anastomosis of ganglionic bowel to functional rectum after resecting out the diseased bowel. With careful dissection, this procedure preserves the pelvic nerves and anal sphincter. Furthermore, complications rate and stricture formation risks can be reduced by avoiding the

dissection of rectum from puborectalis complex and the construction of oblique circumferential anastomosis (65). Currently, Swenson's procedure can be completed through either transabdominal (TAB) or transanal endorectal (TER) approaches; recent evidences have suggested TER approaches yield slightly lower post-operative complication rates (69-71).

6.2. Duhamel procedure

Duhamel procedure is first described in 1956. It is a technical variant of Swenson's procedure with the advantages of avoiding extensive rectum resection and pelvic dissection, thereby preserving complete neuro-muscular complexes of bladder and anal sphincter. The diseased colon is resected with normal colon pulled through the rectrorectal space to create an end-to-side anastomosis to the isolated aganglionic rectum (66). This procedure creates a large anastomosis which reduces stricture-formation risks. Furthermore, the creation of a large "neorectum," which consists of aganglionic colon anteriorly and ganglionic colon posteriorly, provides a helpful "reservoir" for colonic contents in patients with long-segment disease (72).

6.3. Soave and Boley procedures

Soave procedure is introduced in 1964 to minimize the risks of neurovascular injury associated with traditional Swenson's procedure. In this procedure, transabdominal dissection is performed in the submucosal plane to enable endorectal pull-throughs of ganglionic colon through the muscular cuff of aganglionated rectum (68). This surgical approach avoids extensive intra-pelvic dissection and therefore prevents the damage to the pelvic autonomic nervous system. The original Soave procedure leaves the pull-through

colon external to anus for autoanastomosis. This is later modified by Boley (1964) to a single-stage coloanal anastomosis at the time of pull-through (67).

6.4. Other surgical variants

Other less prevalent surgical approaches for HSCR have also been described. For instance, State reported an anterior resection approach in 1952, which involves the resection of aganglionic large colon to the splenic flexure while avoiding the mobilization of the rectum (73). In the following year, Rehbein modified State's technique to include an extraperitoneal and intra-abdominal anastomosis between the colon and rectum following low-anterior resections of rectosigmoid, 2 cm below the peritoneal reflection. This is followed by vigorous sphincter dilatation for sphincter achalasia, which is frequently associated with congenital megacolon (74). Furthermore, following the advancement of laparoscopy, Georgeson performed the first laparoscopic pull-through surgery for HSCR in 1995, which results in similar surgical outcomes but shorter hospital stays comparing to the traditional open procedures (75).

Lastly, the surgical treatment options for long-segment HSCR depend on the length of aganglionic bowel involved. Reconstructive approaches such as standard pull-through (e.g. Swenson, Duhamel, Soave-Boley), colon patch, or J-pouch are considered for colonic aganglionosis with normal small intestine (72, 76). On the other hand, for HSCR patient with short bowel syndrome, bowel-lengthening techniques such as Binachi, serial transverse enteroplasty procedure (STEP), or intestinal transplant are suggested to have modest outcomes (77-79).

7. Postoperative care for Hirschsprung disease

Managements and monitoring for postoperative complications are important to ensure recovery and good quality of life. Short-term postoperative complications include Hirschsprung's disease-associated enterocolitis (HAEC), colonic/rectal strictures, anastomotic leak, perianal excoriations, pelvic abscess, bowel obstruction, wound dehiscence, wound infection, rectovesical or rectovaginal fistulas. On the other hand, up to 15% of patients develop persisting symptoms following initial surgery in the long term (80).

HAEC is the most common postoperative complications following pull-through procedures. It has been suggested that risks of enterocolitis can be reduced by routine post-operative rectal irrigation with normal saline and administration of prophylactic antibiotics such as metronidazole (81, 82). Additionally, potential beneficial effect of probiotics against HAEC have also been suggested (83). Indeed, this is supported by a randomized trial by Wang et al (2015) demonstrating four weeks of triple probiotic regimens (*Bifidobacterium*, *Lactobacillus acidophilus*, and *Enterococcus) not only* reduces the incidence and severity of HAEC but also increases anti-inflammatory cytokines IL-10 (84). However, further supporting studies are required.

The managements of HAEC depends on its severity. Acute HAEC can be classified into three grades based on its classic manifestations of abdominal distension, diarrhea, fever, and hemodynamic compromises. Grade I case consists of potential HAEC patients with mild symptoms. These patients can be managed as outpatients with oral metronidazole, electrolyte-rich hydration, and close monitoring. Grade II cases are confirmed HAEC patients requiring hospital admissions for oral or intravenous hydration, broad-spectrum antibiotics

(and metronidazole), rectal irrigation, and potential nasogastric decompression for any significant abdominal distension. Grade III patients are severe HAEC cases with hemodynamic compromises requiring admission to intensive care unit (ICU) for bowel rest, rectal irrigation, intravenous fluid, and broad-spectrum antibiotics. In severe cases or detection of pneumoperitoneum, surgical diversion or exploration is warranted (82, 85).

For patients with recurrent HAEC, in addition to immediate symptomatic managements, clinical revaluations are required to determine the underlying anatomical or physiological causes. Currently, the efficacy of medical treatments such as the use of prophylactic antibiotic lacks strong supporting evidence. On the other hand, Rinatala and Lindahl (2001) demonstrated the use of sodium cromoglycate, a mast cell stabilizer, can improve HAEC symptoms (86). Expectedly, surgical re-corrections are indicated for patients suffering recurrent HAEC from known anatomical causes, including stricture formation, kinked anastomosis, dilated residual aganglionic segments, obstructive Soave muscular cuff, or enlarged Duhamel pouch. On the other hand, treatment options for physiological or unknown causes are of limited efficacy. For patients with internal anal sphincter or achalasia, intrasphincteric botulinum toxin injection have been shown to reduce hospital admissions but only with short-term improvements; repeated injections are often required (87-89). Furthermore, a small number of studies have shown posterior myotomy/myectomy or internal sphincterotomy can improve obstructive symptoms in recurrent HAEC, with up to 75% response rates (90-92). Lastly, diverting ileostomy or colostomy is indicated for patients with refractory HAEC.

8. Pathogenesis of Hirschsprung disease

The commonly known pathology of HSCR stems on the developmental failure of enteric nervous system (ENS). The pathogenesis of this failure is secondary to the migration failure of enteric neural crest cells (ENCC) to the growing gastrointestinal (GI) tract. The maturation of ENCC is pivotal to the development of myenteric and submucosal plexuses. The ENCC is derived mainly from vagal crest cell with a minor contribution of ~17% from sacral crest cells, which migrates to distal hind gut (93). The migration failure of ENCC ultimately results in variable lengths of hypoganglionic and aganglionic colon (4). These hypoganglionic/aganglionic bowel segments cause hypokinesis of bowel movement and thus obstructions.

8.1. Embryology of gastrointestinal (GI) tract

GI tract is derived from the endoderm of embryo during foetal development. It is classified into three regions based on vascular distributions: foregut, midgut, and hind gut. Foregut is supplied by the celiac trunk. It gives rise to the alimentary tract between the mouth and anterior two-thirds of duodenum with a boundary marked by ampulla of Vater, biliary system, anterior segment of pancreas, and parts of lower respiratory tract. The midgut is supplied by the superior mesenteric artery and forms the distal one-third of duodenum, jejunum, ileum, caecum, appendix, ascending colon, and proximal two-thirds of transverse colon. Finally, the hind gut consists of distal one-third of transverse colon, descending colon, rectum, and superior part of anal canal; it is supplied by the inferior mesenteric artery. For a GI tract to perform peristalsis, control of vascular flow, digestive functions, and maintaining adequate physiological fluid balance, a functional ENS is required (94).

8.2. Enteric nervous system (ENS) and components

ENS is the largest component of peripheral nervous systems (PNS) directly controlling the GI tract and its functions (95). The ENS compromises of outer Auerbach plexus (myenteric) and inner Meissner (submucosal) plexus. These plexi are comprised of interconnected enteric ganglia, which are formed by ENS neurons and glia. The Auerbach plexus develops first and spans across entire GI tract to control the gut motility. On the other hand, development of Meissner plexus occurs 2-3 weeks after the formation of Auerbach plexus; it has limited distribution to small and large intestine. Meissner plexus functions to fine-tune the intestinal motility, circulation, and interepithelial ion transport.

The gut motility is controlled by a combination of enteric ganglia and regional cells, such as interstitial cells of Cajal (ICC). ICC generates and propagates the slow wave potential leading to smooth muscular contractions whereas ENS modifies intestinal movement by fine tuning contraction and relaxation (96). Consistently, the absence of enteric ganglia results in disinhibition of uncontrolled smooth muscle contraction in aganglionic bowel segment due to the predominance of cholinergic over adrenergic stimulation by the extrinsic neural afferent. This manifests as the functional bowel obstructions and forms the basis of HSCR, a neurocristopathy.

8.3. Neural crest cell migration failure in Hirschsprung disease

HSCR, a neurocristopathy, is a disease arise from defective NCC developments. The source of ENCCs for the ENS development originates from vagal (somite 1-7) and sacral (caudal to somite 24) neural crests cells. Vagal neural crest cells first migrate from cranial to caudal axis along the GI tract to sequentially colonize the foregut, midgut, and hindgut. Following the colonization of vagal neural crest cells, sacral neural crest cells enters the distal

hindgut (97, 98). In humans, the duration of ENCC migration lasts up to three weeks, between week-4 and week-7, whereas similar process in mice only lasts six days, from embryonic day (E) 9 to 14.5 (99, 100).

The ENCC colonization process is led by a migratory wavefront, which consists of multipolar and monopolar cells (101, 102). The wavefront cells exhibit high caudal expansion capabilities than the trailing cells and therefore play a significant role in hindgut colonization. However, the hindgut colonization is mainly supported by trans-mesenteric ENCCs (tmENCCs), which traverse the mesentery during the juxtaposition of midgut and hindgut. This hindgut colonization is finalized by partial contribution from sacral-NCCs (98). Since the juxtaposition of midgut and hindgut is limited to E10.5-11.5, a full ENS colonization in hindgut has limited temporal window of opportunities (102). On the other hand, Barlow et al (2012) has demonstrated that complete formation of ENS is possible even with delayed ENCC migration beyond E14.5, suggesting permissive window of colonization may not be as strict as once thought (103).

9. Polygenetic associations of Hirschsprung disease

Several genetic mutations have been identified in the pathogenesis of HSCR and associated syndromes. Currently, ten common affected genes have been identified and contributed to ~50% of total HSCR cases. These include receptor tyrosine kinase (RET), glial cell line derived neurotrophic factor (GDNF), glycosyl phosphatidylinositol (GPI)-anchored cell surface protein (GFRα1), neurturin (NTN), SRY-related high-mobility-group (HMG) box transcription factor (SOX10), endothelin B-receptor (ET_B), endothelin-3 (ET-3), and endothelin converting enzyme-1 (ECE-1) genes (104-115).

9.1. GDNF, RET and GFRα1 pathway

Mutations in GDNF, RET and GFRα1 pathway are the major contributors to HSCR development known currently. Major mutations in RET proto-oncogene, located on chromosome 10q11.2, account for 50% of familial HSCR and 15-20% of sporadic cases (116, 117). On the other hand, mutations of GDNF gene, located on chromosome 5p13.2, are much rarer, causing 0.9% to 5.5% of all HSCR cases (105, 106, 118, 119). Furthermore, although mutation in GFRα1 gene, located on chromosome 10q25-26, has a theoretical potential in causing HSCR, this hypothesis currently lacks supporting evidence (120, 121). Current understanding of the GDNF/GFR α1/RET pathway involves GDNF, a secreted ligand, first forming a complex with GFRα1, which then binds with RET to form an activated complex (122). Subsequently, activated RET autophosphorylates and activates the downstream pathway, promoting ENCC proliferation, survival, apoptosis, migration, and differentiation (117).

This GDNF/RET/GFRα1 pathway is tightly regulated by the spatiotemporal expression of GDNF in the mesoderm. As NCCs entering the gut forming ENCCs, both RET and GFRα1 are expressed in the ENCCs. The migration of ENCCs follows the spatial- and temporal-dependent expression of GDNF from foregut to hindgut (123). Failure in the expression of the three subunits results in ENCC and tmNCC migration failure, which ultimately leads to aganglionosis (102, 124).

9.2. SOX10 pathway

SOX10 gene, located on chromosome 22q13.1, has been well known for regulating the development of neural crests and oligodendrocytes (125). Less than 5% of syndromic and

non-syndromic HSCR are due to mutations in *SOX10*. Past studies suggest that the pathological mechanism behind the *SOX10*-induced HSCR, growth retardation, and dysfunctional nervous system follows haploinsufficiency with incomplete penetrance (108, 126-128).

SOX10 is essential not only for peripheral gliogenesis but also for regulating neuronal differentiation through prolonging the NCC's multi-potency phase (129-131). SOX10 is a transcription factor sharing the same family as SOX8 and SOX9. It is mainly expressed in vagal NCCs during the migration phase (132). SOX 10, similar to SOX 8 and SOX9, contains a well-known DNA-binding motif, the HMG domain(133). In addition, they also have a less-known transactivation domain in the C-terminal and a dimerization domain positioned in front of the HMG domain (134, 135). These domains activate downstream genes through monomeric or dimeric DNA binding in addition to transactivation mechanisms (134). Through these mechanisms, SOX 10 alters the expression of key genes including RET, ET_B, microphthalmia-associated transcription factor (MITF), paired box gene 3 (PAX3), tyrosine-related protein 1 (TYRP1), connexin-32 (CX32), and ciliary neurotrophic factor (CNTF). Ultimately, these processes regulate the development of ENS, melanocytes, and neuroglia (136-141). Consistently, mutations in *SOX10* gene have been known to cause HSCR-associated syndrome WS-II and WS-IV (128).

9.3. ET-3, ECE-1, and ETB pathway

Mutations in ET-3, ECE-1, and ET_B signalling pathway contribute to approximately 5% of HSCR cases and associated WS-IV syndrome (33, 142). ET-3, ET_B, and ECE-1 genes are located on the following respective chromosomal positions: *20q13.32, 1p36.1* and *13q22.3*

(143-145). The true impact of endothelin disruption on HSCR prevalence is likely underestimated as increasing studies demonstrating newly found ET_B mutations in HSCR patients (113, 146-148).

The ET-3/ECE-1/ET_B signalling not only regulates the ENCC migration but also reversibly inhibits premature differentiation of multi-lineage ENS progenitor cells (132, 149). This pathway involves the activation of ET_B on ENCC through its binding with ET-3, which is expressed in the developing intestinal mesenchyme (150). In this process, activation of ET-3 is achieved by post-translational proteolytic modification by ECE-1 on big ET-3 (110, 151). Consistently, mutations in any of these genes have been found to cause Hirschsprung disease Type II (HSCR II) or WS-IV (110, 142).

Waardenburg syndromes (WS) are a group of genetic disorders consist of sensorineural and pigmentary defects. WS has an estimated prevalence of 1 in 42,000 people and account for 1.43% of the congenital deaf population (27). Based on symptomatology, WS is diagnosed and classified into four subtypes, WS-I, -II, -III, and -IV (152). WS-I and WS-II have similar incidence and are more common than WS-III and WS-IV. (153). WS-I and WS-III are caused by loss-of-function mutations in PAX gene, which is located at chromosome 2q36.1; both syndromes follow autosomal dominant inheritance (154-157). In addition to congenital sensorineural hearing loss, WS-I is typified by telecanthus whereas WS-III presented with WS-I features and limb abnormalities (152). WS-II is an autosomal dominant pigmentary disorders with the absence of dystopia canthorum (142). WS-II is caused by mutations in *MITF* gene, located at chromosome 3p13 (158). WS-IV, also known as Waardenburg-Shah syndrome, has an additional distinctive component of failed enteric

nervous system.

Three subtypes of WS-IV have been described based on the mutations of affected genes in ET-3/ECE-1/ET_B signalling pathway: WS-IVa, WS-IVb, and WS-IVc. WS-IV is generally inherited in autosomal dominant fashion with variable penetrance; however, some cases do follow autosomal recessive inheritance (159-161). WS-IVa is caused by either homozygous or heterozygous mutations in ET_B gene, result in ABCD syndrome (albinism, black lock, cell migration disorder of enteric nervous system, and deafness) with increased HSCR risks (160). WS-IVb is due to homozygous or heterozygous mutation of the ET-3 gene, which causes neurocristopathy with phenotypes of bilateral sensorineural hearing deficits, HSCR, and depigmentation (162-164). Lastly, WS-IVc has typical WS-IV phenotypes but with increased propensity for short-segment HSCR; it is caused by mutations in *SOX10* gene (108, 128, 162, 165).

10. Endothelin System

Endothelin (ET) are 21-amino-acid peptides originally identified in 1988 as potent vasoactive peptides opposing the vasodilatory actions of atrial natriuretic peptides (ANP) and nitric oxides (NO). It is isolated from the cultured endothelial cells of porcine aorta (166). Discovery of two additional isopeptides, ET-2 and ET-3, occurred shortly after the initial discovery of ET-1. ET-2 and ET-3 differ from ET-1 by two and six amino acids, respectively. Consequently, three distinct ET genes, *EDN1*, *EDN2*, and *EDN3*, are identified to be responsible for the production of these pharmacologically distinctive 21-amino-acids isopeptides, ET-1, ET-2, and ET-3 respectively (167).

The production of ET is a multi-step process and involves two classes of proteases, as illustrated by Figure 1. This process is initiated by transcription of *EDN* gene, which yields a 2.8-kb mRNA encoding a large biologically inactive preproendothelin (prepro-ET) of ~200 residues in human system (166, 168). This prepro-ET transcriptional process is thought to be regulated by three main elements: (i) phorbol ester-responsive element for the binding of *c-fos* and *c-jun* protein complex, which also interacts with activator protein-1 (AP-1), a transcription factor; (ii) binding motif for nuclear factor-1 that mediates mRNA induction by transforming growth factor β (TGF- β); (iii) binding segments for acute phase reactants (169, 170). Next, guided by a 17-aa leader sequence, preproET-1 translocates into endoplasmic reticulum (ER) and enters the secretory pathway (171). Exocytosis of the peptide is initiated by the cleavage of prepro-ET, which is mediated by furin protease (also known as prohormone convertase), into the inactive prohormone, big-endothelin (big-ET) of 37-40-aa peptides (172). Subsequently, big-ET is metabolized by membrane-bound zinc-metalloproteases, which is known as endothelin converting enzymes (ECEs), to form biologically active 21-amino-acid peptides. The formation of ET-1 and ET-2 requires ECEs to cleave off the C-terminals at the Trp-Val sites where as cleaving for ET-3 occurs at Trp-Ile site (172-174). Active ETs mediate their effect through binding with three different receptors ET_A, ET_B, and ET_c (175, 176).

10.1. Endothelin-converting enzymes (ECEs)

ECE are classified into two families, ECE-1 and ECE-2. ECE1 gene contains 20 exons and is located at chromosome 1p36.12 (177). ECE-1 is widely expressed in various cell types including endothelial cells; however, it is not found in neurons. ECE-1 has peak activity at pH 6.8, consistent with its functions as type II membrane-bound metalloprotease that processes

big ET-1 both intracellularly and on the cell (178).

ECE-2, coded by ECE2 gene at chromosome 3q27.1, is subcategorized to ECE-2A and ECE-2B with a difference of an intracytoplasmic tail (179). Unlike ECE-1, ECE-2 is expressed in neurons; however, ECE-1 has a much higher overall bodily expression than that of ECE-2 (180). ECE-2 has an optimum pH of 5.5, suggesting it acts intracellularly. Although both proteases have different optimal pH, both have strong substrate preference toward big ET-1 over big ET-2 or big ET-3, with big ET-1 conversion rates up to 30-folds higher than those of big ET-2 and big ET-3 (181).

As a side note, ECE-1 is a common mediator shared by ET-1/ECE-1/ET_A and ET-3/ECE-1/ET_B signalling pathway; hence mutations in ECE-1 result in severe neurocristopathy including: Hirschsprung disease, cardiac defects, and autonomic dysfunction (HCAD) (110).

10.2. Endothelin-1 (ET-1)

ET-1, first discovered as a potent vasoconstrictor, is the most prevalent isoforms of endothelin in the body and the predominant isoform in the cardiovascular system (166). It is often considered as the parent compound of endothelin family, coded by *EDN1* gene located at chromosome 6p24.1 (182). It consists of 5 exons encoding a 2026 base pair mRNA; exons are spanned across 6838 base pairs (169).

10.2.1. *Pharmacology of ET-1*

Structurally, ET-1 is a 21-aa peptide with an amino-terminus and a flexible hydrophobic carboxyl-tail, which is vital for its agonist potency (166). It also has two

intrachain disulphide bonds between residues Cys^{1} and Cys^{15}, and Cys^{3} and Cys^{11}, respectively (183). Huggins et al (1993) demonstrated a.a. residues 1, 3, 8, 10, 11, 15, 16, 18, 20 and 21 are preserved across all endothelin, a character also shared by Sarafotoxin-6c (S6c), an ET-1 mimic (184). S6c, a potent ET_B agonist, is a cardiogenic toxin released by a*ctraaspis engaddensis* and known to cause cardiac arrest (185). While ET-1 has been found to have the potential in impairing cardiac function and triggering cardiac arrest by mediating atrioventricular (AV) nodal arrest and vasoconstriction of coronary vessels (186, 187), Hua et al (2014) reported homozygous $ET_A^{-/-}$ and $ET_B^{-/-}$ mouse embryos exhibit normal cardiac system with normal electrocardiography (ECG) morphology and QRS intervals (188). These findings suggest cardiac arrhythmia triggered by ET-1 or ET-1 mimics are likely through excitatory rather than inhibitory mechanisms. This is consistent with evidence supporting ET-1 exerts its effect through the activation of G-protein coupled receptors, mainly ET_A and ET_B receptors in mammals (189-191).

10.2.2. *Distribution of ET-1*

ET-1 has been found in multiple organ systems: cardiovascular (192-195), renal (196, 197), central nervous system (CNS) (198), peripheral nervous system (PNS) (199), respiratory (200), gastrointestinal (201), pituitary (202), adrenal (203, 204), nasal (205), immune (206), hepatic (207), genitourinary (208, 209), and endocrine systems (210). It is primarily produced by the endothelial cells and is the only identified vascular endothelin (166). The bioavailability of ET-1 is thought to be controlled mainly by its transcriptional activities. Additionally, post-translational mechanisms such as the presence of regulatory granules, Weibel-Palade bodies, in the endothelial cells have also been demonstrated to increase ET-1 in response to hypoxia, thrombin, and shear-stress. On the other hand, nitric oxide (NO)

inhibits exocytosis of ET-1 from Weibel-Palade bodies (211). Moreover, the production of ET-1 is also contributed by VSMCs during the inflammatory phases in addition to increased synthesis by macrophages, leukocytes, cardiomyocytes, fibroblasts, renal tubules, and brain neurons (212-215). Overall, the production of ET-1 is known to be upregulated by physiochemical factors (e.g. shear stress, exercise, hypoxia), cardiovascular risk factors (oxidized low-density-lipoproteins (LDL) cholesterol, glucose, obesity, thrombin), and inflammatory mediators (e.g. TGF-β, vascular endothelial growth factors (VEGF), angiotensin II (Ang II)) (166, 216-224). On the other hand, its downregulation is induced by the presence of NO, prostacyclin (PGI_2), atrial natriuretic peptides (ANP), brain natriuretic peptides (BNP), oestradiol, and progesterone (223, 225, 226). Although ubiquitous, the plasma concentration of ET-1 is sub-therapeutic under normal physiological circumstance, ~1pM, which is same as that of big ET-1 (227). In addition, given approximately 80% of ET-1 is synthesized by the endothelial cells and being secreted basolaterally, regional ET-1 concentration in VSMCs can be 100 times higher than that of plasma concentration (224). These observations are consistent with that ET-1 mainly exerting its effect in autocrine and paracrine rather than endocrine fashion (227). Lastly, the clearance of plasma ET-1 mainly occurs in the lung, liver, and kidney via endocytosis and subsequent enzymatic degradation of ET_B-endothelin complex (228, 229).

10.2.3. *Physiology and functions of ET-1*

10.2.3.1. *ET-1 functions in embryological development*

ET-1 has multiple physiological functions in embryological development. Through the ET-1/ECE-1/ET_A signalling pathway, ET-1 is vital to the formation of craniofacial features by coordinating normal cephalic and cardiac NCC patterning. ET-1 acts as a chemoattractant for

ET_A-expressed NCCs to correctly colonize pharyngeal arches, which is required to occur by ~E10 in mice for embryo development (230). Mice with ET-$1^{-/-}$ homozygous mutations are incompatible with life due to anoxia from hypoventilation. Furthermore, they exhibit severe dysmorphic craniofacial features including cleft palate, hypoplastic mandible, deformed thyroid cartilage, and absent auditory ossicles (231). Moreover, because tunica media of the developing vessels arise from cardiac NCCs, past studies also demonstrated ET-$1^{-/-}$ homozygotes exhibit significant cardiovascular malformations, including atrial septal defects, ventricular septal defects, hypoplasia of aortic arch, and the absence of right subclavian artery (232). On the other hand, heterozygous ET-$1^{+/-}$ mice is found to be compatible with life and exhibit only mild hypertension (231).

10.2.3.2. *ET-1 functions in cardiovascular system*

ET-1 has profound effects on the cardiovascular systems through its regulations on vascular tone, mitogenesis, and cytokine productions (166, 233, 234). In mammals, the ET-1 vasoregulates through its interactions with ET_A and ET_B receptors (191). Vasoconstriction is mainly mediated by VSMC through ET-1/ET_A signalling pathway whereas vasodilation acts through ET-1/ET_B pathway in the endothelium (235, 236). Indeed, Vuurmans et al (2003) has shown increased central aortic systolic pressure, arterial pressure, and vascular resistance in healthy men following the infusion of ET-1; these effect are ameliorated by the treatment of VML-588, a competitive ET receptor (ET_R) antagonist predominantly targeting ET_A (237, 238). Consistently, Kurihara et al (1994) demonstrated ET-$1^{+/-}$ mice have an average of 10mmHg increase in blood pressure further support the existence of dual vascular action of ET-1 via ET_A and ET_B binding (231). This elevated pressure may be explained by the increases in renal sympathetic nerve activity from reduced ET-1/ET_B stimulation in renal vascular endothelium

(239, 240). Moreover, ET-1 promotes cellular mitogenesis in addition to the production and release of interleukin-6 (IL-6), interleukin-8 (IL-8), vascular endothelial growth factors (VEGF), fibroblast growth factor-2 (FGF-2), and epiregulin. Indeed, Alberts et al (1993) demonstrated that ET-1/ET_A signalling increases VSMC proliferation, and such an effect is abolished by BQ-123, an ET_A antagonist (241). Further study on human aortic VSMC demonstrated that ET-1 does not directly stimulate mitogenic activity per se but rather trigger mitogen-activated-protein kinase (MAPK) pathway and potentiate the cellular growth effect of platelet-derived growth factor (PDGF) through its interaction with ET_A receptor (242). Consistently, Kimberley et al (1998) found ET-1 and angiotensin II (Ang II) upregulate FGF-2 expression, which promotes VSMC proliferation in rat aortic cells (243). In addition, ET-1 and Ang II simulation increases the expression of VSMC-derived epiregulin, an epidermal growth factor (EGF)-like growth factor that promotes mitogenic activities of rat VSMC (244). Similarly, ET-1, along with ET-3, has been shown to increase IL-6 production through activation of phospholipase C (PLC), which leads to the production of second messengers: inositol 1,4,5-trisphostate (IP_3) and 1,2-diacylglycerol (DAG)(245). IL-6 plays important roles in the regulation of haematopoiesis (246, 247). Moreover, ET-1 upregulates IL-8 production, which promotes polymorphonuclear cell (PMNs) recruitments during ischemic events; this upregulation effect, on the other hand, is abolished by the transforming growth factor β (TGF-β) (248). Additionally, ET-1 promotes VEGF mRNA expression and its secretion in VSMCs. VEGF binds to endothelial *fms*-like tyrosine kinase (Flt) and foetal liver kinase (Flk) receptors thereby upregulates endothelial cells migration, proliferation, and angiogenesis (249). Furthermore, VEGF activation promotes tyrosine phosphorylation of SH2 domain-containing mediators and increases second messengers IP_3 and DAG, which triggers the release of Ca2+ and protein kinase C activation (250). Overall, disruptions in ET-1/ET_A and ET-1/ET_B signalling have strong

implications in the pathogenesis of hypertension, pulmonary hypertension, coronary and vascular artery diseases, and heart failure (193-195, 203).

10.2.3.3. *ET-1 functions in central nervous system*

ET-1 is the predominant neural endothelin in the brain constituents other than the pituitary gland (251, 252). Prior immunohistochemistry and in-situ hybridizations demonstrated ET-1 expression in hypothalamus, pituitary, brainstem, spinal cord, dorsal root ganglia, and vascular endothelium of cerebral vessels (253-256). Furthermore, ET-1 concentration in cerebrospinal fluid (CSF) is found to be much higher than its plasma concentration. It is unable to cross blood brain barrier (257).

ET-1 has a modulatory effect on the autonomic control and cardiorespiratory homeostasis through its binding with ET_A and ET_B receptors. Indeed, Kuwaki et al (1990) showed intracisternal injection of low-dose ET-1 triggers transient sympathetic stimulation and thus elevates heart rate, respiratory rate, and arterial blood pressure. Interestingly, these same parameters are suppressed by the high-dose ET-1 injection (258). This observation suggested a bimodal effect of ET-1 in brain. Furthermore, similar ET-1 dose-dependent responses are observed from the excitations of vasomotor and respiratory neurons situated at the ventral aspect of medulla oblongata. On the other hand, majority of these excitations are inhibited by an ET_A antagonist, FR139317 (259, 260). Consistently, applications of ET-1 on cardiorespiratory control centre of nucleus tractus solitarius and ventrolateral medulla elicit similar responses as intraventricular injections; these responses are diminished by ET_A antagonist, BQ-123, but not affected by ET_B antagonist, BQ-788. Moreover, the vasoconstriction effect of intracerebroventricular ET-1 is mediated by a combination of

increased sympathetic stimulation, increased epinephrine and norepinephrine, and arginine vasopressin (AVP); these effects are abolished by a combination of prazosin, alpha-1 antagonist, and [l-(β-mercapto-β, β-cyclopentamethylenepropionic acid), 2-(O-methyl)-tyrosine] AVP (TMeAVP), an AVP antagonist (261, 262). The importance of ET-1 on respiratory homeostasis is further demonstrated by the higher arterial partial pressure of carbon dioxide ($PaCO_2$) and lower arterial partial pressure of oxygen (PaO_2) seen in heterozygous ET-1 mice with respect to those in wild type mice. This relationship is further complexed by the diminished respiratory response to hypercapnic or hypoxic stresses observed in these mutant mice (263), an observation consistent with Ondine's curse or central hypoventilation syndrome known to associate with HSCR (28). This suggests ET-1 signalling impairment is likely to present in HSCR.

ET-1 is also implicated to exert hormonal control, particularly over hypothalamus-pituitary gland axis. Indeed, using pituitary cell culture and hypothalamic explant, Calogero et al (1994) found ET-1 increases basal release of adrenocorticotrophic hormone (ACTH) whereas ET-3 stimulation decreases corticotrophin-releasing hormone (CRH) (264). This is further supported by Yasin et al (1994), showing ET-1 exhibits no modulatory effect on the release of CRH. In addition, ET-1 has been demonstrated to upregulate the release of vasopressin and oxytocin through ET_A stimulation, an effect inhibitable by BQ-123 (265). Furthermore, Kanyicska et al (1991) showed both ET-1 or ET-3 can stimulate the release of luteinizing hormone (LH) and follicle-stimulating hormone (FSH) from anterior pituitary cell cultures. On the other hand, both endothelin also trigger dose-dependent inhibition to prolactin secretions, with ET-1 having much higher potency than ET-3 (266).

10.2.3.4. *ET-1 functions in respiratory system*

Endothelin pathways are involved in the regulation of airway tone, pulmonary vasculature, and pulmonary remodelling. This is mainly achieved by ET-1 stimulations, which is expressed by pulmonary endothelial cells, epithelial cells of respiratory tract, and PMNs (200, 267). Prior studies have suggested alterations in airway tone are mediated by a combination of ET-1/ET_A and ET-1/ET_B pathways. Indeed, Chalmers et al (1997) reported ET-1 inhalation challenge triggers rapid dose-dependent bronchoconstriction in asthmatics, a response that is rapidly reversed by albuterol (268). This is further supported by a guinea pig study demonstrating dose-dependent increase in airway resistance following ET-1 infusion, a response that is reversible by the administration of ET_A-antagonist, BQ-123 (269). Further analysis on guinea pig demonstrated pre-treatments with ET_A antagonists, BQ-610, or ET_B antagonist, IRL-1038, can both ameliorate the increases in pulmonary resistance mediated by ET-1, suggesting an overlapping control (270). Moreover, ET-1 has been found to induce global pulmonary vasoconstriction, an effect that is blocked by pre-treatment of ET_A antagonist, BQ-610 (271). Additional studies demonstrated ET-1 infusion triggered immediate transient pulmonary vasodilation prior to prolonged vasoconstrictions, suggesting ET-1 mediates dual-vasomotor control (272). Indeed, this phenomenon is further supported by the decreasing pulmonary vascular resistance with ET_A antagonist FR139317 and vice versa with ET_B antagonist RES-701-1 in beagle model of pulmonary hypertension. Concordantly, infusion of S6c, an ET_B agonist, decreases pulmonary hypertension (273).

These findings illustrate the intricate regulatory roles of ET-1 in multiple organ-systems and thus suggest the potential diseases that may arise from ET-1 mutation. Consistently, defects in subsequent ET-1/ET_A and ET-1/ET_B signalling pathways have been

documented in multiple mammalian diseases.

10.3. Endothelin-2 (ET-2)

10.3.1. *Pharmacology of ET-2*

Human ET-2 is a 21-aa peptide ligand acting through ET_A and ET_B receptors, encoded by *EDN2* gene located at chromosome 1p34.2 (182). Comparing to ET-1, less is currently known about ET-2. Using nuclear magnetic resonance (NMR), Arvidsson et al (1998) has demonstrated that ET-2 shares near-identical tertiary structure as ET-1 (274). Consistently, both peptides are expected to share similar potency. Indeed, Roubert et al (1991) reported radiolabelled [^{125}I]-ET_2 and [^{125}I]-ET_1 have similar *in vitro* binding affinity constant (K_D = 111pM and 123pM, respectively) and maximum receptor saturation values against ET_A receptors (46.0 fmol/10^6 cells and 54.1 fmol/10^6 cells, respectively) (275). Furthermore, ET_A antagonist FR139317 inhibits [^{125}I]-ET_2 binding and [^{125}I]-S6b inhibits [^{125}I]-ET_1 binding in human aortic and coronary arteries with similar K_D values (276). Additionally, functional study measuring vasoconstriction response in human saphenous vein, coronary artery, pulmonary artery, internal mammillary artery and aorta also demonstrated ET-2 and ET-1 share similar potency (277).

In general, mammalian ET-2 found in human, monkeys, cats, dogs, and cattle differs from ET-1 by 2 out of 21-aa residues: Trp^6 and Leu^7. As a result of the extra tryptophan at position 6, ET-2 is the most hydrophobic isoform of the endothelin (167). Furthermore, Ishida et al (1989) also identified an murine ET-2 analogue, known as vasoactive intestinal contractor (VIC) for its ability to stimulate ileal contractions (278). Although VIC differs from human ET-2 by one amino acid residue, with Ser^4 in human ET-2 and Asn^4 in rat VIC, both

variants share similar tissue distributions and functions (279-281). Further functional studies also demonstrated VIC is equipotent to ET-1 and ET-2, as demonstrated by mesenteric vasoconstriction and biphasic ileal motion measurements (282, 283).

The production pathway of ET-2 is similar to that of ET-1 previously described. It is generated mainly by intestinal epithelial cells (252). Transcription of *EDN2* gene results in the production of preproendothelin-2, which is cleaved by furin to form the Big ET-2 of 38 amino acid residues. These Big ET-2 are converted into active ET-2 via ECE-1 and ECE-2; however, in vitro study showed these conversion rates of Big ET-2 are only 5-10% of Big ET-1 (181).

10.3.2. *Distribution of ET-2*

The distribution of VIC/ET-2 is more limited than that of ET-1. While the plasma concentration of Big ET-2 is higher than that of Big ET-1, the reverse is true for their respective active peptide concentrations (284). Furthermore, although the breakthrough study on endothelin by Inoue et al (1989) has not identified significant plasma ET-2 mRNA using Northern blot technique, subsequent studies using immunoassay have detected ET-2 mRNA and/or peptide expression in human vascular tissue, heart, lung, kidney and intestine (285-288). Similarly, restricted expression of ET-2/VIC mRNA is also found in rat and mouse. De La Monte et al (1995) reported progressive gradient of ET-2 gene expression from stomach to intestine, with localization of ET-2 peptides in lamina propria stromal cells (289). Uchide et al (1999 and 2000) demonstrated the presence of VIC mRNA in intestine, ovary, and uterus with further identification of VIC peptide in the endometrial epithelial cells, myometrial cells, and vascular smooth muscle cells using immunostaining. More interestingly, RT-PCR showed VIC mRNA concentration varies with reproductive cycle in

pregnancy (290, 291). Subsequently, Masuo et al (2003) also found higher ET-2 mRNA in pituitary gland and medulla oblongata than that of ET-1 (281).

10.3.3. *Physiology and Functions of ET-2*

Consistent with their similarity in pharmacology, production, and distribution, ET-2 exerts strong vasoregulation as ET-1. However, growing evidence has suggested that ET-2 possesses own distinctive physiological functions rather than a mimic of ET-1. For instance, Chang et al (2013) showed ET-$2^{-/-}$ mice have paradoxical features of normal digestive tract in severe growth restrictions, which manifest as hypoglycaemia, ketonemia, and upregulation of starvation-induced genes. Additionally, emphysema and hypothermia are also common associated features (292). These morphological and physiological features are distinctively different from the lethal craniofacial and cardiac malformations arise from the disruptions in ET_A/ET-1 signalling or WS-IV phenotype from ET_B/ET-3 signalling failure, suggesting ET-2 plays a unique role in embryonic development and thermoregulation (142, 231, 232).

10.3.3.1. *ET-2 functions in reproductive system*

Contrary to ET-1 and ET-3, current evidence suggest ET-2 exerts strong temporal and spatial regulations in female reproductive cycles. Indeed, Uchide et al (1999) has first demonstrated high expression of VIC/ET-2 in ovaries (290). Subsequently, Ko et al (2006) and Palanisamy et al (2006) illustrated local surges of ET-2 and ECE-1 expression corresponding to the contractions of follicular smooth muscle wall and subsequent ovulation in rat (293, 294). Concordantly, intraovarian injection of non-selective ET_R antagonist, tezosentan, results in marked reduction in ovulation with fewer corpora lutea and more unruptured follicles on ovarian histology (293). Furthermore, Northern blotting on ovarian ET_R revealed relative

higher ET_B : ETA expression in periovulating ovaries. Additionally, selective ET_B antagonist, BQ-788, causes approximately three times more reduction in ovulation than ET_A antagonist, JKC-301 (294). These reports indicate ovulation is facilitated mainly through ET-2/ET_B signalling; therefore, one may expect HSCR patients to have impaired fertility, particularly in $ET_B^{-/-}$ subtypes.

10.3.3.2. *ET-2 involvements in immunology and oncology*

Current evidence suggest ET-2/ET_B signalling is also involved in the immunomodulation and oncological process. Grimshaw et al (2002) demonstrated that ET-2 acts as a chemoattractant through MAPK signalling for THP-1 macrophages, but not monocytes. Additionally, incubation of THP-1 cells with BQ-788, an ET_B antagonist, abolishes these chemotaxis towards ET-2, a response similar to the inhibitions elicited by hypoxia or PD98059 (MAPK kinase inhibitor) treatment (295). Interestingly, RT-PCR demonstrates increased expression of ET-2 and ET_B mRNA in human grade II infiltrating ductal carcinomas (IDC) with respect to the normal breast tissues. In addition, in vitro study showed hypoxia stimulates elevation of ET-2 and ET_B mRNA in HTH-K tumour cells, a murine breast cancer model. Treatment with BQ-788 enhances hypoxia-induced apoptosis, a response reversible by ET-2 (296). This evidence suggests $ET_B^{-/-}$ HSCR patients may be immunocompromised but may have added protection against cancer.

10.4. Endothelin-3 (ET-3)

10.4.1. *Pharmacology and Productions of ET-3*

ET-3 is coded by *EDN3* gene. Its cDNA clone was first isolated by Bloch et al (1989) from human hypothalamic cDNA library. Subsequently, the *EDN3* gene was mapped on

chromosome 20q13.32 (182, 297). Structural characterization show the -NH_2 terminus of ET-3 is flanked by an arginine dipeptide and its carboxyl terminus by a tryptophan and a hydrophobic residue (297). ET-3 differs from ET-1 in 6 of the 21 peptides: Thr^2, Phe^4, Thr^5, Tyr^6, Lys^7, and Tyr^{14}. Consequently, ET-3 is the most polar isoform of all endothelin (167). This structural difference partially contributes to the selective affinity of ET-3 at physiological concentrations; ET-3 has similar affinity to ET_B as ET-1 and ET-2 but little affinity to ET_A (190, 298).

Contrary to the ET-1 production by vascular endothelial cells, ET-3 is produced by the CNS neurons, renal tubular epithelial cells, and intestinal epithelial cells (252, 299). While the production pathway of ET-3 is similar to those of ET-1 and ET-2 described prior, the contribution of ECE-1 to the conversion of Big ET-3 remains unclear. Yanagisawa et al (2000) provided some evidence on the importance of ECE-1 on ET-3 level, with ECE-1 knock-out mice exhibiting both lower ET-3 tissue concentration and a combined phenotype of defective ET-1/ET_A and ET-3/ET_B signalling (300). On the other hand, D'Orleans-Juste P et al (1991) revealed ECE-1 have little activity on Big ET-3 conversion based on findings from isolated guinea-pig pulmonary vasculature (301).

10.4.2. *Distributions of ET-3*

While the bodily distribution of ET-3 expression is more limited than ET-1, it is more prevalent than ET-2. Although Inoue et al (1989) has not identified significant ET-3 mRNA expression in a number of human tissues using traditional Northern blot, subsequent studies have demonstrated otherwise (167). Indeed, Masumoto et al (1989) has identified ET-3 to be an abundant brain peptide using enzyme-linked immunosorbent assay (ELISA). High

concentrations of immunoreactive ET-3 (ir-ET-3) are also detected in the intestine, lung, cerebellum, cerebrum, and pituitary gland along with modest levels in medulla oblongata, colon, liver and kidney (252). Consistently, Shiba et al (1992) detected preproET-3 mRNA in the GI tract, brain, kidney, spleen, submandibular gland, and eye ball of rat (302). In addition, using reverse-phase high-performance liquid chromatography (RP-HPLC), Plumpton et al (1993) detected ET-3 expression in the heart (287). Other human tissues expressing ET-3 have also been reported, including endometrium and pituitary gland (256, 303). Incidentally, pituitary gland was found to be the only region in the brain with higher ET-3 than ET-1 concentration (252). Furthermore, despite previously documented pressor-response triggered by the ET-3 in guinea-pigs, little detectable ET-3 is found in the murine heart and aorta (252, 301).

Physiological ET-3 levels are detectable in human but can vary in disease states. Using immunoassay, Matsumoto et al (1994) recorded plasma ET-3 concentration of 0.8 pg/mL and Big ET-3 concentration of 25.8pg/mL in 23 healthy volunteers (284). Subsequently, Miyauchi et al (2012) reported significant elevation of Big ET-3 to > 70pg/mL (and other big-ETs) in haemodialysis patients while only modest increase of ET-3 is detected, 1.7pg/mL (304), suggesting upregulation of ET-3 may be limited by ECE saturation. Because ET-3 does not bind to ET_A at physiological concentrations and mainly act through ET_B, consistent ET_B distribution is expected. Additionally, these findings suggest ET-3 expression is an adaptive process to physiological stressors.

10.4.3. *ET-3 Physiology and Function*

10.4.3.1. *ET-3 functions in embryological development*

In contrast to the lack of ET_A action by ET-3, several ET-3/ET_B mediated physiological functions have been reported. As noted previously, disruptions in ET-3/ET_B signalling cause HSCR type II. Indeed, Kurihara et al (1999) demonstrated ET-3's importance to the ENS development: KO mice exhibit defective ENS and melanocytes, corresponding to WS-IV features (300). Consistently, avian model showed ET-3 stimulation triggers dose-dependent proliferation of enteric neural crest cell, which leads to hyperganglionosis in hind-gut by inhibiting premature neuronal differentiation (305).

10.4.3.2. *ET-3 functions in autonomic nervous system*

In autonomic nervous system, ET-3 is found to mediate vasoconstriction as ET-1, but at a much lower potency (301). It has been shown that intracisternal injection or topical application of ET-3 onto the ventral surface of the medulla (VSM) elevates arterial pressure, heart rate, and renal nerve activity; these actions are likely mediated through sympathetic pathway (306). Furthermore, in vitro study on pituitary cell culture demonstrated ET-3 stimulation triggers the release of TSH, FSH, and LH while inhibiting the prolactin secretion, suggesting possible neuroendocrine control (307). Subtle roles of ET-3 on central autonomic control have also been reported. Samson et al (1991) and Zhu and Herbert (1996) showed intracerebroventricular injection of ET-3 triggers reduction in core temperature and suppresses thirst response in water-deprived or angiotensin II-treated rats (308, 309). These multifunction of ET-3 are likely mediated through ET_B activation as suggested by its binding-affinity preference.

10.5. Endothelin receptors (ET_R)

Endothelin receptors (ET_R) are a group of seven-transmembrane G-protein coupled

receptors (GPCR). GPCR-mediated signalling pathways often converge to regulate the intracellular [Ca2+] via voltage-sensitive Ca2+ channels and the productions of IP_3 and DAG; these ultimately lead to muscular contraction (310, 311). To date, there are 5 endothelin receptors reported: mammalian ET_A (190) and ET_B (298), Ang II/ET-1 receptor in rat (312), avian ET_B (313), and ET-3 selective ET_C found in frogs (313). This section will only focus on the discussion of mammalian endothelin receptors, ET_A and ET_B, for their impacts on mammalian physiology and pathophysiology.

10.5.1. *Distribution of ET_R*

ET_A and ET_B are first discovered in 1990; however, the official classification by International Union of Pharmacology (IUPHAR) has not occurred until 1994 (190, 298). The expression of endothelin receptor is ubiquitous. Regard et al (2008) reported prominent ET_A mRNA in VSMCs and ET_B mRNA in endothelial cells of 41 adult mouse tissues receiving blood supply (314). Indeed, mammalian ET_A and ET_B are distributed widely but differentially in vascular and peripheral organ systems. For instance, the receptor distribution varies with different vascular bed, veins generally having lower ET_A : ET_B ratios than arteries (315). In addition, radio-ligand studies demonstrated that while ET_A are more prevalent than ET_B in the heart and large vessels, i.e. > 60%, the reverse ratio is true in the CNS, lung, kidney, and liver (314, 316).

10.5.1.1. *ET_R distribution in Central Nervous System (CNS)*

Endothelin receptor expression are widely detected in human CNS, with ET_B being the predominant subtype. For instance, Harland et al (1995) reported 90% of ET_R in human cerebral cortex consists of ET_B, which mainly localized in neuronal sections. Additionally,

Morton and Davenport (1992) have indirectly illustrated the presence of ET_B in cerebellar glial cells (317). On the hand, other than its presence in leptomeninges, ET_A is mainly found in pial and intraparenchymal vessels (318). Consistently, functional studies illustrated that cerebral perfusion is controlled by ET-1/ET_A-activated VSMC constrictions; these vessels include cerebral, meningeal, temporal, and pial arteries (319, 320). Interestingly, the ET_R expression seems to be a dynamic process in response to physiological stressors. Johansson et al (2012) reported that the upregulation of ET_B and 5-hydroxytryptamine receptor (5-HT_{1B}) expression in VSMCs of rat cerebral arteries following forebrain ischemic stroke; these increases correspond to increased post-ischemic vasoconstriction and cerebral hypoperfusion (321). Similar upregulations of ET_B and 5-HT_{1B} are also observed in rats with induced subarachnoid haemorrhagic (SAH) stroke; promisingly, this upregulation is abolished with MEK1/2 inhibitor, U0126 (322), suggesting a potential treatment target. Moreover, Kelly-Cobbs et al (2011) reported that diabetes causes elevated expression of ET_A and ET_B in VSMC and subsequent cerebrovascular remodelling, both responses are abolished by a non-selective ET_R antagonist, bosentan (323). These studies suggested that ET_R plays important developmental roles and may act as a potential pharmacological target to improve stroke outcomes. Additionally, these dynamic changes imply $ET_B^{-/-}$-HSCR subjects may suffer neurological growth impairments in the absence of neuronal and endothelial ET_B, but at the same time, exhibit partial protection from worsening cerebral ischemia in diseased states.

10.5.1.2. *ET_R distribution in cardiovascular system*

In human cardiovascular system, both ET_R subtypes are presented in the coronary artery and the myocardium within the atria and ventricles (324). ET_A is the predominant ET_R subtype in cardiomyocytes, comprising up to 90% of the total (325). Consistently, MacCarthy

et al (2000) illustrated that ET-1 exerts a positive inotropy through ET_A activation in healthy hearts but the opposite is true in patients with dilated cardiomyopathy (326). Further autoradiography analysis showed both ET_R are expressed in the septal and atrioventricular conducting system. ET_B has higher expressions in atrioventricular node (AV node) and bundle of His than its presence in the interatrial and interventricular septum; ET_A has opposite distribution pattern. The mRNAs of both ET_R are also detected in the endocardial cell by in situ hybridization (327). Additionally, Bacon and Davenport (1996) reported a predominant ET_A expression in the VSMC of aorta and coronary artery, with a minor and variable ET_B expression in coronary artery. Furthermore, [^{125}I]-ET-3 did not reveal ET_B binding site in human aorta (276).

Similar to that of CNS, expression of cardiovascular ET_R changes with pathophysiological states. For instance, elevated ET_A expression is detected in the right ventricle and the media of pulmonary artery in pulmonary arterial hypertension (PAH) patients (328). Similarly, higher ET_A presence is found in the left ventricle of patients with dilated cardiomyopathy (329). Moreover, Dagassan et al (1996) detected higher ET_B expression in the left anterior descending artery (LAD) from patients with arterial atherosclerosis (330), suggesting ET_B-mediated vasodilation may be an important adaptive response to hypoperfusion. Similarly, increased ET_B expressions have also been found in other vascular diseases (330-332).

10.5.1.3. *ET_R distribution in other peripheral organs: Lung, Kidney, Liver*

The ET_R expression in other major peripheral organs has also been evaluated, with ET_B being slightly more abundant than ET_A in the lung, kidney, and liver. In general, the

respiratory system has high ET_R density but with tissue-specific distributions (333). ET_A expression predominates in the VSMC of the pulmonary artery and therefore mediates major vasoconstrictions (334). ET_B, on the other hand, is mainly found in the endothelium of pulmonary vessels where it mediates vasodilation. Furthermore, ET_B is presented, to a larger extent, in the smooth muscles of bronchial airway where it mediates bronchoconstriction (334). Interestingly, variations in ET_R density distribution are non-uniform across different disease states. For instance, Knott et al (1995) has showed no significant changes in ET_A and ET_B distribution density in asthmatic lung (335) whereas Hall et al (2011) has detected elevated expression of ET_B, but not of ET_A, in the pulmonary arterial smooth muscle of patients with untreated idiopathic pulmonary hypertension (336). These findings suggested that the regulation of ET_R expression are likely regional-dependent, possibly corresponding to the autocrine and paracrine characteristics of endothelin (227). Moreover, animal studies showed that ET_R are presented in the renal vasculature and medullary and cortical nephrons. ET_B is more highly expressed than ET_A on the epithelial cells of inner medullary collecting ducts; however, this relationship is reversed in renal vessels (337, 338). Lastly, ET_A and ET_B have roughly similar density in hepatobiliary systems (314). These differential distributions likely correspond to their functional difference and the predominance of endothelial cell distribution in these tissues.

10.5.2. *Non-selective receptor antagonists*

Given ET_A and ET_B have selective affinities to different ETs, several antagonists have been developed. While there are no standardized criteria in classifying receptor selectivity, it is commonly accepted that ET_A- or ET_B-selective molecules are to exhibit greater than 100-fold affinity for its respective receptor. Non-selective molecules are considered to have less-

than 100-fold selectivity (339). Few examples of clinically relevant non-selective antagonist include bosentan, tezosentan, and macitentan. Bosentan is approved for the treatment of PAH (340), with a half-life ($T_{1/2}$) of 5.4 hours and ~ 50% bioavailability (341). While Kioswki et al (1995) has reported bosentan improves cardiac index by 13.6% and reduces systemic (16.5%) and pulmonary vascular resistance (33.2%) in chronic heart failure, its potential risks of hepatotoxicity and undetermined long-term mortality and morbidity benefits in congestive heart failure limit its broader use (342, 343). Hepatotoxicity caused by bosentan is thought to be due to bile salt accumulation from its inhibition on bile salt export pump. Similarly, tezosentan is designed for the treatment of acute heart failure. However, VERITAS trial failed to demonstrate improvement in clinical outcomes (344). On the other hand, animal studies demonstrated tezosentan can potentially improve the survival outcomes of liver cirrhosis, providing an alternative clinical application (345). Lastly, macitentan with a $T_{1/2}$ of 16 hours, is approved for the treatment of PAH in 2013 with SERAPHIN trial demonstrated morbidity and mortality benefits; however, the study sample size was small (346).

10.5.3. *Endothelin A receptor (ET_A)*

10.5.3.1. *Structure and genetics of ET_A*

ET_A is a 7α helical transmembrane molecule composed of 427 amino acid (a.a.) residues in human. It shares 63% structural similarity with ET_B (347). ET_A is encoded by *EDNRA* gene located at chromosome *4q31.22*, which contains eight exons and seven introns spanning across 40 kilobases (348). Similarly, the rat homologue of ET_A is composed of 426 a.a. residue and encoded by *Ednra* gene located at chromosome *19q11* (349).

Since ET_A belongs to class A of G-protein-coupled-receptors, several mechanisms can

modify its functions, including sequence mutations and post-translational phosphorylation and palmitoylation. For instance, mutations in a.a. Gly^{97}, Lys^{140}, Lys^{159}, Gln^{165}, and Phe^{315} reduce ET-1 affinity and thus downstream signalling (350). Moreover, Horstmeyer et al (1996) reported that cysteine mutations in the cytoplasmic tail of ET receptors can abolish palmitoylation, which results in the loss of phospholipase C activation and the subsequent elevation of cytoplasmic calcium (351). Furthermore, unlike ET_B, ET_A does not undergo ligand-induced phosphorylation for rapid receptor inactivation, thereby enables a long-lasting constrictor effect (352). Lastly, consistent with other G-protein-coupled receptors, rapid desensitization of activated ET_A can be regulated by the expression of G protein-coupled receptor kinases (GRKs) (353). All of these findings suggest ET_A can be an important potential pharmacological target for treatments.

10.5.3.2. *ET_A physiology and functions*

10.5.3.2.1. *ET_A functions in embryological development*

As described previously, ET_A plays pivotal roles in embryological development by regulating cephalic and cardiac NCC migration through ET-1/ECE/ET_A signalling pathway. Indeed, knock-out mutations of ET_A receptor results in severe morphological abnormalities. As shown by Hosoda et al (1994), neonatal $ET_A^{-/-}$ mice suffer early death from respiratory failure due to severe craniofacial dysmorphology. Furthermore, these mice exhibit features mimicking the velocardiofacial or CATCH22 syndrome in human, which includes craniofacial and cardiovascular outflow tract aberrations (354).

10.5.3.2.2. *ET_A functions in systemic and peripheral vasoregulation*

ET_A's functions closely correspond to its distributions. As mentioned prior, ET_A is

widely distributed throughout the cardiovascular system, and particularly in the smooth muscles of vascular systems supplying the peripheral end-organs (260). It exerts a strong vascular control through the vasoconstriction activated by ET-1 binding. Indeed, Haynes and Webb (1994) showed infusion of BQ-123, an ET_A antagonist, via brachial artery triggers vasodilation in healthy volunteers, a phenomenon potentially mediated by the increased production of nitric oxide (NO) as a result of ET_A inhibition. Concordantly, suppression of NO production diminishes this vasodilation by 95% (355). Moreover, Montanari et al (2000) demonstrated that the crosstalk between ET_A activity and endogenous NO production plays important regulatory roles in vascular homeostasis. The co-administration of BQ-123 with N-nitro-L-arginine methyl ester (L-NAME, a nitric oxide synthase inhibitor) in healthy volunteers diminishes the elevations in mean arterial pressure (MAP) and the reduction in renal perfusion, which are caused by the inhibition of NO production (356). Conversely, Verhaar et al (1998) reported that the infusion of an ET_B antagonist, BQ-788, triggers vasoconstriction (355), suggesting endothelial ET_B mediates basal vasodilation under normal physiological state (357). Indeed, ET-1 is found to also stimulate vasoconstriction in isolated renal arteries and veins; however, little response is triggered by ET-3 or sarafotoxin 6c, an ET_B agonist. This supported the presence of a predominant ET_A-mediated vasoconstrictive action. Affirmatively, ET-1 mediated contraction is fully reversed by BQ-123, an ET_A antagonist (358). Finally, Maguire and Davenport (1995) detected similar vasoactive responses in isolated epicardial coronary artery, internal mammary artery, pulmonary artery, and aorta, and saphenous vein (277).

10.5.3.3. *ET_A antagonists*

ET_A binds to three naturally occurred endothelin peptides: ET-1, ET-2, and ET-3.

ET-1 and ET-2 share similar affinity to ET_A, this binding affinity is >100 times greater than that of ET-3 (359). Expectedly, several clinical antagonists have been produced, including sitaxentan, ambrisentan, zibotentan, atrasentan, darusentan, and avosentan.

While several ET_A antagonists have been proposed, few are currently approved for clinical use due to unsatisfactory trial results or safety concerns. Sitaxentan was first approved in 2006 for the treatment of PAH by inhibiting ET-1/ET_A-mediated vasoconstriction. Additionally, Givertz et al (2000) reported sitaxentan reduces plasma ET-1 in chronic heart failure with promising results (360). However, sitaxentan was withdrawn in 2010 for multiple cases of associated hepatic failure (361). Ambrisentan is a competitive ET_A antagonist, approved in 2007 for treatment of PAH. Although ambrisentan is less ET_A-selective than sitaxentan, it has high bioavailability, longer $T_{1/2}$ (15 hours), and better safety profiles including lower hepatotoxicity (362). Zibotentan is the most ET_A-selective molecules to date with adequate safety profile. It was initially developed for the treatment of refractory prostate cancer; however, phase III ENTHUSE (EndoThelin A USE) trials failed to demonstrate significant clinical improvement (363). Atrasentan was initially developed for the treatment of non-small cell lung cancer but unfortunately showed no additive benefits in the clinical trial (364). On the other hand, de Zeeuw et al (104) demonstrated promising results of atrasentan reducing albuminuria, 24-hour blood pressure, cholesterol, and triglyceride levels in patients with diabetic nephropathy (365). Currently, Study of Diabetic Nephropathy with Atrasentan (SONAR) Phase III clinical trial is pending to be concluded (clinicaltrials.gov). Other clinical trials that have stopped prematurely including DAR-312/DORADO-AC, a phase III clinical trial failed to show added benefit of darusentan in the treatment of refractory hypertension (clinical trials.gov). Lastly, while Mann et al (2010) have demonstrated that

daily dosing of 25mg or 50mg of avosentan markedly reduces albuminuria in diabetic nephropathy in type II diabetes; however, the trial was ceased prematurely due to the increased adverse effects of fluid retention and congestive heart failure (366). On the other hand, Baltatu et al (2014) reported that a combinational therapy of reduced-dose of avosentan and valsartan may be protective against hypertensive nephropathy in transgenic hypertensive rats without adverse effect of fluid retention (367). Although the inhibition of ET_A is likely beneficial in various diseases, ongoing trials are still required for further validation.

Conversely, no ET_A-selective agonist has been produced up to this day.

10.5.4. *Endothelin B receptor (ET_B)*

10.5.4.1. *Structure and genetics of ET_B*

Human ET_B is encoded by *EDNRB* gene comprising of seven exons and six introns at chromosome *13q22.3*; its rat homolog is positioned on chromosome 15 (368). Structurally, ET_B is a G-protein coupled receptor of 442 a.a. with a 7-transmembrane domain, a cleavable long N-terminus, and a carboxyl terminus vital to intracellular signalling (350).

Like ET_A, ET_B's activity can be modified by posttranslational palmitoylation and phosphorylation. Indeed, Okamoto (1997) showed serine substitutions of Cys^{402}, Cys^{403}, and Cys^{405} of cytoplasmic tail can inhibit ET_B palmitoylation and thereby uncouples it from G_i protein, an adenylyl cyclase inhibitor (369). Additionally, Stannard et al (2003) identified 4 palmitoylation and 13 phosphorylation sites that are responsible for downstream signalling modifications (370). The degrees of palmitoylation and phosphorylation may act as signalling

regulators; this is exemplified by the palmitoylation-dependent ET_B-mediated ERK/MAPK activation and the phosphorylation-dependent ET_B desensitization, both of which are regulated by the GRKs activities (353, 371).

10.5.4.2. *ET_B physiology and functions*

In general, ET_B plays important roles in four major physiological domains: embryological development and mitogenic effect, systemic and peripheral vasoregulation, endothelin metabolism, and renal salt and water regulations.

10.5.4.2.1. *ET_B function in embryological developments and mitogenesis*

As previously discussed, normal development of ENS is dependent on the successful migration of enteric NCC and melanoblast during embryological stage, which is regulated through ET-3/ECE/ET_B signalling pathway. Activation of ET_B through interaction with ET-3 prevents premature differentiation of neural crest cells and thereby ensures appropriate colonization for a functional enteric nervous system. Disruption in this pathway results in Type II HSCR or WS-IV as previously discussed. Additionally, *in vitro* study found ET_B activation by ET-1 promotes the endothelial proliferation and suppresses apoptosis induced by serum starvation. These responses are inhibited by BQ-788 but not BQ-123, supporting endothelial proliferation is dependent on functional ET_B but not ET_A (372). Consequently, dysfunctional ET_B in *sl/sl* rats may cause vasodysregulation due to impaired endothelial development.

10.5.4.2.2. *ET_B functions in systemic and peripheral vasoregulation*

The vasoregulatory impact of ET_B has been overshadowed by the predominant

vasoconstrictive effect of ET_A until recently. Although some studies have reported detectable ET_B in VSMC, its distribution is minor and arguably carrying little vasoconstrictive impact. Indeed, White et al (1993) has cleverly demonstrated VSMC constrictions triggered by ET_A stimulations are ~100-folds more potent than those mediated by ET-3/S6c-ET_B signalling in endothelium-denuded rat thoracic aorta and rabbit carotid artery (373). Moreover, many studies have demonstrated that endothelial ET_B undoubtedly mediates basal vasodilation across various human and animal tissues. For instance, Wright and Fozard (1988) have cleverly showed continuous ET-1 infusion triggers initial vasodilation by ET_B activation, which is then overridden by prolonged ET_A-mediated vasoconstriction (374). The initial reduction in vascular resistance is likely mediated by the endothelial NO and PGI_2 generated from ET_B activation (189). Indeed, Berti et al (1993) demonstrated the inhibition of respective NO and PGI_2 production or administration of ET_B antagonist diminish the vasodilatory effect in isolated rabbit coronary artery; similar observation is also noted in conscious rats (375, 376). Concordantly, Ohuchi et al (1999) showed crossbred mice of ET_B-deficient and piebald mutation, $ET_B^{-/s}$, have ~20mmHg higher blood pressure (BP) than the mice with at least one copy of functional ET_B gene. Similarly, infusion of BQ-788 triggers elevated basal BP in $ET_B^{+/s}$ or $ET_B^{+/+}$ mice but not in mutants. This pressor effect of BQ-788 can be attenuated by the pre-treatment with indomethacin or accentuated by the co-administration of NG-monomethyl-L-arginine (L-NMMA) in wild type mice (377). These findings reaffirm the hypothesis that basal vasodilation mediated by ET_B is acted through NO and PGI_2. Additionally, Love et al (2000) illustrated intra-arterial infusion of BQ-123 (ET_A antagonist) causes progressive vasodilation whereas applications of BQ-788 (ET_B antagonist) causes vasoconstriction and reduces forearm perfusion in both control and heart failure patients (378). These evidence support the notion that endothelial ET_B activation acts as a feedback

system to ET-1/ET_A signalling and thereby limiting pressor effect while at the same time provides basal vasodilation for peripheral perfusion. Similarly, using BQ-788 and BQ-123, Bohm et al (2003) illustrated ET_B has opposite effect to ET_A in other vascular beds of healthy volunteers. While isolated infusion of BQ-123 did not alter arterial blood pressure and vascular resistance in renal or splanchnic vasculature, co-administration of ET-1 and BQ-123 abolishes ET-1 induced vasoconstriction. Conversely, BQ-788 infusion elevates vascular resistance and potentiates ET-1/ET_A-induced pressor effect; this is consistent with the notion that ET-1/ET_B mediates basal vasodilation and ET-1 clearance (379).

10.5.4.2.3. *ET_B functions in endothelin metabolism*

Various animal studies have demonstrated that much of the ET-1 clearance occurs in the lung, kidney, and liver; up to 80% of which is mediated by ligand-ET_B binding. Little, if any, is carried out by ET-1 and ET_A interaction (228, 380). This is supported by the elevated plasma ET-1 level in *sl/sl* rats when comparing to the wild type rats, 13.2 pg/mL and 2.1 pg/mL, respectively (381). Accordingly, elevated plasma level and reduced clearance of ET-1 are detected in patients with PAH, liver cirrhosis, or chronic renal failure, in which ET_B-rich organs are heavily impaired by the diseased states (382-384). Moreover, chronic heart failure trials showed plasma ET-1 nearly doubled following treatments of oral or intravascular bosentan when comparing to the placebo groups, suggesting non-selective inhibition of ET_R impedes ET-1 clearance (343, 385). Pivotally, using immunofluorescence and $ET_B^{-/-}$ mice, Kelland et al (2010) located the cellular sites of ET-1 clearance with the endothelial cells, corresponds well with the predominant ET_B distribution. Furthermore, the clearance of intravenous bolus of radiolabelled [^{125}I]-ET-1 is significantly lowered in $ET_B^{-/-}$ mice and in wild type mice pre-treated with ET_B antagonist A192621; same level of clearance impairment is not seen in

animals treated with ET_A antagonists (386). This evidence supports ET_B's role in ET-1 clearance.

Although both ET_A- and ET_B-mediated ligand-receptor internalizations are dependent on the arrestin and dynamin, ET_A-directed pathway leads to a recycling pathway whereas the endocytosis of endothelin/ET_B complex follows an endosomal/lysosomal pathway, by which endothelin and ET_B are eventually degraded (387). Consequently, loss-of-function or inhibition of ET_B can cause significant elevations in plasma ET-1 concentration. Indeed, *in vivo* positron emission tomography (PET) imaging revealed pre-infusion of BQ-788 reduces the clearance of ^{18}F-labelled endothelin-1 (^{18}F-ET-1) by up to 85% in the lung and kidney. On the other hand, BQ-788 does not displace the ligand if it is applied after ^{18}F-ET-1/ET_B complex has formed. This is consistent with the proposed endocytosis mechanism (388). Additionally, activation of ET_B by ET-1 provides a negative feedback on the endothelial ECE-1 expression and thus suppresses the production of ET-1 (389). Therefore, in $ET_B^{-/-}$ individuals or animal, one would expect hyper-stimulation of ET_A signalling pathway from elevated ET-1 secondary to the loss of ET_B-mediated endocytosis and inhibition on ECE-1.

In theory, ET-1 clearance by endothelial ET_B has great importance in diseased states. For instance, cerebral hypoperfusion from vasoconstriction and vasospasm in post-SAH patients have been implicated to associate with elevated plasma ET-1 (390). Affirmatively, Zimmermann (1997) showed RO 47-0203 (later known as bosentan) decreases the reduction in basilar artery diameter and thereby prevents cerebral vasospasm in post-SAH beagles (391). Similarly, an atherosclerosis study showed that rabbits with high-cholesterol diet have up to 6.8-fold higher aortic tissue ET-1 level than that of the control group (392).

Furthermore, selective ET_A antagonist, BMS-182874, reduces the aortic fatty streak and macrophage colonies in the atherosclerotic plaque of cholesterol-fed hamster (393). Moreover, elevated plasma ET-1, up to 12-fold, is also detected in patients with acute myocardial infarction (394). Consistently, infusion of BQ-123 following induced myocardial infarction in Mongrel dogs improves coronary reperfusion and reduces infarct size by 37% with no added risks of arrhythmia (395). Together, these results suggested vascular injury triggers elevated ET-1, which interacts with ET_A to further promote inflammatory response and vascular constrictions, result in worsening end-organ perfusion. Therefore, it is intuitive to expect ET_B inhibition or loss-of-ET_B function, as in WS-IV patients, removes the protective mechanism of ET-1 clearance and increases the risks of ischemic injuries following the initial insult.

10.5.4.2.4. *ET_B functions in renal regulation*

Corresponding to its distribution, ET_B also plays important roles in renal physiology. ET_B regulates salt clearance and water excretion and thereby exerts blood pressure control through its interaction with ET-1. While ET_A is the predominant subtype in renal vessel mediating renal blood flow, high density of ET_B is found on the epithelial cells of medullary collecting duct (337, 396). Accordingly, Pollock and Opgenorth (1994) recorded renal arterial infusion of ET-1 or Big ET-1 reduces renal blood flow, glomerular filtration, and elevates MAP in anaesthetized Sprague-Dawley rats. These responses are inhibited by the co-infusion with BQ-123, supporting them being ET_A-mediated originally. On the other hand, natriuresis and diuresis triggered by Big ET-1 infusion are not reversed by the application of BQ-123 (397). Consistently, Edward et al (1993) showed perfusion of 10nM S6c or ET-1 inhibits the effects of vasopressin (AVP): increasing water permeability in the collecting duct and the

accumulation of cAMP. These inhibitions are not reversed by BQ-123, supporting that the activations of ET_B promotes excretion of sodium and water and subsequently reduces the blood pressure (398). Furthermore, Gariepy et al (2000) cleverly demonstrated that high sodium diet triggers significantly higher MAP in *sl/sl* rats ($ET_B^{-/-}$), with increases up to 40mmHg. This response is ameliorated by the treatment of amiloride, an epithelial sodium channel (ENaC) blocker promoting sodium excretion. On the other hand, this BP elevation is unaffected by treatment with captopril, an angiotensin converting enzyme inhibitor, suggesting ET_B's potassium-sparing diuretic effect is not mediated via the renin-angiotensin-aldosterone pathway (381). Collectively, these findings suggested dysfunctional ET_B leads to higher risks of renovascular diseases secondary to combinations of impaired salt excretion and basal vasodilation.

10.5.4.3. *ET_B agonists and antagonists*

Contrary to ET_A, ET_B have equal affinity to all three naturally occurring endothelin isoforms: ET-1, ET-2, and ET-3 (298). Accordingly, ET-3 is the only isoform distinguishing the receptor subtypes at physiological concentrations, with an ET_B-affinity two orders of magnitude higher than that of ET_A. Consistent with the proposed beneficial impact of ET_B, many preliminary selective agonists and antagonists have been developed, as summarized in Table 1.

10.5.4.3.1. *ET_B Agonists*

Three synthetic ET_B agonists are commonly available, including: S6c, IRL-1620, and BQ-3020. S6c is initially isolated from the snake venom and found to be highly selective to rat ET_B, with up to 200,000 folds higher affinity for rat ET_B than ET_A, although this selectivity is

slightly lower with human ET_B (185, 399). Pre-treatment with S6c has been shown to reduce myocardial infarction and risks of cardiac vt/arrhythmia in New Zealand White rabbits. This cardioprotection is mediated by the direct release of NO and selective activation of ATP-sensitive potassium channel (K_{ATP} channel) in cardiomyocytes through ET_B activation (400). While IRL-1620 (N-Succinyl- [Glu^9, $Ala^{11,15}$]-Endothelin-1_{8-21},) may not be as selective as S6c, it is the most specific. With up to 120,000 folds higher affinity for ET_B than for ET_A, it is the most widely used synthetic ET_B agonist. It shares similar potency as ET-1 and ET-3 when used to stimulate guinea-pig tracheal contractions (401). Pre-clinical study on rat model also showed IRL-1620 yields promising result in slowing the progression of Alzheimer's disease. ET_B stimulation by IRL-1620 triggers neurovascular remodelling through enhanced angiogenesis and neurogenesis. This positive response is abolished by the pre-treatment of BQ-788, further confirming the action of ET_B (402). BQ-3020 (Acetyl-[$Ala^{11,15}$]-ET-1) is another selective agonist with 4,700 times higher affinity for porcine-cerebellar ET_B than for ET_A. It also mediates endothelium-dependent vasodilation in isolated porcine pulmonary artery through ET_B activation (403). Its radio-labelled isoform, [^{125}I]-BQ-3020 has also been used to characterize ET_R population in human kidney with successful localization of ET_B in the renal collecting duct (404). Additionally, competitive study further characterized [^{125}I]-BQ-3020's reversible binding property to ET_B is species-dependent: highest affinity to rat cerebellar ET_B but lower affinity to human and canine pulmonary ET_B (405). Collectively, while these ET_B agonists currently produce promising results in preclinical study, due to the potency and selectivity difference across different species, further human trials such as SPI-1620 are warranted prior to clinical applications (406).

10.5.4.3.2. *ET_B Antagonists*

There are no clinically approved ET_B antagonists currently, consistent with the proposed beneficial roles of ET_B. However, three common experimental molecules have been described: BQ-788, RES-701-1, and IRL-2500.

BQ-788, also known as [N-cis-2,6-dimethylpiperidinocarbonyl-L-gamma-methylleucyl-D-1-methoxycarbonyltryptophanyl-D-norleucine], is the first identified and most extensively used ET_B antagonist due to its high selectivity. BQ-788 is a potent competitive peptide inhibitor to ET_B, with IC50 of 1.2nM when testing on human Girardi heart cells, albeit it also exhibits minor but detectable binding to ET_A (407). In vitro study showed BQ-788 inhibits [^{125}I]-ET-1 binding to porcine cerebellar membranes, where ET_B is the predominant ET_R subtype. Furthermore, functional studies showed BQ-788 attenuates ET_B-mediated vasoconstriction in rabbit pulmonary artery, bronchoconstriction in human bronchi, and pulmonary ET-1 clearance in rat lung; all of which are unaffected by ET_A antagonists (408). IRL-2500, or [N-(3,5-dimethylbenzoyl)-N-methyl-(D) -(4-phenylphenyl)-alanyl l-L-tryptophan], is another ET_B-selective antagonist with low-molecular-weight. It has strong affinity for ET_B receptor in isolated guinea pig trachea, Ki (ET_B) = 1nM as opposed to Ki (ET_A) = 440nM (409). Accordingly, Webb et al (1995) recorded attenuated ET-1- and IRL-1620-induced vasodilator responses following the pre-treatment of IRL-2500 to conscious spontaneously hypertensive rats, reflecting inhibited ET_B activity (410). Moreover, Tanaka et al (1994) reported cyclic RES-701-1 inhibits [^{125}I]-ET-1 binding to ET_B in bovine cerebellar membrane and lung membranes, with an IC50 of 10nM. Similar to responses triggered by other ET_B antagonists, infusion of RES-701-1 also abolishes the initial vasodilatory response and potentiates vasopressor effect triggered by ET-1 in anaesthetized rats (411). Overall, BQ-788 is the most widely-used ET_B antagonist for its high potency and selectivity and is currently the only one trialled in human

study (378).

10.5.4.4. *Spotting-lethal (sl/sl) rat and ET_B mutation*

As identified in "spotting-lethal" (*sl/sl*) rat, homozygous ET_B knock-out mutations cause WS-IV- and HSCR-like phenotypes due to disruption in ET-3/ET_B signalling. *sl/sl* rats derived from a naturally occurred 301-base pair deletion in ET_B gene; this deletion is spanned between the exon 1 and intron 1 of *EDNRB* gene. While the ET_B-deficient animal may survive birth, distinctive aganglionic megacolon secondary to incomplete ENS development limits their lifespan. In addition, they often exhibit pigmentary disorders and hearing deficits due to the failure of epidermal melanoblast colonization (300). Additionally, because ET_B mediates endothelin clearance, plasma ETs are elevated in ET_B deficient animals. Moreover, Hocher et al (2001) reported glomerular filtration rate (GFR) is 72% lower and fractional sodium excretion is 84% lower in homozygous ET_B-deficient rats when comparing to the wild type rats. Conversely, homozygous ET_B-deficient rats have 7.9mmgHg higher mean arterial pressure (412). These findings support *sl/sl* rat to be a good model for studying the multi-organ effect of ET_B.

Research Questions: Does *sl/sl* rat, a homozygous ET_B knock-out HSCR model, exhibit global structural changes and growth retardations?

Because ET_B's involvements in neurogenesis, angiogenesis, inflammatory responses, vasoregulation, and its intertwined relationships with ET_A signalling pathway, we suspect *sl/sl* rat, a model animal of HSCR and WS-IV syndrome, exhibits external morphological changes and growth impairments in the central nervous and cardiovascular organs. Consequently, we

adopted modified micro-CT scanning protocols to quantitatively analyse the anatomical changes associated with $ET_B^{-/-}$ HSCR model.

Given a functional ET_B is pivotal to endothelin clearance, loss-of-function of ET_B destabilize the equilibrium in the endothelin system. While past study has demonstrated loss of ET-1/ET_A signalling results in craniofacial dysmorphology, little is known about the morphogenesis from the overstimulation in ET-1/ET_A pathway. In this series of study, we first provide the dimensional measurements on the external craniofacial features of *sl/sl* rat, followed by the volumetric analyses on the intracranial and cardiovascular organs. While only subtle craniofacial dysmorphology may be detected with ET_B mutation due to the intact ET-1/ET_A signalling, we suspect *sl/sl* rat to exhibit significant structural changes and growth impairment in the central nervous and cardiovascular systems. As the development of these organs are highly perfusion-dependent, end-organ hypoperfusion from reduced basal vasodilation and unchecked vasoconstriction triggered by ET_B dysfunction will have detrimental impact. Additionally, loss of ET-1/ET_B signalling reduces endothelial proliferation and inhibition of endothelial apoptosis will further impair angiogenesis and organ growth.

In summary, we explored the following targets sequentially in this series of studies:

1. Devise a functional imaging workflow for high-definition visualization and analysis of animal central nervous system.
2. Devise a functional micro-CT scanning protocol for the cardiovascular system of neonatal animal.
3. Identify the craniofacial changes, if any, associated with $ET_B^{-/-}$ Hirschsprung model, spotting-lethal rat.

4. Quantitatively measure the neuroanatomical changes in $ET_B^{-/-}$ Hirschsprung model, spotting-lethal rat.
5. Quantitatively measure the cardiovascular structural changes in $ET_B^{-/-}$ Hirschsprung model, spotting-lethal rat.

Chapter 2 Tables:

	Agonists	*Antagonists*
Non-selective ET_R		Bosentan (RO 47-0203)
		macitentan
		tezosentan
ET_A	ET-1	BMS-182874
	ET-2	BQ-123
		BQ-610
		FR139317
		JKC-301
		VML-588
		Ambrisentan
		Atrasentan
		Avosentan
		Darusentan
		Sitaxentan
		Zibotentan
ET_B	ET-1	A192621
	ET-2	BQ-788
	ET-3	IRL-2500
	S6c	IRL-1038
	IRL-1620	RES-701-1
	BQ-3020	

Table 1: A summary of agonist and antagonist for ET_R

Common agonists and antagonists for mammalian ET_R are listed. While there are no ligands with complete ET_A or ET_B selectivity, categorization is based on each ligand's respective dominant binding-affinity to respective receptor subtype. There are no ET_A agonists discovered currently except the naturally occurring ET-1 and ET-2. On the other hand, several experimental ET_B agonists have been proposed. A wide array of experimental and clinical antagonists for both ET_R showed promising results but only bosentan is currently approved for clinical use.

Chapter 2 Figures:

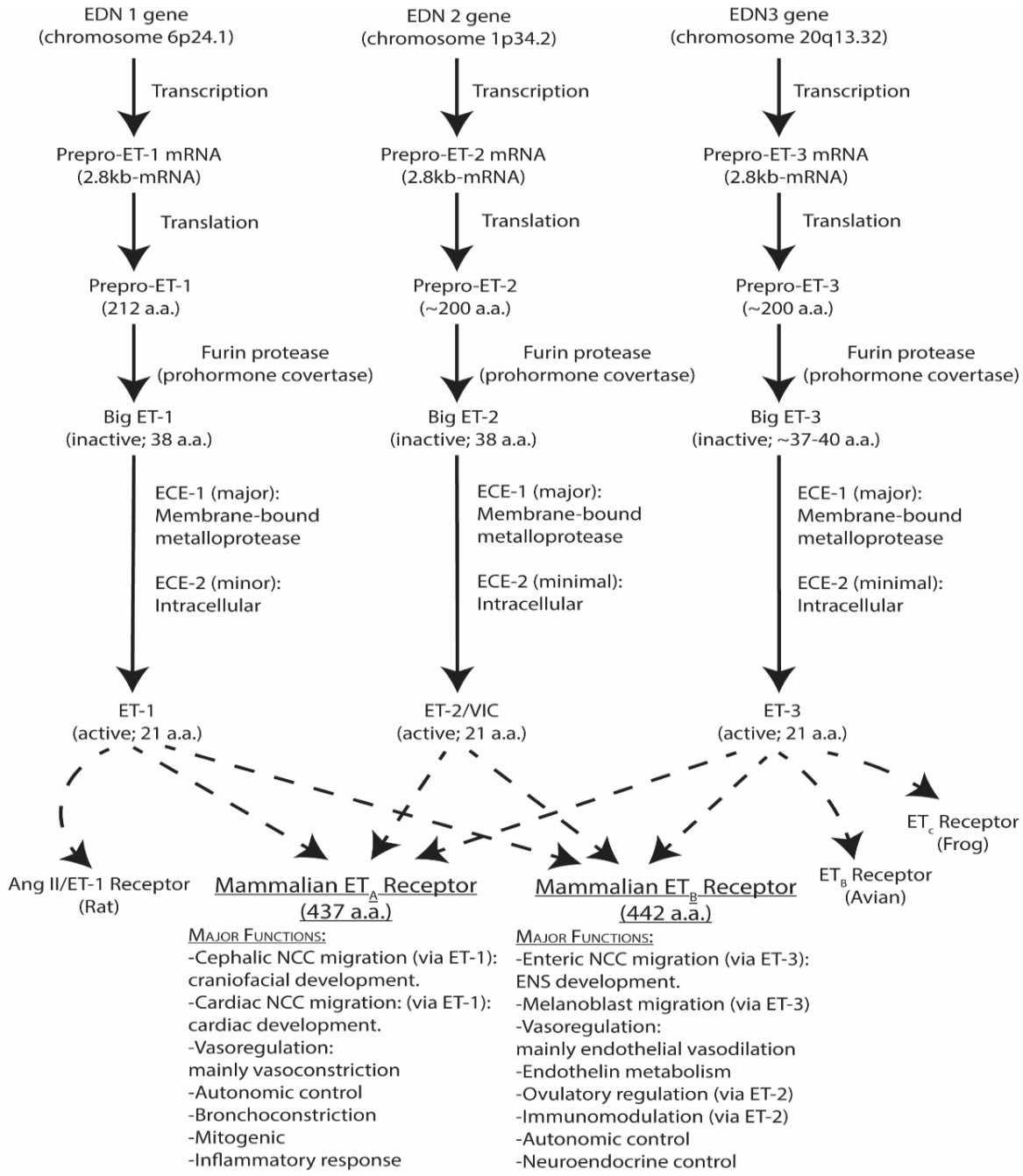

Figure 1: Production of endothelin and interactions to endothelin receptors.

The synthesis of all endothelin (ET-1, ET-2, and ET-3) follows four major steps: transcription of endothelin (EDN) gene, translation of preproendothelin mRNA, cleaving of prepro-ET to Big-ET precursors by furin protease, and final conversion to active ETs by ECE. While ECE-1 has greatest binding affinity to Big ET-1, it still is the major converter for all Big-ET when comparing to ECE-2. The active ETs bind to the five ET_R with different affinities. The functions of mammalian ET_R, ET_A and ET_B, are currently more well known.
ECE: endothelin converting enzyme; *Ang II/ET-1* receptor: angiotensin-II/endothelin-1 receptor; *ET-2/VIC*: endothelin-2/vasoactive intestinal contractor, a murine ET-2 analogue; *NCC*: neural crest cell.

Chapter 3: Methods

1. Preface

The following sections provide basic descriptions on the background of the spotting-lethal (*sl/sl*) rats and X-ray micro-computed tomography (micro-CT) system utilized in this series of study. This is followed by two subchapters detailing the tissue preparation and scanning protocols for successful soft tissue scanning used in later chapters.

2. Background of spotting-lethal (*sl/sl*) rat colony in ANU

As mentioned previously, we adopted *sl/sl* rat as the animal model for studying the global anatomical changes associated with HSCR and dysfunctional ET_B. *sl/sl rat* is a naturally occurred null mutant of ET_B ($ET_B^{-/-}$). It exhibits the phenotypes of aganglionic megacolon and white coat colour (413). The pathogenesis of knockout ET_B leading to abnormal phenotype is also affirmed by Matsushima et al (2002) using a mouse model: a deletion of 301-bp spanning across the junction between exon1 and intron1 of the *EDNRB* gene causes aberrantly spliced *EDNRB* mRNA and thus defective ET_B. This $ET_B^{-/-}$ mouse displays phenotypes consistent with WS-IV: hypopigmentation, megacolon, and congenital hearing loss (413, 414).

In this series of studies, the rat samples were generated through crossbreeding among the heterozygous rats ($ET_B^{+/-}$). This heterozygous breeding colony has been maintained in the Australian National University (ANU) over the past 15 years. The typical external morphology of these rats is shown by Figure 1, with *sl/sl* rats having the spotless skin, partial pigmentation in the eye, and abdominal distension. Furthermore, *sl/sl* rats

generated by these breeding strains have typical lifespan of 1-2 weeks, after which death would occur naturally due to the complications of severe bowel obstruction. Although there was a policy to euthanatize *sl/sl* animals as soon as diagnosed, we have inevitably recorded a specimen with a lifespan of 38 days in our 15-year colony data. This recording suggested severity of intestinal dysfunction is likely non-uniform in different specimen.

2.1. Genetic inheritance and gender association of *sl/sl* rat colony in ANU

The segregation analysis was completed on the 864 pups of heterozygous parents. The genotype of the offspring showed consistent Mendelian inheritance to the expected 1:2:1 ratio, *p-value* = 0.001, Table 1. Among the 864 offspring, the gender of 565 were accurately identified and recorded, which showed a slight male propensity in the populations of homozygous *sl/sl* and wild-type rats, Table 2. This suggested a potential sex-linkage with ET_B gene, which is consistent with male predominance in HSCR incidence (10); however, chi-squared test performed on colony data was unable to reject the null hypothesis, with respective *p-values* of 0.15 in *sl/sl* group and 0.25 in heterozygous group.

2.2. Phenotypic parameters of *sl/sl* rat colony in ANU

The enteric intestine of 475 genotyped rats were reviewed following successful H&E and acetylcholinesterase staining. The results of intestinal aganglionosis were presented in Table 3, illustrating high genetic penetrance of *sl/sl* traits, up to 95% in male and 90% in female group. Aganglionosis were confirmed in all diseased rats albeit varying genetic expressivity were observed: length of diseased bowel segment was not uniform. Additionally, rare incidence of aganglionic bowel was observed in wild-type (1%) and heterozygous (3%) groups, which was in accordance with possible *de novo* mutations.

Consistent with the observation made by Dembowski et al (2000) that *sl/sl* rat suffers growth retardation from as early as 7 days of age (415), our colony data demonstrate that reduced body weight and growth rates, albeit small, can occur in *sl/sl* mutants from as early as 48-hours of age. This body weight disparity between the control (wild type and heterozygotes) and *sl/sl* group only became grossly apparent after the age of 168-hours, showing a difference of 12.8%, Figure 2. Interestingly, *sl/sl* rat did not seem to have compromised body size within the first 24 hours of birth, but in fact larger based on our colony data. This suggests growth retardation secondary to bowel dysfunction in mutant is likely a delayed process and contributes little to the developmental delay at early ages, Figure 2. Consequently, animals used in this study are deliberately sacrificed within the first 4 days of life to minimize confounding effect of malnutrition.

As a side note, we acknowledge the body weight measurement may be confounded by potential faecal loading in diseased rat; however, due to the limited intestinal storage capacity in neonatal rats, the effect of this confounding factor is likely small with respect to the actual weight gain from body growth. Ideally, 3-D whole body volumetric measurements would provide the most valid data in terms of determining body growth; however, this is not feasible based on current image segmentation tool available. Nevertheless, as later chapters have shown, lower intracranial and cardiac growth rate in *sl/sl* rat may indirectly support lower bodily growth.

Overall, our colony data supports the notion that the causes for anatomical changes, if any, observed in neonatal *sl/sl* rats are likely multi-factorial. These factors may include

intrinsic neural crest failure, vascular dysregulation from endothelin signalling dysfunction, and global body growth retardation from enteric dysfunction.

2.3. Phenotypic parameters of sample rats used in this series of study

A total of fourteen neonatal rats are culled with an average age of 90-hours. As illustrated by Figure 3, the PCR-genotyping revealed 4 wildtypes, 4 heterozygotes, 5 *sl/sl* rats, and 1 inconclusive due to DNA degradation.

The physical parameter of the 13 genotyped samples showed the control group (wild type and heterozygotes) has 15.78% higher bodyweight than *sl/sl* rats, *p-value* = 0.02; on the other hand, their respective growth rates showed only minor difference, Figure 3. Furthermore, basic splenic parameters of sacrificed rats are measured for possible ET_B receptor effect on immune system (416). As shown by Figure 4, *sl/sl* rats have statistically significant smaller spleen weight (0.063g vs 0.092g, *p-value* = 0.01) and spleen growth rate (0.00075g/Hr vs 0.00097g/Hr, *p-value* = 0.04) than the control groups. This supports that *sl/sl* rats may have impaired development in the immunological system, possibly through disruptions in the ET-2/ET_B signalling as previously suggested.

In the subsequent morphological studies, three rat samples are excluded for the following reasons: one with inconclusive genotyping due to DNA degradation (Figure 3, Lane 1.3), one with unsatisfactory micro-CT scan, and one reserved for H&E processing, as summarized in Table 4.

3. Micro-computed tomography (micro-CT) systems

Micro-CT scanning is a tissue-preserving whole-volume imaging method first developed by Jim Elliott in early 1980s. It has the benefits of offering high resolution images with detailed and accurate anatomical information. Thanks to the improvements made on the micro-CT scanners and software in recent years, detections of subtle volumetric and dimensional changes of biological tissues are now possible with this new non-destructive approach.

3.1. Basic principles of micro-CT

X-ray micro-CT is a non-destructive three-dimensional (3-D) imaging method. A detailed description of this imaging method can be found in Kak and Slaney (417). The first generation of CT scanners are introduced in 1974 for medical use. Since then, improvements in computational power, detector technology and hardware have led to progressively higher resolution tomography, right down to the micron scale; this scanning system has been referred as "micro-CT technology" subsequently (418-421). Given a good image contrast relies heavily on the high intrinsic X-ray attenuation of the inorganic materials, micro-CT has been used but limited to a number of studies in the biomedical and biomechanics fields of implants in the past (422-426). However, with the recent introduction of staining techniques for soft tissues, further applications of micro-CT have now taken place in various study types, including embryology, oncology, histology, angiogenesis, and bioengineering (427-436).

The acquisition of a standard micro-CT image involves placing a sample in between an X-ray source and a detector (scintillator/charge-coupled device). The detector acquires two-dimensional (2-D) projections of X-ray data from the sample at multiple azimuthal orientations. A 3-D image is then reconstructed from the full set of 2-D projection data by

computation. The achievable spatial resolution depends on the setting of geometrical magnification, as illustrated by Figure 6. Based on the equation listed in the caption of Figure 6, the resolution in the sample plane (R_s) can be estimated as R_s = max ((*PS* × *SSD*)/*SDD*, (*SS* × *DSD*)/*SDD*), where *SDD* = source-detector distance = *DSD* + *SSD*, and other defined variables listed in the figure. The resolution can be optimized by using a detector with small pixel size (small *PS*), positioning the sample close to the source (small *SSD*), increasing source-detector distance (large *SDD*), minimizing spot size (small *SS*) by reducing the X-ray tube power, and focusing the electron beam onto the target from the source using an objective lens (437, 438).

3.2. Differences between the *ex vivo* and *in vivo* micro-CT setups

Current micro-CT systems are generally classified into *in vivo* and *ex vivo* based on system setups. These terminologies are not to be confused with their standard definitions in biomedical science but rather as descriptions of micro-CT setups (439).

The *in vivo* micro-CT system (Figure 7A) is set up as a mini-medical CT system. It incorporates a rotating system of X-ray source and detector rotating around a stationary sample, achieving a maximal spatial resolution of 10-100 µm/voxel. A voxel is a graphic unit in 3-D space, defined by x, y, and z coordinates. The spatial resolution is limited by the fixed distance between the X-ray source and detector. The advantages of *in vivo* micro-CT include a shorter scanning time and lower radiation exposure, both of which are essential for live animal study.

In contrast, the *ex vivo* micro-CT system involves placing a sample on a rotational

stage in between a stationary but adjustable system of X-ray source and detector, as illustrated by Figure 7B. The focus of this system is to achieve high resolution and detailed images for structural analysis at the expense of scanning time and radiation dose. While a decent *ex vivo* micro-CT scanner can achieve a maximal spatial resolution of 1 μm/voxel currently, its radiation dosage limits its use from live animal study.

As a side note, because the adjustable X-ray source can be brought much closer to the sample (limited by the sample size) in *ex vivo* than *in vivo* micro-CT setup, higher resolution and signal-to-noise ratio are achievable. The same cannot be achieved with *in vivo* micro-CT setup due to current constructional constraints of fitting sufficient X-ray sources and detectors onto a small rotational stand. This is by definition the fundamental difference between the two platforms and the defining reasons why *ex vivo* micro-CT image quality is superior to *in vivo* micro-CT images.

Chapter 3 Figures:

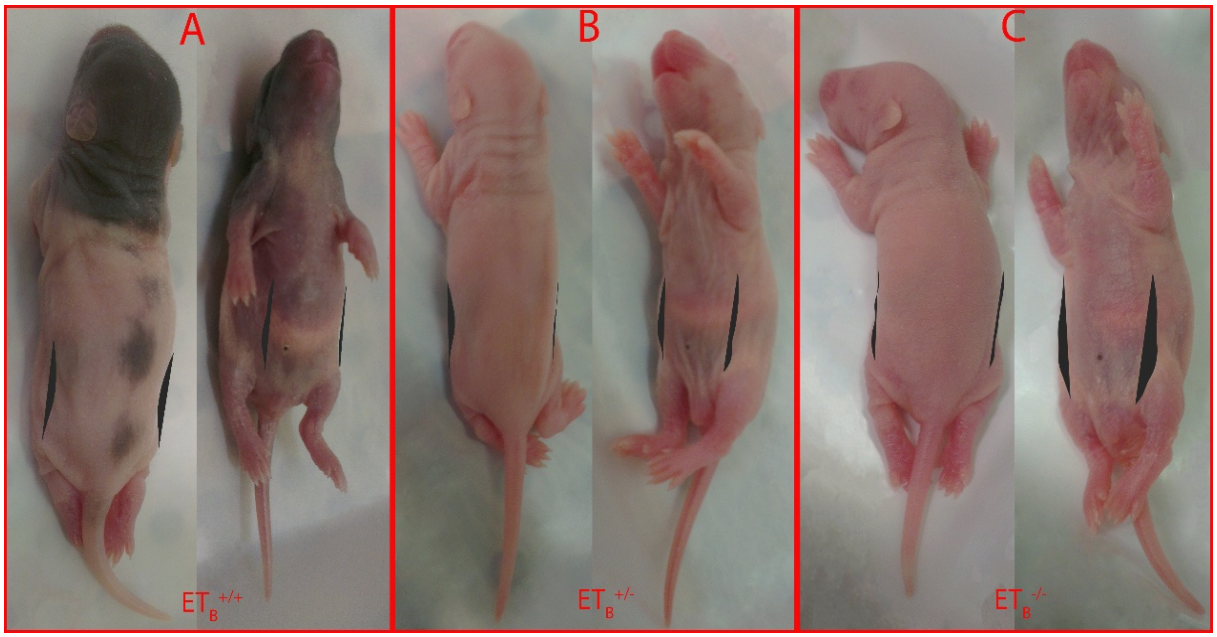

Figure 1: Phenotype of homozygous wild type ($ET_B^{+/+}$), heterozygous ($ET_B^{+/-}$), and homozygous *sl/sl* rats ($ET_B^{-/-}$) of same age.

Figure 1A: wild type rats display normal spotting coat pigmentation and lack of abdominal distension as shown by the abdominal curvature. **Figure 1B**: heterozygous rats show a lack of skin pigmentation and normal abdominal curvature; although not shown, skin pigmentation can exist with heterozygous rats. Figure 1C: *sl/sl* rats demonstrate lack of spotting pigmentation and marked of abdominal distension with the loss of concave abdominal curvature.

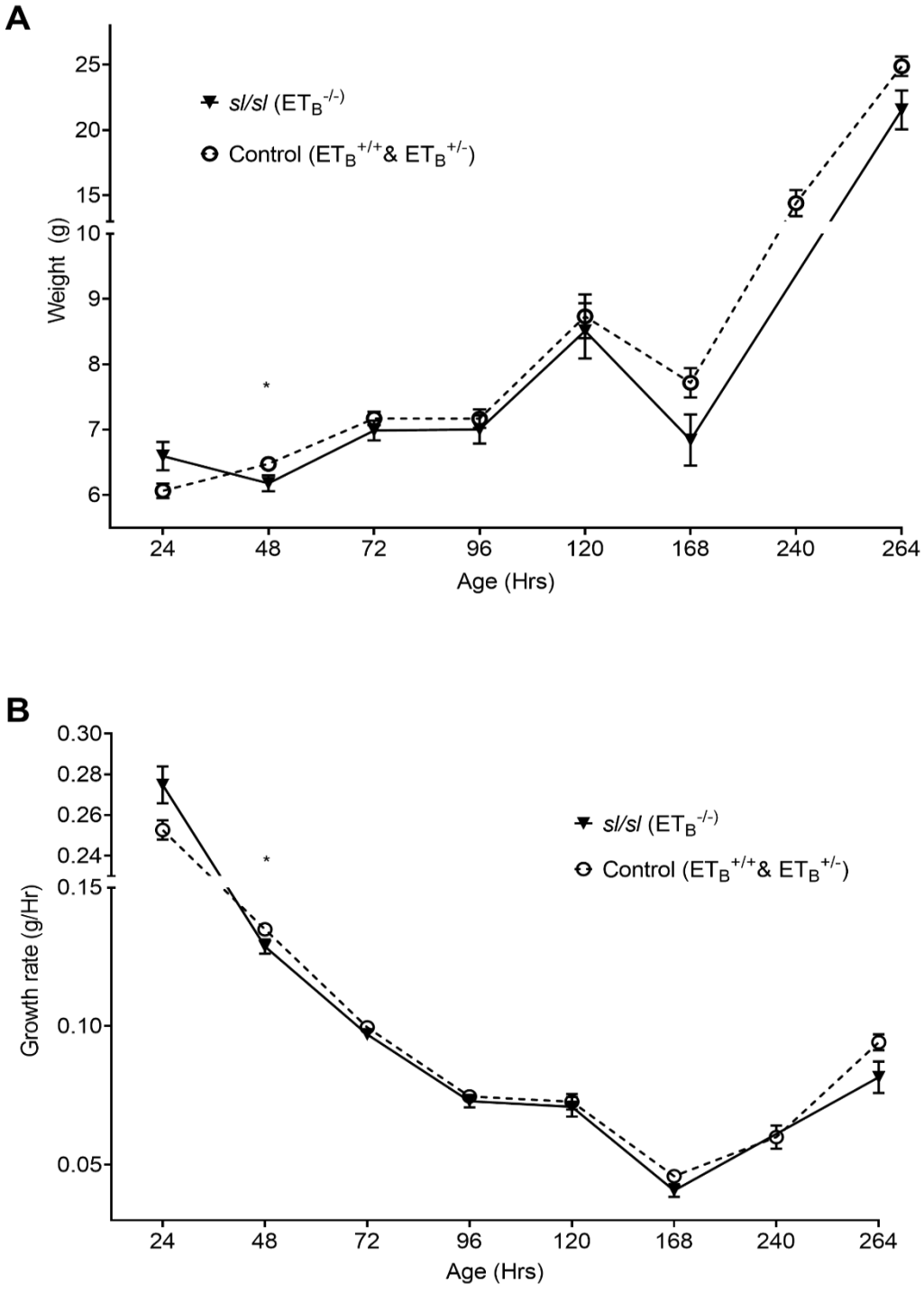

Figure 2: Growth retardation associated with ET_B mutation occurs after 168 hours of age based on colony data of 852 rats.

While *sl/sl* rats have smaller body size **(Figure 2A**) and slower body growth (**Figure 2B**) than the control group from the age of 48 hours and onward, the opposite was true for rats with age < 24hours. Furthermore, markedly lower bodyweight and growth rate in *sl/sl* rats are observed only after the age of 168 hours, consistent with the delayed process of obstructive intestinal complications.

*: statistically significant difference between control and *sl/sl* groups, $p < 0.05$

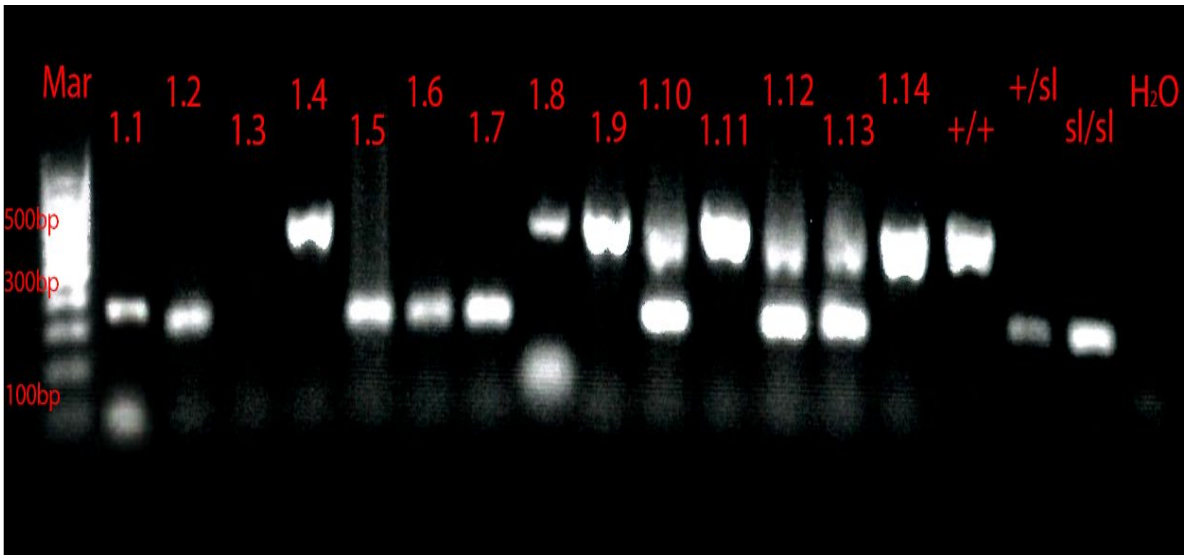

Figure 3: PCR-Genotyping of rat samples used.

PCR-genotyping of the fourteen rats sacrificed. Four homozygous wild types ($ET_B^{+/+}$) were identified with single 527kp band: 1.4, 1.9, 1.11, and 1.14. Four heterozygotes ($ET_B^{+/-}$) identified with double-bands of 527kp and 206bp: 1.8, 1.10, 1.12, and 1.13. Lastly, five *sl/sl* ($ET_B^{-/-}$) rats identified with single 206 bp band: 1.1. 1.2, 1.5, 1.6, and 1.7. Unfortunately, sample 1.3 yielded inconclusive genotyping.

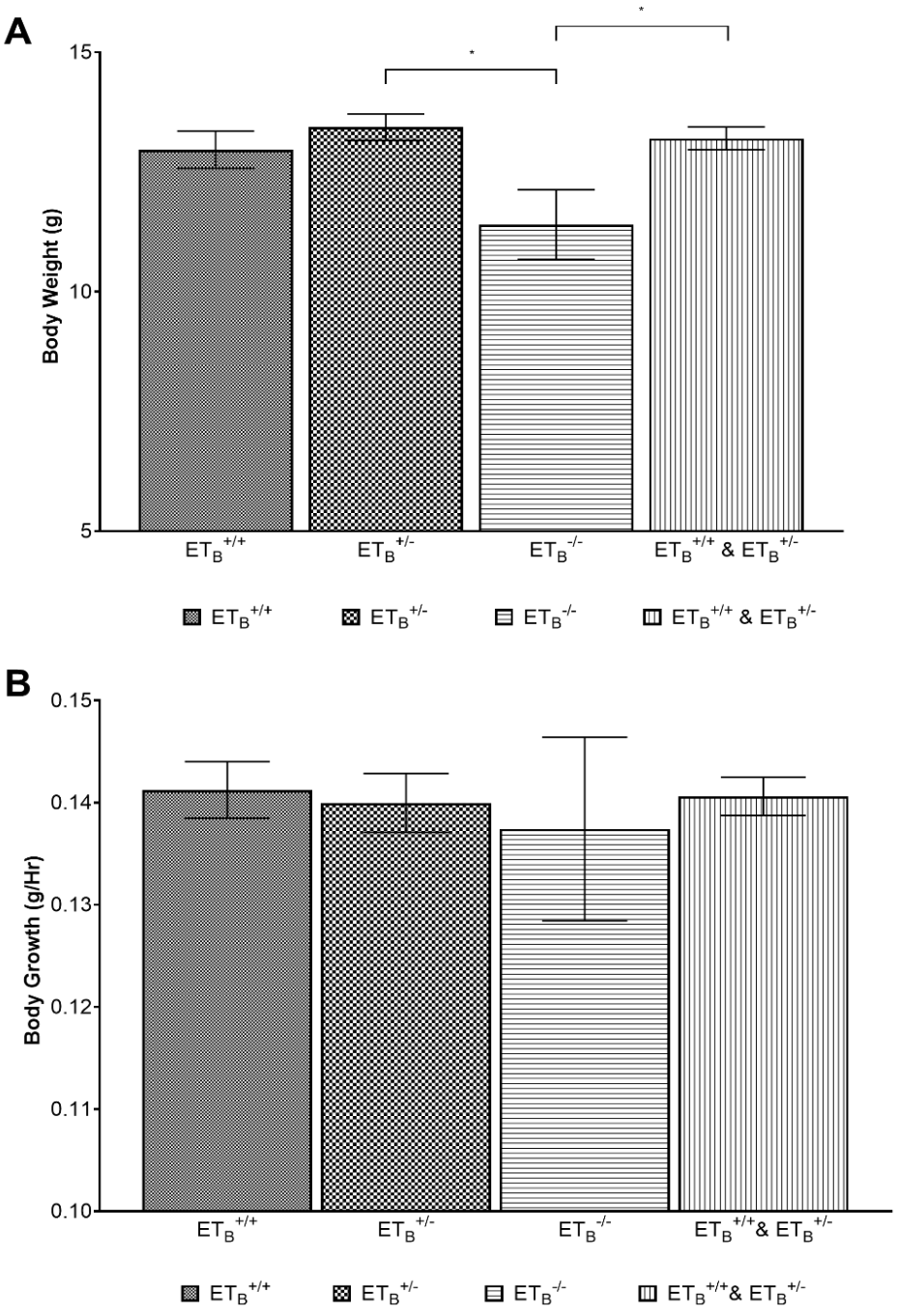

Figure 4: Body size and growth parameters of the study samples.

Based on the data of 13 rat samples, ET_B mutation is associated with reduced bodyweight and growth rate. **Figure 4A**: *sl/sl* ($ET_B^{-/-}$) rats have a 15.78% smaller bodyweight than the control ($ET_B^{+/+}$ & $ET_B^{+/-}$) group; similar trend was also observed when comparing *sl/sl* to individual sub-groups: wild-types ($ET_B^{+/+}$) and heterozygotes ($ET_B^{+/-}$). When comparing the growth rates of respective groups, **Figure 4B**, similar trend was observed, with *sl/sl* group having the lowest growth rate. Moreover, minimal variability in body growth were seen between the wild type and heterozygotes, supporting the notion that ET_B mutation exerts its negative effect on body growth in an autosomal recessive manner.
*: statistically significant, $p < 0.05$

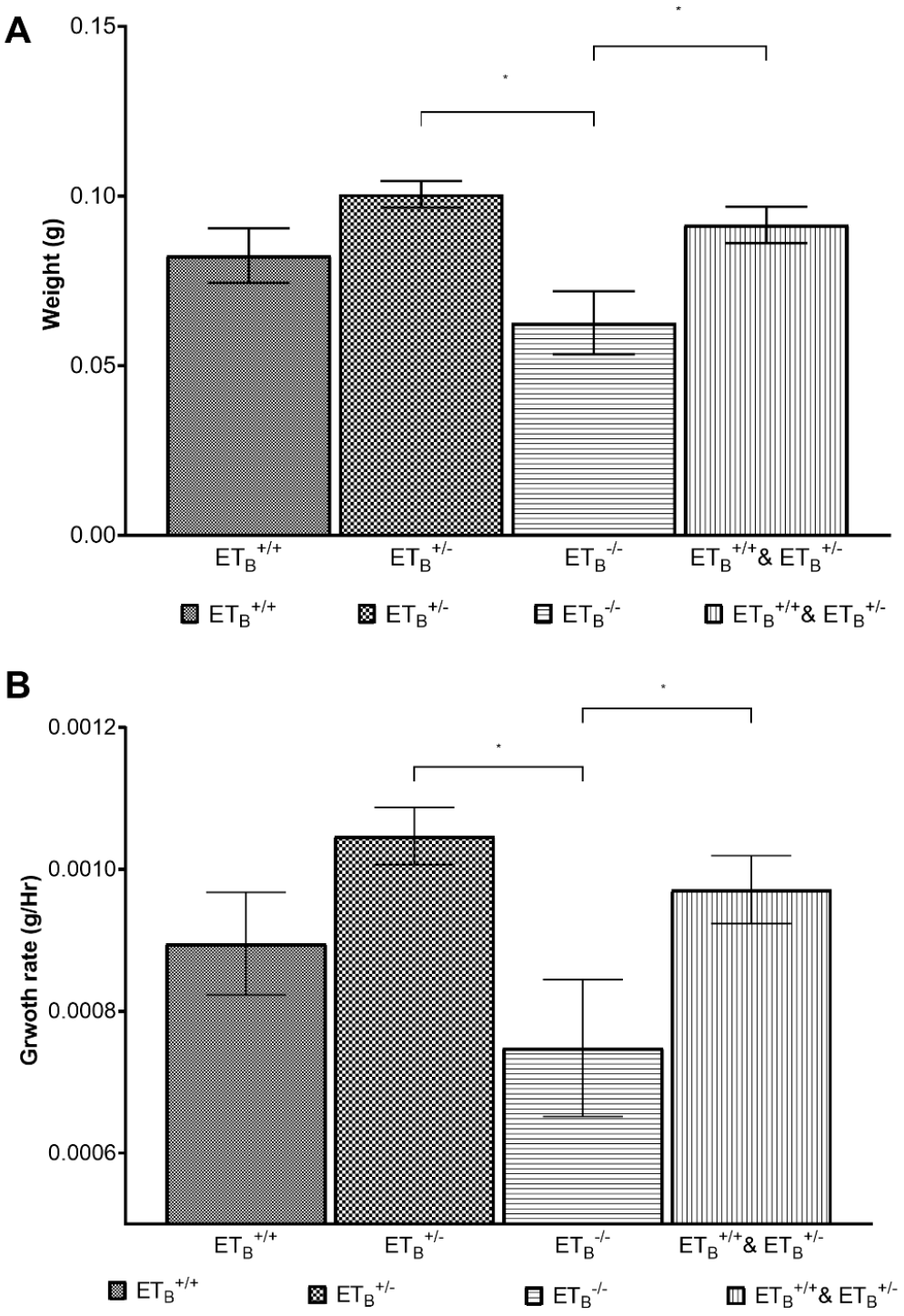

Figure 5: Splenic size and growths of rat samples

Potential impairment in the development of immune system may be associated with ET_B mutation. **Figure 5A**: *sl/sl* ($ET_B^{-/-}$) rat was associated with 46.13% smaller spleens than the control ($ET_B^{+/+}$ & $ET_B^{+/-}$) group. Similarly, wild type ($ET_B^{+/+}$) and heterozygotes ($ET_B^{+/-}$) have larger spleens than *sl/sl* rats. Consistent pattern was observed in the splenic growth rates comparison, **Figure 5B**.

*: statistically significant, $p < 0.05$

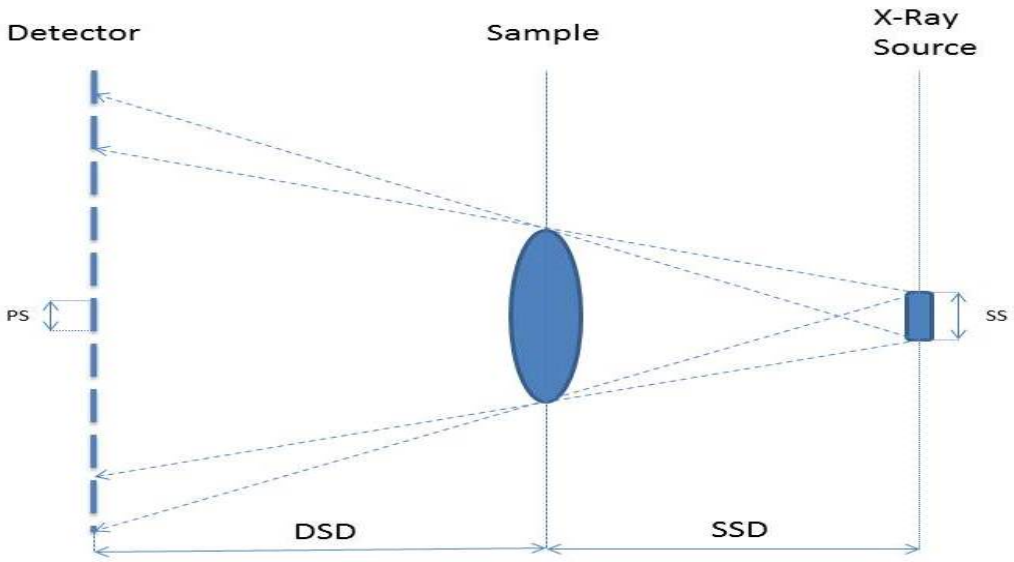

Figure 6: Basic principle of micro-CT setup

The maximal spatial resolution of a micro-CT image is dependent on the geometrical magnification of the system, which is determined by the positions of X-Ray source, sample and detector. Resolution (R) at the detector is determined by the following equation:

$$R = \max (PS, SS \times DSD / SSD),$$

Where PS = Pixel Size; SS = Spot Size; DSD = Detector-Sample Distance; SSD = Source-Sample Distance.

Theoretically, maximal magnification can be achieved by maximizing DSD while minimizing SSD; however, DSD is restricted by the physical size of the scanner while SSD is limited by the sample size (440).

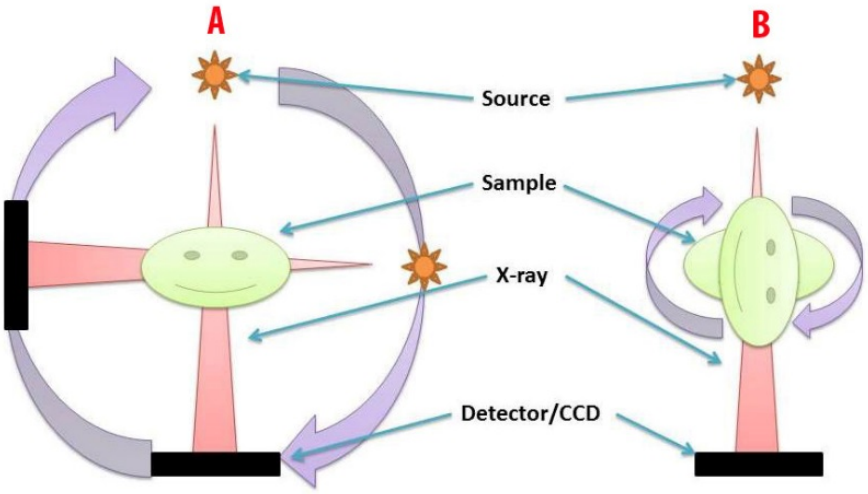

Figure 7: A depiction of *in vivo* and *ex vivo* micro-CT set up.

While both *in vivo* and *ex vivo* micro-CT scanners consist of an X-ray source, a sample stage, and a detector, their respective setups are different. **Figure 7A**: *in vivo* micro-CT placed a fixed sample-stage in between a rotational system of X-ray source and detector. On the other hand, **Figure 7B**, *ex vivo* micro-CT incorporates a rotating sample-stage with adjustable X-ray source and detector, both of which can be changed to increase magnification.

Chapter 3 Tables:

Genotype	*Number of subjects (n=)*	*Proportionality of Total population (%=)*
Wild type ($ET_B^{+/+}$)	203	24%
Heterozygotes ($ET_B^{+/-}$ & $ET_B^{-/+}$)	398	46%
sl/sl ($ET_B^{-/-}$)	263	30%
Total	**864**	**100%**

Table 1: Genetic makeup of the colony offspring.

Colony data of 864 offspring generated from heterozygous breeding ($ET_B^{+/-}$ x $ET_B^{+/-}$) showed a genetic composition of 24% wild type, 46% heterozygote, and 30% *sl/sl* mutant. This inheritance pattern is in accordance with Mendelian ratio of 1:2:1, *p-value* = 0.001. Accordingly, our colony data support that *sl/sl* genotype is an autosomal recessive genetic condition.

Genotype	*Gender (M/F)*	*Number of subjects (n=)*	*Proportionality of Total population (%=)*
Wild type ($ET_B^{+/+}$)	M	102	55%
	F	83	45%
Heterozygotes ($ET_B^{+/-}$ & $ET_B^{-/+}$)	M	124	51%
	F	119	49%
sl/sl ($ET_B^{-/-}$)	M	77	56%
	F	60	44%

Table 2: Gender distribution among each genotype.

Gender distribution of 565 rat data showed consistent male propensity among the three genotypes. Among the homozygous wild type ($ET_B^{+/+}$) and *sl/sl* ($ET_B^{-/-}$) mutants, male is ~10% higher proportion than female. The gender distributional difference in heterozygotes, on the other hand, is minimal. This suggests ET_B is likely sex-linked, consistent with HSCR traits.

Genotype	*Gender (M/F)*	*Enteric Morphology*	*Number of subjects (n=)*	*Proportionality of Total population (%=)*
Wild type ($ET_B^{+/+}$)	M	Aganglionic	1	1%
		Normal	86	99%
	F	Aganglionic	0	0%
		Normal	70	100%
Heterozygotes ($ET_B^{+/-}$ & $ET_B^{-/+}$)	M	Aganglionic	5	3%
		Normal	187	97%
	F	Aganglionic	2	1%
		Normal	175	99%
sl/sl ($ET_B^{-/-}$)	M	Aganglionic	55	95%
		Normal	3	5%
	F	Aganglionic	43	90%
		Normal	5	10%

Table 3: High genetic penetrance of autosomal recessive traits is observed in *sl/sl* rats.

The enteric system of 475 rats with known genotype showed a degree of high genetic penetrance of the autosomal recessive traits. Over 90% of s*l/sl* rats exhibited aganglionic intestine as opposed to less than 3% in the wild type and heterozygous rats. Additionally, male *sl/sl* rats have higher diseased population than female *sl/sl* rats, 95% vs 90%, supporting a possible sex linkage. Lastly, both wild type and heterozygous group shared a high percentage of population with normal phenotypes, supporting ET_B mutation as an autosomal recessive condition.

Rat	Genotype (ET_B)	Weight at Sacrifice (g)	Age at Sacrifice (hours)	Spleen Weight (g)	Morphological Study Inclusion
1.1	-/-	10.4376	80	0.0386	Y
1.2	-/-	12.8401	80	0.0749	Y
1.3			80	0.0688	N
1.4	+/+	11.8741	80	0.0700	Y
1.5	-/-	9.0197	80	0.0439	Y
1.6	-/-	12.4492	80	0.0684	Y
1.7	-/-	12.2679	96	0.0872	Y
1.8	+/-	13.9730	96	0.1023	Y
1.9	+/+	13.6915	96	0.1045	Y
1.10	+/-	13.1977	96	0.0953	Y
1.11	+/+	13.0398	96	0.0845	Y
1.12	+/-	13.8007	96	0.1107	Y
1.13	+/-	12.7777	96	0.0937	N
1.14	+/+	13.2607	96	0.0708	N

Table 4: Summary of the sample rats used in this series of study.

A total of 14 rats were sacrificed, with age between 80 and 96 hours. The control group ($ET_B^{+/+}$ and $ET_B^{+/-}$) in general has larger bodyweight than *sl/sl* ($ET_B^{-/-}$) rats. As illustrated, this study consisted of 4 wildtypes, 4 heterozygotes, and 5 *sl/sl* mutants. Rat1.3 was completely excluded from data pool due to DNA degradation during genotyping. Rat 1.13 and Rat 1.14 were excluded from morphological analysis due to failed micro-CT scanning and tissue destruction following H&E microscopy.

Chapter 3.1.: High-Definition neural visualization of rodent brain using micro-CT scanning and non-local-means processing

Chapter 3.1 Highlights

- Micro-CT scanning, a structural-preserved and versatile imaging methodology, offers detailed neuroanatomical information comparable to that of 4x microscopy.
- *Ex vivo* micro-CT scanner yields much higher signal-to-noise and hence more refined rat brain images than *in vivo* micro-CT scanners.
- Staining is required for neural tissue visualization in micro-CT scanning; iodine diffusion staining is fast, safe, and effective.
- Small craniotomy is required for diffusion staining the rat brains encapsulated in calcified skulls, both in neonatal and adult rats.
- Post-imaging processing using non-local means (NLM) algorithm provides a modest enhancement to *ex vivo* micro-CT scans and a moderate improvement to *in vivo* micro-CT scans of rat brains.
- NLM processing is recommended for *in vivo* micro-CT scans for better tissue differentiation and hence more accurate quantitative analysis.

Chapter 3.1 Abstract

Background
Micro-CT holds promising potential for phenotyping and histological purposes. However, few have clarified the difference in the neuroimaging quality between *ex vivo* and *in vivo* micro-CT scanners. In addition, no direct comparison has been made between micro-CT scans and standard microscopy. Furthermore, while the efficacy of various stains for yielding soft tissue contrast in CT scans have been compared in other studies made on embryos, staining protocols for larger samples have yet to be clarified. Lastly, post-acquisition processing for image enhancements have not been addressed.

Methods
Comparisons of postnatal rat brain micro-CT scans were made between those obtained from a custom-built *ex vivo* micro-CT scanner and a commercially available *in vivo* micro-CT scanner. Subsequently, the scanned rat brains were H&E stained for microscopy. Anatomical information on micro-CT scanning and 4x microscopy of rat brain were then compared.

Diffusion and perfusion staining using iodine or PTA were trialled on adult and neonatal encapsulated rat brains. Different combinations of contrast concentration and staining time were trialled.

Post-acquisition denoising with NLM filter was completed using a modern General Purpose Graphic Processing Unit (GPGPU) and custom code for prompt processing.

Results
Ex vivo micro-CT scans of iodine-stained rat brains yields 3D images with details comparable to 4x H&E light micrographs. Neural features illustrated by the *ex vivo* micro-CT scans were significantly more distinct than those by the *in vivo* micro-CT scans.

Both *ex vivo* and *in vivo* micro-CT scans required diffusion staining through small craniotomy. Perfusion staining is ineffective. Iodine staining was more efficient than PTA in terms of time.

Enhancement made by NLM denoising on *in vivo* micro-CT images were more pronounced than that on *ex vivo* micro-CT scans due to their intrinsic difference in image signal-to-noise indexes.

Conclusions
Micro-CT scanning is a powerful and versatile visualization tool available for qualitative and potentially quantitative anatomical analysis. Simple diffusion staining via a small craniotomy with 1.5% iodine is an effective and minimal structural-invasive method for both *in vivo* and *ex vivo* micro-CT scanning. Post-acquisition NLM filtering is an effective enhancement technique for *in vivo* micro-CT brain scans.

1. Background

Non-destructive whole-volumetric phenotyping studies through three-dimensional (3D) image reconstruction have gained increasing popularity among biomedical researchers over recent decades, especially with recent advancements in imaging acquisition and processing techniques. Three-dimensional visualization techniques may be divided into two categories: serial sectional image reconstruction and whole-volume imaging. The former includes confocal microscopy, episcopic microscopy (441); the latter includes optical projection tomography (OPT) (442), micro-magnetic resonance imaging (micro-MRI) (443, 444), and micro-computed tomography (micro-CT) (431).

Whole-volumetric imaging is superior to serial imaging in many aspects. Serial imaging reconstructions such as confocal microscopy or confocal laser scanning microscopy (CLSM) can provide detailed and fluorescence-labelled representations of the sample, but of only limited thickness, typically < 2-300 μm due to the need for optical transparency (445). Although image reconstruction may be employed to obtain the entire 3D view of the sample, the process is laborious and often with operator-dependent results. Episcopic microscopy overcomes this shortfall by adopting automatic serial slice alignment, and reconstructs relatively well-preserved images; however, such a process destroys the tissue sample post-imaging and prohibits further sample use (441, 446). Whole-volumetric imaging, on the other hand, does not have the above restrictions. For example, optical projection tomography (OPT) can be used to localize and measure structures within a whole organ, but only for restricted sample thicknesses (447). Micro-MRI can offer images with great soft tissue contrast and adequate resolution, but its use is limited by its restricted availability, high cost and extended scanning time (444, 448, 449). Micro-CT is now a widely accessible

imaging modality, offering a mean for accurate visualization of three-dimensional structures, quantitative volumetric measurements, and tissue characterizations such as bone stress and vascular density (422-425, 450). Although many are still unaware of this versatile tool, micro-CT has gradually become a popular whole-volume scanning research method, in large part due to its versatility for volume exploration, ease of tissue preparation, and quantitative analytic potentials.

Although many recent papers have published various staining techniques for successful micro-CT scanning of biological samples, including chicken embryo, *Xenopus* embryo, mouse embryo, tumour angiogenesis, and other animal internal organs (431, 451, 452), few study have clarified the scanning protocols for micro-CT scans on postnatal animal model or made direct comparisons between the *ex vivo* micro-CT, *in vivo* micro-CT, and histology scans of rat neuroanatomy. Furthermore, even though prior study has suggested staining with iodine or phosphotungstic acid (PTA) are efficient and effective for embryos, no comments have been made on their staining power for postnatal animals (431). In addition, the effect of iodine and PTA staining on subsequent microscopy processing has not been illustrated in the past. Lastly, we are also not aware of studies trialling image processing protocols on the rat brain micro-CT scans, which may facilitate future quantitative analysis.

Our study aims to complement previous studies by illustrating the following:

1. Simple, safe, and effective staining method for successful micro-CT scans on both small and large rat brains.

2. The neuroanatomical details of rat brain and maximal image magnification and resolution achievable by micro-CT scanning using one of the most high-powered *ex vivo* micro-CT scanners available currently.
3. Validate neuroanatomical information of micro-CT scan by direct comparison with H&E light microscopy.
4. The difference in image quality between *in vivo* and *ex vivo* micro-CT scans of rat brain.
5. Effectively improve image clarity and potentiate organs of interest through non-local means (NLM) denoising algorithms.

2. Method

2.1. Compliance with Ethical practice

All tissues and animals used in this study were handled with strict adherence to the requirements of the ACT Health Human Research Ethics Committee (ACTH-HREC) and Australian National University Animal Experimentation Ethics Committee (ANU-AEEC), project number A2011/67.

2.2. Differences between the principles of *ex vivo* and *in vivo* micro-CT setups

We have chosen the Caliper Quantum FX machine (Figure 1A) as representative of *in vivo* micro-CT setup and a custom-built micro-CT system by ANU Applied Mathematical Department as representative of *ex vivo* micro-CT setup (Figure 1B).

The *in vivo* micro-CT system is set up as a mini-medical CT system. It incorporates an X-ray source and detectors rotating around a stationary sample, achieving a spatial resolution

of 10-100 µm/voxel, which is restricted by the fixed distance between X-ray source and detector. In the Caliper Quantum FX, the tissue specimen was placed in a stationary loading dock positioned between the rotating system of X-ray source plus detector. The scanning time was pre-set between 17s and 4.5min, depending on the field of view (FOV; ranging from 5–75 mm in diameter) and imaging quality selected (ranging from “standard” to “fine”). The advantages of *in vivo* micro-CT scanners including a shorter scanning time and lower radiation exposure, both of which were essential for live animal study. The resultant images were stored as DICOM series and visualized with FIJI and Drishti, both of which were open-source software (453, 454).

In contrast, the *ex vivo* micro-CT system involves a specimen placed on a rotating stage between a stationary but adjustable system of X-ray source and detector. Its focus is to achieve high spatial resolution, up to 1 µm/voxel, with high signal-to-noise ratio images. These benefits are achieved at the expense of longer scanning time and hence higher radiation dose. It is therefore mainly used for tissue study. The custom-built micro-CT system at the ANU Department of Applied Mathematics requires the sample to be fixed within an aluminium tube before being placed on the rotational sample stage between the adjustable X-ray source and scintillator-coupled-CCD, at a position that depends on the resolution desired. All samples are allocated at least 15 hours of scanning time, with a subsequent 8 hours of image-processing time required at the National Computational Infrastructure (NCI). The maximal achievable resolution is 1 µm/voxel, limited by the physical size of the sample. The resultant images are stored as netCDF files and visualized with Drishti. Segmentation for organs of interest is performed semi-automatically using Drishti paint, a component of Drishti open-source software (453).

As a side note, because the adjustable X-ray source can be brought much closer to the sample (limited by the sample size) with ex vivo than *in vivo* micro-CT setup, higher resolution is achievable. The same cannot be achieved with *in vivo* micro-CT setup due to the current constructional challenges of fitting X-ray sources and sufficient number of detectors onto a small rotational stand.

2.3. Tissue samples and staining preparations for micro-CT scanning

2.3.1. *Adult rats and neonatal rat culling*

Five fully-grown rats (>21 and 27 days) and thirteen 24- and 48- hours old rats were over-anaesthetized with 5 % isoflurane and then culled via abdominal aortotomy. Each rat was weighed. One adult rat is prepared through the perfusion protocol and the remaining rats were prepared via the diffusion protocol, as described below.

2.3.2. *Perfusion protocol for adult rat brains*

To test the staining potential of perfusion protocols, we culled one 27-days-old rat via cardiotomy with a 22G cannula. The rat was then perfused with 200 mL of 0.1M phosphate-buffered saline (PBS) solution and subsequently 200 mL of 4% formalin for successful fixation, indicated by tail rigidity; each stage took about 45 minutes. The perfusate exited the vascular system through inferior vena cava venotomy. Next, the rat was perfused with a series of progressively concentrated ethanol solutions (20%, 50%, 70%, 90%) to replace intravascular formalin for subsequent staining. Each concentration of ethanol was run over one hour. Staining was then attempted by perfusing the animal with 1.5% iodine (in 90% ethanol) through left ventricles for 2.5 hours in a lab basin.

2.3.3. *Diffusion staining protocols for encapsulated adult and neonatal rat brains and isolated rat brains*

To explore the alternative staining techniques, we attempted diffusion staining by the following. Four adult rats' heads (average age 25 days) were isolated from the neck and up following culling. A diamond-shaped craniotomy of twenty-millimetres in diameter on parietal bones was created for staining. The craniotomy was completed firstly by a superficial cross-incision of twenty millimetres in diameter (through the thickness of the skull) using a dissection scalpel followed by diagonal excisions of skull using iris scissors. Superficial dissection was carefully performed to avoid brain tissue damage. Minimal damage of the brain was confirmed by the absence of brain tissue destruction in the subsequent micro-CT scans.

Four percent formalin was first used to fixate the rat head for 24 hours followed by washout with graded ethanol in the following steps. Each fixed tissue was immersed in progressive concentrated ethanol (EtOH) series to replace formalin solution for 4 days: 20%, 50%, 70%, and 90% ethanol. Each sample was then stained in 1.5% iodine (with 90% EtOH) or 0.5% phosphotungstic acid (PTA) or 1% PTA in 70% EtOH for various durations (listed in Supplementary Table 1) as attempts to find the most effective staining time for successful CT scanning. Contrast concentration was decided based on the successful results of previous studies on embryo staining (431, 451).

Similarly, diffusion staining on thirteen neonatal rat brains was achieved through similar processes: isolation of upper body from the level of diaphragm, creation of a five-

millimetres in diameter diamond-shaped craniotomy on parietal bones, 4% formalin-fixation for storage, progressive ethanol washout prior to staining, and diffusion staining with 1.5% iodine, 0.5% PTA, or 1.0% PTA for various periods (listed in Supplementary Table 1).

Lastly, three 24-hours-old rat brains were dissected and fixed as described above prior to staining with 1.5% iodine and 1.5% PTA, respectively. Macroscopic views of PTA- and iodine- stained brains are shown by Supplementary Figure 1 and 2.

2.4. Hematoxylin and Eosin (H&E) histology preparations for comparison with micro-CT scans

To confirm the neuroanatomical details on the micro-CT scan and assess the potential tissue distortion created by the iodine or PTA staining process, as shown by the macroscopic brown-discoloration of brain tissues due to iodine staining (Supplementary Figure 1 and 2), we processed the stained rat samples with standard H&E protocols (53).

H&E processing were conducted in the following steps. The iodine- or PTA- stained tissues were first sectioned sagittally into blocks of 4mm in thickness to fit in cassettes. These tissue blocks were then transferred to 90% EtOH for 48 hours for contrast washout and dehydration. Next, the alcohol was cleared by xylol prior to paraffin embedding at 60°C. Following embedment, samples were sliced into tissue-sheets of 4 µm in thickness using a microtome. These tissue-sheets were then laid in water-bath of 5-6°C to minimize wrinkles while being positioned onto the pre-labelled glass slides. These slides were dried overnight at 37°C. H&E staining was completed by progressive staining. The slides were placed in alum-hematoxylin solutions until dark red colour was visualized. This was followed by washing and

then ‘bluing’ with lithium carbonate solution. The slides were then washed before counter-stained with 0.5% eosin alcoholic solution.

All H&E slides were then examined with an Olympus IX71 Microscope with 4x, 20x, and 40x magnification.

2.5. Post-acquisition image processing: Non-Local Means (NLM) denoising

To improve the micro-CT image clarity, we denoised the acquired images to enhance image signal-to-noise ratios using NLM algorithm, which was first developed by Buades et al (455). The algorithm was based on the premises that similarity exists between different regions of an image if these region sizes were kept relatively small. Using these similarity characteristics, image noise could be removed through averaging the similar parts of the image. For more accurate removal of the image noise, we used standard NLM with locally adaptive estimates for both types of micro-CT scans. Traditionally, this process was time-consuming due to the high demand on computational power thus making its computer-processing-unit (CPU) runtime unacceptably high for all but the smaller 2-dimentional (2D) images. However, we adopted parallel processing using a General-Purpose Graphic Processing Unit (GPGPU) and shortened the processing time to one minute and thirsty seconds for a 512^3 sample, rendering this process effective and efficient for regular research use.

This code was implemented on an Intel (R) Core ™ i7-4770K CPU @3.5GHz with 32G of RAM and Nvidia GeForce GTX Titan Black Kepler GK110 architecture running Linux. The processed CT data were then reviewed using Fiji (456).

2.5.1. *Implementation of the NLM algorithm*

A brief description of our NLM implementation is provided as follow. The vast majority of the NLM runtime is spent on computing the sum of squared differences (ssd). The ssd computation for adjacent voxels is highly similar. We can exploit this similarity by using a pseudo moving average filter (MAF) to perform the ssd from one pixel/voxel to the next. For 2D, the square area of intensities used for one voxel's ssd search neighbourhood differs from an adjacent voxel's search neighbourhood only in the end rows or columns. The same principle applies in 3D, adjacent cubes differ only in two end slices.

In 3D, if M is the number of voxels of the inner ssd cube and N is the total number of cubes that we performed the ssd on, then the total number of difference operations: with no MAF, we performed N x M^3 difference operations; with the MAF, we performed M^3+ (N-1) x 2 x M^2 difference operations. For a large N, this becomes a significant reduction in computation. As a simple example, if M is 100 voxels and N is a billion, the second operation is then a two-orders of magnitude less operation.

The most implementations of the NLM require the user to specify at least 3 parameters: an estimate of the image noise standard deviation, an outer search window size, and an inner search neighbourhood size. All these factors influence the quality of the de-noise operation. An accurate estimate of the noise and the size of the search window and neighbourhood are generally impossible and often the user has not even the vaguest notion of what the optimized values may be. This leads to tedious and time-consuming testing and retesting of the de-noising operation with different parameters until acceptable results are

obtained. Our implementation does not require these unknown and often arbitrarily chosen parameters to be specified. Our implementation automatically computes an estimate of the noise in the local area of the pixel/voxel being de-noised. Each local noise estimate is combined with internally computed parameters determined from various image properties such as the number of intensity values i.e. 256 or 65K, to compute the final smoothing parameter of the NLM algorithm automatically.

The computation of the smoothing parameter and estimation of the image noise is adapted from Coupe et al., 2008 (457). Our implementation differs from theirs in that the computation of a unique noise estimate for local sub blocks of the image, as opposed to a single value for the entire image. We also consider the grey scale value (gsv) intensity range in the calculation of the smoothing parameter. The inclusion of the gsv intensity range was found empirically to be a significant factor in the success of the automatic de-noising over a range of different image types i.e. CT, scanning electron microscopy (SEM), ultrasound etc. Our implementation of NLM follows the original model of Additive Gaussian White Noise (AGWN) but also allows for some adjustment on the shape of the Gaussian kernel to better approximate the real noise distribution for images with non-AGWN.

As with Coupe et al., 2008 (457), we also concluded that the best de-noising quality is achieved by a local estimate of the noise, the correction factor for non-AGWN images, and fixed window sizes. Little, if any, gain in quality was obtained with larger search window sizes. It is obvious that in many cases, image quality degrades with larger search window sizes as the statistics of the similarity between these regions degrades.

3. Results

3.1. Simple tissue preparation for successful micro-CT scanning

In the first part of study, we proceeded to elaborate the simple staining process for postnatal rat samples required to achieve successful micro-CT scanning of the brains. The results of various combinations of contrast agent, stain concentration, and contrast types were summarized in Supplementary Tables 1.

3.1.1. *Staining of encapsulated postnatal rat brains for successful micro-CT neural imaging*

We first attempted 1.5% iodine perfusion staining in an adult rat of 27 days but with little success, as shown by Figure 2A. Intracranial neural tissue has little X-ray attenuation and thus minimal neuroanatomy differentiation was observed. The same rat's head with intact skull was re-scanned following 14-days of 1.5% iodine diffusion-staining with no improvement in image quality (Figures not shown). Subsequently, 44-days of iodine diffusion-staining through craniotomy was trialled on a 25-days-old rat's head; micro-CT scan demonstrated differentiated intracranial details as shown by Figure 2B: neural tissue differentiation became apparent. Consistently, same staining techniques also worked for neonatal rat brains but required only a staining period of 16 days; the resultant micro-CT scans yielded good neural anatomical information, as shown by Figure 2C.

As an attempt to find an alternative contrast agent, we explored PTA diffusion staining using both 0.5% and 1.0% concentration solutions. Figure 2D and 2E are micro-CT scans of adult rat brains (25-days-old) acquired from a 2.5 years of PTA staining period; both showed only peripheral brain of 2-4mm in thickness. Similarly, as shown by Figure 2F and 2G, incomplete neuroanatomy visualization was observed on micro-CT scans of neonatal rat's

head despite prolonged staining of 148 days. Interestingly, lower concentrations of PTA seemed to achieve more pervasive staining than the higher concentrated solutions, Figure 2F vs 2G, although neither performed well.

3.1.2. *Staining of dissected neonatal rat brains for successful micro-CT neural imaging*

Given the PTA staining was found to have a suboptimal staining power with encapsulated postnatal rat brain, we then evaluated its staining potential with dissected rat brains, namely $1cm^3$ in size. The result showed that PTA staining, although slow, did achieve full-staining and yield a neural micro-CT scan with quality similar to that derived from iodine staining. The comparison between the temporal series of iodine stained (Figure 2I – 2K) and PTA stained (Figure 2L – 2N) rat brains demonstrated the efficiency of iodine contrast. As Figure 2J demonstrated, iodine staining was completed within 6 hours; further staining did not improve image quality and tissue differentiation, Figure 2K. On the other hand, only a modest staining progression was made from 3 hours of PTA staining, Figure 2L. It took 6 days to complete a full staining, Figure 2N. There was no significant image quality difference between the micro-CT scans derived from iodine-stained and PTA-stained rat brains.

In both cases, contrast staining was faster with isolated brain than with skull-encapsulated brain, Figures 2C. However, all scans of isolated brain revealed microscopic tissue damages of the rat brains from dissections and handling, as indicated by the arrow labelling across Figure 2H – 2N, despite macroscopically intact appearance, as shown by Supplementary Figure 2s. Similar brain damages were not seen on the micro-CT scans of encapsulated brains, Figure 2B and 2C.

3.2. Image quality of micro-CT scans

In the second part of the study, we explored the image details and 3D-visualization capability of rat brain micro-CT scans.

3.2.1. *High display versatility of micro-CT scan data using 3D-volume rendering*

In this study, we demonstrated the investigatory power of micro-CT scanning by providing examples of the full visualization capability of current *ex vivo* micro-CT scanning through 3D-volume rendering. Figure 3 show the 3D-volume rendering of neonatal rat brain in high definition, 2048*2048*2048 voxels, with a resolution of 10.7 µm/voxel. Through manipulations of visual planes, one can identify and analyse organs of interest. For instance, the dorsal and ventral external features of the neonatal rats are illustrated in Figures 3A and 3B, respectively. In addition, Figures 3C - 3E show internal organs visualized in parasagittal and sagittal planes, ranging from salivary glands, musculatures, nasal cavity, oral cavity, and neuroanatomy. Figures 3C and 3D show progressive high-definition views of the brain and identify organs such as olfactory bulb, cerebral cortex, cerebellum, and cochlea in structural-preserved manner. Similarly, progressive anterior to posterior axial views, Figure 3F - 3H, provide alternative visualizations of cross-sectional rat brain anatomy that are difficult to appreciate in other views, such as cingulate gyrus, lateral thalamus and ventral thalamus. Overall, Figures 3A - 3H demonstrate that through different visual-planes exploration, various external and internal features of buccal, nasal, and intracranial organs can be visualized with excellent tissue contrast. Additionally, simple quantitative size measurement can be made with reference to the scale bar listed.

3.2.2. *Validating Neuroanatomical information offered by micro-CT scans with H&E histology*

To validate the micro-CT scanning method and explore potential microscopic tissue

distortion as a result of the staining preparations, we compared the *ex vivo* micro-CT scan, Figure 4A, to H&E microscopy, Figure 4B, both of which were derived from the same iodine-stained rat brain. This comparison demonstrated that the 3D rendering of the rat brain micro-CT scan offers neuroanatomical information comparable to those shown in 4x H&E microscopy. The grayscale distribution of micro-CT scans correlated strongly to the H&E distribution and therefore enabled successful neural structure distinguishment including olfactory bulb, caudate putamen, frontal cortex, thalamus, medulla, and cerebellum. Furthermore, the tissue integrity was well preserved in micro-CT scans when comparing to the H&E light microscopy, Figure 4B – 4D, which demonstrated micro-tears as a result of sectioning and H&E staining process. Moreover, successful light microscopy of iodine-stained rat brain demonstrated macroscopic discoloration by iodine, Supplementary Figure 1B, does not prohibit tissue from further histology processing. Furthermore, high magnifications of microscopy can be achieved with the iodine-stained sample, Figure 4C (20x magnification) and 4D (40x magnification), where nuclei can be visualized clearly.

3.2.3. *Direct Comparison of image quality of in vivo and ex vivo micro-CT scanning*

We illustrated the image quality difference between the *in vivo* and *ex vivo* micro-CT scans using the same iodine-stained rat brain, as shown by Figure 5. This direct comparison demonstrated the *in vivo* micro-CT scan's imaging limitations.

Both types of scans offered adequate information on gross anatomy; however, *ex vivo* micro-CT scans provided significantly more detailed neuroanatomy and sharper outlines than those on *in vivo* micro-CT scans. By comparing Figures 5Aa and 5Ba, the respective *ex vivo* and *in vivo* micro-CT scans of a 24-hour-old rat brain, one could clearly appreciate the frontal

cortex, caudate putamen, superior and inferior colliculus, and trabeculae of the skull; all of which were well-defined in Figure 5Aa. Higher magnification of the distinctive morphology in and around the cerebellum was chosen to further demonstrate how this difference can impact potential qualitative and quantitative analysis, as shown by Figure 5Ab (*ex vivo* micro-CT scan) and 5Bb (*in vivo* micro-CT scan). While the rough outline of cerebellar fissures and vermis were still discernible in the *in vivo* micro-CT scan (Figure 5Bb), intrinsic noise and oversaturation of the scan render the boundaries much less crisply than those shown in the *ex vivo* micro-CT scan (Figure 5Ab). Hence, one can easily define the ten cerebellar vermis and their respective sizes in Figure 5Ab but not in Figure 5Bb. This demonstrated the analytic limitations of *in vivo* micro-CT scans. In addition, the volumetric measurements of brain made based on the segmentations of *in vivo* micro-CT scans differed slightly to that of *ex vivo* micro-CT scans, 424.75 mm^3 vs 395.54 mm^3. Although small, this discrepancy was due to the image quality difference and thus resulted in less precise segmentation from *in vivo* micro-CT scans.

3.3. Post-acquisition image processing: Non-Local Means (NLM) denoising

Post-acquisition image processing using NLM algorithm was incorporated into this study as attempts to improve CT image quality for better visualization on the neural tissues through denoising. This process was particularly useful for *in vivo* micro-CT scans due to their high intrinsic images noise. Pre- and post- processing of *ex vivo* micro-CT scans, Figure 6Aa and 6Ba, show organ boundaries are subtly enhanced by NLM processing. This was more evident in their respective magnified views, namely the bordering of caudate putamen and external capsule, as demonstrated by Figure 6Ab and 6Bb. In addition, their respective grayscale line profiles showed reductions in the intensity spread, Figure 6Ac and 6Bc, and

thus demonstrated image noise reduction following NLM filtering. Similarly, the same but more prominent effect can be seen from the NLM filtering of *in vivo* micro-CT scans. As shown by Figure 6Ca and 6Da, edge enhancements of caudate putamen, lateral ventricles, and external capsules could be appreciated; however, the differences were even more obvious in their respective magnified views, Figure 6Cb and 6Db. The comparison of their respective grayscale line profiles also demonstrated decreases in intensity variability, Figure 6Cc and 6Dc.

4. Discussion

Through proper micro-CT setup, sample preparation, and image processing, informative neural micro-CT scans can be generated with postnatal animals. These scans enable internal visualization and potential quantitative analyses including volumetric and dimensional measurements by providing images with neural tissue differentiation. The image quality of these micro-CT scans are comparable, if not better, to micro-MRI brain scans, as illustrated Denic et al (2011) (458). Although a prolonged scanning time of 16 hours may be required, *ex vivo* micro-CT scan has a maximal spatial resolution of 1 µm/voxel, significantly higher than the resolution of 20 µm/voxel of micro-MRI, which requires 24 hours of high-magnetic-fields scanning (444, 459). Consistently, this high magnification power of micro-CT provides anatomical and histological details comparable to those shown on 4X H&E light-microscopy, Figure 4B. As a result of these characteristics, 3D rendering of the *ex vivo* micro-CT scans can show detailed and refined micro-neuroanatomy, Figure 3s. This function can therefore be applied to morphological study on genetic model animals or cancer studies. Moreover, because tissue sample can be preserved following micro-CT scanning for H&E processing, Figure 4C and 4D, micro-CT scan can serve as a screening tool for an area of

interest in the brain prior to further histology analysis. Although high-resolution micro-CT has the drawback of large dataset size, >4.6 GB/dataset, the high demand in computational and storage power for image analysis are met by the recent advancement in computing hardware, rendering this a practical research modality.

Although the difference between *ex vivo* and *in vivo* micro-CT has been addressed in previous studies, few have made direct comparisons on the quality difference of postnatal neural scans using these two modalities (439, 460). In this study, we demonstrated the difference in magnification and resolution potentials of micro-CT scans using a custom-built *ex vivo* micro-CT scanner versus a standard commercial *in vivo* micro-CT scanner, as shown by Figure 5. Consistent with expectations, our results have shown that *ex vivo* micro-CT scans offer finer detailed scans than *in vivo* micro-CT scans, due to the higher magnification achieved by allowing the X-ray source able to be brought closer to the sample (i.e., a short source-sample distance, *SSD*). In theory, reducing the *SSD* increases the image noises and blurs the object edges, an effect clearly shown by Figure 5Ba and 5Bb. However, image degradation can be minimized by using a low source current and a careful focusing to minimize source spot size to obtain the best resolution of < 2–3 μm/voxel while at the same time extend the scanning time to over 15 hours to achieve high signal-to-noise ratios. In comparison, commercial *in vivo* micro-CT scanners have limited magnifications and thus lower resolution due to the pre-set values of SSD. Furthermore, higher image noise in *in vivo* micro-CT scans is due to the shorter scanning time pre-set to minimize the radiation exposure in live animal study. In general, the best image quality needs the longest possible scanning time in either *ex vivo* or *in vivo* micro-CT setups.

Based on the prior successes made on embryo study, we compared two contrast agents, iodine and PTA, for postnatal neural tissue staining (451). The contrasts were chosen for their safety, ease of handling, and the likely effectiveness based on prior studies. Perfusion was first trialled in the hope of preserving rat skull integrity. Unfortunately, iodine staining is ineffective when introduced this way, likely due to poor penetration through the blood brain barrier and the slow diffusion rate through capillary walls to end organs (461, 462). Contrary to prior embryo studies, simple diffusion staining with intact skull was also trialled with little success, suggesting contrast penetration through calcified skull was not possible (451). Hence, diffusion-staining through a small craniotomy was subsequently adopted and found effective with iodine staining on all tested tissues. However, PTA is less effective as a stain using the same protocols on partially encapsulated tissues, especially on large adult rat brains; staining remained incomplete even after 2.5 years, Figure 2D and 2E, rendering this method impractical.

Due to the concerns of prolonged staining may cause structural damage and prohibit tissues from future histology uses, as shown in Supplementary Figure 1, we tested PTA and iodine staining on dissected rat brains of small sizes with the hope to shorten tissue preparation time, Supplementary Figures 2. The result showed both contrasts yield similar quality of rat brain micro-CT images, as demonstrated by Figure 2K and 2N. However, iodine is able to complete tissue staining faster than PTA due to its higher penetration. In addition, iodine was better in staining poorly vascularized tissues such as the central nervous system, where PTA had little success in staining tissues with size greater than $1cm^3$. This is likely due to the size and polarity difference of the two contrast agents: iodine is a non-polar molecule which is about 20 times smaller than the polytungstate anion of PTA (463-466). Nevertheless,

we found PTA staining times to be significantly longer than previously described (431, 451). To compensate for the lower penetration of PTA, limiting tissue volume to $1cm^3$ and complete organ isolation through dissection may be required for successful staining. While these modifications to the method have proven effective, adopting such an approach defeats the purpose of using micro-CT, since dissection and excessive handling increase the risks of structural damage, even by experienced dissectors, as illustrated by the micro-tears shown by micro-CT scans, Figure 2H through 2N. Based on our findings and the known difference in the properties of iodine and PTA, we recommend diffusion iodine-staining with partial craniotomy as the method of choice for micro-CT scans of postnatal rat brains. Additionally, successful H&E processing on both iodine- and PTA- stained brain tissues confirmed that prolonged contrast staining for micro-CT scanning compromises little, if any, tissue integrity. As shown by Figure 4C and 4D, neuronal cell bodies can be visualized in higher magnification light micrographs. This suggests micro-CT scans may serve as a targeting tool for regions of interest and reduce unnecessary histopathology processing in pathology study, thus reduce labour and time.

Post-acquisition image processing through NLM filtering is performed to enhance image clarity and structural boundaries. NLM algorithm is chosen for its property of spatial detail preservation (455). Although denoising only modestly improves *ex vivo* micro-CT scans, Figure 6Aa and 6Ba, due to the scan's high intrinsic signal-to-noise ratio, it has proven useful for *in vivo* micro-CT scans, which has high intrinsic image noises, Figure 6Ca. This images noise is significantly reduced after processing, Figure 6Da. These improvements are obvious in selected magnified views of caudate putamen, Figure 6Cb and 6Db. We appreciate that commercially available *in vivo* micro-CT scanners are more widely available than custom built *ex vivo* micro-CT scanners. By demonstrating the quality of *in vivo* micro-CT scans can be

effectively improved through adoption of NLM algorithms, we provide supports that *in vivo* micro-CT data can also offer accurate anatomical visualizations and quantitative analysis. Lastly, denoising reduces the image noise, as demonstrated by the reduction in the variability of intensity profiles, Figure 6Bc and 6Dc; this is an important step for the developments of accurate automated segmentation for the organs of interests.

5. Conclusion

Micro-CT scanning, using either *ex vivo* or *in vivo* micro-CT scanners, can be a powerful and effective neuroanatomy visualization modality for lab animals. Furthermore, micro-CT digital data is easy to store and manipulate. The anatomical details and accuracy offered by micro-CT scanning have been validated with the traditional H&E-stained light micrograph. Moreover, the safety, simplicity, and tissue-preserving characteristic of the iodine-diffusion staining through small craniotomy render micro-CT scanning a very easy-to-use imaging modality. Lastly, we appreciate that the *in vivo* micro-CT scanners are more widely accessible and have a faster image processing time than the *ex vivo* micro-CT scanners; thus, the low signal-to-noise ratio due to the physical data acquisition restraints of *in vivo* micro-CT scans has been addressed. The improvement made by a simple and efficient post-acquisition NLM processing reduces image degradation and enhances anatomical clarity, particularly with *in vivo* micro-CT scans, thus promoting versatile structural segmentation for quantitative analysis of animal morphology, including volumetric measurements. Based on the described imaging methods, future studies may include: 1. internal organ visualization and quantitative analysis on animal models of genetic disease, e.g. Hirschsprung's disease; 2. cancer treatment response studies on animal models; 3. identifying areas of interest for histological processing in pathology studies.

Chapter 3.1 Figures:

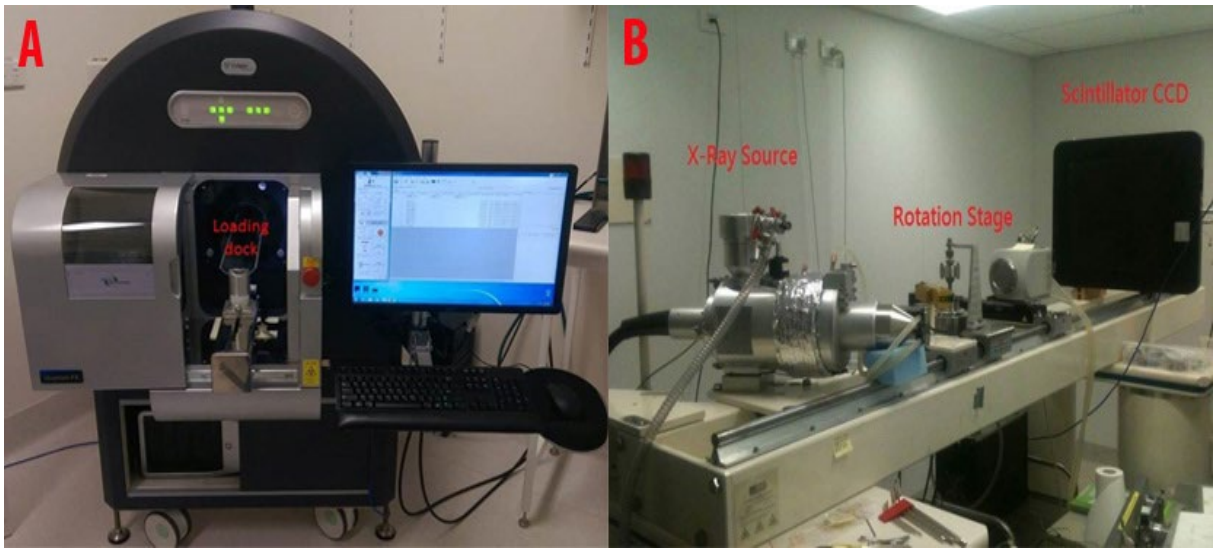

Figure 1: *in vivo* and *ex vivo* micro-CT machines utilized in this study.

(a): The Caliper Quantum FX machine as a representative of *in vivo* micro-CT setup, with loading dock labelled and situated in between a rotating X-ray source and detectors; X-ray source and detector are hidden within the casing. (b): The custom-built *ex vivo* micro-CT scanner by ANU applied mathematical department. The rotational sample stage is placed in-between the adjustable X-ray source and scintillator/detector for maximal magnification.

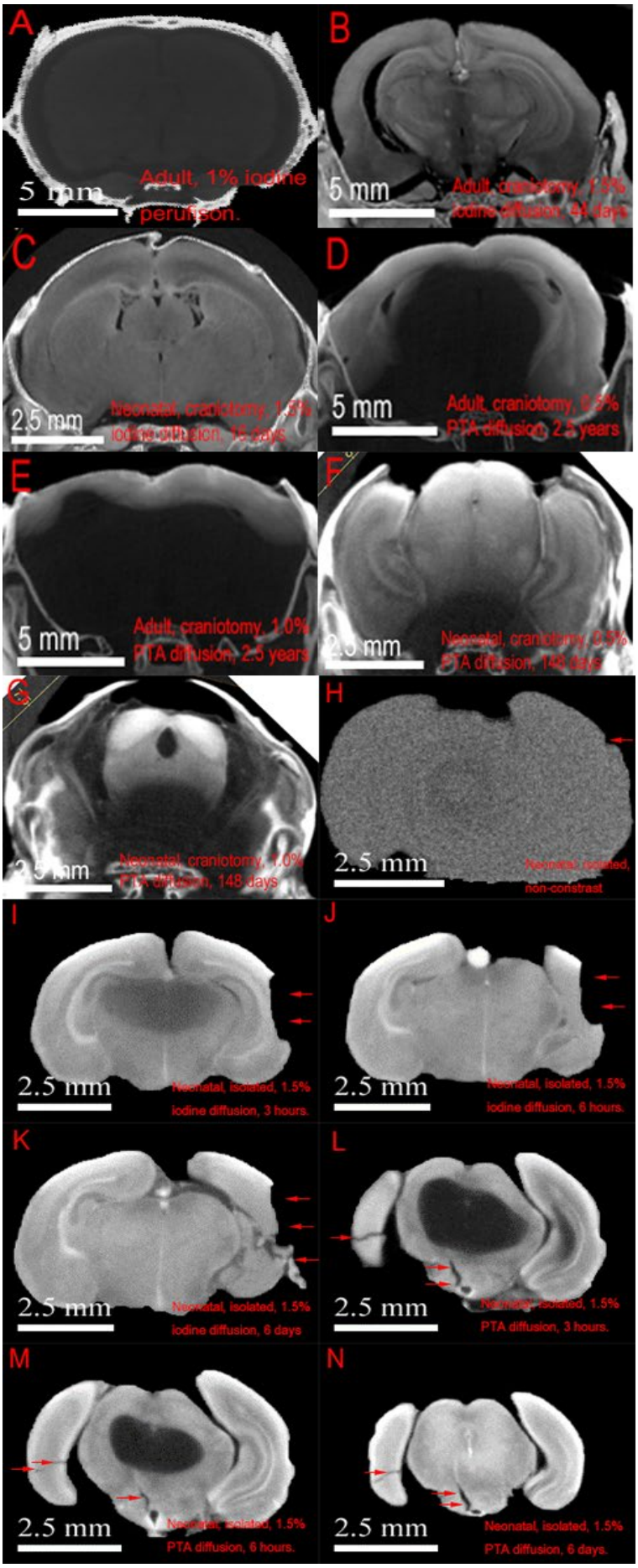
A
5 mm
Adult, 1% iodine perfusion.
B
5 mm
Adult, craniotomy, 1.5% iodine diffusion, 44 days
C
2.5 mm
Neonatal, craniotomy, 1.5% iodine diffusion, 15 days
D
5 mm
Adult, craniotomy, 0.5% PTA diffusion, 2.5 years
E
5 mm
Adult, craniotomy, 1.0% PTA diffusion, 2.5 years
F
Neonatal, craniotomy, 0.5% PTA diffusion, 148 days
G
Neonatal, craniotomy, 1.0% PTA diffusion, 148 days
H
2.5 mm
Neonatal, isolated, non-constrast
I
2.5 mm
Neonatal, isolated, 1.5% iodine diffusion, 3 hours.
J
2.5 mm
Neonatal, isolated, 1.5% iodine diffusion, 6 hours.
K
2.5 mm
Neonatal, isolated, 1.5% iodine diffusion, 6 days
L
2.5 mm
Neonatal, isolated, 1.5% PTA diffusion, 3 hours.
M
2.5 mm
Neonatal, isolated, 1.5% PTA diffusion, 6 hours.
N
2.5 mm
Neonatal, isolated, 1.5% PTA diffusion, 6 days.

Figure 2: Successful tissue differentiation on micro-CT scans demonstrating iodine diffusion staining technique is a practical method for both large (age of 25 days) and small (age of 36 hours) postnatal encapsulated rat brain, Figure (A) – (G).

(A) demonstrates unsuccessful neural tissue scanning after using 1.0% iodine perfusion staining for adult rat, whereas (B) and (C) show 1.5% iodine diffusion staining yield good neural tissue contrast with adult and neonatal rat brains after respective staining period of 44 and 16 days. However, the same staining techniques using 0.5% and 1.0% PTA yield little success on adult rat brains, (D) and (E), even after 2.5 years. Similarly, (F) and (G) show incomplete tissue differentiation of neonatal rat brains despite prolonged staining of 148 days with 0.5% and 1.0% PTA, respectively. Because PTA staining was non-uniform, selected coronal views are chosen to illustrate the regions of incomplete tissue differentiation: (A) – (D) are anterior coronal views while (E) – (G) are posterior coronal views.
Figure (H) – (N) illustrate iodine diffusion staining is equally effective but more efficient than PTA staining temporally for preparing small and isolated neural tissues tissue for micro-CT scanning. (H) shows a lack of tissue differentiation when scanning without contrast staining. (I) – (K) illustrate a progressive improvement of anatomical details shown by progressive 1.5% iodine staining time: 3 hours, 6 hours, and 6 days, respectively. Similarly, (L) – (N) show the same progression but with 1.5% PTA staining over the same respective durations. Iodine staining was significantly faster.

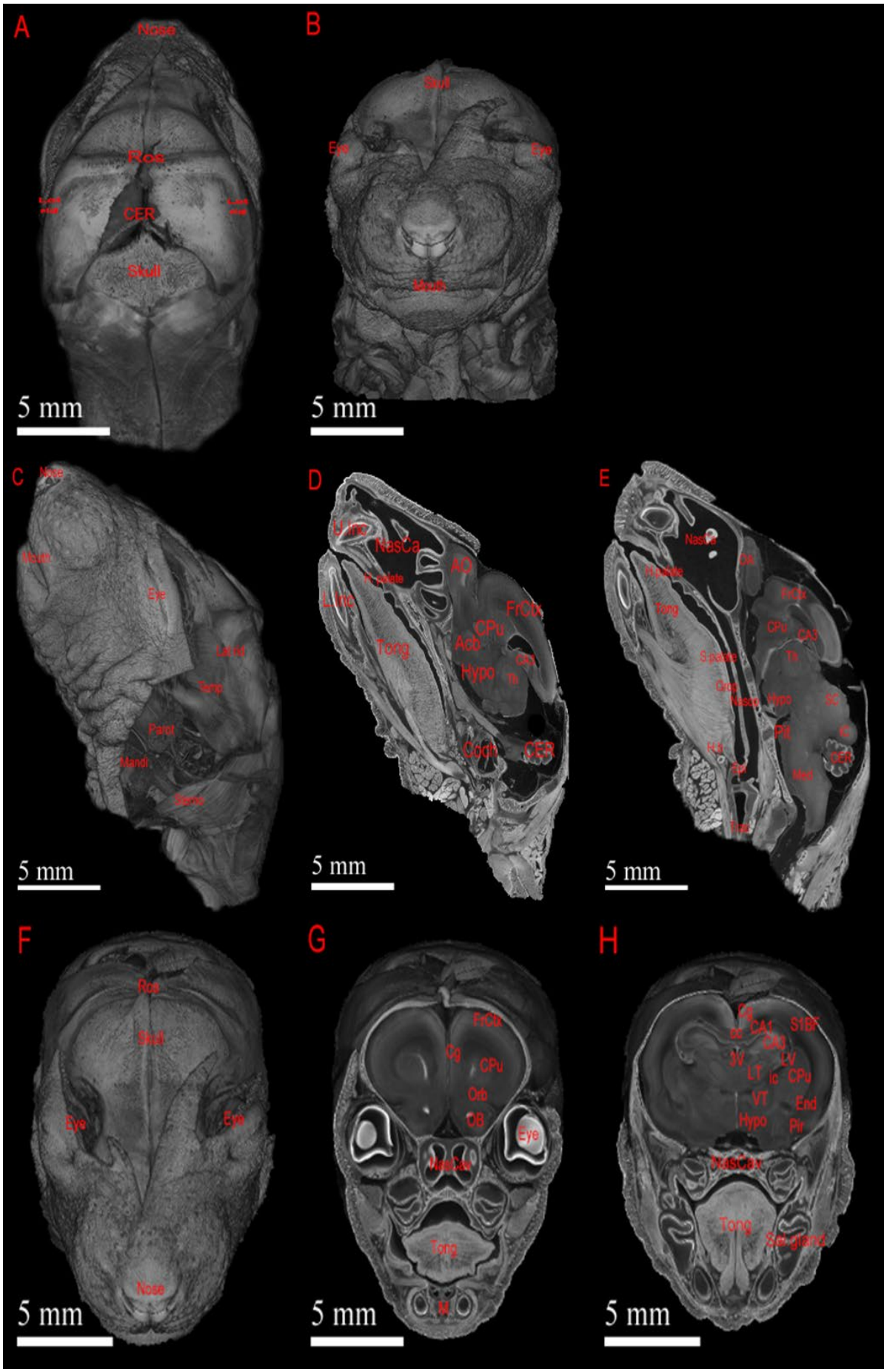
A
Nose
Ros
CER
Skull
5 mm
B
Skull
Eye
Eye
Mouth
5 mm
C
Nose
Mouth
Eye
Lat Vt
Temp
Parot
Mandi
Sterno
5 mm
D
U.Inc
NasCa
AO
H.palate
L.Inc
FrCtx
CPu
Acb
Tong
Hypo
Th
Cpd
Codh
CER
5 mm
E
NasCa
OA
H.palate
FrCtx
Tong
CPu
CA3
Th
S.palate
Hypo
SC
Pit
IC
H.f
Cer
Med
5 mm
F
Ros
Skull
Eye
Eye
Nose
5 mm
G
FrCtx
Cg
CPu
Orb
OB
Eye
NasCav
Tong
M
5 mm
H
Cg
CA1
S1BF
cc
CA3
3V
LV
LT
ic
CPu
VT
End
Hypo
Pir
NasCav
Tong
Sal gland
5 mm

Figure 3: Volumetric rendering of ex vivo micro-CT scan of neonatal rat's head enables detailed visualization and potential high-powered quantitative analysis.

(A) and (B) illustrate respective anterior and posterior views of external features of rat's head and neck, including mouth, nose, and muscular distributions. (C), (D), and (E) are respective external, parasagittal, and sagittal views of rat's head and neck. (F), (G), and (H) are progressive coronal explorations of the same rat. These different views demonstrate the high-resolution power and flexibility of micro-CT scans. These exploration images show blood vessels, parotid glands, nasal anatomy, oral anatomy, and intracranial anatomy along with obvious muscular features throughout the head.

Anatomical structures are labelled as follow: *Acb = accumbens nucleus; AO = anterior olfactory bulb; apons = anterior pons; ATh = anterior thalamus; CA1 = CA1 field of hippocampus; CA3 = CA3 field of hippocampus; cc = corpus callosum; CER = cerebellum; Cg = cingulate gyrus; Coch = cochlea; CPu = caudate putamen; End = Endopiriform nucleus; Epi = epiglottis; EPi = external plexiform layer; FrCtx = frontal cortex; H. b = hyoid bone; H. palate = hard palate; Hypo = hypothalamus; IC = inferior colliculus; ic = internal capsule; Lat rid = lateral ridge of skull; L. Inc = lower incisor; LT = lateral thalamus; LV = lateral ventricle; M = mandible; Mandi = mandibular gland; Med = medulla; NasCa = nasal cavity; Nasop = nasopharynx; OB = olfactory bulb; Orb = orbital cortex; OV = olfactory ventricle; Parot = parotid gland; Pir = piriform cortex; Pit = pituitary gland; PTh = posterior thalamus; ROS = rostral ridge of skull; Sal. Gland = salivary gland; SC = superior colliculus; S. palate = soft palate; S1BF = Somatosensory 1 Barrel Field; Sterno = sternomastoideus; Temp = temporalis; 3V = 3rd ventricle; Th = thalamus; Tong = tongue; Trac = trachea; U. Inc = upper incisor; VT = ventral thalamus*

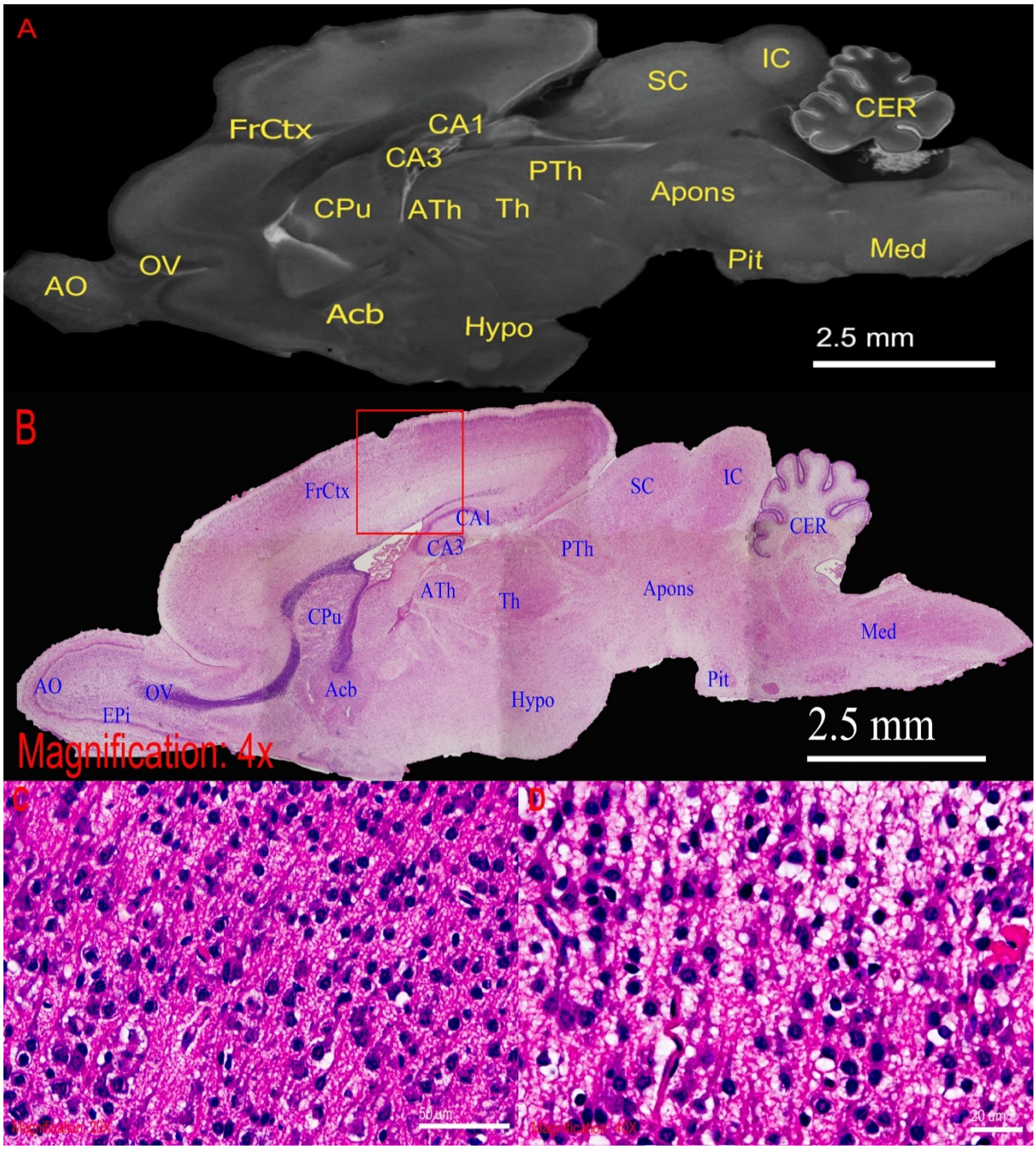

Figure 4: High-powered demonstration of rat brain by *ex vivo* micro-CT scan.

Direct comparison between the sagittal section of rat brain in (A), micro-CT slice, and (B), H&E stained 4x light micrograph. Similar structural details are seen in these two images. (C) and (D) are respective 20x and 40x light micrographs of selected FrCtX region, demonstrating neuronal cell bodies and cellular structures are relatively intact in iodine-treated samples.

Anatomical structures of comparable visibility are labelled as follows: *Acb = accumbens nucleus; AO = anterior olfactory bulb; apons = anterior pons; ATh = anterior thalamus; CA1 = CA1 field of hippocampus;* CA3 = CA3 field of hippocampus; *CER = cerebellum; CPu = caudate putamen; EPi = external plexiform layer; FrCtx = frontal cortex; Hypo = hypothalamus; IC = inferior colliculus; Med = medulla; OV = olfactory ventricle; Pit = pituitary gland*; PTh = posterior thalamus; *SC = superior colliculus; Th = thalamus.*

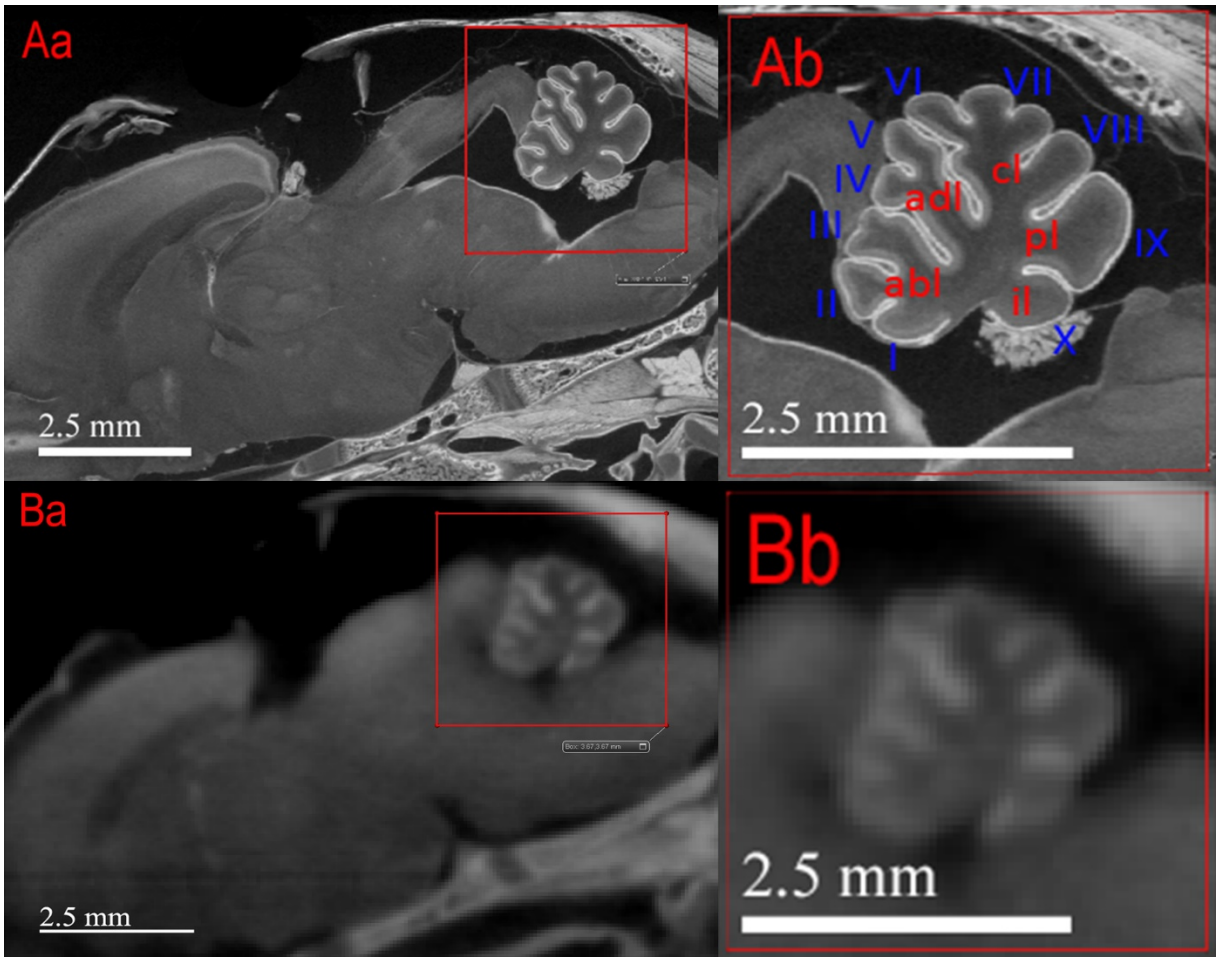

Figure 5: The image quality difference between the *ex vivo* (spatial resolution of 10.7 µm/voxel) and *in vivo* (spatial resolution of 20 µm/voxel) micro-CT scans obtained from the same 24-hours-old rat brain.

(Aa) and (Ba) are sagittal illustrations of *ex vivo* and *in vivo* micro-CT scans, respectively. Gross neuroanatomy can be visualized in both scans with subtle difference appreciated by close viewing, (Ab) and (Bb). Detailed cerebellar fissures, vermis (I-X), and lobes, can only be appreciated on *ex vivo* scans: *abl = anterobasal lobe; adl = anterodorsal lobe; cl = central lobe; pl = posterior lobe; il = inferior lobe*.

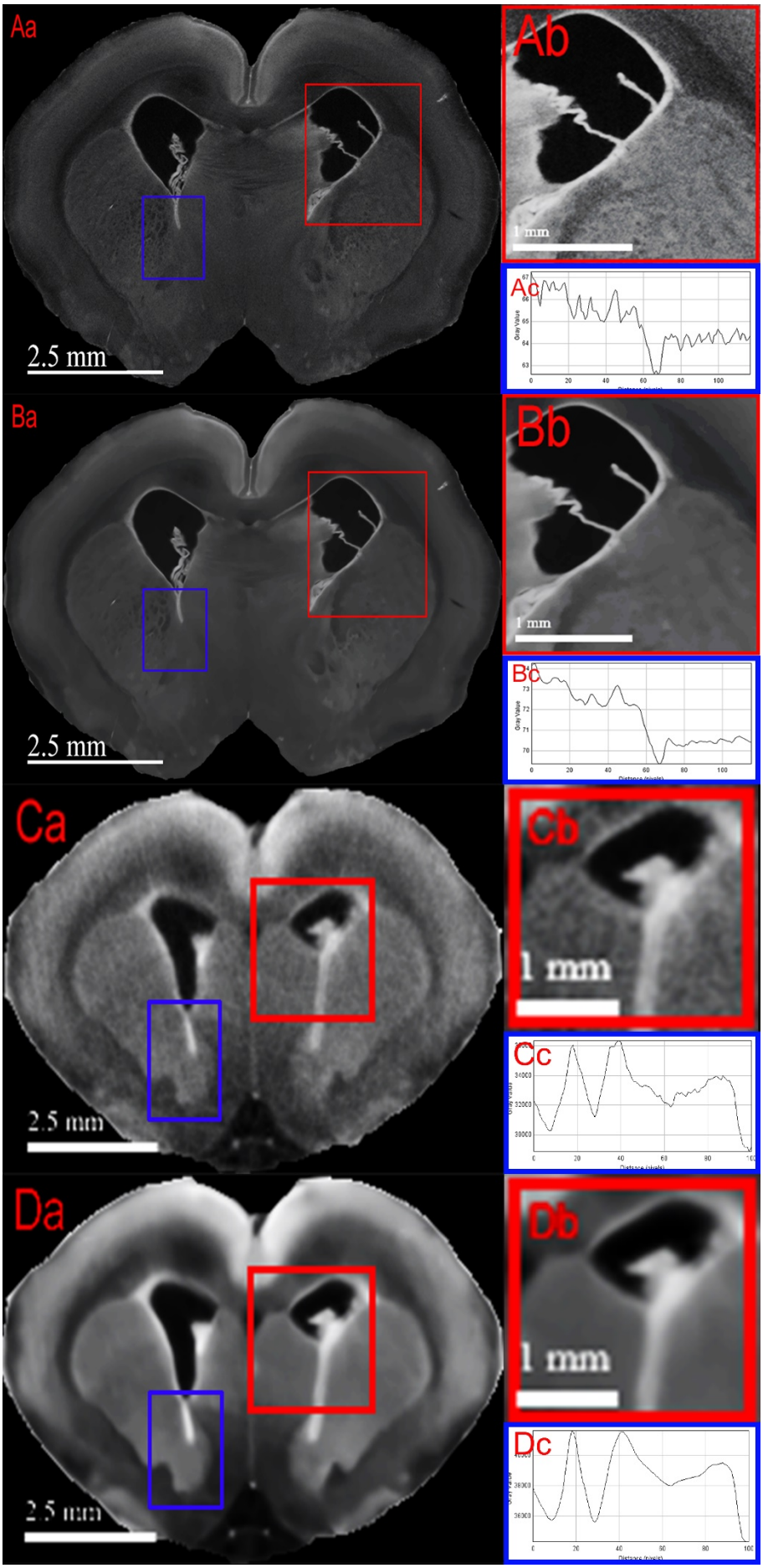
Aa
Ab
1 mm
Ac
2.5 mm
Ba
Bb
1 mm
Bc
2.5 mm
Ca
Cb
1 mm
Cc
2.5 mm
Da
Db
1 mm
Dc
2.5 mm

Figure 6: Neuroanatomical tissue differentiation of both *ex vivo* and *in vivo* micro-CT scan are enhanced by NLM denoising.

The original (Aa) and denoised (Ba) *ex vivo* scans illustrate sharper periventricular edges seen in (Ba) while gross neuroanatomical details are preserved in both. Similar but more prominent edge enhancements is shown by the comparison of (Ca) and (Da), original and denoised *in vivo* micro-CT scans, respectively. The respective grayscale line profile of each scan reveals reductions in intensity variability in denoised group, (Bc) and (Dc), in comparison to the originals, (Ac) and (Cc).

Chapter 3.1 Supplementary Figures:

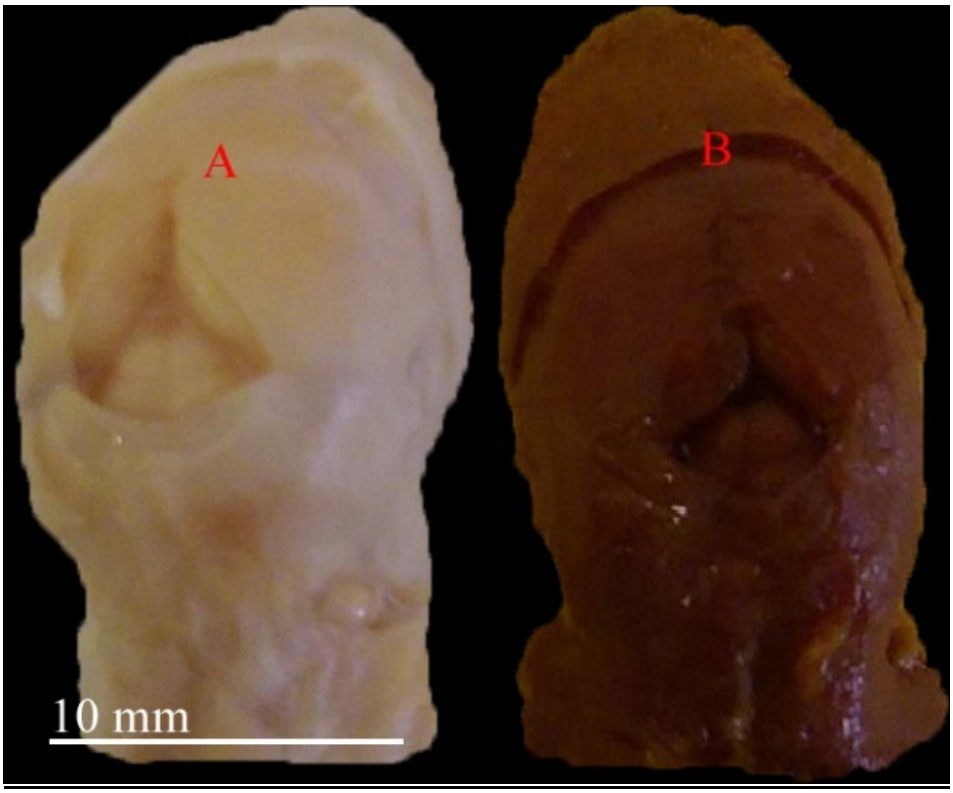

Supplementary Figure 1: Rat pup head after the removal of fur and creation of rhomb-shaped opening in skull for staining.

(a) represents sample post-PTA staining and (b) post-iodine staining.

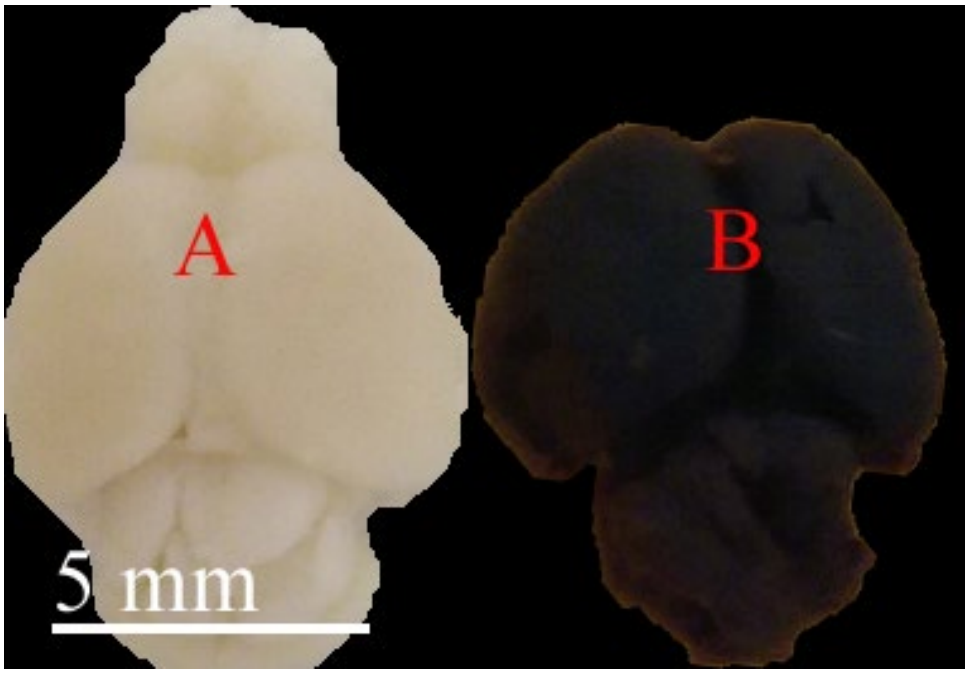

Supplementary Figure 2: Stained isolated rat brains.

(a) shows the effect of PTA staining and (b) iodine staining.

Chapter 3.1 Supplementary Tables:

Tissue Type	Stain type	Stain concentration	Staining method	Staining duration	Micro-CT type	Results*
Adult rat brain 1	Iodine	1.0%	Perfusion	2.5 hours	*Ex vivo*	Incomplete - Figure 2A
Adult rat brain 2.	Iodine	1.5%	Diffusion	44 days	*Ex vivo*	Excellent - Figure 2B.
Adult rat brain 3	PTA	0.5%	Diffusion	2.5 years	*In vivo*	Incomplete - Figure 2D
Adult rat brain 4	PTA	1.0%	Diffusion	2.5 years	*In vivo*	Incomplete - Figure 2E.
Neonatal rat brain 1	Iodine	1.5%	Diffusion	16 days	*Ex vivo*	Excellent - Figure 2C.
Neonatal rat brain 2	PTA	0.5%	Diffusion	148 days	*In vivo*	Incomplete - Figure 2F
Neonatal rat brain 3	PTA	1.0%	Diffusion	148 days	*In vivo*	Incomplete - Figure 2G
Isolated neonatal Rat Brain 1	Non-Contrast				*In vivo*	Incomplete - Figure 2H
Isolated neonatal Rat Brain 2	Iodine	1.5%	Diffusion	3 hours	*In vivo*	Poor - Figure 2I
Isolated neonatal Rat Brain 3	Iodine	1.5%	Diffusion	6 hours	*In vivo*	Good - Figure 2J
Isolated neonatal Rat Brain 4	Iodine	1.5%	Diffusion	6 days	*In vivo*	Good - Figure 2K
Isolated neonatal Rat Brain 5	PTA	1.5%	Diffusion	3 hours	*In vivo*	Incomplete - Figure 2L
Isolated neonatal Rat Brain 6	PTA	1.5%	Diffusion	6 hours	*In vivo*	Incomplete - Figure 2M
Isolated neonatal Rat Brain 7	PTA	1.5%	Diffusion	6 days	*In vivo*	Good - Figure 2N

***Excellent**-Detailed anatomy; **Good**-Gross anatomy; **Poor**-Gross anatomy, blurry border; **Incomplete**-Undifferentiated anatomy

Supplementary Table 1: Summary of various tissue staining and micro-CT setups for different rat brains with respective image results.

Chapter 3.2: High-Definition heart visualization using micro-CT scanning on experimental rats

Chapter 3.2 Highlights

- Micro-CT scanning offers a structural-preserving visualization tool for studying the cardiovascular anatomy of small animal.
- Diffusion staining using iodine or PTA yields excellent soft tissue differentiation on micro-CT scans; however, iodine is significantly more efficient.
- *Ex vivo* micro-CT scan generates high-resolution detail of cardiovascular systems comparable to that of 4x H&E light microscopy.
- Image degradation of *in vivo* micro-CT heart scan can be improved by raising the voltage and/or current of X-ray source.
- Post-acquisition NLM filtering modestly reduces image noises and potentiates tissue boundary clarity, allowing for better organ differentiation and further quantitative analysis.

Chapter 3.2 Abstract

Background
Micro-CT provides detailed 3D visualizations of cardiovascular tissues of experimental rats. Image quality of *in vivo* and *ex vivo* micro-CT scans of the heart not been compared nor evaluated against traditional H&E light microscopy. Micro-CT setting and image processing methods to improve micro-CT clarity of cardiac tissue also needs to be addressed.

Methods
Ex vivo and *in vivo* micro-CT scans of rats' hearts were obtained following diffusion staining. This was followed by prompt NLM filtering using custom code on a modern GPGPU for image enhancement. Cardiac tissues were processed for H&E light microscopy post-CT scanning.

Results
Ex vivo micro-CT generated high-definition 3D images with structural details comparable to those on H&E light microscopy. Cardiac features shown on *ex vivo* micro-CT scans were more distinctive and defined than those on *in vivo* micro-CT scans.

Increasing X-ray source voltage, current, and scanning time increased signal-to-noise ratio of *in vivo* micro-CT images. Enhancement made by NLM denoising were more pronounced with *in vivo* micro-CT images due to its intrinsic lower signal-to-noise indexes.

Conclusions
Micro-CT offers a high-definition tissue-preserving visualization tool for qualitative and quantitative anatomical analysis. While custom-built *ex vivo* micro-CT scanner can provide excellent cardiac images, the more accessible *in vivo* micro-CT scanners may not. To improve *in vivo* micro-CT images, adjustments on X-ray source's voltage, current, and CT scanning time in addition to the administration of post-acquisition filtering can be effective.

1. Introduction

Three-dimensional (3D) micro-visualizations of biological tissues provide valuable means for morphology study. A wide range of imaging techniques have been described, including confocal microscopy, episcopic microscopy, optical projection tomography (OPT), micro-magnetic resonance imaging (micro-MRI), and micro-computed tomography (micro-CT) (445, 446, 465, 467-469). Tissue processing for confocal and episcopic microscopy, both of which are serial sectional imaging techniques, destroys tissue integrity and prohibits their future use (445, 446). Whole-volume imaging techniques such as OPT, micro-MRI, and micro-CT allow tissue preservation; however, OPT has limitations on tissue size (468) and micro-MRI requires prolonged scanning time for maximal resolution of 20 μm/voxel (469). Micro-CT, on the other hand, has recently attracted a great attention from researchers for its high-resolution, versatility, availability, and ease of use characteristics (422-424, 431, 450).

Traditionally, micro-CT has limited roles in biomedical studies due to its X-ray attenuation demands from tissue samples. These limitations, however, have been lifted by the establishment of new staining methods, which show promising findings in embryology, oncology, histology, angiogenesis, and bioengineering studies (422, 425, 431, 447, 451, 465, 470-474). Although these studies have established successful staining and micro-CT scanning protocols for small tissues and animal embryos, methods for postnatal animals with developed skeletal systems have not been addressed. Additionally, Metscher (2009) has reported that both iodine and phosphotungstic acid (PTA) are safe and effective contrasts for chicken embryos staining (431), but they have not been tested staining on postnatal animals, cardiac tissues in particular. Furthermore, image quality and anatomical details of the heart shown by the *in vivo* and *ex vivo* micro-CT scans have not been evaluated against the H&E

light microscopy. Moreover, the effects of CT perimeters and potential impact of de-noising algorithms on the image quality of cardiovascular micro-CT should be clarified.

Poor image signal-to-noise indexes has always been a challenge for biomedical image analysis, especially in X-ray dependent imaging modalities. This is often a result of non-uniform x-ray attenuation associated with different tissue types in a body. It is therefore conceivable that different denoising algorithms have been developed over the years as attempts to improve image quality, these include median (475-477), anisotropic (478, 479), total variation (480-482), and block-matching 3-dimensional (BM3D) (483, 484). Although each of these techniques has slightly different approaches to image filtering, they are all developed for the goal of noise removal while preserving the image features, in particular for the edge enhancements of different objects. We have chosen to implement the non-local means (NLM) denoising filter in both 2-dimensional (2D) and 3-dimensional (3D) data for its excellent edge preserving property and relative simplicity in application using a modern general-purpose-graphic-processing unit (GPGPU).

In this study, we aim to complement the established tissue preparation and micro-CT scanning protocols to create a workflow for animal hearts and demonstrate the following:

1. The cardiovascular details illustrated by micro-CT scans are comparable to those of low-field H&E light microscopy.
2. Reduction in the voltage and current of X-ray source can increase *in vivo* micro-CT image degradation. Voltage changes have more detrimental impact than current.
3. Image clarity is proportional to CT scanning time.
4. Iodine is more efficient than PTA in generating uniform staining.

5. Non-uniform contrast staining potentiates the image degradation caused by the perimeter changes of X-ray source.
6. Both iodine- and PTA-stained heart tissue can be used for subsequent histology processing without structural compromise.
7. Post-acquisition NLM filtering can provide modest improvement in image quality, particularly with the *in vivo* micro-CT heart scans.

2. Materials and Methods

2.1. Compliance with Ethical practice

All tissues and animals used in this study were handled with strict compliance to ACT Health Human Research Ethics Committee (ACTH-HREC) and Australian National University Animal Experimentation Ethics Committee (ANU-AEEC).

2.2. Iodine and PTA diffusion staining protocols

Thirteen 72- or 96-hours old neonatal rats were tested. These rats were over anaesthetized with 5 % isoflurane and carefully culled via abdominal aortotomy and subsequent thoracotomy. The cardiothoracic tissues were washed with 10% PBS solution for 30 minutes to remove residual bloods. Next, the tissues were fixed in 4% formalin solution for 24 hours until tissue staining.

Two different contrasts were tested based on the promising results of previous study: iodine and PTA (431). Staining was completed by first subjecting the formalin-fixed tissues to progressive ethanol series to remove formalin: 20%, 50%, 70%, and 90%, each for 1 day respectively. The ethanol-fixed rat's body was then immersed in 1.5% Iodine (in 90%

ethanol), 0.5% PTA (in 70% ethanol), and 1.0% PTA (in 70% ethanol) for various periods prior to scanning as listed in Table 1.

2.3. *in vivo* and *ex vivo* micro-CT scanning

Current micro-CT systems are generally classified into *in vivo* micro-CT and *ex vivo* micro-CT based on the system setups; these terminologies are not related to their standard definitions in biomedical science but rather as descriptions for micro-CT system setups (439). *In vivo* micro-CT scanner incorporates a stationary sample positioned in between a rotational system of x-ray source and detector. On the contrary, e*x vivo* micro-CT system involves a rotational sample stage situated in between an adjustable x-ray source and detectors; this setup can yield a more magnified image by shortening the distance between the sample and x-ray source (438, 485). Furthermore, it can generate a high signal-to-noise ratio image through prolonging the scanning time while keeping X-ray source current low. One of the advantage of keeping low X-ray source low is to minimize X-ray source spot-size and thereby enabling higher visual resolution, up to <2 µm/voxel (486).

In this study, a commercially available Caliper Quantum FX machine was chosen to represent the *in vivo* micro-CT scanner and a custom-built micro-CT system by Applied Mathematical Department of Australian National University (ANU) was used to represent *ex vivo* micro-CT system.

Using the Caliper Quantum FX, a tissue specimen was placed on a stationery loading dock positioned in between the rotating system of X-ray source and detector. The scanning time was pre-set between 27s and 4.5min depending on the field of view (FOV; ranging from

5-75mm in diameter) and the modes of quality chosen (ranging from standard to fine). The maximum resolution achievable was 10 µm/voxel. In this study, different combinations of scanning perimeters including scanning time, voltage, and current adjustments were explored to find their effects on imaging quality, as summarized in table 1. The resultant images were stored as DICOM series and visualized with FIJI and Drishti, both of which were open-source software. Semi-automatic organ segmentation is performed using Drishti paint, a function of Drishti (456, 487).

The custom-built micro-CT system by ANU Applied Mathematical Department requires the sample to be fixed within an aluminium tube. This tissue-tube was then placed on a rotational stage situated in-between an adjustable X-ray source and scintillator CCD. X-ray source and sample distance was adjusted according to the resolution desired (486). All samples were allocated with 15 hours of scanning time and an additional 8 hours of image processing and reconstruction time via National Computational Infrastructure (NCI) services. The maximum resolution was 1 µm/voxel, limited by the physical size of the sample. The resultant images were stored as netCDF files and visualized with Drishti (487).

2.4. H&E-stained microscopy

Following micro-CT scanning of the hearts, the tissues were processed with standard H&E protocols for light microscopy (53).

H&E processing were conducted in the following steps. Firstly, the iodine-stained hearts were sectioned sagittally into 4mm-thickness blocks and placed in cassettes. Next, these tissue-blocks underwent contrast washout and dehydration in 90% EtOH for 48 hours.

Xylol was then used to clear alcohol before paraffin-embedment at 60°C. Afterward, the tissue samples were sliced into tissue-sheets of 10 µm in thickness using a microtome. These tissue-sheets were laid in water-bath of 5-6°C to reduce wrinkles while being positioned onto the pre-labelled glass slides. Dehydration was then completed overnight at 37°C. Finally, the coverslip was fixed to the slide using Eukitt® resinous medium.

Progressive H&E staining was adopted. The slides were first stained in alum-hematoxylin solutions until the appearance of dark red colour; this was followed by washing and 'bluing' with lithium carbonate solution. Finally, the slides were then washed followed by counter-stained with 0.5% eosin alcoholic solution.

All tissue slides were examined using Olympus IX 71 microscope.

2.5. Post-acquisition image processing: Non-Local Means (NLM) filtering

As an attempt to improve image clarity and edge-sharpness of cardiovascular micro-CT scan, we trialled NLM filtering using custom-code.

NLM algorithm is first developed by Buades et al. (455) under the premises that similarity exists among different regions of an image provided that these regional sizes are 'relatively' small. This self-similarity enables noise cancelling by averaging these similar parts of the image. Genin et al (2012) has illustrated that the computational principle of this algorithm (488). In 2D images, this process creates a cube, whereas in 3D images, this generates a 4-dimensional (4D) hyperplane. This now gives the most similar pixels/voxels in the image and the denoising or smoothing operation is completed based on this higher

dimensional object. This operation is feature-preserving and enables automated noise removal. This NLM algorithm is widely considered as a state-of-the-art denoising filter. The large number of computations required to perform the basic NLM, however, making its computational-processing-unit (CPU) runtime unacceptably high for all but the smallest 2D images.

The method utilized in this paper uses a standard NLM but with locally adaptive estimates of noise, which result in more accurate removal of noise. Given all images in this study were 3D data, 3D cubes were used for the similarity measures and therefore required the use of the 4D hyperplane. Images presented in this paper ranging from 512^3 voxels for the *in vivo* micro-CT scans to the full 2048^3 voxels for the *ex vivo* micro-CT scans. Using our proposed protocol (unpublished), the computing time for the NLM was reduced to approximately one-minute-thirty-seconds for a 512^3-voxel sample on a system with a single graphics-processing-unit (GPU) card. This was significantly faster than the current commercial vendors requiring processing time up to three hours for a similar sample size.

A brief discussion of NLM implementation used in this study is described as follow. Traditionally, a great majority of the NLM runtime is spent on the computations of the sum of squared differences (ssd). Given the ssd computation for adjacent voxels is highly similar, we exploit this similarity by adopting a pseudo moving average filter (MAF) to perform the ssd calculations from one pixel/voxel to the next. For 2D images, the squared area of intensities used for one voxel's ssd-search-neighbourhood differs from an adjacent voxel's ssd-search-neighbourhood only in the end rows or columns. The same principle also applies to 3D data, with adjacent cubes differ only in two end slices. To illustrate further, if M is the number of

voxels of the inner ssd cube and N is the number of cubes requiring ssd calculations, then the total number of difference-operations is as follows: with no MAF, we perform N x M^3 operations; with the MAF, we perform M^3+ (N-1) x 2 x M^2 operations. Based on this, we can expect a significant computational reduction when N is large. This is indeed the case when handing the *ex vivo* micro-CT data, where each dataset has an average of 4.7 GB in size, the second operation become at least a two-orders of magnitude less in computations.

The computation of the smoothing parameter and estimation of the image noise is adapted from Coupe et al., 2008 (457). However, our implementations are unique in the fact that we compute individual noise estimate for each sub blocks of the image rather than assigning a single estimate for the entire image. Furthermore, the grey-scale-value (gsv) intensity range has also been considered in our computations for the smoothing parameter. The gsv inclusion is found to be empirically important for the success of de-noising a range of image types including computed tomography (CT), scanning electron microscopy (SEM), and ultrasound etc. Moreover, our implementation of NLM follows the original model of Additive Gaussian White Noise (AGWN); however, it also allows adjustments on the shape of the Gaussian kernel to better approximate the real noise distribution for images with non-AGWN.

Our empirical testing confirms that through local estimation of the noise, inclusion of correction factor for non-AGWN, and fixed window sizes, improvement on de-noised quality can be achieved. Little, if any, gains in quality improvement is obtained with larger search window sizes. On the contrary, image quality may degrade with larger search window sizes. These conclusions are drawn based on the qualitative and quantitative measures such as

peak signal to noise ratio (PSNR), line tests, and residual images for a wide range of image types. Similar finding are also found in Coupe et al., 2008 (457).

In this study, the implementation command was run on a Linux operating system fitted with Intel (R) Core ™ i7-4770K CPU @3.5GHz, 32 GB of RAM, and a Nvidia GeForce GTX Titan Black Kepler GK110 architecture. The processed CT data were reviewed using Fiji and Drishti (453, 456).

3. Results

3.1. Image quality: comparing light microscopy, *ex vivo*, and *in vivo* micro-CT scans of cardiovascular tissues of postnatal rat

To demonstrate the visualization power and versatility of the proposed method for cardiovascular tissue, we compared H&E light micrograph, *ex vivo* micro-CT scan, and *in vivo* micro-CT scans of the same heart, as shown by Figure 2. Although good tissue contrast is observed throughout Figure 2b to 2e, only *ex vivo* micro-CT scans, Figure 2b and 2c, provide good anatomical visualization with details comparable to those seen on 4x H&E light micrographs, Figure 2a. Furthermore, tissue preservation is observed only in micro-CT scans as opposed to apparent micro-tears shown by H&E light micrograph. Moreover, Figures 2b to 2e illustrated the versatility and ease of manipulations through different visual planes of the heart with micro-CT data; this was difficult to achieve with light microscopy. Additionally, when setting both *ex vivo* and *in vivo* cardiac micro-CT scans with similar field of view for comparison, the resolution limitations of *in vivo* micro-CT scans, Figure 2d and 2e, are obvious in comparison to *ex vivo* micro-CT scans, Figure 2b and 2c. The respective resolutions of *in vivo* micro-CT and *ex vivo* micro-CT scans are 40 µm/voxel and 10.7 µm/voxel. In fact, *in*

vivo micro-CT scans can only show macroscopic anatomical details such as atria, ventricles, papillary muscles, and aortic semilunar valves, whereas smaller structures including coronary arteries and even cardiac tissue striations can be easily appreciated in *ex vivo* micro-CT scans. Overall, *in vivo* micro-CT scans offer less image clarity and anatomical details than those of *ex vivo* micro-CT scans and H&E light microscopy.

3.2. Effect of X-ray source voltage, current and CT scanning time on the image quality of low resolution (20 µm/voxel) and high resolution (10 µm/voxel) *in vivo* micro-CT heart scans

Since *in vivo* micro-CT has less-than-ideal image quality, we explored potential methods for improvement through adjusting CT perimeters. We first tested these settings on low-resolution micro-CT scans (20 µm/voxel) derived from an iodine-stained heart. As shown by Figures 3a to 3d, gradual reductions in X-ray source voltage result in progressive worsening of image clarity. Minor image degradation is observed with voltage reduction from 90kV to 70kV; the overall heart structures remain discernible. On the other hand, non-meaningful image is generated when setting X-ray source voltage to 30kV, Figure 3d. Furthermore, shortening the CT scanning time from 3min to 26s results in significantly blurrier images as exemplified by the compromised pulmonary and aortic vessel definitions, Figure 3e. Unexpectedly, halving the X-ray source current only modestly reduces the image sharpness, Figure 3f.

To investigate further, we tested the effect of similar perimeter adjustments on high-resolution micro-CT scans (10 µm/voxel) using the same iodine-stained heart. Consistent with low-resolution image series, voltage reduction corresponds to poorer image quality, Figure 4a to 4c; however, image degradation associated with reduction in X-ray source

voltage or current is more prominent in high-resolution images. Indeed, direct comparison between Figure 4c and Figure 3c, both derived from an X-ray source voltage setting of 50kV, shows significant higher image noise and blurrier cardiac edges in 10 µm/voxel heart scans. Interestingly, halving the current setting from 200µA to 100µA, Figure 4d, yields similar image quality as Figure 4b, a scan generated by 70kV X-ray source, which is only a 22% reduction from a standard 90kV setting, Figure 4a.

3.3. Effect of CT scanning time on micro-CT scans of fully PTA-stained (1.0%) heart

PTA staining was tested for the search of an alternative contrast to iodine. High radiopaque micro-CT scans was generated with a fully PTA-stained heart, Figure 5. However, a prolonged staining period of 148 days was required to guarantee successful diffusion staining of a neonatal rat's heart using 1.0% PTA. Furthermore, although PTA staining yielded good soft-tissue contrast, its high radiopacity reduces the visibility of structural details, such as the loss of vessel boundary between the aorta and pulmonary artery or indistinguishable borders between the right auricle and ventricle, shown by Figure 5a. Furthermore, shortening CT scanning time caused significant higher image degradation with PTA-stained heart, Figure 5b; this was much more prominent than that of iodine-stained heart, Figure 3e.

3.4. Effect of X-ray source voltage on micro-CT scans of non-homogenous PTA-stained (0.5%) heart

To investigate whether high radiopacity of PTA-stained cardiac scan can be corrected by reducing the contrast concentration, we tried diffusion staining with 0.5% PTA for 699 days but with little success. As shown by Figure 6a, peripheral cardiac tissue stained by PTA exhibits significant high opacity while internal structures cannot be delineated due to

incomplete staining. Furthermore, non-homogenous PTA staining amplifies the image degradation on micro-CT heart scan from lower X-ray voltage settings, as shown by Figure 6b.

3.5. Effect of NLM denoising algorithms on the *ex vivo* and *in vivo* micro-CT rat heart scan

As attempts to improve image quality, we applied the NLM denoising algorithm to both *ex vivo* and *in vivo* micro-CT scans for structural feature enhancements and image noise removal. Due to the high signal-to-noise ratio of the original *ex vivo* micro-CT scan, Figure 7a, only subtle improvement such as boundary differentiation can be appreciated post-filtering, Figure 7b. The subtle improvement is better appreciated by comparing their respective magnified views of intraventricular edges. Furthermore, through NLM filtering, structural boundaries demonstrated *in vivo* micro-CT scans have become modestly more defined, Figure 7d, when comparing to the original scan, Figure 7c. This can be appreciated by reviewing the aortic and intraventricular edges. In addition, the comparison of their respective intensity histogram also demonstrates significant narrowing of histogram spread.

4. Discussion

Our study demonstrated micro-CT scanners, with proper tissue staining, can generate scans illustrating detailed cardiovascular anatomy of postnatal rats. These anatomical details revealed by the *ex vivo* micro-CT scans not only share similar soft-tissue differentiation with micro-MRI scans but offer high structural details comparable to the low-magnification H&E light microscopy, Figure 2a (489). This easy, versatile, tissue-preserving methodology offers a potential alternative method to conventional pathology and morphology study (490, 491). In addition, the benefits of 3D rendering and the ability to accommodate a relatively large sample size allow for better internal anatomical visualization and appreciation of disease

processes. Although adopting micro-CT methodology into the clinical practices may still be years away, micro-CT has already taken important research roles with the use of appropriate tissue preparations.

As previously expected, we confirmed that *ex vivo* micro-CT scanners can offer significantly more detailed and clearer images than *in vivo* micro-CT scanners, as shown by Figure 2. Figure 2b and 2c demonstrate *ex vivo* micro-CT scans can provide well defined illustrations of cardiac anatomy in addition to cardiac parenchymal distribution and muscle striations at a level of details comparable to those of 4x H&E light micrograph, Figure 2a. On the contrary, this is not achievable by *in vivo* micro-CT scans, Figure 4a, despite having similar high-resolution settings, 10μm/voxel (*in vivo* micro-CT scan) and 10.7μm/voxel (*ex vivo* micro-CT scan). The difference in image quality is due to the intrinsically high signal-to-noise ratio achieved by the extended scanning time of the *ex vivo* micro-CT scanner, i.e. 15 hours, comparing to the relatively short scanning period of the *in vivo* micro-CT scan, 3 min. The limited scanning time of the *in vivo* micro-CT scanner is designed to minimize radiation exposure in view of potential live animal study; however, this also significantly reduces physical raw data for the downstream image reconstruction. This ultimately results in lower signal-to-noise index and compromised image quality.

Due to the wider availability and lower cost of *in vivo* micro-CT scanners, we explored various CT scanner settings to improve the quality of both low- and high-resolution micro-CT scans. These perimeters include X-ray source's voltage, current, and CT scanning time. Although the full extent of electromagnetism and photoelectric effect of X-ray physics is beyond the scope of this study, for the practical purposes of manipulating the settings of *in*

vivo micro-CT scanners, we found our scan result is consistent with the following:

$$Image\ clarity\ \propto CT\ Scanning\ time * \text{Xray}\ Current * Xray\ Voltage$$

We confirmed the signal-to-noise ratios of the micro-CT data can be improved by increasing the current of X-ray source and thereby generating a higher number of photons within a short period of time. This benefit is illustrated by the comparison between Figure 3a and 3f. Consistently, image degradation associated with lower current setting is more prominent in high-resolution images, as shown by the comparison of Figure 4a and 4d. Moreover, reduced image quality from lower current setting can be rescued by longer scanning time, as demonstrated by the comparison of Figures 3a and 3e.

Furthermore, we reported that X-ray source voltage has an important effect on both image acquisition and signal-to-noise ratio. Given that a majority of the ionizing electromagnetic radiation, X-ray, is generated through the *Bremsstrahlung* process, radiation emission from the "braking of electrons," a continuous spectrum of the X-ray energy is generated based on the anode voltage of X-ray tube. As shown in Figure 3d, when setting the anode voltage to < 50kV, no meaningful image can be generated from our *in vivo* micro-CT scan trials. This can be explained by the fact that the wide-angle Compton scattering, prominent Rayleigh scattering, and less photoelectric effect predominate at low voltage setting, resulting in less X-ray production (492). On the other hand, high-voltage setting minimizes Rayleigh scattering, increases the narrow-angle Compton scattering and potentiates photoelectric effect. This creates sharper-edge image through x-ray spectrum changes: generating more narrow-angled scattering photons with higher penetration power. However, this change also increases the risk of "over-exposure" (493). This effect can be seen promptly in high-spatial-resolution images, Figure 4b and 4c, and less prominent in low-

spatial-resolution scans, Figure 3b to 3d. Expectedly, image noises from suboptimal voltage or current setting are accentuated by inadequate staining, as shown by Figure 6b, likely due to the uneven photon scattering caused by non-homogenous distribution of staining effect.

Based on our results, we suggest titrating up the X-ray source current of *in vivo* micro-CT scanner before altering the voltage to achieve for better image quality while minimizing the risk of overexposure. On the other hand, when the desired resolution is < 2µm/voxel, an upper limitation of current size exists due to the finite size of generated photon beams, which can be greater than 2µm and hence unable to project the fine differentiations of the objects. However, to our best understanding, no commercial *in vivo* scanners can offer spatial resolution higher than 10 µm/voxel currently.

From this study, we illustrated that intact cardiovascular tissues can be visualized using micro-CT scanners with iodine or PTA tissue-staining, provided that prolonged PTA staining time can be allocated. Contrary to previous study on animal embryos, diffusion staining on postnatal rat hearts requires much longer staining time to guarantee success, up to 16 days when using 1.5% iodine solution and 148 days with 1.0% PTA (431, 451). Staining with 0.5% PTA for 699 days is not successful. The difference in the required staining time is likely due to their size and polarity differences, with iodine being non-polar and about 20 times smaller than the ionic PTA (494, 495). In addition, due to PTA's high molecular size and higher mass absorption coefficient, we found attempting to acquire high-resolution images (i.e. 10µm/voxel) using *in vivo* micro-CT scanner runs a higher risk of generating "over-attenuated" image, as shown by Figure 6a (496). This observation is consistent with Lambert's law (497, 498):

$$I = I_0 e^{-\mu p t}$$

Where, I = resultant intensity, I_0= initial intensity, μ= mass absorption coefficient (cm^2/g), p= density (g/cm^3), t=thickness (cm).

We implemented NLM algorithms to explore rescuing measures for suboptimal cardiac micro-CT images. NLM process is known to be time consuming due to high computational demand; however, this has been improved with parallel processing using GPGPU. Although high signal-to-noise *ex vivo* micro-CT scans benefits little from NLM filtering, Figure 7a and 7b, improvements made on low signal-to-noise *in vivo* micro-CT scans are more prominent, as shown by Figure 7c and 7d. By adopting this process, accuracy of quantitative analysis may be improved from clearer images. While our implementation is still in trial phase and not available for public domain, other alternative opensource projects are available for NLM implementation, including Fiji, albeit the processing may be slower with more artefact in resultant images (456). Although improvement from NLM may be minor currently, de-noising can facilitate future development of automated segmentation and hence accurate automated quantitative analysis including measurement of organ sizes.

In conclusion, we demonstrated that micro-CT is a useful tissue-preserving scanning modality with the ability to provide detailed cardiovascular anatomy and great tissue differentiation. This potentially opens different applications for micro-CT scans. Contrary to prior findings from embryo study, we recommend iodine as the preferred contrast for efficient and reliable results. Ideally, we recommend *ex vivo* over *in vivo* micro-CT scanner for achieving high-definition heart images. However, if an *in vivo* micro-CT scan needs to be used, we recommend increasing the current and/or CT scanning time before adjusting the X-

ray voltage towards the extreme for best quality images. Lastly, despite macroscopic coloration by iodine staining, we confirm such processing does not interfere with future H&E staining on the same tissue. Through the same process, we also illustrated that *ex vivo* micro-CT scans can offer similar cardiac details as low-power microscopy, as shown by Figure 2a to 2c. Furthermore, quantitative study for cardiac fibrosis post-myocardial infarction may be possible through measurements on the loss of cardiac muscle striation with volume rendering software, such as Drishti (453). Furthermore, quantitative analysis on the gross anatomy of aortic dimensions, ventricular volumes, valvular sizes, and muscular hypertrophy can be completed with micro-CT data. Lastly, considering the quality improvement made by the NLM application, we recommend all *in vivo* micro-CT images to be processed by NLM algorithms prior to quantitative analysis.

Chapter 3.2 Figures:

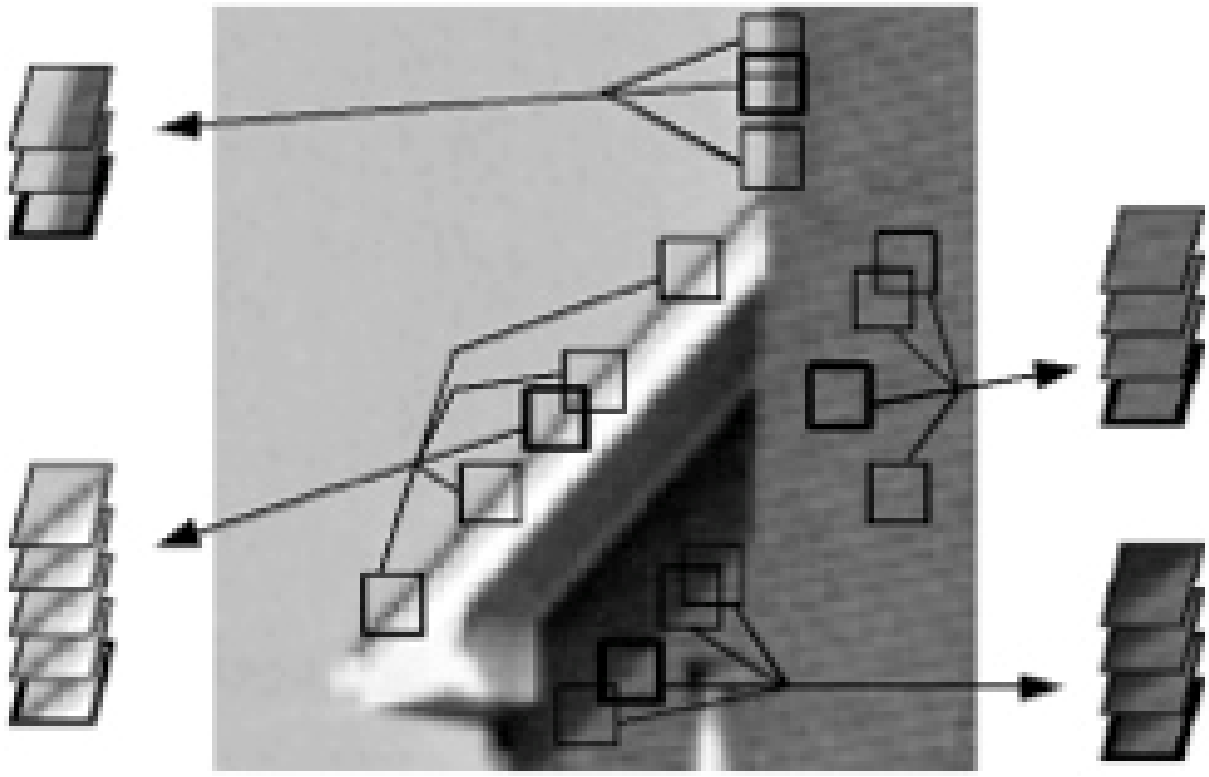

Figure 1: Illustration of region-matching of high similar measures in NLM processing.

A pixel/voxel is chosen, a voxel being the smallest unit of a 3D volume, analogous to a pixel in 2D image. A neighbouring region with high similar measures around this selected pixel/voxel is then chosen. This neighbouring-region is a square in 2D and a cube in 3D. A sum of the squared difference is used to determine which neighbourhoods are the most similar to the current region of interest; this is then ranked and put into a higher dimensional stack. Various groups of high-association groups of images are selected based on their similarity measures to each selected reference patches, highlighted in thick black boxes (455).

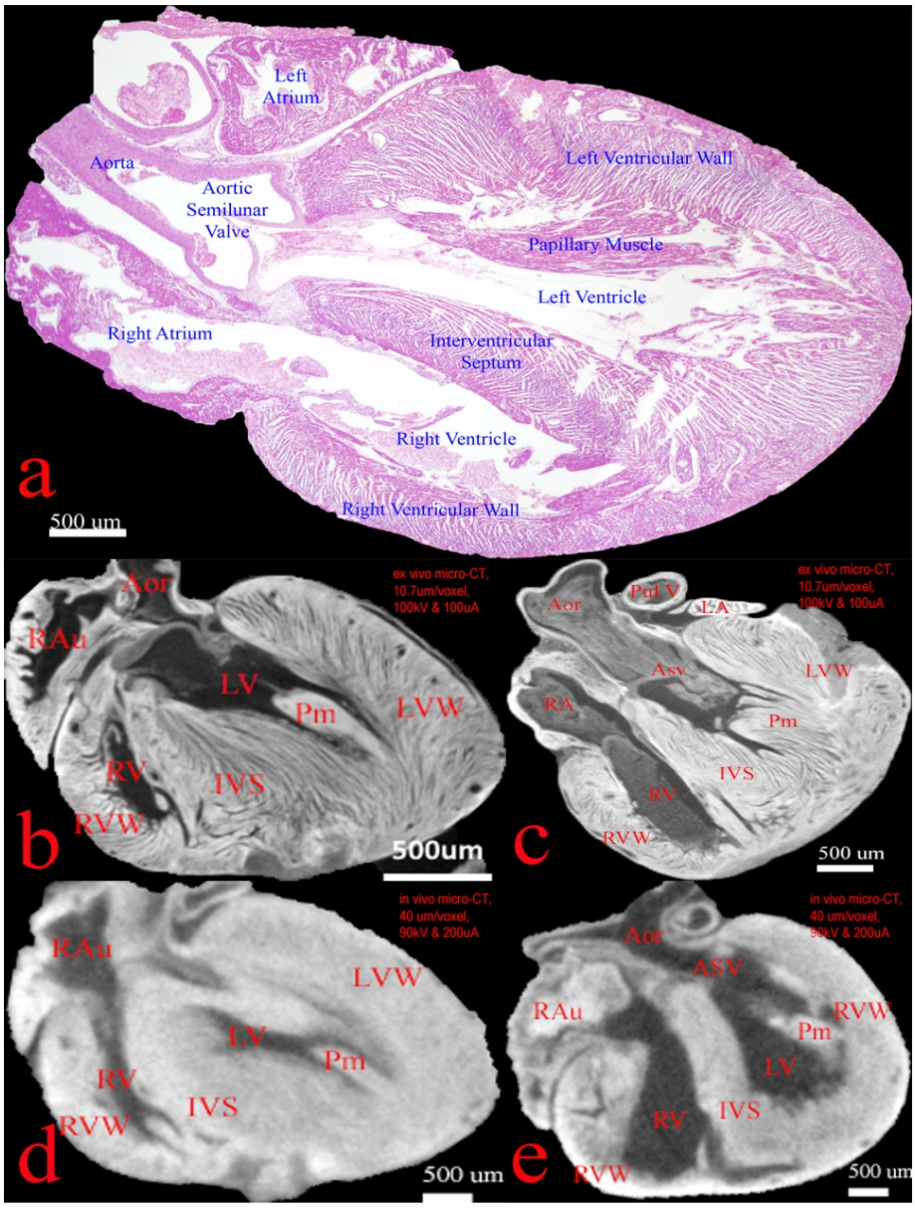

Figure 2: Comparison of H&E microscopy, *ex vivo* and *in vivo* micro-CT scans of neonatal rat heart.

Figure 2a (H&E microscopy, 4X magnification): 2D view of major heart structures as labelled. Muscle fibre and micro-tears at the base of interventricular septum caused by tissue processing are also illustrated.
Figure 2b and 2c (*ex vivo* micro-CT, resolution 10.7µm/voxel): structurally intact 3D visualization of heart structures with details comparable to that of H&E light micrograph, Figure 2a. In addition, cross sections of coronary artery and vessel wall thickness can be appreciated.
Figure 2d and 2e (*in vivo* micro-CT, resolution 40µm/voxel): sagittal and parasagittal view of *in vivo* micro-CT heart scans showing gross but limited macroscopic 3D visualization of heart structures.
Aor=Aorta; RAu=Right Auricle; RA=Right Atrium; RV=Right Ventricle; RVW=Right Ventricular Wall; IVS=Interventricular Septum; LA=Left Atrium; LV=Left Ventricle; LVW=Left Ventricular Wall; Pm=Papillary Muscle; Pul V=Pulmonary Vessel; Asv=Aortic Semilunar Valve.

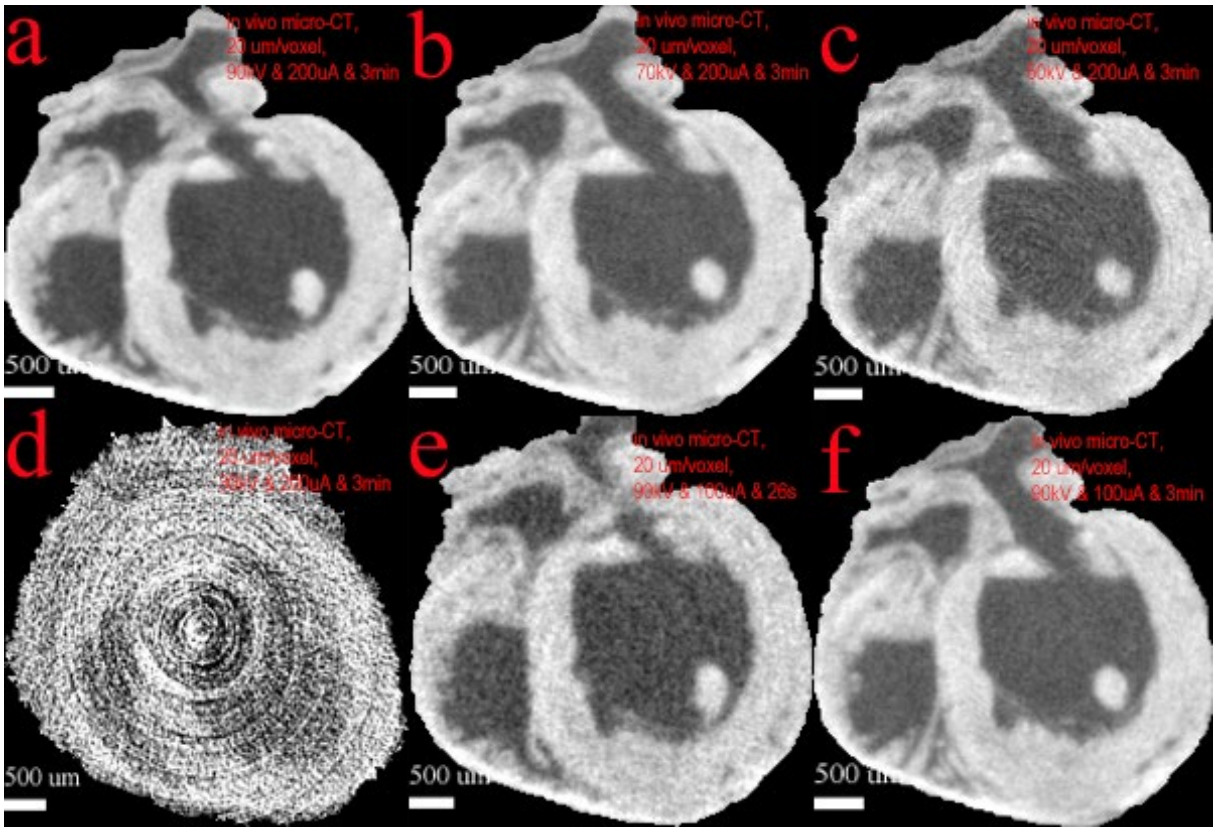

Figure 3: Effect of micro-CT voltage, current, and scanning time on low-resolution (20µm/voxel) *in vivo* micro-CT images of rat heart.

Figure 3a (90kV), 3b (70kV), 3c (50kV), and 3d (30kV): demonstrate lowering voltage setting results in blurrier structural border, which is best appreciated by the gradual loss of right ventricular papillary muscle outlining as shown by 3a to 3d. Furthermore, minimal anatomical information can be detained from figure 3d.
Figure 3a (3min) and 3e (26s): Short CT scanning time generates less homogenous cardiac scan with blurrier edges.
Figure 3a (200µA) and 3f (100µA): reducing x-ray source current yields compromised cardiac image with lower tissue-cavity contrast.

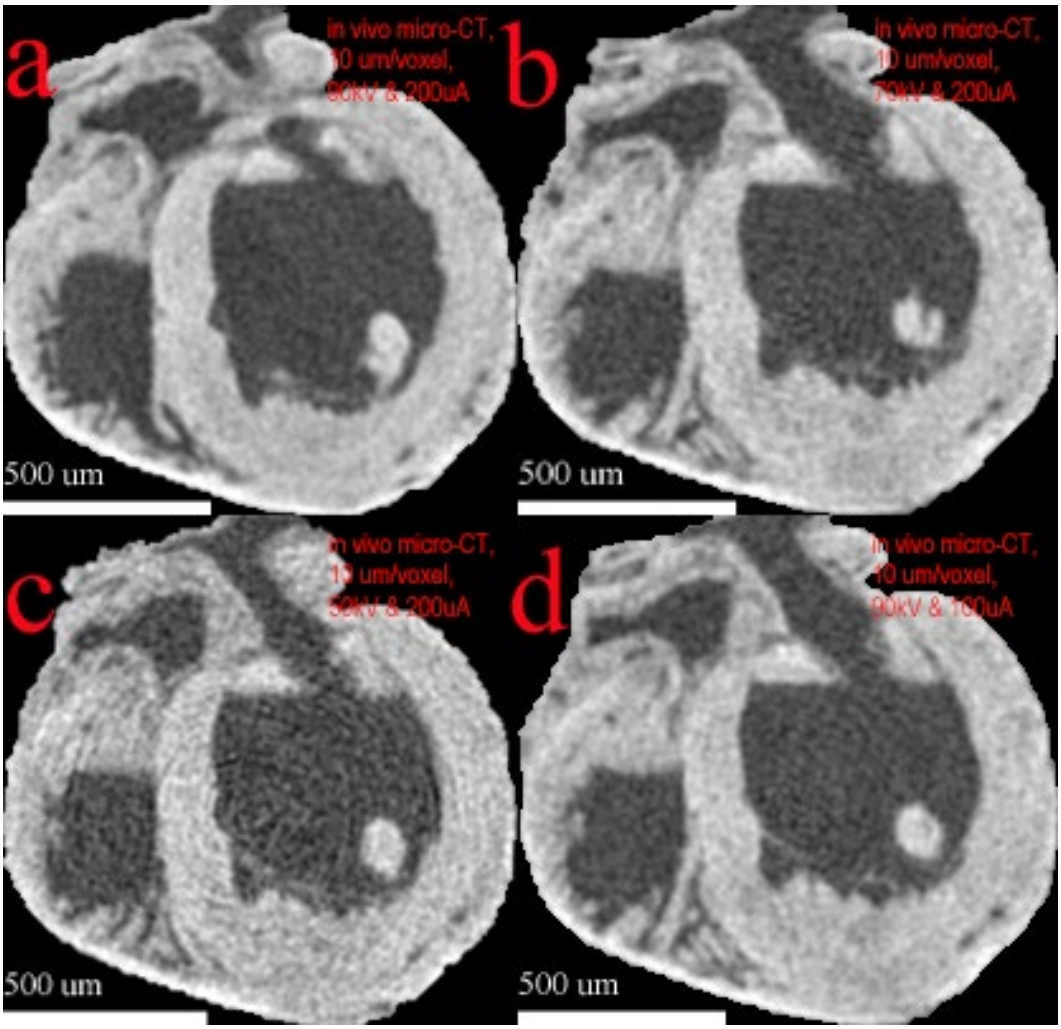

Figure 4: Effect of micro-CT voltage and current on high-resolution (10µm/voxel) *in vivo* micro-CT images of rat heart.

Figure 4a (90kV), 4b (70kV), and 4c (50kV): longitudinal views of micro-CT heart scans showing reduction of x-ray source voltage results in higher image noise. Image clarity gradually reduced from Figure 4a to 4c as demonstrated by less demarcated ventricular borders. However, macroscopic information including heart chamber dimensions, ventricular wall thickness, and outlining of papillary muscles are preserved, which is best illustrated in left ventricle.

Figure 4a (200 µA) and 4d (100 µA): demonstrates halving the micro-CT current setting results in higher image noise. Internal ventricular border shown by Figure 4d is blurrier than that shown by Figure 4a.

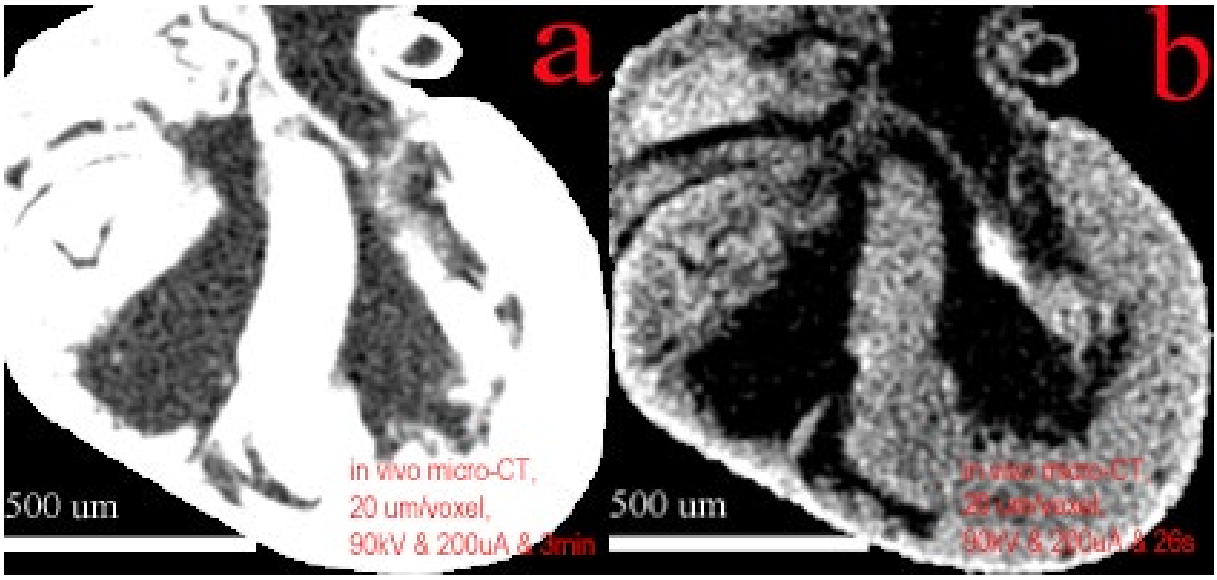

Figure 5: Effects of PTA staining and scanning time on micro-CT scans of neonatal rat heart-148 staining days.

Figure 5a (1.0% PTA, 3min): presents micro-CT scans of a fully PTA-stained heart with strong cardiac parenchyma and cavities contrast. However, due to the strong radio opacity, adjacent structures such as pulmonary and aortic vessel walls cannot be differentiated.
Figure 5b (1.0% PTA, 26s): shorter scanning time CT scanning time gives poor structural details due to higher image noises.

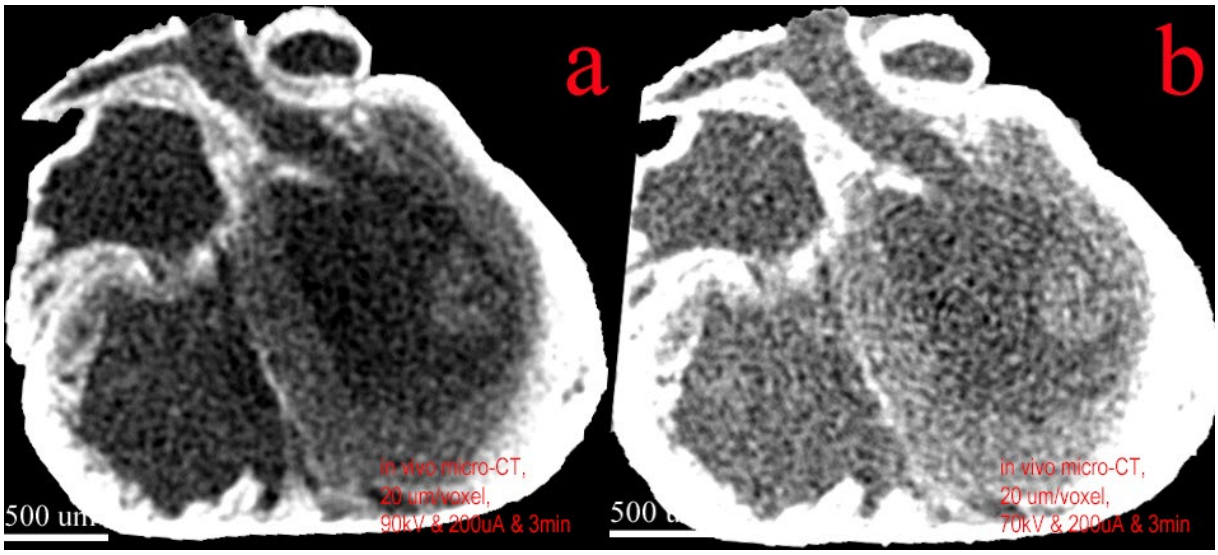

Figure 6: The effect of non-uniform staining on cardiac tissue micro-CT image-699 days of staining.

Figure 6a (0.5% PTA, 90kV) shows moderate contrast details at the outer rims of the heart with limited internal clarity. Internal structures such as interventricular septum are poorly defined.
Figure 6b (0.5% PTA, 70kV) shows rough outer boundary of stained regions, mainly the outer rims of the ventricles. The boundary of internal ventricular wall and septum cannot be delineated.

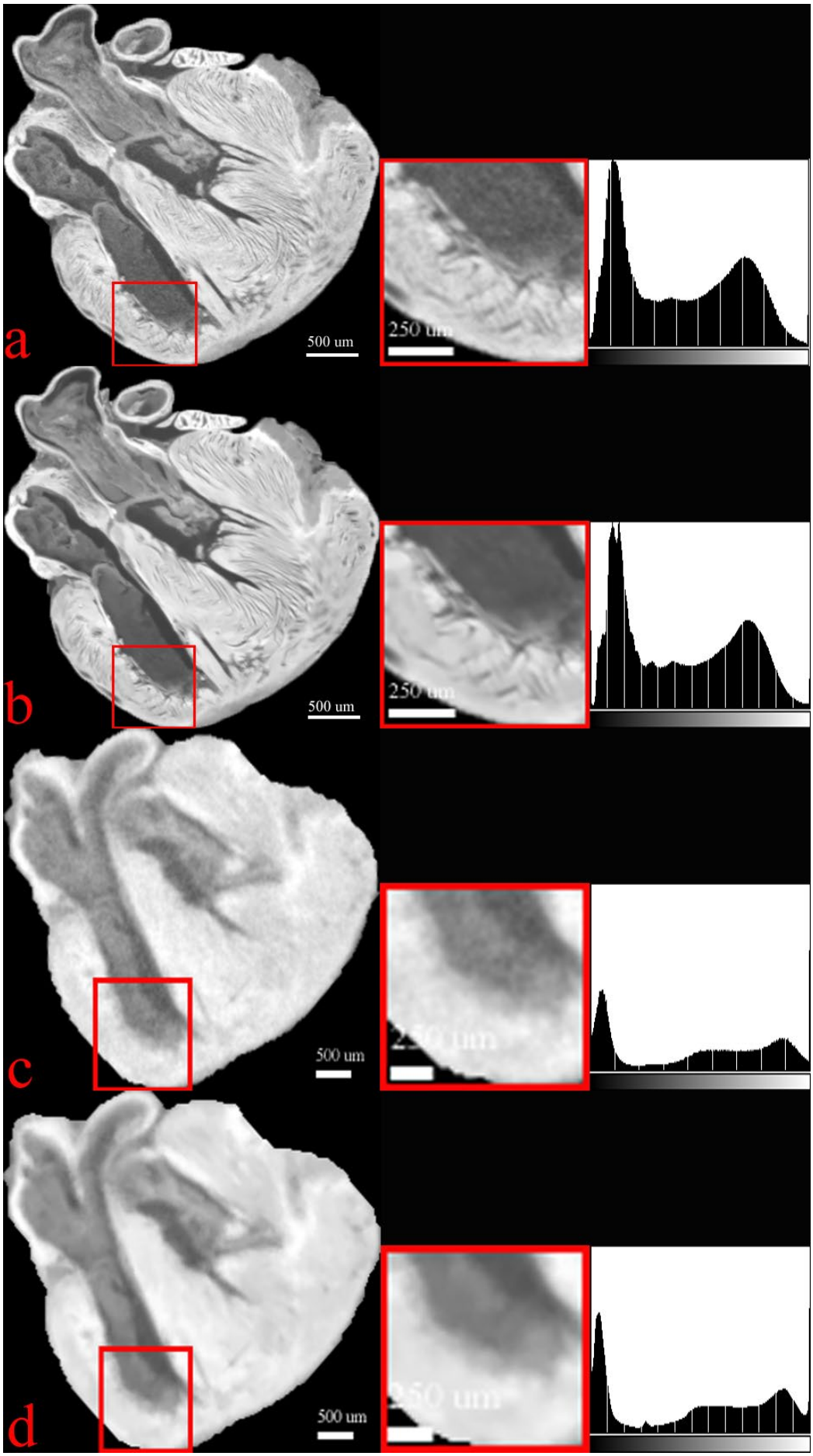
a
500 um
250 um
b
500 um
250 um
c
500 um
d
500 um

Figure 7: Cardiac anatomical differentiation of both *ex vivo* and *in vivo* micro-CT scans are enhanced by NLM filtering.

The original (7a) and denoised (7b) ex vivo scans illustrate that mildly enhanced cardiovascular parenchymal edges in denoised (7b) while anatomical information is unaltered in both. Similar but slightly more prominent enhancements are in 7c and 7d, original and denoised in vivo micro-CT scans, respectively. The respective contrast histograms of each scans revealed narrower histogram peaks in denoised group, 7b and 7d, in comparison to their respective originals, 7a and 7c.

Chapter 3.2 Tables:

Rat heart, (Rat age)	Stain type	Stain concentration	Effective Staining duration	Micro-CT type	Scanning time	Resolution (um)	Voltage (kV)	Current (uA)	Results *
72 hours	Iodine	1.5% in 90% Ethanol	48 days	Ex vivo	15 hours	10.7	100	100	Excellent-Figure 2b and 2c
72 hours	Iodine	1.5% in 90% Ethanol	16 days	In vivo	4.5 min	40	90	200	Good-Figure 2d
96 hours	PTA	1.0% in 70% Ethanol	148 days	In vivo	4.5 min	40	90	200	Good-Figure 2e
72hours	Iodine	1.5% in 90% Ethanol	16 days	In vivo	3 min	10	90	200	Good-Figure 3a
72hours			16 days		3 min		70	200	Good-Figure 3b
72hours			16 days		3 min		50	200	Poor-Figure 3c
72hours			16 days		3 min		30	200	Incomplete
72hours			16 days		3 min		90	100	Good-Figure 3d
72hours	Iodine	1.5% in 90% Ethanol	16 days	In vivo	3min	20	90	200	Good-Figure 4a
72hours			16 days		3 min		70	200	Good-Figure 4b
72hours			16 days		3 min		50	200	Poor-Figure 4c
72hours			16 days		3 min		30	200	Incomplete-Figure 4d
72hours			16 days		26 s		90	200	Good-Figure 4e
72hours			16 days		3 min		90	100	Poor-Figure 4f
96 hours	PTA	1.0% in 70% Ethanol	148 days	In vivo	3 min	20	90	200	Good-Figure 5a
96 hours			148 days		26 s		90	200	Poor-Figure 5b
96 hours	PTA	0.5% in 70% Ethanol	699 days	In vivo	3 min	20	90	200	Incomplete-Figure 6a
			699 days		3min		70	200	Incomplete-Figure 6b

***Excellent**-Detailed anatomy; **Good**-Gross anatomy, sharp border; **Poor**-Gross anatomy, blurry border; **Incomplete**-Undifferentiated anatomy

Table 1: Summary of various tissue staining and micro-CT setups for different rat hearts with respective image results

Chapter 4: Craniofacial dysmorphology resembling domestication syndrome may be associated with spotting-lethal rat, a model of Hirschsprung disease

Chapter 4 Highlights

- *sl/sl* rat, an $ET_B^{-/-}$ HSCR model, exhibits subtle craniofacial features resembling to those of domestication syndrome.
- *sl/sl* rat has a flatter cranium, a smaller maxilla, a larger mandible, and a disproportionally shorter but wider nose than the control group.
- *sl/sl* rat has a slightly larger W-index than the control group, consistent with the presence of dystopia canthorum, a feature seen in the analogous condition, Waardenburg syndrome.
- Although all dental elements are presented, *sl/sl* rat has smaller superior incisor and molar beds.
- if our animal findings are extrapolatable to human, our finding of a shorter but broader nose, smaller mid-face, and shorter molar beds in *sl/s* rat may suggest an increased risks for obstructive sleep apnoea and dental malocclusion in some $ET_B^{-/-}$ HSCR patients.

Chapter 4 Abstract

Background

$ET_B^{-/-}$ mutation is a major cause of HSCR, a neurocristopathy known for its enteric nervous system failure. Other than regulating ENCC migration, ET_B mediates ET-1 clearance. Consequently, ET_B may indirectly affect ET-1/ET_A signalling, which controls CNCC migration and craniofacial development. Interestingly, it was hypothesized that "domestication syndrome" arise from changes in neural crest determining genes, including ET_A and ET_B. Although $ET_A^{-/-}$ animals are known to suffer severe dysmorphology resembling CATCH22 syndrome, we hypothesize that *sl/sl* rat, an $ET_B^{-/-}$ HSCR model animal, may also exhibit subtle craniofacial changes through indirect control. These features may share resemblance to those of domestication syndrome.

Methods

Ten rat pups with an average age of 88 hours were anaesthetized with 5% isoflurane and culled via exsanguination. Tail tips were removed for genotyping. Head tissues were stained in 1.5% iodine for two weeks prior to micro-CT scanning. *In vivo* micro-CT scanning of cranial specimen was performed followed by *ex vivo* micro-CT scanning of 2 samples for image quality control. 3D visualization and analyses were performed using an open-source program, Drishti. Cephalometric measurements were made on selected craniofacial landmarks. Comparisons were made between *sl/sl* rats and the control group, which consisted of wild-type and heterozygotes.

Results

Subtle reductions in facial measurements were seen in *sl/sl* rats when compared with the control group, ranging from 1.4% to 15%. These changes were observed in cranial, maxillary and mandibular parameters: total skull length, nasal length, nasal width, nasal cavity width, interorbital width, interlens distance, inner and outer canthal distance, maximal skull height, cranial length, intracranial length and width, interorbital width, and interzygomatic width. Consistently, craniofacial ratio indices showed *sl/sl* rat has a flatter cranium (skull height/skull length: 0.393 vs 0.413) and a shorter but broader nose (nasal width/nasal length: 0.794 vs 0.874). Additionally, subtle dystopia canthorum may be presented in *sl/sl* rat based on increased W index. While there was no discrepancy in dental number and morphology between the control and *sl/sl* groups, dimensional difference was detected.

Conclusions

This study demonstrated subtle craniofacial changes are presented in $ET_B^{-/-}$ HSCR model, supporting the idea that ET_B regulates CNCC migration. The findings also implicate $ET_B^{-/-}$ HSCR patient may have predisposing risks for conditions such as obstructive sleep apnoea, cleft palate, or dental malocclusion. Lastly, these changes share resemblance with described domestication syndrome, supporting NCC-determining gene, ET_B, may play a role in the formation of domestication.

1. Introduction

Colonic aganglionosis are diseases affecting both humans and animals, with Hirschsprung disease (HSCR) being the human eponym. While HSCR is once thought of as a single organ disease, it has become apparent that as a neurocristopathy, multi-systems are likely involved. Indeed, a number of congenital abnormalities of the central nervous system including microcephaly, agenesis of the corpus callosum, asymmetry of lateral ventricles, central hypoventilation syndrome, sensorineural deafness, seizures, mental retardation and autonomic nervous abnormalities have all been reported to associate with HSCR (28, 115, 499-501). Additionally, it is widely accepted that HSCR is associated with a number of genetic syndromes including Shah-Waardenburg syndrome (WS-IV), Down's syndrome (DS), and Mowat-Wilson syndrome (MWS) (502). Furthermore, we also recorded a smaller head circumference in paediatric HSCR surgical patients than that in general paediatric surgical population. This observation is more pronounced in males, consistent with HSCR's male predominance (10). This evidence suggests that the developmental failure in HSCR is not limited to, at least in some cases, the enteric nervous system but more diffusely affecting central nervous, cardiovascular, and craniofacial systems. This relationship can be exemplified by MWS. In this study, we focus on the external morphological changes associated with $ET_B^{-/-}$ HSCR phenotype.

Several genes have been identified in the pathogenesis of HSCR. A major susceptible gene is *RET*, which contributes 5-25% of all cases based on the findings of genetic screening series (503). Additionally, the endothelin signalling pathway also plays important role in the pathogenesis of HSCR; mutations in either endothelin B receptor (ET_B) or endothelin-3 (ET-3) genes can lead to HSCR, as identified in both HSCR patients and rat models (113, 413). ET_B is

the second most susceptible gene for causing HSCR, accounting for approximately 5% of human cases (503). The loss-of-ET_B-function results in WS-IV and other developmental sequelae due to the signalling disruptions in the endothelin system.

Endothelin signalling is an intricate system, encompassing two major endothelin receptors, ET_A and ET_B. Their respective signalling pathways have distinctive different yet intertwined physiological functions. While a functional ET_B is known to play pivotal role in the development of ENS, it also mediates basal endothelial vasodilation and up to 80% of ET-1 clearance; the latter of which is less well known (380). Binding of ET-1 to ET_A mediates strong vasoconstriction through vascular smooth muscle contractions, and importantly, is essential for the craniofacial morphogenesis during development. Indeed, Clouthier et al (1998) demonstrated mice with ET_A knock-out mutations exhibit features resembling human CATCH 22 or velocardiofacial syndrome, including: smaller mandible, shortened neck, underdeveloped pinnae, and deformed cardiovascular outflow tracts (230).

Bony and cartilaginous craniofacial morphogenesis are heavily dependent on three major stages of CNCC developments: migration of CNCC from rhombomere to pharyngeal arches forming the ectomesenchymal cells, propagation of ectomesenchymal cells within the pharyngeal arches, and terminal differentiation to mature structures (e.g. cartilage, dentine, and bones) following interactions with ectoderm (504). While the precise mechanisms of ET-1/ET_A signalling on the developing CNCC are yet to be confirmed, the current consensus is as follows: ET-1 expressed in the pharyngeal arch epithelium and paraxial mesoderm-derived arch core acts as a chemoattractant for the ET_A-expressing ectomesenchymal cells to appropriate position prior to end-organ differentiation (230). Therefore, disruptions or

hypostimulations in ET-1/ECE-1/ET_A pathway leads to CNCC migration failure and severe craniofacial defects ultimately result in mechanical asphyxia post birth (230, 232, 505). Additionally, the ectomesenchymal cells originated from cardiac neural crest cells (CaNCC) migrate to pharyngeal arches 3, 4, and 6 to form the aortic pulmonary system; disruptions in the ET-1/ET_A system can thus cause ventricular septal defects and aortic hypoplasia or interruptions (232).

Interestingly, the multi-genetic "domestication syndrome" also exhibits mild variant craniofacial dysmorphology seen in velocardiofacial syndrome and Waardenburg syndrome (WS); both of which arise from mutations in the endothelin system (27, 506). Domestication syndrome is a concept first introduced by Charles Darwin in 1868 to describe a range of behavioural, morphological and physiological traits difference between the domesticated animals and their wild forbearers (507). Since then, its genetics and implications have been the focus of extensive researches (508). The domestication syndrome refers to a combination of traits observed in domesticated animals including increased docility, tameness and prolonged juvenile behaviour, depigmentation, ear and tail form, shorter nose, reduced tooth size, alterations in adrenocorticotropic hormone levels, altered concentrations of several neurotransmitters, and a reduction in total brain size and particular brain regions (508-510). Many of the similar characteristics are also observed in HSCR-associated syndromes, suggesting potential common aetiology. Indeed, recent researches have suggested that features of domestication may arise from alterations in neural crest cells and neural crest determining genes, including RET, GDNF, SOX10, MITF, PAX3, ET-1, ET-3, ET_A, and ET_B; all of which play crucial roles in neural crest cell specification, migration, and post-migratory interaction (19, 113, 162, 178, 231, 511-513). Consistently, animals with these

dysfunctional genes may display a range of abnormalities, ranging from mild domestication syndrome to debilitating or lethal neurocristopathy such as HSCR or Waardenburg syndromes (19, 508).

Although we do not expect ET_B-knockout mutants to exhibit gross dysmorphic features from the migration failure of cephalic neural crest cell (CNCC) as seen in ET-1/ET_A mutants, we ponder the potential impact of elevated ET-1 on the development of HSCR subjects. To study the potential changes associated with HSCR, we adopted spotting-lethal (*sl/sl*) rat as our study model.

sl/sl rat is an autosomal recessive $ET_B^{-/-}$ mutant with high adherence to Mendelian inheritance. Pathogenically, *sl/sl* rat carries a naturally-occurring 301 base-pair deletions in ET_B gene which causes ET-3/ET_B signalling dysfunction (413). Phenotypically, *sl/sl* rat exhibits features resembling HSCR and WS-IV patients including: histologically-confirmed aganglionic bowel, pigmentation defects, and hearing deficits (413, 439). Based on the colony data of 475 rats, we observed high genetic penetrance of intestinal aganglionosis in up to 95% of homozygous *sl/sl* rats. Additionally, Gariepy et al (2000) showed that *sl/sl* rats have approximately six-times higher ET-1 level than that of wild type rats due to impaired clearance from the absence of functional ET_B (381). This is also supported by the consistent finding that ET_B inhibition by BQ-788 causes significant elevation in ET-1 levels (514). Consequently, we suspect potential developmental changes in craniofacial features to occur in *sl/sl* rats due to elevated ET-1 levels and subsequent changes in ET_A-mediated signalling.

Given *sl/sl* rat is a single-gene HSCR model with high genetic penetrance, changes observed in mutants can provide further clarifications on ET_B functions and the potential impairments associated with HSCR. In addition to skin depigmentation, we ponder *sl/sl* rats may display some structural characteristics of domestications, including craniofacial changes.

This study aims to extrapolate the impact of ET_B on the craniofacial morphology by quantitatively comparing the external morphology of *sl/sl* rat to that of control group. All measurements are made on three-dimensional (3-D) rendering of structurally preserved micro-CT data. We hypothesized that *sl/sl* rats may possess altered craniofacial morphology resembling some domestication features, including smaller a shorter and flatter face.

2. Materials and Methods

2.1. Compliance with Ethical practice

All animal tissues used in this study were handled with strict compliance to ACT Health Human Research Ethics Committee (ACTH-HREC) and Australian National University Animal Experimentation Ethics Committee (ANU-AEEC), project number A2011/67.

2.2. Tissue preparation and staining

Ten rat pups with an average age of 88 hours were used this study. They were derived from crossbreeding between the heterozygous carriers for the ET_B mutation. Their coat pattern, age, gender, weight, and colonic appearance were recorded prior to culling. The culling process involved over-anesthetizing the rats with 5% isoflurane followed by thoracotomy and abdominal aortomy. Five-millimetre tail tips of each rat were resected and stored for subsequent genotyping.

To facilitate successful micro-CT scanning with adequate tissue differentiation, diffusion staining with iodine solution was performed prior to scanning. A rhomboid-shaped craniotomy of five-millimetre in diameter was created on the parietal bones to facilitate tissue staining. The rat samples were first washed in 10% PBS solution for 30 minutes followed by 4% formalin fixation for 24 hours. Next, formalin was replaced by progressive ethanol (EtOH) series: 20%, 50%, 70% and 90% for 24 hours each. Finally, the ethanol-fixed rat bodies were stained in 1.5% iodine solution for a minimum of 7 days prior to micro-CT scanning.

2.3. Micro-CT scanning

We have chosen micro-CT scanning for its high image-resolution power to secure accurate and detailed anatomical information. The image scanning was performed using a commercially available *in vivo* micro-CT scanner (Caliper Quantum FX) followed by a validation scan with a custom-built *ex vivo* micro-CT system at the Department of Applied Mathematics of Australian National University (ANU). Due to its limited accesses, the latter was only used for image quality control. The terminology of "*in vivo*" and "*ex vivo*" described here were not to be confused with their standard definitions in biomedical science but rather as descriptions of micro-CT system setups (439). The *in vivo* micro-CT system consists of a stationary sample positioned in between a rotational system of X-ray source and detector with the aims to reduce radiation exposure while acquiring satisfactory images. On the contrary, the *ex vivo* micro-CT system positions a rotating sample in between an adjustable X-ray source and a detector. This setup renders high magnification image with high signal-to-noise ratios possible.

The Caliper Quantum FX required a scanning time of 4.5 minutes for images with maximal resolutions of 10 µm/voxel. The resultant images were stored as DICOM series. On the other hand, the *ex vivo* micro-CT system of ANU Applied Mathematical Department allocated 15 hours of scanning time per scan with additional 8 hours of image processing time in National Computational Infrastructure (NCI) services. The maximal resolution achievable was 1 µm/voxel, limited by the physical size of the sample. The resultant images were stored as netCDF files. Both series of image formats were visualized and analysed using Drishti, an opensource software (453).

2.4. Genotyping

Following the cephalometric analysis on acquired micro-CT data, genotyping was completed by standard PCR protocols. Three homozygous wild type ($ET_B^{+/+}$), two heterozygotes ($ET_B^{+/-}$), and five homozygous spotting-lethal (*sl/sl*; genotype $ET_B^{-/-}$) rats were identified.

Genotyping was performed with following protocols. Cells of the isolated five-millimetre rat-tail segments were lysed using Proteinase K in lysis buffer, which consisted of 100mM Tris pH 8, 5mM EDTA, 0.2% SDS, 200mM NaCl in distilled water. DNAs were extracted via standardized protocols: vortex heating, supernatant separation via centrifuging, and washing and drying DNA pellet with 70% EtOH. The extracted DNA was quantified with spectrophotometry.

Next, PCR was completed using “Master-Mix” reagents composed of 10*PCR buffer,

Qiagen-contained $MgCl_2$, dNTP (10mM), Primer PS 7 (33.3µM, 5'-CCACTAAGACCTCCTGGACT-3'), Primer PS 15 (33.3µM, 5'-AGTGTAGCTTTCTAAGTCGTGA-3') and DNA polymerase (515). The Mater-Mix reagents were pipetted onto the PCR plates with 13 DNA samples, including 3 controls ($ET_B^{+/+}$, $ET_B^{+/-}$ and $ET_B^{-/-}$). PCR was conducted in the Veriti 96-Well Thermal-Cycler. Finally, the DNA identification against the controls was performed by running electrophoresis at 100V and 55mA with molecular-weight ladder (MassRuler, #SM1263, Fermentas) for one hour. The electrophoresis gel was visualized with Gel Documentation System DOC-PrintVX5 (Vilber Lourmat).

2.5. Cephalometric Analysis

A selection of cranial, maxillary, mandibular, and dental structures were chosen for analysis. The anatomical landmarks in this study were made based on anthropometric and cephalometric references in previous studies (516-519). These descriptions were outlined in Figure 1 and Table 1. Based on these craniofacial landmarks, direct dimensional measurements, as outlined in Figure 2 and Table 2, were completed using Drishti (453).

Cephalometric points were identified in several cross-sectional planes. Surface measurements were obtained from the external morphology of the rat head. Maximal skull height and incisor measurements were taken in the midsagittal plane while mandibular measurements were taken in the parasagittal plane passing through the buccal mucosa. Axial and maxillary measurements were obtained in the para-axial planes where the points of maximal lens protrusion and the midpoint of the philtrum were found, respectively. Based on these direct measurements, a selection of ratio indices was calculated to assess the proportional changes in the craniofacial features. These indices include W index, surface

nasal length/skull length ratio, surface nasal width/nasal length ratio, intracranial width/intracranial length ratio, skull height/skull length ratio, maxillary width/maxillary length ratio, mandibular length/skull length ratio, mandibular corpus height/mandibular corpus length ratio, and mandibular ramus/mandibular length ratio.

ET_B mutation has been known to associate with WS-II and WS-IVa (520). A key clinical characteristic of WS-I was the presence of dystopia canthorum (506). To assess the presence of this phenotypic feature, the W formula, as defined for human WS, was applied (Equation 1) to model animal measurements. As the eyelids of the neonatal rats were still fused, lens distance was used as a substitute for papillary distance.

Equation 1: W index for Dystopia Canthorum

$$W = X + Y + \frac{a}{b}$$

Where X= (2a-0.2119c-3.909)/c; Y= (2a-0.22479b-3.909)/b

a is the internal intercanthal distance, b is the interpupillary distance, and c is the external intercanthal distance (506).

2.6. Statistical Analysis

A total of ten rats were included in analysis and divided into a control and *sl/sl* group. The control group was composed of two wildtype ($ET_B^{+/+}$) and three heterozygous ($ET_B^{+/-}$) rat pups and five spotting lethal ($ET_B^{-/-}$) rats. Data was assessed for normality and Student's t test was applied for comparison between the control and mutant groups. A result was considered statistically significant at *p-value* $\leq$ 0.05. Analysis was conducted using SPSS software.

2.7. Measures of statistical error

To ensure validity of this study, researchers undertaking cephalometric measurements were blinded to the genotype of rats until the finalization of data analysis. To ensure accuracy and reproducibility, all measurements were repeated by the same researcher two weeks after the initial analysis. The difference between the two measures was determined with random error calculation, Dahlberg's error (517, 521). The Dahlberg statistic reported the average amount of disparity between the measurement sessions.

$$D = \sqrt{\frac{\sum d^2}{2\mathrm{N}}}$$

Where d is the difference between replicate measures and N is the number of cases.

3. Results

The basic parameters of the rat pups were listed in Table 3. The control and *sl/sl* groups have respective average bodyweight of 13.16 ± 0.81g and 11.40 ± 1.62g, *p-value* = 0.063, translating to a difference of 13%. There was a positive correlation between bodyweight and the cephalometric measurements, with the control group generally having larger craniofacial measures than those of *sl/sl* rats, apart from the average inferior incisor length, Table 4 and 5. In addition to this positive correlation, *sl/sl* rat exhibited several morphological features different from the control group, as revealed by dimensional-ratio index, Table 6.

3.1. Cranial Measures

Fifteen craniofacial dimensions were taken in the surface, parasagittal, and axial

planes to assess cranial structures, as reported in Table 4. The control rats have detectably larger, ranging from 1.5-14%, cranial dimensions than *sl/sl* rats in the following parameters: total skull length, surface nasal length, surface nasal width, nasal cavity width, interorbital width, interlens distance, inner and outer canthal distance, maximal skull height, cranial length, intracranial length and width, interorbital width, and interzygomatic width. While statistically significance was only found in the respective comparison of surface nasal lengths and interlens distance between the two groups, the trend of *sl/sl* having smaller features was consistent across all findings measured in various planes.

3.2. Orbital Measures

Seven measures were taken to assess the orbital size and positioning in the context of the face, Table 5. Orbital dimensions were taken from both eyes followed by averaging these findings for comparison. While the control rats exhibited larger orbits than the *sl/sl* rats in terms of length, width, and circumference, these differences were small, ranging from 0.03 to 3.12%. On the other hand, statistical significantly shorter interlens distance was noted in *sl/sl* rats, 6.74% smaller with *p-value* = 0.015, suggesting medial displacement of the lens.

3.3. Maxillary measures

Six measures were made to assess changes of maxillary structure in *sl/sl* mutants. Maxillary dimensions of *sl/sl* rat group were 4.53% to 5.45% smaller than the control group, Table 5. This was reflected by the measurements of maxillary length, maxillary width and incisive foramen width, albeit statistical significance was not achieved. On the other hand, statistically significant reductions were seen in U6 intermolar width, U8 intermolar width, and molar plate length of *sl/sl* rats. These observations suggested *sl/sl* rats having a smaller

mouth and a narrower mid-face in comparison to the control group.

3.4. Mandibular measures

To assess the lower facial changes associated with ET_B mutation, five mandibular measures were compared, including mandibular length, ramus height, corpus length, and corpus height, Table 5. While these measurements showed a general trend of subtle size reduction in *sl/sl* rats, ranging from 1.69% to 2.91%, none of these measures reached statistical significance. Furthermore, comparison of mandibular plane angle showed little difference between the control and *sl/sl* groups. These findings suggested ET_B mutation may have little impact on mandibular development.

3.5. Dental measures

Because dental development was dependent on CNCC migration, a process partially regulated by ET_B signalling, dentitions of *sl/sl* rat were examined in this study. As shown by Table 5, there was no discrepancy in terms of dentition number between the control and *sl/sl* groups. Additionally, we detected no difference in dental morphology between the two groups. On the other hand, the superior incisor length of *sl/sl* mutant was 10.83% smaller than the control rat while the opposite trend was true for inferior incisor length, 6.11% larger. Although these findings did not reach strict statistical significance, *p-value* < 0.05, they were consistent with the change patterns observed in the maxillary and mandibular measurements.

3.6. Comparison of Craniofacial indices

Ratio indices were calculated to determine the dimensional proportionality in

individual craniofacial features.

Cranial dimensional ratios were first compared, as shown by Table 6. While there was no difference in the intracranial width/intracranial length ratio between the control and *sl/sl* groups, the latter has smaller skull height/skull length ratio, indicating the presence of a flatter head. Additionally, comparisons made on the indices of surface nasal length/skull length and surface nasal width/surface nasal length demonstrated a disproportionally shorter but wider nose in *sl/sl* rat. Furthermore, while the absolute maxillary and mandibular measurements were smaller in *sl/sl* group, its respective dimensional indices were similar to those of control group, Table 6, suggesting proportional changes.

Lastly, the W index was used to assess for the presence of dystopia canthorum, a major clinical sign of WS, occurring in up to 98% of WS-I. The W index of *sl/sl* rat was found to be greater than that of control group, 3.328 versus 3.245 with *p-value* = 0.017, Table 6.

4. Discussion

HSCR has been traditionally regarded as a single-organ disease despite multi-genetic involvement. ET_B mutation is one of the major causes for HSCR. While ET_B is known to exert direct control on ENCC migration through ET-3/ET_B signalling, we found dysfunctional ET_B may also lead to subtle craniofacial changes with resemblance to those of “domestication syndrome.” These similarities include depigmentation, a flatter head, a shorter but broader nose, and smaller teeth (508). Our finding supports the long held hypothesis that genetic alterations in the development of NCCs contribute, at least partially, to the formation of domestication syndrome (508). The culprit, in this instance, is the ET_B mutation.

In this study, we reported craniofacial changes found in *sl/sl* rat, an autosomal recessive $ET_B^{-/-}$ HSCR model with high genetic penetrance. While there is no direct signalling linkage between ET_B and the development of CNCC documented in current literature, we found *sl/sl* rats exhibit reduced cranial, nasal, maxillary, and mandibular dimensions. As shown by Table 4 and 5, *sl/sl* rat has a smaller midface, a narrowed and shortened molar bed, a shortened muzzle, and a flattened cranium when comparing to those of the control group. Albeit small, ranging from 5-15%, these observed changes in conjunction with previously described depigmentation and reduced adrenal size (Lopez Dee, unpublished data) of *sl/sl* rat support the notion that ET_B may act as a mediator for domestication syndrome.

Additionally, dental changes resembling domestication are observed in *sl/sl* rats. The incisor size is different between the *sl/sl* and control rats; superior incisor length is ~10% smaller whereas inferior incisor length is ~6% larger in the *sl/sl* rats. Although this observation is not fully consistent with the domestication features of global dental size reduction, this variance may be explained by the young age of studied rats, 3.5 days. Since rat's dental eruption occurs at eight to ten days postnatally and maturates between forty to fifty days after birth (522, 523), the full dental features of domestication may not be appreciated prior to maturation age. Nevertheless, given the domestication feature is influenced by a combination of genetic and behavioural factors, our finding on *sl/sl* rat supports the notion that ET_B mutation may be a predisposing factor for dental changes. On the other hand, the presence of normal dental anatomy and molar teeth number in each quadrant of both the control and *sl/sl* groups suggest ET_B's impact may be small in dental

development. While individual molar dimensions are not measured, size reductions in maxillary molar plate and mandible are seen in *sl/sl* rats, Table 5. This decreased molar bed may predispose matured *sl/sl* rat to have decreased molar size and increased risks of molar overcrowding, features consistent with domestication.

Craniofacial morphogenesis is known to be dictated by ET-1/ET_A signalling, and hypostimulation of which leads to premature arrest of CNCC migration. This severe craniofacial dysmorphology seen in CATCH 22 or velocardiofacial syndrome results in mechanical asphyxia and early death (230). Although the subtle changes identified in *sl/sl* rats are not as drastic, they nevertheless provide suggesting evidence that $ET_B^{-/-}$ HSCR children may suffer subtle craniofacial maldevelopment. These facial feature changes not only may affect patients aesthetically, such as cleft-palate (524), but more importantly increases the health risks. These risks may include the development of obstructive sleep apnoea or chronic sinusitis due to a shorter but wider nose in addition to dysphagia from a smaller oral orifice; all of which can impair children's growth. Furthermore, our findings are consistent with the notion that ET_B mediates the endocytic degradation of ET-1 and thereby indirectly affecting ET-1/ET_A signalling. As reported by Gariepy et al (2000), *sl/sl* rat has ~6-folds higher ET-1 due to impaired clearance (381). This likely hyperstimulates ET_A pathway, as demonstrated by the increased vascular tone in ET_B-deficient mice (377). Consequently, a modulatory mechanism rather than a complete arrest of CNCC migration is the likely cause leading to the subtle craniofacial changes observed.

Moreover, ET_B mutation is known to associate with WS, particularly in the pathogenesis of WS-II and WS-IV (142). WS is a group of sensorineural and pigmentary

disorders that are subcategorized into four subtypes based on distinctive phenotypes: dystopia canthorum (WS-I), upper limb deformity (WS-III), and HSCR (WS-IV). WS-II, on the other hand, does not have any additional symptom (525). While dystopia canthorum was previously reported in PAX3-induced WS-I, we found increased W index in the $ET_B^{-/-}$ WS-IV model with respect to the control group, 3.245 vs 3.328, *p-value* = 0.017. Although this statistically significant change is small, in conjunction with other changes observed, it raises the possibility of overlapping control between PAX3 and ET_B on the CNCC migration. On the other hand, other than the surface nasal dimensional indices showing distinctive shorter but wider nose in *sl/sl* rat, the dimensional ratio indices made on cranium, maxilla, and mandible show little difference between *sl/sl* and control groups, Table 6. These proportional reductions in the facial features of *sl/sl* rats suggests ET_B mutation exerts a global inhibition on cephalic growth.

It is worth noting that the control group has a larger body size than *sl/sl* rats at culling despite having similar ages, suggesting malnutrition from a dysfunctional enteric system may contribute to the craniofacial difference observed. While this positive bodyweight and cranial size correlation is consistent with report made by Miller and German (1999) (526), it fails to explain the presence of non-uniform dimensional-ratio indices, Table 6. This suggests an additional independent factor is likely to have contributed to the formation of flatter cranium and shorter muzzle in *sl/sl* rats.

The findings of this study, if translatable to human HSCR patients, have several clinical implications for patient management. A genome-wide association study has recently identified ET_B gene as a major susceptibility locus for craniofacial microcephaly (527), a fact

that is consistent with the craniofacial alterations observed in the *sl/sl* rat. In addition to those described in syndromic HSCR (DS, MWS, and Goldberg-Shprintzen syndrome), additional craniofacial anomalies have also been reported in non-syndromic HSCR patients, including cleft palate, broad nasal root, microcephaly, and hypertelorism (29, 502, 528-532). Our dimensional finding supports these reports with quantitative measures. Of the craniofacial alterations identified in the *sl/sl* rat, shorter but broader nose, smaller mid-face, and decreased length of the molar bed suggest $ET_B^{-/-}$ HSCR patients may be predispose to obstructive sleep apnoea and dental malocclusion (533); both of which instigate with adverse health outcomes and require intervention. Additionally, we may find $ET_B^{-/-}$ HSCR patients with higher risks of clinical midfacial hypoplasia based on animal findings.

We acknowledge the power of this study can benefit from a larger sample size. Furthermore, the inherent limitation of an animal study prohibits us from making definitive comments on the effect of ET_B mutation on human craniofacial morphology. Nevertheless, the presence of multiple craniofacial alterations in *sl/sl* rats cannot be overlooked, and this study offers some grounds to suggest that $ET_B^{-/-}$ HSCR individuals may be at risk of craniofacial changes; further study is required. Moreover, this study setup is consistent with the autosomal recessive mendelian traits of *sl/sl* rat, the potential dose-dependent response of ET_B remains unclear. Future research may aim to include a larger sample size study or corresponding morphological study on $ET_B^{-/-}$ HSCR patients.

5. Conclusion

Overall, this study demonstrates that subtle craniofacial changes in an $ET_B^{-/-}$ HSCR model and provides some support for the hypothesis of neural crest gene involvement in

domestication. ET_B may be one of these genes. Furthermore, this study provides additional support to the growing body of literature stating that multi-organ manifestations may be associated with HSCR. Our animal findings, if extrapolatable to human, suggest $ET_B^{-/-}$ individuals may have subtle craniofacial malformations and thus increased risks for obstructive sleep apnoea, cleft palate, or dental malocclusion. However, confirmatory clinical studies on human subjects are required to clarify this relationship.

Chapter 4 Figures:

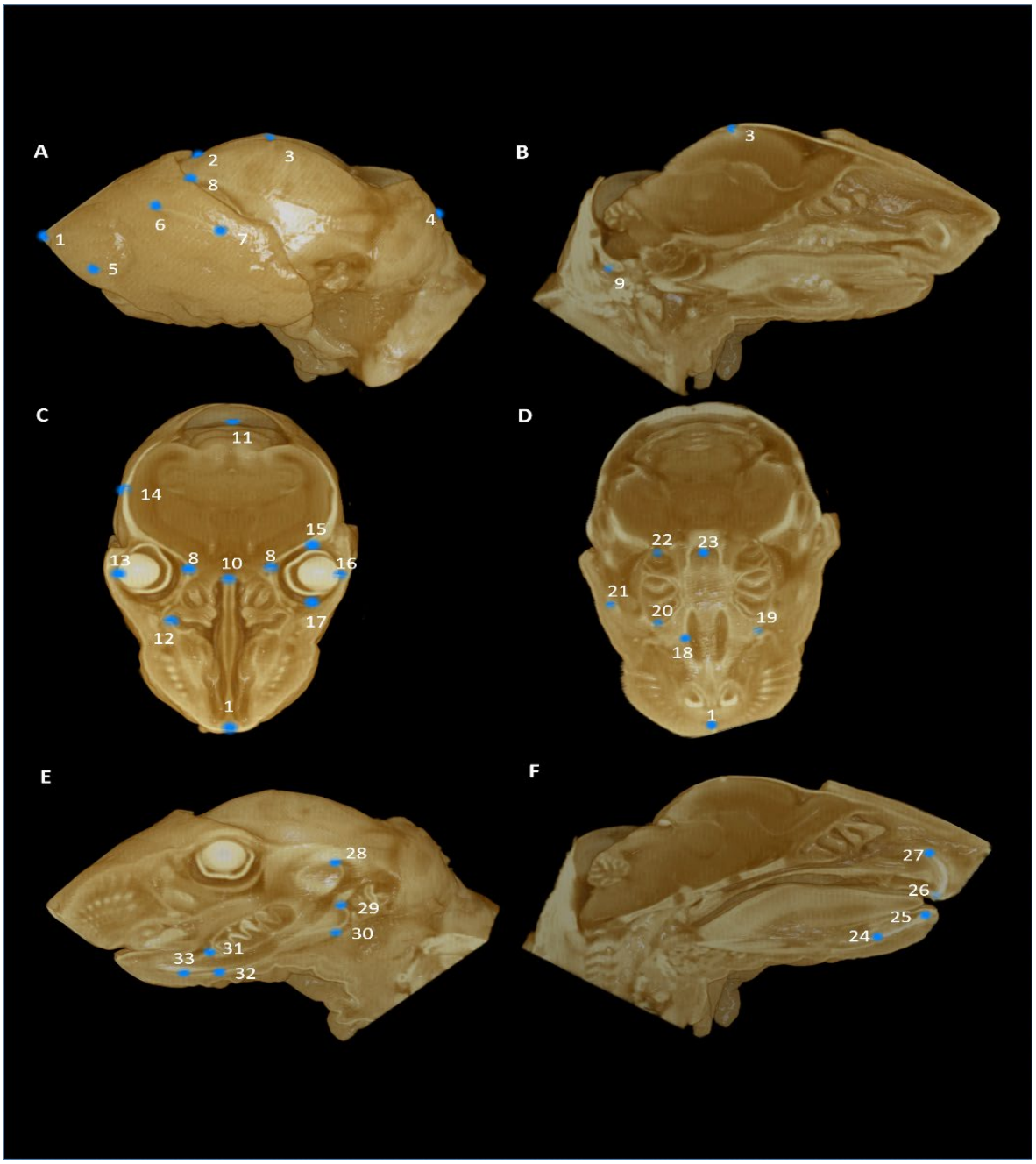

Figure 1: 3-D model of rat head composed from micro-CT scans demonstrating anthropometric landmarks selected for craniofacial cephalometric analysis.

A description of each numbered point is provided in Table 1. Figure 1A: surface cranial cephalometric points. Figure 1B: cranial cephalometric points in the mid sagittal plane. Figure 1C: cranial cephalometric points in the axial plane cut at the point of maximal lens protrusion. Figure 1D: maxillary cephalometric points in the axial plane cut at the midpoint of the philtrum. Figure 1E: mandibular cephalometric points cut in the sagittal plane through the buccal mucosa. Figure 1F: cephalometric points used to assess incisor length cut in the mid sagittal plane.

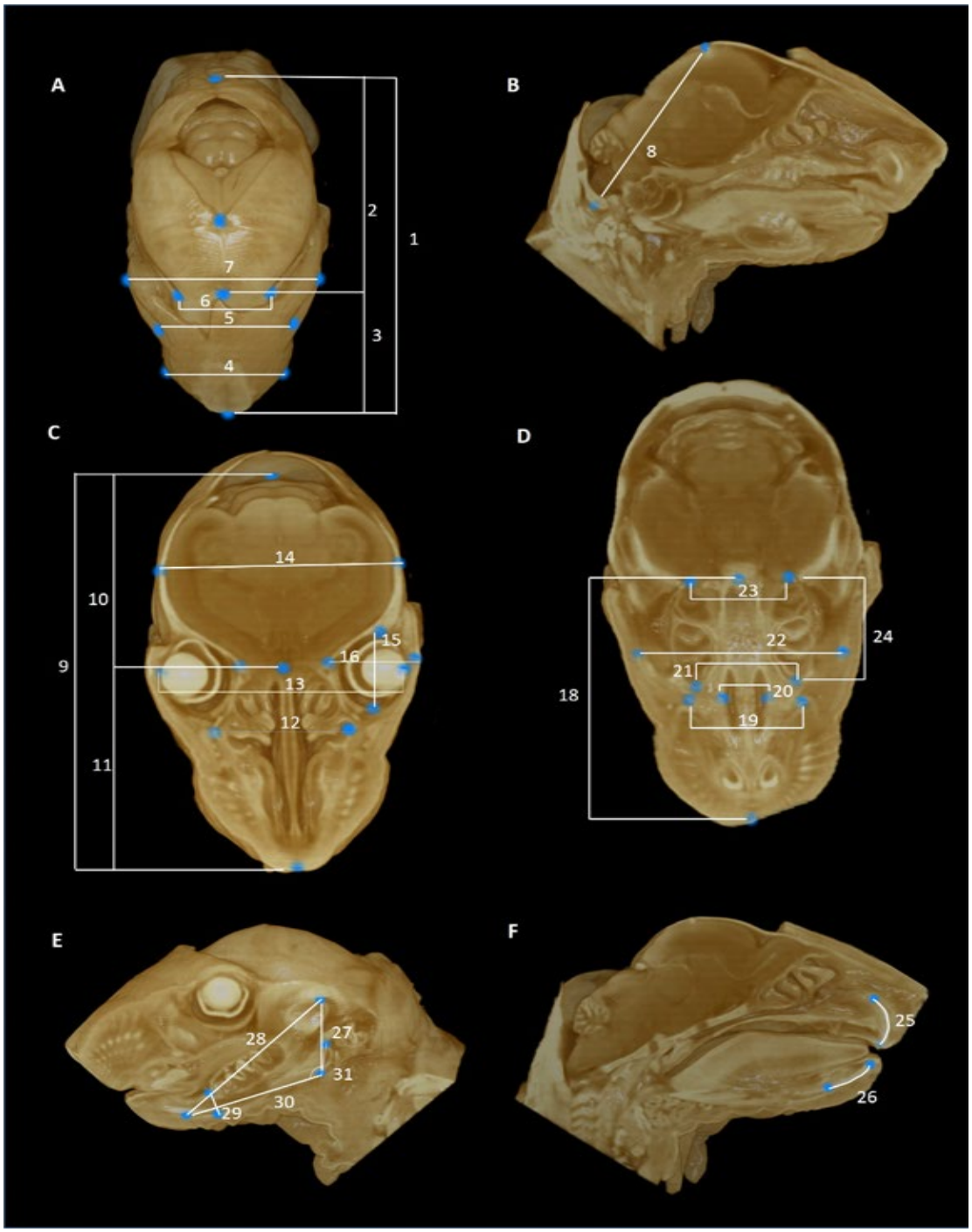

Figure 2: 3-D model of rat head composed from micro-CT scans demonstrating cephalometric measurements selected for analysis.

A description of each numbered point is provided in Table 2. Figure 2A: Cranial cephalometric measures made from the surface of the cranium. Figure 2B: Cranial cephalometric measurements made in the mid sagittal plane. Figure 2C: cranial cephalometric measurements in the axial plane which cuts at the point of maximal lens protrusion. Figure 2D: maxillary cephalometric measurements in the axial plane which cuts at the midpoint of the philtrum. Figure 2E: mandibular cephalometric measurements in the sagittal plane that cut through the buccal mucosa. Figure 2F: cephalometric measurements for assessing the incisor length in the mid sagittal plane.

Chapter 4 Tables:

	Cephalometric Point	Description
Surface Cranial Cephalometric Points		
1	Internasal Point	The most anterior point of the internasal suture in the mid sagittal plane
2	Nasofrontal point	Intersection of the nasofrontal suture and the internasal suture on the midsagittal plane
3	Frontoparietal Point	The intersection of the frontoparietal suture and the interparietal suture on the midsagittal plane
4	Occipital point 1	The most posterior point on the external occipital crest
5	Lateral Nasal Point	The most lateral point of the external snout
6	Inner canthal point	The most medial point of the margin on the eyelid
7	Outer canthal point	The most lateral point of the margin of the eyelid
8	Orbital Point	The most superior and medial point of the orbit
9	Tympanic point	The most inferior point of the tympanic process in the midsagittal plane.
Axial Cranial Cephalometric Points		
10	Posterior Nasal Spine 1	The most posterior point of the posterior nasal spine on an axial slice taken at the point of maximal lens protrusion
11	Occipital point 2	The most posterior point on the occipital bone, measured in the axial plane
12	Internal Nasal Point	The most lateral point of the nasal cavity
13	External lens point	The post lateral point of the lens
14	Temporal point	The most lateral point on the temporal bone from the midsagittal plane
15	Superior orbital point	The most superior point of the orbit
16	Lateral Orbit point	The most lateral point of the orbit
17	Inferior Orbit point	The most inferior point of the orbit
Maxillary Cephalometric Points		
18	Incisive foramen lateral point	The most lateral point of the incisive foramen
19	Key ridge point	Most lateral point of the maxilla at the join of the maxilla and zygoma
20	U6 mesial point	most anterior point of the U6 molar
21	Zygomatic point	The most lateral and inferior point of the zygomatic arc
22	U8 distal point	most posterior point of the U8 molar
23	Posterior Nasal Spine 2	The most posterior point of the posterior nasal spine on an axial slice at the midpoint of the philtrum

Dental Cephalometric Points		
24	Inferior incisor, inferior point	The most superior tip of the inferior incisor
25	Inferior incisor, superior point	The most posterior point of the inferior incisor.
26	Superior incisor, inferior point	The most posterior point of the superior incisor.
27	Superior incisor, superior point	The most inferior tip of the superior incisor
Mandibular Cephalometric Points		
28	Condylion point	The most posterior and superior point on the mandibular condyle
29	Gonion point	The most posterior point of the spinalis of the bony contour of the conial angle of the mandible
30	Gnathion	Lowest angle of mandible
31	Mandibular alveolar point	The deepest point on the upper part of the mandibular alveolar crest between the lower incisor and the first lower molar.
32	Menton point	The most inferior point of the mandibular ramus
33	Inferior incisive alveolar point	The most inferior edge point on the vestibular marginal alveolar bone of the lower incisor

*: refers to numbers shown in **Figure 1**

Table 1: Description of cephalometric points used for analysis.

A total of 33 anatomical landmarks are selected and described for cephalometric measurements. These anatomical points are identified in the surface, axial, and parasagittal planes. Figurative depictions of each point are illustrated in Figure 1. Various interpoints distance are measured based on these landmarks to explore the craniofacial morphology of the control ($ET_B^{+/+}$ and $ET_B^{+/-}$) and *sl/sl* ($ET_B^{-/-}$) rats.

Number*	Measurement	Description
Surface Cranial Cephalometric Measurements		
1	Total skull length	Distance between the occipital point (4) and internasal point (1)
2	Surface Cranial Length	Distance between the occipital point (4) and nasofrontal point (2) following the curvature of the skull.
3	Surface Nasal Length	Distance between the nasofrontal point (2) and internasal point (1)
4	Surface Nasal Width	Distance between the two lateral nasal points (5)
5	Inner inter-canthal distance	Distance between the inner canthal points (6)
6	External interorbital width	Distance between the two orbital points (8)
7	Outer inter-canthal distance	Distance between the outer canthal points (7)
Sagittal Cranial Cephalometric Measurements		
8	Maximum skull height	Distance between the tympanic point (9) and the frontoparietal point (3)
Axial Cranial Cephalometric Measurements		
9	Axial Skull length	Distance between the occipital point 2 (11) and the internasal point (1)
10	Axial Intracranial Length	Distance between occipital point 2 (11) and posterior nasal spine point (10)
11	Nasal cavity Length	Distance between the posterior nasal spine (10) and the intranasal point (1)
12	Nasal cavity Width	Distance between the two internal nasal points (12)
13	Interlens distance	Distance between the two external lens points (13)
14	Intracranial width	Distance between the two temporal points (14)
15	Orbit length	Distance between the superior orbital point (15) and the inferior orbital points (17)
16	Orbit Width	Distance between the occipital point (8) and the lateral occipital point (16).
17	Orbit Circumference	Distance measured between the superior, lateral, inferior and medial orbit points, following the border of the orbit.
Maxillary Cephalometric Measures		
18	Maxillary Length	Distance between the posterior nasal spine 2 point (23) and the internasal point (1)
19	Maxillary width	Distance between the two key ridge points (19)
20	Incisive foramen width	Distance between the two lateral incisive foramen points (18)
21	U6 width	Distance between the two U6 mesial points
22	Interzygomatic width	Distance between the two zygomatic points (21)
23	U8 width	Distance between the U8 distal points (22)
24	intermolar length	Distance between the U8 distal point (22) and the U6 mesial point (21)

Dental Cephalometric Measurements		
25	Superior Incisor length	Distance between the superior incisor superior point (27) and superior incisor inferior point (26), following the curve of the incisor
26	Inferior incisor length	Distance between the inferior incisor superior point (25) and inferior incisor inferior point (24), following the curve of the incisor
Mandibular Cephalometric Measurements		
27	Ramus height	Distance between the Condylion point (28) and the gnathion point (30)
28	Mandibular Length	Distance between the Condylion point (28) and the inferior incisive alveolar point (33)
29	Corpus Height	Distance between the Menton point (32) and the mandibular alveolar point (31)
30	Corpus length	Distance between the gnathion point (30) and the inferior incisive alveolar point (33)
31	Mandibular plane angle	The angle at the gnathion point (30) bounded by the Gonion point (29) and the inferior incisive alveolar point (31)

*: refers to numbers listed in **Figure 2**.
(): bracketed numbers in the measurement description refer to anatomical landmarks described in **Table 1** and **Figure 1**.

Table 2: Description of cephalometric measurements.

A list of 31 cephalometric dimensional measurements made in different planes with figurative reference in Figure 2. The reference points of each dimensional measurements are defined in Figure 1 and Table 1. These measurements made in *sl/sl* and the control group are compared to delineate potential impact of ET_B mutation on cranial morphology.

Rat	Genotype	Rat number (n)	Average Weight (g)
Control group	$ET_B^{+/+}$ & $ET_B^{+/-}$	5	13.1552
sl/sl	$ET_B^{-/-}$	5	11.4029

Table 3: Basic characteristics of study population.

A total of 10 rats are selected, with an average age of 88 hours. The control group consist of wild type ($ET_B^{+/+}$) and heterozygotes ($ET_B^{+/-}$). On average, the five control rats have larger bodyweight than five *sl/sl* rats, 13.1552g versus 11.4029g.

Craniofacial measurement	Control		Spotting-lethal		Spotting-lethal/Control Ratio	Dahlberg error*	Student's t test
	Mean (mm)	Sd (mm)	Mean (mm)	Sd (mm)			
Surface measurements							
Surface skull length	23.318	0.554	22.778	1.276	98.23%	0.210	0.411
Surface nasal length	10.062	0.395	8.729	0.849	86.75%	0.859	0.013
Surface nasal width	7.994	0.275	7.625	0.470	95.38%	0.649	0.168
Surface Interorbital width	5.735	0.515	5.331	0.553	92.96%	0.587	0.266
Inner canthal distance	8.365	0.243	8.248	0.125	98.60%	0.109	0.414
Outer canthal distance	12.191	0.585	11.749	0.404	96.37%	0.255	0.242
Sagittal Measurements							
Maximal skull height	11.887	0.458	11.567	0.276	97.31%	0.339	0.217
Axial Measurements							
Axial skull length	22.21	0.819	21.391	0.379	96.31%	0.419	0.77
Intracranial length	12.424	0.648	11.959	0.469	96.25%	0.429	0.23
Intracranial width	11.134	0.265	10.756	0.397	96.60%	0.580	0.114
Nasal cavity length	9.786	0.297	9.432	0.340	96.38%	0.278	0.118
Nasal cavity width	5.713	0.346	5.464	0.309	95.64%	0.239	0.265
Axial interorbital width	3.696	0.105	3.543	0.263	95.86%	0.278	0.262
Interzygomatic width	12.244	0.344	11.583	0.577	94.60%	0.318	0.059

* Dahlberg errors were given for standalone measurements. Errors were unable to be calculated for averaged data.

Table 4: Detectable morphological difference between the control ($ET_B^{+/+}$ and $ET_B^{+/-}$) and *sl/sl* ($ET_B^{-/-}$) rats.

Surface anatomical measurements showed *sl/sl* group having shorter skull and reduced size in facial features including surface nasal length, surface nasal width, interorbital width, and inner and outer inter-canthal distance. Similar trends are observed and verified by the measurements made in axial and sagittal planes on the following: skull height, intracranial length, intracranial width, nasal cavity length, nasal cavity width, interorbital width and interzygomatic width. Overall, approximately 5% reductions are observed across all dimensional measurements except surface nasal length, which exhibits 14% reduction.

Maxillary-facial measurement	Control		Spotting-lethal		Spotting-lethal/ Control Ratio	Dahlberg error*	Student's t test
	Mean (mm)	Sd (mm)	Mean (mm)	Sd (mm)			
Orbital Measurements							
Interlens distance	10.873	0.439	10.14	0.303	93.26%	0.101	0.015
Average orbit length	3.715	0.063	3.64	0.116	97.99%	-	0.244
Average orbit width	3.325	0.153	3.324	0.157	99.97%	-	0.992
Average orbit circumference	11.012	0.309	10.668	0.359	96.88%	-	0.143
Maxillary Measurements							
Maxillary length	11.007	0.540	10.506	0.557	95.45%	0.350	0.187
Maxillary width	6.444	0.496	6.113	0.272	94.86%	0.552	0.227
Incisive foramen width	2.031	0.114	1.941	0.061	95.57%	0.083	0.159
U6 intermolar width	5.886	0.076	5.624	0.105	95.55%	0.155	0.002
U8 intermolar width	6.186	0.167	5.851	0.152	94.58%	0.235	0.011
Average molar plate length	4.847	0.180	4.582	0.169	94.55%	-	0.044
Mandibular Measurements							
Average mandibular length	10.581	0.114	10.354	0.347	97.85%	-	0.202
Average ramus height	4.392	0.129	4.264	0.214	97.09%	-	0.286
Average corpus length	9.503	0.246	9.343	0.242	98.31%	-	0.329
Average corpus height	1.514	0.129	1.483	0.135	97.92%	-	0.716
Average mandibular plane angle	99.6	5.897	97.106	3.521	97.50%	-	0.440
Dentition Measurements							
Average superior incisor length	2.762	0.299	2.463	0.204	89.17%	-	0.102
Average inferior incisor length	4.131	0.299	4.383	0.276	106.11%	-	0.203
Dentition Number	**Control**				**Spotting-lethal**		
Average no superior molar	6				6		
Average no inferior molar	6				6		

Table 5: Orbital and maxillary-facial reductions were associated with *sl/sl* rats.

In addition to minor changes in orbital and mandibular dimensions, multiplane measurements demonstrate approximately 5% size reductions in maxilla and molar plate of *sl/sl* rats. While both control and *sl/sl* groups have equal number of molar teeth in upper and lower quadrants, *sl/sl* rats have ~10% smaller superior incisor and 6% larger inferior incisor than those of control rats. These findings support ET_B exerts minor modulatory effect on facial morphogenesis.

Organ dimensional ratio	Control	Spotting lethal	Spotting-lethal/ Control *100%
Intracranial width/intracranial length (axial)	0.896	0.899	100.36%
Skull height/Skull length (sagittal)	0.413	0.393	95.23%
Surface nasal length/Skull length	0.357	0.315	88.31%
Surface nasal width/surface nasal length	0.794	0.874	109.95%
Maxillary width/Maxillary length	0.315	0.317	100.74%
Mandibular length/Skull length	0.375	0.373	99.61%
Mandibular corpus height/Mandibular length	0.160	0.159	99.60%
Mandibular ramus/Mandibular length	0.415	0.412	99.21%
W index	3.245	3.328	102.56%

Table 6: Organ dimensional ratios showed *sl/sl* rats having a flatter cranium and a shorter but wider muzzle.

Changes in structural morphology are shown by disproportional dimensional changes in *sl/sl* rats based on the following ratios: skull height/skull length (~5% reduction), surface nasal length/skull length (~12% reduction), and surface nasal width/surface nasal length (~10% increase). On the other hand, trivial difference is seen between the control and *sl/sl* rats in maxillary and mandibular dimensional ratios, suggesting structural morphology is preserved despite size reduction. Lastly, W index of *sl/sl* rats is higher than that of control group (p-value = 0.017), supporting the possible presence of dystopia canthorum.

Chapter 4 Supplementary Tables:

Rat	Genotype (ET_B)	Weight at Sacrifice (g)
1	+/+	11.8741
2	-/-	9.0197
3	-/-	12.4492
4	-/-	12.2679
5	+/-	13.9730
6	+/+	13.6915
7	+/-	13.1977
8	+/+	13.0398
9	-/-	10.4376
10	-/-	12.8401
Wild-type average	**+/+**	**12.8685**
Heterozygotes	**+/-**	**13.5854**
Control group average	**+/+ and +/-**	**13.1552**
***sl/sl* average**	**-/-**	**11.4029**

Supplementary Table 1: Basic characteristics of study rat population.

A total of 10 rats are selected, with an average age of 88 hours. The control group consists of wild type ($ET_B^{+/+}$) and heterozygotes ($ET_B^{+/-}$). In general, control group has larger bodyweight than *sl/sl* ($ET_B^{-/-}$) rats.

Chapter 5: Brain size reductions associated with endothelin B receptor mutation, a cause of Hirschsprung's disease

Chapter 5 Highlights

- $ET_B^{-/-}$ HSCR is associated with body growth impairment; neonatal *sl/sl* rat has 16% less bodyweight than the control group.
- *sl/sl* rat has a grossly normal cranial morphology.
- Significant reductions are detected in the brain *sl/sl* rats: 20.33% in brain volume and 7.35% in brain growth rate. Similar reductions are seen in cerebral cortex, caudate putamen, olfactory bulb, medulla, and pituitary gland.
- Minor changes in cerebellum and superior/inferior colliculus despite overall body-size reduction hint potential regional-dependent neuroprotection by ET_B mutation, possibly through differential vasoregulation.
- No consistent gene dose effect is seen between ET_B genotype and brain growth.
- These animal findings, if extrapolatable to human, suggest that $ET_B^{-/-}$ HSCR patients may have increased risks for reduction in intracranial volume and possible associated neurological impairment; wholistic post-operative care may be considered.
- In consideration of the result of this paper, genetic counselling, and familial screen for HSCR patients may be beneficial.

Chapter 5 Abstract

Background
ET_B has been reported to regulate neurogenesis and vasoregulation in foetal development. Its dysfunction is known to cause HSCR, an aganglionic colonic disorder with syndromic forms reported to associate with both small heads and developmental delay. We therefore ask, "is CNS maldevelopment a more general feature of ET_B mutation?" To investigate, we review the micro-CT scans of $ET_B^{-/-}$ model animal, *sl/sl* rat, and quantitatively evaluated the structural changes of its brain constituents.

Methods
Eleven neonatal rats generated from $ET_B^{+/-}$ cross breeding were sacrificed. Micro-CT scans were completed following 1.5% iodine staining protocols. All scans were reviewed for morphological changes. Selected organs were segmented semi-automatically post-NLM filtering: TBr, T-CC, T-CP, OB, Med, Cer, Pit, and S&I Col. Volumetric measurements were made using Drishti rendering software. Rat genotyping was completed following analysis. Statistical comparisons on organ volume, organ growth rate, and organ volume/bodyweight ratios were made between *sl/sl* and the control groups based on autosomal recessive inheritance. One-way ANOVA was also performed to evaluate potential dose-dependent effect.

Results
sl/sl rat has 16.32% lower bodyweight with 3.53% lower growth rate than the control group. Gross intracranial morphology is preserved in *sl/sl* rats. However, significant volumetric reduction of 20.33% is detected in TBr; similar reductions are extended to the measurements of T-CC, T-CP, OB, Med, and Pit. Consistently, lower brain and selected constituent growth rates are detected in *sl/sl* rat, ranging from 6.21% to 11.51% reduction.
Lower organ volume/bodyweight ratio is detected in sl/sl rats, reflecting disproportional neural changes with respect to body size. No consistent linear relationships exist between ET_B copies and intracranial organ size or growth rates.

Discussion
Although $ET_B^{-/-}$ mutant has a normal CNS morphology, significant size reductions in brain and constituents are detected. These structural changes likely arise from a combination of factors secondary to dysfunctional ET-1/ET-3/ET_B signalling, including global growth impairment from HSCR-induced malnutrition and dysregulations in the neurogenesis, angiogenesis, and cerebral vascular control. These changes have important clinical implications, such as autonomic dysfunction or intellectual delay. Although further human study is warranted, our study suggest comprehensive managements are required for HSCR patients, at least in $ET_B^{-/-}$ subtype.

Key Words: neuroanatomy, Endothelin-B mutation, neural impairment, spotting-lethal rat, Hirschsprung disease

1. Introduction

Endothelin receptor B (ET_B) is a widely expressed seven-transmembrane G-protein coupled receptor (GPCR) with multiple regulatory controls on embryological development, vasoregulation, and endothelin metabolism (9, 534-536). Although ET_B mutation has been well documented to cause Hirschsprung's disease (HSCR), a paediatric intestinal disease affecting 1/5000 live births, we suspect concurrent intracranial changes is also likely due to the impaired neurogenesis (9, 21, 380). In this study, we evaluate the neuroanatomical changes associated with ET_B mutation by studying the changes detected in spotting-lethal (*sl/sl*) rat, a HSCR animal model. We hope these findings can provide additional evidence to support ET_B's importance on anatomical development and the notion that HSCR is likely a multi-organ disease, at least in $ET_B^{-/-}$ subtype.

Although HSCR is best known for its clinical manifestations of intestinal dilatation and toxic megacolon sequelae, multi-organ dysfunctions have also been documented (188, 537). Indeed, clinical impairments of central nervous system and autonomic system have been exemplified by HSCR-associated syndromes, including Down syndrome, Waardenburg-Shah syndrome (WS-IV), Haddad syndrome, Goldberg-Shprintzen, and Smith-Lemli-Opitz syndrome (10, 21, 31, 127, 538). This is partially attributable to the polygenetic causes of HSCR, including mutations in several common genes: proto-oncogene RET (RET), glial cell line derived neurotrophic factor (GDNF), endothelin B-receptor (ET_B), endothelin-3 (ET-3), SOX10, endothelin converting enzyme-1 (ECE-1), neurturin (NTN), and Smad interacting protein 1 (SIP1) genes (109, 127). Among these, RET mutations are the most common, accounting for 50% of familial cases and 15-20% of sporadic cases of HSCR. This is followed by the mutations in ET_B (5%) and ET-3 genes (<5%) (109, 539). Puffenberger *et al* (1994), however,

demonstrated a W276C missense mutation in ET_B gene of an inbred kindred can result in 74% and 21% risks for HSCR development in homozygotes and heterozygotes, respectively (113). This suggested potential dose effect of ET_B and the likely underestimation in its true impact on HSCR and embryological development, possibly due to ET_B's multi-regulatory functions. This notion is further supported by the increasing identifications of novel ET_B mutations and polymorphism in sporadic HSCR patients, which further emphasizes its developmental importance (147, 148).

Endothelin receptors (A and B; abbreviated respectively as ET_A and ET_B) have been reported to involve in the neurogenesis of both central and peripheral nervous systems. Mutations in endothelin receptors and endothelin (1, 2, and 3; abbreviated respectively as ET-1, 2, and 3) can cause defective embryonic development in neural crest derived structures, in particular melanocytes and enteric nervous systems (ENS) from ET_B mutations (354). Although the importance of ET-3/ET_B signalling for migrating neural crest cells for ENS development is well documented, maintaining the pluripotency of neural crest cells, its impact on the development of central nervous system remains unclear (151, 540). As previously shown, ET_B is widely expressed in mammalian brains, including medulla oblongata, cerebral cortex, hippocampus, cerebellum, and striatum (541-544). Similar distribution is shared by ET-1 and ET-3 (545). Their co-expressions, therefore, are likely to reflect an undocumented importance.

ET_B activation by the endothelin mediates vasoregulation, smooth muscle contractions, neuropeptide transmission, neuronal apoptosis, and potential autonomic control (166, 546, 547). Past studies showed that the ET_B mutations and variants have strong

links to hearing deficit, mental retardations, and microcephaly (9, 414). Concordantly, Yuen et al (2013) demonstrated marked ET_B upregulation in the oligodendrocytes of active multiple sclerosis tissue during remyelination, suggesting an active role in neuromodulation. Further studies using rat cerebellar cultures showed ET_B agonist (BQ-3020) and antagonist (BQ-788) promotes and inhibits the remyelination processes, respectively (548). Although no significant difference in oligodendrocyte number is detected between the control and ET_B-knockout mice, Swire et al (2019) reported significantly reduced myelin sheaths in ET_B-deficient oligodendrocytes. This phenotypically coincides with the decreased sociability among the affected animals (549). Furthermore, increased neuronal apoptosis have also been detected in the dentate gyrus, hippocampus, and cerebellum of ET_B deficient animals (550-552). These reports therefore suggested that ET_B exerts a positive impact on neurogenesis.

On the other hand, several reports have suggested ET_B inhibition may be beneficial for remyelination, possibly through its regulation on astrocyte proliferation and vascular control. Back et al (2005) reported that high molecular weight hyaluronan produced by astrocytes can inhibit oligodendrocyte progenitors (OPCs) maturation, which is vital to remyelination post-injury (553). Consistently, Hammond et al (2015) reported that the inhibition or absence of ET-1/ET_B signalling in astrocytes enables oligodendrocyte progenitor cell maturation and promotes remyelination following brain injury (554). Gadea et al (2008) also demonstrated that the infusion of ET_B antagonist, BQ-788, to rat corpus callosum can suppress the upregulations of reactive astrogliosis following acute demyelination injury. Further studies on cell culture suggested that this ET-1/ET_B activated astrocyte proliferation is mediated by ERK- and JNK- dependent pathways. Inhibitions of these pathways or ET_B

deficiency may therefore be beneficial to myelination (555). Furthermore, Grell et al (2014) and Spray et al (2017) showed ET_B antagonist can suppress cerebral hypoperfusion by inhibiting the vasoconstriction in cerebral arteries. Together, these studies suggested $ET_B^{-/-}$ mutants may exhibit neuroprotection through the absence of ET_B signalling (556, 557). Given the omnipresence of ET_B and its obvious multimodal actions on neural structures and functions, we adopt a macroscopic approach to investigate its effect on brain anatomy and growth.

Prior cell culture studies have suggested possible bimodal actions of ET_B on myelination. Although increased neural apoptosis has been reported in ET_B deficient animals using immunohistochemistry methodology, to the best of our knowledge, no macroscopic analysis has been completed to evaluate the intracranial changes associated with ET_B mutations or HSCR. At most, one anecdotal inference was made from a cohort study showing the regional prevalence of intracranial abnormalities associated with Mowat-Wilson syndrome, a HSCR-associated syndrome caused by mutations in *ZEB2* gene; however, no direct comments have been made on the physical brain size (558). We aim to complement previous studies with further anatomical evidence to support ET_B's importance on the brain development and to clarify potential correlation between HSCR and intracranial changes.

In this study, we have chosen *sl/sl* rat as the study subject. It is a naturally occurred $ET_B^{-/-}$ animal model analogous to human WS-IV syndrome with the following characteristics: HSCR, hypopigmentation, and congenital hearing loss (413). Confirmatory study showed a deletion of 301-bp spanning at the junction between exon1 and intron1 of the ET_B gene leads to a defective G-protein-coupled receptor and thus *sl/sl* rat (413, 414). Segregation analysis

from our rat colony data (n=475) showed *sl/sl* rat follows autosomal recessive inheritance (*p-value* = 0.001) with 95% genetic penetrance for HSCR phenotype, supporting *sl/sl* rat as a good candidate for studying the phenotype of ET_B mutation.

To examine neuroanatomical difference between *sl/sl* rat and the control group, image acquisitions are performed using X-ray micro-computed tomography (micro-CT) and previously described tissue preparation protocols (435). Thorough review on the brain morphology is made and followed by volumetric measurements of selected brain structures. Because neonatal *sl/sl* rat has not reached growth maturity and may suffer HSCR-induced growth impairment, organ growth rate and organ volume/bodyweight ratios are also determined for further comparison.

In this study, we hypothesize the following:

1. Gross intracranial morphology may be preserved in $ET_B^{-/-}$ animals.
2. Reductions in the brain and constituent sizes may be presented in $ET_B^{-/-}$ animals with respect to those of the control group ($ET_B^{+/+}$ & $ET_B^{+/-}$). This reducing trend may also extend to the organ growth rate and organ volume/bodyweight ratios of $ET_B^{-/-}$ animals.
3. Non-uniform anatomical changes associated with homozygous ET_B mutation may be presented across different neural constituents; effect of ET_B mutation on neuroanatomy may be regional-dependent.

2. Methods

2.1. Compliance with ethical practice

All tissues and animals used in this study were handled with strict compliance to both approval bodies: Australian Capital Territory Health-Human Research Ethics Committee (ACTH-HREC) and Australian National University-Animal Experimentation Ethics Committee (ANU-AEEC), approval project number A2011/67.

2.2. Rat culling and method of euthanasia

Rat samples were generated from cross breeding the heterozygous rats ($ET_B^{+/-}$). The breeding colony was initially derived from a naturally occurring mutation; this colony has been maintained in the Australian National University (ANU) over the past 15 years.

Eleven neonatal rats were sacrificed in this study, with an average age of 88 hours. Each rat was anaesthetized with 5% isoflurane for 15 minutes and culled via abdominal aortotomy. The age, gender, weight, and colonic appearance were recorded prior to staining. Five-millimetre tail tip of each rat was removed and stored for subsequent genotyping.

2.3. Tissue preparation and diffusion staining protocols

Following the culling, rats' heads were isolated from the neck and up in preparation for micro-CT scanning. To ensure successful tissue staining, a diamond-shaped craniotomy in parietal bone was created through the following: five-millimetre cross-incision through the skull using a dissection scalpel followed by diagonal excisions of skull using iris scissors.

Following craniotomy, these tissues were immersed in 10% PBS solution for 30 minutes to wash out residual body fluid. This was followed by tissue fixation in 4% formalin solution for 24 hours. Next, the formalin was washed out with graded ethanol (EtOH) series

over four days: 20%, 50%, 70%, and 90% for 1 day each. This tissue preparation was finalized by seven days of staining with 1.5% iodine solution in 90% EtOH.

2.4. Image acquisition by micro-CT scanning

All micro-CT datasets of the rats were acquired using a commercially available Caliper Quantum FX *in vivo* micro-CT scanner. At the expense of 4.5 minutes scanning time per scan, acquired *in vivo* micro-CT data has an image resolution of 20 µm/voxel. The resultant images were stored as DICOM series with average dataset size of 256MB.

Prior to quantitative analysis, images of *in vivo* micro-CT scans were validated with two sets of *ex vivo* micro-CT scans for quality control. The *ex vivo* micro-CT scans were acquired by scanning two of the eleven rat tissues using custom-built micro-CT system at the Applied Mathematic Department of Australian National University. Because *ex vivo* micro-CT scans have significantly higher signal-to-noise ratio than *in vivo* micro-CT images, they provided good reference for image quality control; however, accesses to *ex vivo* micro-CT scanner were limited. *Ex vivo* micro-CT data with resolution of 10.7 µm/voxel required fifteen hours of scanning time with additional eight hours of image processing time via National Computational Infrastructure (NCI) services. The resultant images were stored as netCDF files with each dataset size of 12 GB. All datasets were visualized and analysed with FIJI and Drishti, opensource image rendering software (453, 456).

2.5. Image segmentation and volumetric measurements

All acquired *in vivo* micro-CT raw data were denoised using non-local-means (NLM) algorithms to improve signal-to-noise ratio and hence image clarity for segmentation (559).

This code was implemented on a computing server built from Intel (R) Core ™ i7-4770K CPU @3.5GHz with 32GB of RAM and Nvidia GeForce GTX Titan Black Kepler GK110 architecture running Linux.

Following image denoising, micro-CT images were segmented semi-automatically through individual CT-slices for organs of interest using Drishti paint. This segmentation was verified by two operators. A number of neural organs were selected based on prior literature and organ differentiation on micro-CT scan: total brain (TBr), total cerebral cortex (T-CC), total caudate putamen (T-CP), olfactory bulb (OB), medulla (Med), cerebellum (Cer), pituitary gland (Pit), and superior and inferior colliculus (S&I Col). The posterior border of TBr was standardized to 1st cervical spine for comparison across different samples. Cerebral cortex and caudate putamen were segmented and analysed in respective left and right hemispheres prior to amalgamation of measurements. Superior and inferior colliculus were measured together due to poor differentiation between the two regions on micro-CT scans.

Lastly, the segmented data were rendered, visualized, and volumetrically measured with Drishti for volumetric exploration and presentation (453).

2.6. H&E light microscopy

H&E light microscopy was completed for two of eleven rats following micro-CT scanning for verification of neuroanatomical detail presented by micro-CT scans. The tissue processing was conducted in the following steps. The iodine-stained tissues were sectioned longitudinally into blocks of 4mm in thickness and placed in cassettes. Contrast washout and dehydration were then performed in 90% EtOH for 48 hours prior to paraffin embedment at

60°C. Next, the samples were sliced with a microtome for tissue sheets of 4 µm in thickness. These tissue sheets were then laid in water bath of 5-6°C while being positioned onto pre-labelled glass slides. These slides were dried overnight at 37°C.

Progressive H&E staining was then performed. The slides were placed in alum-hematoxylin solutions until visualization of dark red colour. This was followed by washing and 'bluing' with lithium carbonate solution. Finally, the slides were washed before counter-stained with 0.5% eosin alcoholic solution.

All H&E slides were examined with an Olympus IX71 microscope with 4x magnification.

2.7. Genotyping

Genotyping was completed following the completion of the quantitative image analysis of rat data to avoid observational bias. It was completed by standard PCR methods. Three wild types ($ET_B^{+/+}$), three heterozygotes ($ET_B^{+/-}$), and five *sl/sl* ($ET_B^{-/-}$) rats were identified. The average ages of wild type, heterozygotes, and *sl/sl* groups were 90.7 hours, 96 hours, and 83.2 hours, respectively.

PCR genotyping was processed through the following. Five-millimetre tail tips from each of the eleven rats were isolated for lysis using Proteinase K in lysis buffer, which consisted of 100mM Tris pH 8, 5mM EDTA, 0.2% SDS, and 200mM NaCl in distilled water. The DNA was extracted via vortex heating and centrifuging to separate DNA-containing supernatant from the undigested materials. Afterwards, the supernatant was further

vortexed and centrifuged to isolate the DNA pellet, followed by 70% EtOH washing and drying. The DNA was then suspended and quantified with spectrophotometry. Next, PCR was completed with "Master-Mix" reagent: 10*PCR buffer Qiagen-contained MgCl2, dNTP (10mM), Primer PS7 (33.3µM; 5'-CCA CTA AGA CCT CCT GGA CT-3'), Primer PS15 (33.3µM; 5'-TCA CGA CTT AGA AAG CTA CAC T-3') and DNA polymerase (515). The Master-Mix reagent was then pipetted onto PCR plates with fourteen rat DNAs (including the known controls) and placed in Veriti 96-Well Thermal-Cycler for PCR. Lastly, electrophoresis was run at 100V and 55mA for 1 hour. Eleven test-subject DNAs were run against positive controls for wild-type, heterozygote, and *sl/sl* with molecular weight marker (MassRuler, #SM1263, Fermentas) by the side. Electrophoresis gel was visualized with Gel Documentation System DOC-Print VX5 (Vilber Lourmat).

2.8. Comparison and Statistical analysis

Based on segregation analysis on cumulative colony data, *sl/sl* rat phenotype followed autosomal recessive inheritance (*p-value* = 0.001) with high genetic penetrance, up to 95% of *sl/sl* rat exhibited HSCR. Statistical comparisons were made between *sl/sl* ($ET_B^{-/-}$) and the control group ($ET_B^{+/+}$ & $ET_B^{+/-}$) to determine the effect of ET_B on structural changes and growth. This approach was consistent with the autosomal recessive inheritance of human WS-IV, a disease caused by $ET_B^{-/-}$ genotype. Nonetheless, we also performed one-way ANOVA analysis and post hoc Tukey to assess the potential relations between ET_B gene dose and the following selected parameters.

The parameters included for comparison were as follow: bodyweight (g), bodyweight growth rates (g/Hr), organ volume (mL), organ volume growth rates (mL/Hr), and organ

volume/bodyweight ratios (mL/g). The bodyweight growth rate (g/Hr) was calculated by dividing each rat's bodyweight (g) to its respective age (Hr) at culling; these were followed by statistical comparison between the control and mutant groups. Similarly, organ volume growth rate (mL/Hr) and organ volume/bodyweight ratios (mL/g) were calculated from respective volumetric measurements (mL), age (Hr), and bodyweight (g) at the times of culling.

Standardized comparisons of organ volume growth rate and organ volume/bodyweight ratios were made to exclude potential confounding factors of age and body-size variance. Additionally, these measures provided estimating metrics for the organ changes upon developmental maturation of the animals. Moreover, the proportionality of individual neural substituent with respect to the total brain (organ/total brain) was compared to explore potential regional-dependent effect of ET_B. All parameters were expressed as mean +/- sem in figures. The relative parametric difference (%) between *sl/sl* and the control group was also calculated and reported throughout this study for better appreciation on the degrees of difference.

3. Results

3.1. $ET_B^{-/-}$ mutant has lower bodyweight and body growth rate

We compared the bodyweight of the studied animals to evaluate potential growth reduction associated with $ET_B^{-/-}$ mutation. As shown by Figure 1A, *sl/sl* rat has 16.32% lower bodyweight than the control group, *p-value* = 0.03. Although not reaching statistical significance, a 3.53% deduction in growth rate was also detected, Figure 1B. Both findings supported potential impairments in global body growth. On the other hand, one-way ANOVA

demonstrated no significant variability in bodyweight or body growth rate among the three genotypes, as shown by Supplementary Table 1. These observations suggested ET_B mutation may be associated with body growth impairment in an autosomal recessive manner.

3.2. Gross intracranial morphology is overall preserved in $ET_B^{-/-}$ mutant

Previous study has suggested disruptions in the endothelin system can lead to cephalic neural crest cell (CNCC) migration failure and thus marked craniofacial defects (230). However, thorough reviews of *sl/sl* rat scan (Figure 2B) demonstrated grossly normal cranial morphology, similar to that of wild type rat (Figure 2C). As shown by the parasagittal view of micro-CT images and H&E microscopy, Figure 2B – 2D, *sl/sl* rat brain contains all the major components as the control group: accumbens nucleus, anterior olfactory bulb, anterior pons, hippocampus, cerebellum, caudate putamen, frontal cortex, hypothalamus, inferior colliculus, medulla, pituitary gland, posterior thalamus, superior colliculus, and thalamus. Additionally, review of facial anatomy did not reveal obvious disfiguration, as shown by Figure 2A. These suggested intracranial impairments associated with ET_B mutation, if any, may be subtle and limited to size variance rather than constituent agenesis or morphological changes.

3.3. Homozygous ET_B mutation is associated with significant decreases in brain size

While the gross morphology might be preserved, moderate volumetric reductions in the brain and constituents were detected in *sl/sl* mutants. As demonstrated by Figure 3A, a significant reduction of 20.33% was observed in the brain of *sl/sl* rat, *p-value* = 0.02. Furthermore, an average of 20% volumetric reduction was detected across all neural constituents analysed in the *sl/sl* rat. Structures with statistically significant difference

between *sl/sl* and the control groups were as follow: T-CC (24.60%, *p-value* = 0.02); T-CP (24.68%, *p-value* = 0.03); OB (19.13%, *p-value* = 0.02); Pit (30.08%, *p-value* = 0.02). Although not reaching the statistical power, the reducing trend in *sl/sl* rat was also evident in the following: Med (21.05%, *p-value* = 0.11), Cer (14.22%, *p-value* = 0.22); S&I col (9.73%, *p-value* = 0.10).

Additionally, one-way ANOVA showed statistically significant volumetric variation in TB, T-CC, and Pit of the three genotypes, as shown by Supplementary Table 2A. However, post hoc Tukey revealed significant differences were only presented between *sl/sl* and the heterozygous group; consistent ET_B dose-dependent trend was not seen in the wild type, as shown by Supplementary Table 2B.

3.4. Homozygous ET_B mutation is associated with significantly lower intracranial growth rate

Reduced intracranial organ growth rate was observed in *sl/sl* group; however, this margin of reduction was smaller than that detected in the volumetric changes. An approximately 10% reduction in growth rate was observed across various brain components in *sl/sl* rat.

As shown by Figure 3B, the TBr growth rate of *sl/sl* rat was 7.35% lower than that of the control group, *p-value* = 0.07. Consistent decreasing trends were also presented in the following: T-CC (11.42%, *p-value* = 0.04), T-CP (11.51%, *p-value* = 0.05), and OB (6.21%, *p-value* = 0.05). Furthermore, although not reaching the statistical power, similar reductions were observed in the medulla (8.48%, *p-value* = 0.30) and pituitary gland (15.62%, *p-value* =

0.06) of *sl/sl* rat. Unexpectedly, no significant change was detected in the growth rate of Cer (1.60%, *p-value* = 0.85) and S&I Col (2.72%, *p-value* = 0.60). Lastly, no consistent linear relationship was detected between the neural growth rates and ET_B gene dose, as shown by one-way ANOVA analysis in Supplementary Table 3A.

Overall, we found homozygous ET_B mutation was associated with reduced neural growth rate during development, an effect likely to persist until maturation age.

3.5. Homozygous ET_B mutation is associated with lower brain volume/bodyweight indices

sl/sl rat has disproportionally larger reductions in its brain volumes than the decreases in its bodyweight. As illustrated by Figure 3C, *sl/sl* rat has lower organ volume/bodyweight ratios than the control group: TBr (2.60%, *p-value* = 0.57), T-CC (6.21%, *p-value* = 0.15), T-CP (6.30%, *p-value* = 0.27), OB (1.28%, *p-value* = 0.60), Med (3.22%, *p-value* = 0.87), and Pit (11.18%, *p-value* = 0.08). Albeit statistically underpowered, these findings suggested neural development was more sensitive to ET_B dysfunction than the bodily growth. And although homozygous ET_B mutation seemed to predominantly affect growth negatively, *sl/sl* rat was found to have larger organ/bodyweight ratios in its Cer (3.17%, *p-val*ue = 0.47) and S&I Col (6.84%, *p-value* = 0.23). This raised the possibility that a potential protective mechanism associated with $ET_B^{-/-}$ may be presented, albeit this protective effect was likely small. Additionally, non-uniform changes were recorded from different neural structures of *sl/sl* rat, suggesting the impact of ET_B mutation on anatomical development may be dependent on organ location.

3.6. $ET_B^{-/-}$ mutant has subtle and non-uniform changes across different neural constituent/total brain indices

As showed by Figure 3D, *sl/sl* rat and the control group shared subtle difference between their respective neural organ/TBr indices. Although these differences may be small, ranging from 2 to 8%, they reflected disproportional changes in different neural constituents of $ET_B^{-/-}$ rat. These variations suggested that the effect of ET_B on structural growth may be influenced by the target organ locations within the brain.

4. Discussion

As evidenced by the anatomical changes detected, we support the notion that homozygous ET_B mutation and associated HSCR are likely linked with intracranial changes, at least in the sense of volumetric measurements. This finding is consistent with previous *in vitro* studies and clinical reports citing HSCR's associations with neurological deficits, as exemplified by Down's syndrome, Haddad syndrome, Mowat-Wilson syndrome, and WS-IV (9, 28, 530, 537, 560, 561).

It has been suggested that disruption in ET-1/ECE/ET_A pathway system can lead to marked craniofacial dysmorphism. (230). Additionally, agenesis of corpus callosum and hippocampus have also been reported in HSCR associated syndromes (561, 562). Regardless, these gross abnormalities are not detected in *sl/sl* rat, as demonstrated by Figure 2. This observation suggests that while ET_B mutation may disrupt enteric neural crest cell migration, its direct impact on the migration of cephalic and vagal neural crest precursors may be limited. On the other hand, neurogenic modelling mediated by ET_B signalling and the clinical reporting of HSCR-associated mental retardation support the notion that ET_B may possess an

adjunct but important role in neural development (535, 563). Quantitative analysis on the neuroanatomy is therefore an intuitive investigation.

Many previous studies demonstrate ET_B receptors in olfactory bulb, cerebral cortex, caudate putamen, thalamus, hypothalamus, pituitary gland, brain stem and limbic system through a combined use of immunohistochemistry and ET_B's agonist or antagonists; this omnipresence suggests ET_B's likely importance in brain structures and functions (564-567). Indeed, two-dimensional (2D) immunofluorescence studies demonstrate that ET_B stimulation by IRL-1620 can lead to neurogenic remodelling, which is likely achieved by the increased neurogenesis and angiogenesis through upregulating vascular endothelial growth factor (VEGF) and nerve growth factor (NGF) (402, 534, 535). Furthermore, activation of endothelial ET_B by ET-1 triggers vasodilation in basilar artery by increasing the production of nitric oxide (568); this ultimately improves cerebral perfusion. Consequently, these studies support the notion that ET_B activation promotes neuroprotection. This is indeed consistent with the overall brain size reduction observed in *sl/sl* rat, which lacks functional ET_B during its development. On the other hand, *in vitro* studies using U0126, a mithramycin A (MitA) or mitogen-activated protein kinase (MEK) 1/2 inhibitor, blocks the elevation of ET_B-mediated vasoconstriction following cerebral ischemic events, thus suggesting ET_B stimulation in vascular smooth muscle cells (VSMC) may worsens neural damage (322, 556, 569) by triggering further cerebral hypoperfusion. These conflicting findings suggest ET_B's effect on brain growth may be dynamic and regional-dependent, a pattern consistent with our finding, Figure 3D, showing variability in organ changes with respect to the global brain size reduction.

Despite the preservation of a grossly normal brain morphology, a significant structural reduction of 20.33% (*p-value* = 0.02) is found in the brain volume of neonatal *sl/sl* rat. Consistently, a reduction of 7.35% (*p-value* = 0.07) in brain growth rate also suggest its structural impairment may likely worsen upon developmental maturity. Several factors can contribute to these impairments. As previously reported by McDougall et al (2017), intrauterine growth restriction alters the postnatal cerebellum development (570). Although we did not detect an underdevelopment in the birthweight of *sl/sl* rat from our colony data of 864 rats, we did find a bodyweight reduction of 16.32% at the age of 88 hours in our studied rats, Figure 1. This may be explained by the fact that adequate maternal uterine perfusion can be achieved through ET_B-mediated vasodilation in the heterozygous parents (571); however, postnatal growth of *sl/sl* rat may deteriorate due to HSCR-induced malnutrition and $ET_B^{-/-}$-mediated mesenteric hypoperfusion (9, 283). Furthermore, disproportionally larger reductions in *sl/sl* rat brain size with respect to its bodyweight changes suggest additional intrinsic ET_B mechanisms on the brain development, Figure 3C. Indeed, *sl/sl* rat has 1.26% to 11.18% smaller organ volume/bodyweight indices in TBr, T-CC, TCP, OB, Med, and Pit. On the other hand, Cer and S&I Col of *sl/sl* rat have 3.17% and 6.84% higher indices, respectively. Consistent with ET_B's functional duality on vasoregulation and neurogenesis reported previously, our observations likely reflect a potential regional-specific neuroprotection by ET_B mutation despite its overwhelming negative effects (402, 535, 550-552, 554, 556, 568).

Dysregulation in the neurogenesis, angiogenesis, and cerebral vascular tone likely contributes to the observed structural changes in *sl/sl* rat. This may be mediated directly by the ET_B expression on neuroblasts or neural tissue, which promotes cell division and inhibits

apoptosis, or by indirect mechanisms including vascular growth stimulation and vasospasm inhibition. Indeed, Nishikawa et al (2011) reported that ET_B-stimulation by IRL-1620 accelerates interkinetic nuclear migration (INC) of cortical neural progenitor cells (NPC), whereas inhibition by BQ-788 decelerates INC migration and subsequent NPC mislocalization (572). Additionally, intracerebroventricular ET_B stimulation increases the vascular endothelial growth factor A (VEGF-A), thereby triggering VEGF-receptor signalling in cerebrum but not hippocampus. This suggests regional-dependent neuroprotective effect of ET_B, possibly via vascular control (573). Moreover, sl/sl rat has significantly elevated ET-1 level due to dysfunctional clearance; this may further exacerbate ET-1/ET_A-mediated hyper-vasoconstriction in cerebral vasculature (381). Albeit minor, endothelial-mediated basal vasodilation from ET-1/ET_B stimulation is also lost in *sl/sl* rat (189, 536). Together, these impaired neurogenesis and cerebral perfusion retard cerebral growth. Conversely, small elevation in Cer/bodyweight and S&I Col/bodyweight indices lend some support that regional brain development of *sl/sl* rat may benefit from to reduced ET_B-mediated vasoconstriction, for instance, in the VSMC of collicular artery (556). However, this mutation-associated beneficial effect is likely minor when comparing to the dominant ET-1/ET_A effect (556, 569, 574).

If our finding is extrapolatable to human subjects, then the observed structural impairments may lend some supports to several HSCR-associated clinical anomalies. For instance, marked reductions in total brain (20.33%), cerebral cortex (24.60%), and caudate putamen (24.68%) are not only consistent with prior observations of mental delay in some HSCR patients and but also raise the questions that these patients may be more susceptible to Parkinson's disease or depression from potential dopamine deficiency (575, 576). This is

consistent with the demonstration that ET-1 stimulation to rat striatum via activation of ET_B triggers the release of dopamine (542). Moreover, medulla shrinkage (21.05%) provides some anatomical supports for the dysregulated autonomic functions seen in some HSCR patients, for instance, Haddad syndrome, congenital central hypoventilation syndrome, and cardiac arrhythmias, just to name a few (28, 577). In addition, volumetric reduction in cerebellum, up to 14.22%, supports clinical reports of ataxia in WSI-IV patients (127). This is also consistent with the increased neural apoptosis and reduced neural proliferations detected in the cerebellum of *sl/sl* rat (550, 552). Lastly, size reductions in olfactory bulb (19.13%) and pituitary gland (30.08%) of *sl/sl* rat are in accordance with the current known ET_B distribution (403, 541-544). Although there is no distinctive clinical syndrome known to associate HSCR with pituitary dysfunctions currently, pituitary structural defects in $ET_B^{-/-}$ patients may be linked to increased risks for familial medullary carcinoma (FMTC) and multiple endocrine neoplasia type II (MEN II) (578-580). It is again worth noting that these reported measurements are made on immature animals, and as suggested by the growth rate discrepancy illustrated in Figure 3B, structural defects in $ET_B^{-/-}$ individuals are therefore likely to worsen. Hence, more prominent structural impairments are likely to reflect certain HSCR-associated functional declines upon maturity.

Lastly, we compare the structural differences among the three genotypes to explore potential dose-dependent effect of ET_B. While heterozygote has significantly larger TB, TCC and Pit than those of *sl/sl* rats, no linear relationship can be drawn from its comparison with the wild type, Supplementary Table 2B. We suspect statistical under-power is the likely explanation. However, we also acknowledge that, in conjunction with some reports, our observation may be partially consistent with the notion that a single functional ET_B gene may

be sufficient to prevent neuroapoptosis and mediate ET-1 clearance in some structures, thereby improving cerebral perfusion and exerting some neuroprotection (322, 381, 402, 534, 535, 556, 569). Overall, it is of little doubt that homozygous ET_B mutation impairs brain structures. Furthermore, our findings are consistent with ET_B mutation acting as an autosomal recessive condition with high penetrance.

In summary, we provide quantitative 3D evidence illustrating structural changes in the brain of an $ET_B^{-/-}$ HSCR animal model. These detrimental effects are not uniform across different brain structures. Minor protective effects may be presented, Figure 3C and 3D, potentially through reduced cranial vessel tone. Nevertheless, overall findings remain consistent with several proposed mechanisms of action by ET_B, including regulations on angiogenesis, neurogenesis and vasoconstriction (322, 402, 534, 535, 556, 569, 572-574). Our results support functional ET_B have predominantly neuroprotective benefits during neonatal development.

We acknowledge the intrinsic limitation of animal study. Although we have shown ET_B mutation affects brain growth in animal model, further study is warranted. We also acknowledge a larger sample size, and a more efficient image-analysing software will be beneficial for improving the statistical power; nevertheless, current finding cannot be overlooked. More importantly, given that we have macroscopically identified ET_B-affected neural organs, future cell proliferation studies using 5-bromo-2'-deoxyuridine (BrdU) labelling can be useful in confirming reduced neural proliferation microscopically (552). This can also be supplemented by the measurements of VEGF to confirm the angiogenesis reduction in *sl/sl* rats (534). Lastly, confirmatory study on basilar arterial dilatation using

pressure myography may clarify vasoprotective mechanism mediated by ET_B (557).

5. Conclusion

Despite having a grossly normal cranial morphology, $ET_B^{-/-}$ HSCR model has an average of 20% volumetric reduction in its brain and constituents. With no significant differences seen between the wild type and heterozygotes, these changes associated with ET_B mutation are consistent with autosomal recessive inheritance. The non-uniform neuroanatomical changes across different constituents support prior studies on differential ET_B distribution, neurogenesis, and vasoregulation in the brain. Interestingly, ET_B may exert a regional-dependent protection, potentially corresponding to the circulatory distribution through ET-1/ET_B-mediated vasoregulation. Overall, our findings support the notion that $ET_B^{-/-}$ HSCR patients may exhibit neuroanatomical impairments, in accordance with prior clinical reports. Although further study involving human subjects is required, this study supports the importance to a more comprehensive management plan for HSCR patients, at least in $ET_B^{-/-}$ subtype.

Chapter 5 Figures:

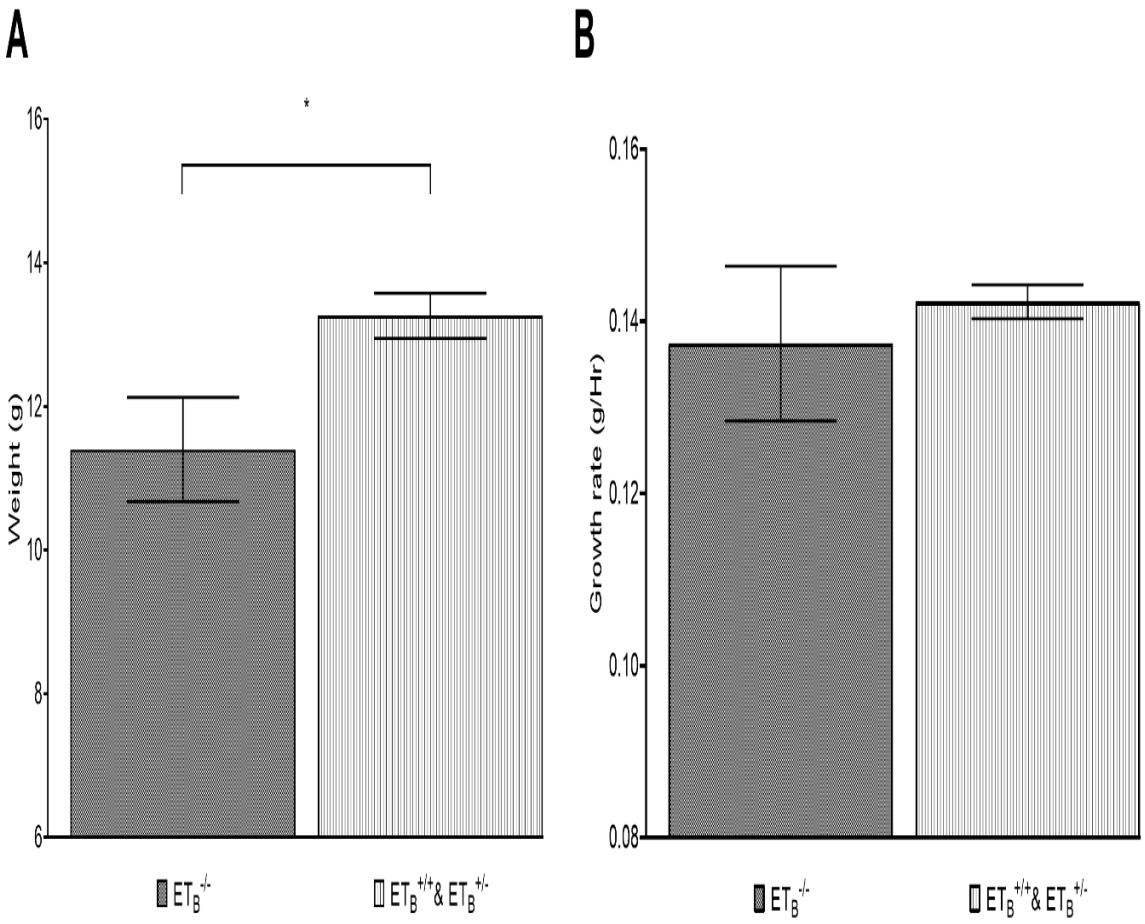

Figure 1: Homozygous ET_B mutation is associated with reductions in bodyweight (A) and bodyweight growth rate (B).

sl/sl ($ET_B^{-/-}$) rat has a significantly lower bodyweight than that of the control group ($ET_B^{+/+}$ & $ET_B^{+/-}$), 11.40g versus 13.26g (df = 9, t-value = 2.51, *p-value* = 0.03), Figure 1A. A similar but smaller difference is observed in the comparison of body growth rate, 0.137g/Hr versus 0.142g/Hr (df = 9, t-value = 0.58, *p-value* = 0.58), Figure 1B. This suggests that *sl/sl* rat is likely to have a proportional organ size shrinkage; furthermore, reduced body growth rate suggests developmental impairment may continue to worsen until maturity.
**: statistically significant, p-value ≤ 0.05.*

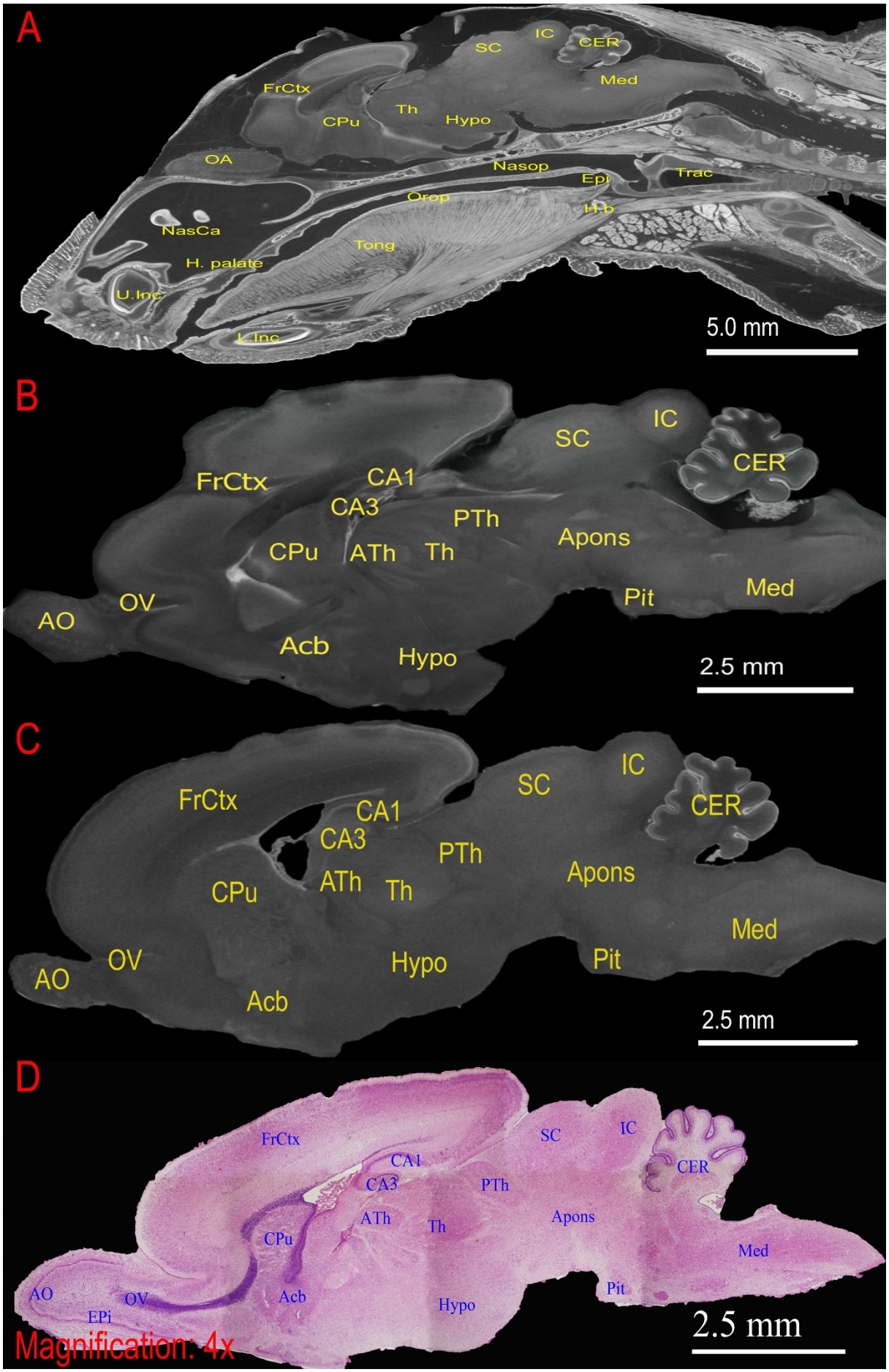
A
IC
SC
CER
Med
FrCtx
Th
CPu
Hypo
OA
Nasop
Epi
Trac
Orop
H-b
NasCa
Tong
H. palate
U.Inc
L.Inc
5.0 mm
B
SC
IC
CER
FrCtx
CA1
CA3
PTh
Apons
CPu
ATh
Th
Pit
Med
OV
AO
Acb
Hypo
2.5 mm
C
IC
SC
CER
FrCtx
CA1
CA3
PTh
Apons
CPu
ATh
Th
Med
OV
Hypo
Pit
AO
Acb
2.5 mm
D
FrCtx
SC
IC
CA1
CER
CA3
PTh
ATh
Th
Apons
CPu
Med
AO
OV
Acb
Hypo
Pit
EPi
2.5 mm
Magnification: 4x

Figure 2: *$ET_B^{-/-}$* rat has a grossly normal intracranial morphology.

Figure 2A and **Figure 2B** represent respective parasagittal micro-CT views of intracranial morphology and isolated brain of *sl/sl* ($ET_B^{-/-}$) rat. **Figure 2A** demonstrates the presence of major craniofacial features and neural structures. **Figure 2B** illustrates magnified micro-CT view of the $ET_B^{-/-}$ brain with additional details, which are also presented in the micro-CT scans of wildtype ($ET_B^{+/+}$) rat, **Figure 2C**. Lastly, H&E micrograph of the micro-CT scanned *sl/sl* rat brain confirms the presence of the identified structures, **Figure 2D**.

The anatomical features identified are labelled as follows: *Acb= accumbens nucleus; AO = anterior olfactory bulb; apons = anterior pons; CA1 = CA1 field of hippocampus; CA3 = CA3 field of hippocampus; CER = cerebellum; Cpu = caudate putamen; FrCtx = frontal cortex; Hypo = hypothalamus; IC = inferior colliculus; med = medulla; Pit = pituitary gland; PTh= posterior thalamus; SC = superior colliculus; Th = thalamus; U. Inc = upper incisor; Tong = tongue; Trac = trachea; Epi = epiglottis; H. b = hyoid bone; H. palate = hard palate; L. Inc = lower incisor; NasCa = nasal cavity; Nasop = nasopharynx; Orop = oropharynx.*

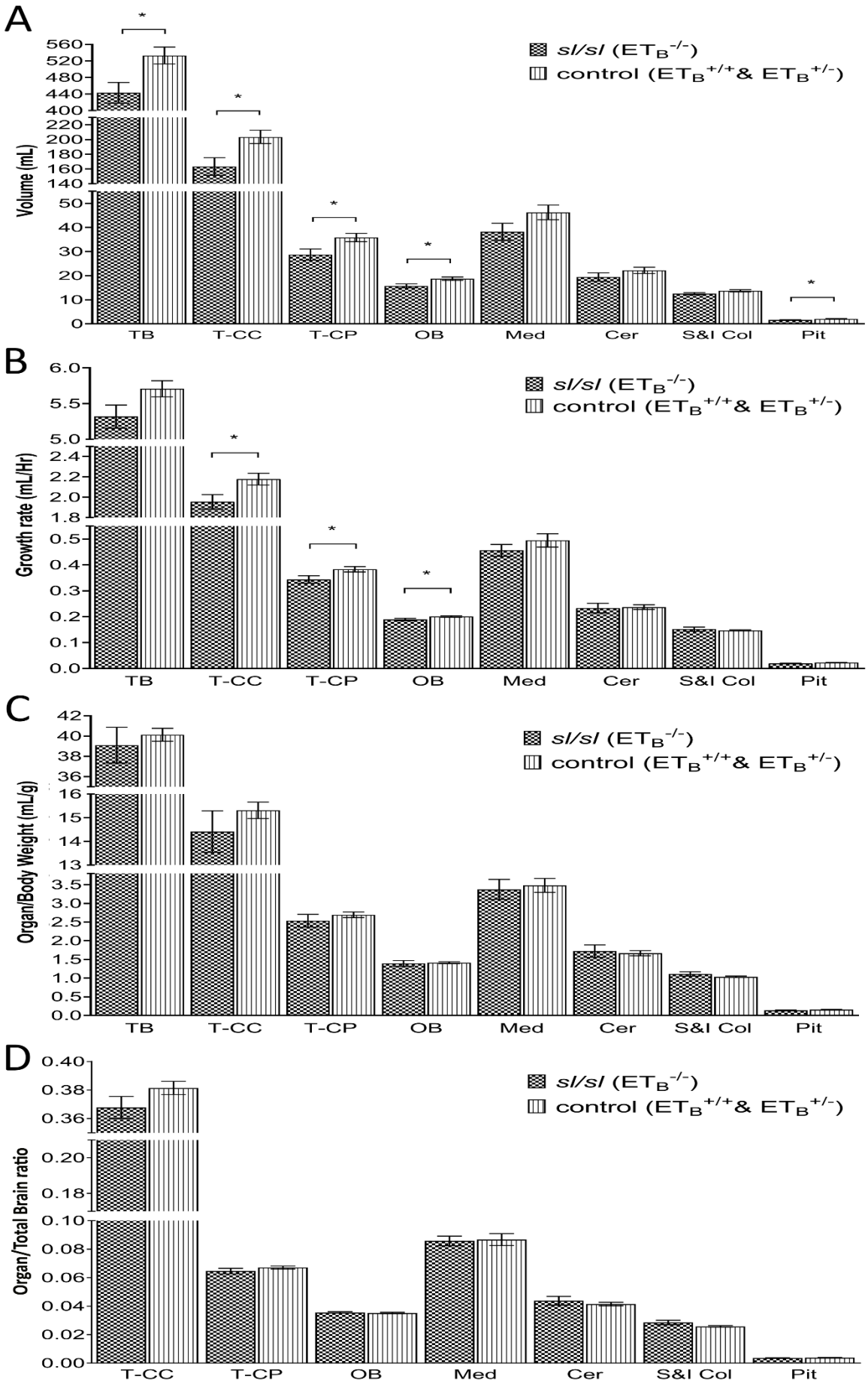
A
Volume (mL)
sl/sl (ET_B^-/-)
control (ET_B^+/+ & ET_B^+/-)
TB
T-CC
T-CP
OB
Med
Cer
S&I Col
Pit
B
Growth rate (mL/Hr)
C
Organ/Body Weight (mL/g)
D
Organ/Total Brain ratio

Figure 3: $ET_B^{-/-}$ mutant has reduced neural organ volume, organ growth rate, organ volume/bodyweight indices, and organ/total brain ratios.

Figure 3A: Significant volumetric reductions in brain and constituents are detected in young $ET_B^{-/-}$ animals. *sl/sl* rat has statistically smaller TB than the control rat: 443.02 mm^3 versus 533.12 mm^3 (df = 9, t-value = 2.82, *p-value* = 0.02). Similar trend is extended across the following: T-CC (163.36 mm^3 versus 203.55 mm^3, df = 9, t-value = 2.73, *p-value* = 0.02), T-CP (28.75 mm^3 versus 35.84 mm^3, df = 9, t-value = 2.49, *p-value* = 0.03), OB (15.73 mm^3 versus 18.74 mm^3, df = 9, t-value = 2.78, *p-value* = 0.02), and Pit (1.60 mm^3 versus 2.09 mm^3, df = 9, t-value = 2.95, *p-value* = 0.02). Although not reaching the statistical power, measurements of Med (38.22 mm^3 versus 46.27 mm^3, df = 9, t-value = 1.74, *p-value* = 0.12), Cer (19.43 mm^3 versus 22.19 mm^3, df = 9, t-value = 1.30, *p-value* = 0.23), and S&I Col (12.51 mm^3 versus 13.73 mm^3, df = 9, t-value = 1.84, *p-value* = 0.10) also demonstrate detectable reduction in *sl/sl* rats.

Figure 3B: $ET_B^{-/-}$ rat has significantly lower growth rates across different parts of brain. Lower TBr growth rate is observed in *sl/sl* rat with respect to the control animal, 5.32mm^3/Hr versus 5.71mm^3/Hr (df = 9, t-value = 2.03, *p-value* = 0.07). Consistent difference between the two groups is also seen in the following: T-CC (1.96mm^3/Hr versus 2.18mm^3/Hr, df = 9, t-value = 2.46, *p-value* = 0.04), T-CP (0.34mm^3/Hr versus 0.38mm^3/Hr, df = 9, t-value = 2.26, *p-value* = 0.05), OB (0.19mm^3/Hr versus 0.20mm^3/Hr, df = 9, t-value = 2.23, *p-value* = 0.05), Med (0.46mm^3/Hr versus 0.50mm^3/Hr, df = 9, t-value = 1.10, *p-value* = 0.30), and Pit (0.019mm^3/Hr versus 0.022mm^3/Hr, df = 9, t-value = 2.11, *p-value* = 0.06). On the other hand, minimal difference between the two groups is detected in the following: Cer (0.23mm^3/Hr versus 0.24mm^3/Hr, df = 9, t-value = 0.19, *p-value* = 0.85) and S&I Col (0.15mm^3/Hr versus 0.15mm^3/Hr, df = 9, t-value = -0.55, *p-value* = 0.60).

Figure 3C: $ET_B^{-/-}$ rat has lower neural organ/bodyweight ratios, suggesting intrinsic ET_B effects on brain development.
sl/sl rat has lower a TBr/bodyweight ratio than that of the control group, 39.1mm^3/g versus 40.12mm^3/g (df = 9, t-value = 0.58, *p-value* = 0.57), reflecting a disproportionally larger reduction in TBr with respect to changes in its bodyweight. Similar trends are also seen in the following: T-CC (14.42mm^3/g versus 15.31 mm^3/g, df = 9, t-value = 1.02, *p-value* = 0.34), T-CP (2.53mm^3/g versus 2.69 mm^3/g, df = 9, t-value = 0.91, *p-value* = 0.39), OB (1.39mm^3/g versus 1.41mm^3/g, df = 9, t-value = 0.23, *p-value* = 0.82), Med (3.37mm^3/g versus 3.48mm^3/g, df = 9, t-value = 0.34, *p-value* = 0.74), and Pit (0.14mm^3/g versus 0.16mm^3/g, df = 9, t-value = 2.00, *p-value* = 0.08). On the other hand, *sl/sl* rat has slightly larger indices in the following: Cer (1.72mm^3/g versus 1.67mm^3/g, df = 9, t-value = -0.32, *p-value* = 0.75) and S&I Col (1.11mm^3/g versus 1.03mm^3/g, df = 9, t-value = -1.29, *p-value* = 0.23). Overall, ET_B mutation is associated with more marked changes in neural organs. In addition, variability in the difference of organ/bodyweight ratios between *sl/sl* rat and the control group suggest the effect of ET_B mutation maybe spatially dependent within the brain.

Figure 3D: Disproportional changes in the neural organ/total brain indices of $ET_B^{-/-}$ rat suggested non-uniform ET_B effect in different parts of the brain.
sl/sl rat has disproportional changes in its neural constituents with respect to global brain shrinkage. Reduced organ/total brain ratios are seen in the following structures of *sl/sl* rat: T-CC (0.37 versus 0.38, df = 9, t-value = 1.58, *p-value* = 0.15), T-CP (0.065 versus 0.067, df = 9, t-

value = 1.17, *p-value* = 0.27), Med (0.086 versus 0.087, df = 9, t-value = 0.17, *p-value* = 0.87), and Pit (0.0036 versus 0.0039, df = 9, t-value = 1.54, *p-value* = 0.16). On the contrary, organ/total-brain indices of OB (0.036 versus 0.035, df = 9, t-value = -0.54, *p-value* = 0.60), Cer (0.044 versus 0.041, df = 9, t-value = -0.75, *p-value* = 0.47) and S&I Col (0.029 versus 0.026, df = 9, t-value = -1.78, *p-value* = 0.11) are larger in *sl/sl* rats. This variation suggests that ET_B effect may be regional dependent within the brain.

TB=Total Brain; T-CC=Total Cerebral Cortex; T-CP=Total Caudate Putamen; OB=Olfactory Bulb; Med=Medulla; Cer=Cerebellum; S&I Col=Superior and Inferior Colliculus; Pit=Pituitary gland.
**: statistically significant, p-value $\leq$ 0.05.*

Chapter 5 Supplementary Tables:

Supplementary Table1: One-Way ANOVA for Body Parameters					
	Sum of Squares	df	Mean Square	F	Significance
Bodyweight					
Between Groups	10.40	2	5.201	F (2,10) = 3.927	P=0.0551
Within Groups	13.24	10	1.324		
Total	23.64	12			
Body Growth Rate					
Between Groups	3.454e-005	2	1.727e-005	F (2,10) = 0.09568	P=0.9096
Within Groups	0.001805	10	0.0001805		
Total	0.001840	12			

Supplementary Table 1: One-way ANOVA for body parameters

No significant variation is detected in the mean bodyweight (p = 0.0551) or mean body growth rate (p = 0.9096) of the studied rats, which consist of three genotypes: $ET_B^{+/+}$, $ET_B^{+/-}$, and $ET_B^{-/-}$. This suggests bodily growth restriction associated with ET_B mutation, if presented, is not a dose-dependent relationship.

Supplementary Table 2A: One-Way ANOVA for Volumetric Measurements

	Sum of Squares	df	Mean Square	F	Significance
TB Volume					
Between Groups	25476	2	12738	F (2,8) = 4.699	P=0.0447
Within Groups	21685	8	2711		
Total	47160	10			
TCC Volume					
Between Groups	5252	2	2626	F (2,8) = 4.711	P=0.0445
Within Groups	4460	8	557.4		
Total	9711	10			
TCP Volume					
Between Groups	146.5	2	73.27	F (2,8) = 3.072	P=0.1023
Within Groups	190.8	8	23.85		
Total	337.3	10			
OB Volume					
Between Groups	27.66	2	13.83	F (2,8) = 4.273	P=0.0546
Within Groups	25.90	8	3.237		
Total	53.56	10			
Med Volume					
Between Groups	181.9	2	90.96	F (2,8) = 1.394	P=0.3023
Within Groups	521.9	8	65.23		
Total	703.8	10			
Cer Volume					
Between Groups	23.92	2	11.96	F (2,8) = 0.8828	P=0.4504
Within Groups	108.4	8	13.55		
Total	132.3	10			
Pit Volume					
Between Groups	0.7341	2	0.3671	F (2,8) = 5.274	P=0.0346
Within Groups	0.5568	8	0.0696		
Total	1.291	10			
S&I Col Volume					
Between Groups	4.240	2	2.120	F (2,8) = 1.605	P=0.2594
Within Groups	10.57	8	1.321		
Total	14.81	10			

Supplementary Table 2B: Tukey post-hoc for Volumetric Measurements

TB Volume						
(A)	(B)	Mean Difference (A-B)	Std Error of Difference	Sig	Lower Bound	Upper Bound
$ET_B^{+/+}$	$ET_B^{+/-}$	-47.17	42.51	0.5350	-168.6	74.30
$ET_B^{+/+}$	$ET_B^{-/-}$	66.51	38.02	0.2463	-42.13	175.2
$ET_B^{+/-}$	$ET_B^{-/-}$	113.7	38.02	0.0412	5.036	222.3
T-CC Volume						
(A)	(B)	Mean Difference (A-B)	Std Error of Difference	Sig	Lower Bound	Upper Bound
$ET_B^{+/+}$	$ET_B^{+/-}$	-23.77	19.28	0.4683	-78.85	31.32
$ET_B^{+/+}$	$ET_B^{-/-}$	28.30	17.24	0.2843	-20.97	77.57
$ET_B^{+/-}$	$ET_B^{-/-}$	52.07	17.24	0.0394	2.801	101.3
Pit Volume						
(A)	(B)	Mean Difference (A-B)	Std Error of Difference	Sig	Lower Bound	Upper Bound
$ET_B^{+/+}$	$ET_B^{+/-}$	-0.2582	0.2154	0.4865	-0.8737	0.3573
$ET_B^{+/+}$	$ET_B^{-/-}$	0.3531	0.1927	0.2199	-0.1974	0.9036
$ET_B^{+/-}$	$ET_B^{-/-}$	0.6113	0.1927	0.0315	0.06078	1.162

Supplementary Table 2: One-way ANOVA for volumetric measurements

One-way ANOVA show statistically significant variations in the TBr, TCC, and Pit volumetric means of the studied rats: $ET_B^{+/+}$, $ET_B^{+/-}$, and $ET_B^{-/-}$. On the contrary, no significant variation is detected in other organ measurements of the three genotypes, as shown by **Supplementary Table 2A**.

Post-hoc Tukey show significant volumetric difference between the heterozygote ($ET_B^{+/-}$) and *sl/sl* ($ET_B^{-/-}$) in TBr (mean difference 113.7, SE 38.02, p = 0.0412), TCC (mean difference 52.07, SE 17.24, p = 0.0394), and Pit (mean difference 0.6113, SE 0.1927, p = 0.0315). However, measurement of the wild type ($ET_B^{+/+}$) is not significantly different from those of the other two groups, as shown by **Supplementary Table 2B.**

Supplementary Table 3A: One-Way ANOVA for Growth Measurements					
	Sum of Squares	df	Mean Square	F	Significance

TB Growth					
Between Groups	0.4669	2	0.2335	F (2,8) = 2.162	P=0.1776
Within Groups	0.8640	8	0.1080		
Total	1.331	10			
TCC Growth					
Between Groups	0.1620	2	0.08101	F (2,8) = 3.692	P=0.0731
Within Groups	0.1756	8	0.02195		
Total	0.3376	10			
TCP Growth					
Between Groups	0.004326	2	0.002163	F (2,8) = 2.321	P=0.1604
Within Groups	0.007456	8	0.0009320		
Total	0.01178	10			
OB Growth					
Between Groups	0.0003987	2	0.0001993	F (2,8) = 2.426	P=0.1502
Within Groups	0.0006574	8	8.217e-005		
Total	0.001056	10			
Med Growth					
Between Groups	0.004125	2	0.002062	F (2,8) = 0.5419	P=0.6015
Within Groups	0.03044	8	0.003805		
Total	0.03457	10			
Cer Growth					
Between Groups	5.588e-005	2	2.794e-005	F (2,8) = 0.02401	P=0.9763
Within Groups	0.009309	8	0.001164		
Total	0.009365	10			
Pit Growth					
Between Groups	2.830e-005	2	1.415e-005	F (2,8) = 2.435	P=0.1493
Within Groups	4.649e-005	8	5.811e-006		
Total	7.479e-005	10			
S&I Col Growth					
Between Groups	8.009e-005	2	4.005e-005	F (2,8) = 0.2403	P=0.8193
Within Groups	0.001568	8	0.0001960		
Total	0.001648	10			

Supplementary Table 3B: One-Way ANOVA for Volumetric / Bodyweight ratios					
	Sum of Squares	df	Mean Square	F	Significance

TB Volume / Bodyweight ratio					
Between Groups	5.046	2	2.523	F (2,8) = 0.2800	P=0.7629
Within Groups	72.09	8	9.011		
Total	77.14	10			
TCC Volume / Bodyweight ratio					
Between Groups	3.427	2	1.713	F (2,8) = 0.7730	P=0.4932
Within Groups	17.73	8	2.216		
Total	21.16	10			
TCP Volume / Bodyweight ratio					
Between Groups	0.07151	2	0.03575	F (2,8) = 3.3791	P=0.6961
Within Groups	0.7544	8	0.09430		
Total	0.8259	10			
OB Volume / Bodyweight ratio					
Between Groups	0.001785	2	0.0008926	F (2,8) = 0.04974	P=0.9518
Within Groups	0.1436	8	0.01795		
Total	0.1454	10			
Med Volume / Bodyweight ratio					
Between Groups	0.03546	2	0.01773	F (2,8) = 0.05759	P=0.9444
Within Groups	2.463	8	0.3078		
Total	2.498	10			
Cer Volume / Bodyweight ratio					
Between Groups	0.008488	2	0.004244	F (2,8) = 0.04889	P=0.9526
Within Groups	0.6944	8	0.08680		
Total	0.7029	10			
Pit Volume / Bodyweight ratio					
Between Groups	0.0008387	2	0.0004193	F (2,8) = 2.453	P=0.1477
Within Groups	0.001368	8	0.0001710		
Total	0.002207	10			
S&I Col Volume / Bodyweight ratio					
Between Groups	0.01715	2	0.008575	F (2,8) = 0.8153	P=0.4762
Within Groups	0.08414	8	0.01052		
Total	0.1013	10			

Supplementary Table 3C: One-Way ANOVA for Organ / Total brain ratios					
	Sum of Squares	df	Mean Square	F	Significance

TCC / Total brain ratio					
Between Groups	0.0007006	2	0.0003503	F (2,8) = 1.699	P=0.2427
Within Groups	0.001650	8	0.0002062		
Total	0.002350	10			
TCP / Total brain ratio					
Between Groups	1.830e-005	2	9.151e-006	F (2,8) = 0.6731	P=0.5368
Within Groups	0.0001088	8	1.360e-005		
Total	0.0001271	10			
OB / Total brain ratio					
Between Groups	6.605e-007	2	3.303e-007	F (2,8) = 0.2201	P=0.8071
Within Groups	1.200e-005	8	1.500e-006		
Total	1.266e-005	10			
Med / Total brain ratio					
Between Groups	2.227e-005	2	1.113e-005	F (2,8) = 0.1216	P=0.8871
Within Groups	0.0007325	8	9.157e-005		
Total	0.0007548	10			
Cer / Total brain ratio					
Between Groups	1.572e-005	2	7.859e-006	F (2,8) = 0.2704	P=0.7698
Within Groups	0.0002326	8	2.907e-005		
Total	0.0002483	10			
Pit / Total brain ratio					
Between Groups	2.332e-007	2	1.166e-007	F (2,8) = 1.238	P=0.3402
Within Groups	7.538e-007	8	9.423e-008		
Total	9.871e-007	10			
S&I Col / Total brain ratio					
Between Groups	2.379e-005	2	1.190e-005	F (2,8) = 1.742	P=0.2355
Within Groups	5.464e-005	8	6.830e-006		
Total	7.843e-005	10			

Supplementary Table 3: One-way ANOVA comparison on growth rates, organ volume/bodyweight ratios, and organ / total brain ratios

One-way ANOVA comparison show no significant difference is detected in the mean organ growth (**Supplementary Table 3A**), volumetric/bodyweight ratios (**Supplementary Table 3B**), and organ/whole brain ratios (**Supplementary Table 3C**) of the three genotype rats: $ET_B^{+/+}$, $ET_B^{+/-}$, and $ET_B^{-/-}$. These findings suggest that the effect of ET_B mutation is likely non-linear.

Chapter 6: Structural heart defects associated with ET_B mutation, a cause of Hirschsprung disease.

Chapter 6 Highlights

- $ET_B^{-/-}$ HSCR model is associated with body growth impairment; neonatal *sl/sl* rat has 16% less bodyweight than the control group.
- *sl/sl* rat has a normal cardiac morphology.
- *sl/sl* rat has significant reductions in cardiac structures: 40% in whole heart volume, 20% in heart growth rate, and 25% in whole heart/bodyweight ratios. Similar trend is observed in the measurements of LA, LV, RA, and RV
- No correlation is seen between ET_B genotype and aortic arch size.
- These animal findings, if extrapolatable to human subjects, suggest $ET_B^{-/-}$ HSCR patients may have various degrees of neonatal cardiac anomalies.

Chapter 6 Abstracts

Background
HSCR, a colonic neurocristopathy affecting 1/5000 births, is suggested to associate with cardiac septal defects and conotruncal malformations. However, we question subtle cardiac changes maybe more commonly presented due to multi-regulations by HSCR candidate

genes, in this instance, ET_B. To investigate, we compare the cardiac morphology and quantitative measurements of *sl/sl* rat to those of the control group

Methods
Eleven neonatal rats were generated from heterozygote ($ET_B^{+/-}$) crossbreeding. Age and bodyweight were recorded at time of sacrifice. Diffusion-staining protocols with 1.5% iodine solution was completed prior to micro-CT scanning. All rats were scanned using an *in vivo* micro-CT scanner, Caliper Quantum FX, followed by two quality-control scans using a custom-built *ex vivo* micro-CT system. All scans were reviewed for gross cardiac dysmorphology. Micro-CT data were segmented semi-automatically following NLM filtering for: whole heart, LV, RV, LA, RA, and aortic arch. Measurements were taken with Drishti. Following image analysis, PCR genotyping of rats was performed: five *sl/sl* rats, three wildtype, and three heterozygotes. Statistical comparisons on organ volume, growth rate, and organ volume/bodyweight ratios were made between *sl/sl* and the control group.

Results
Cardiac morphology and constituents are preserved. However, *sl/sl* rat has significant volumetric reductions in cardiac structures: whole heart (38.70%, *p-value* = 0.02); LV (41.22%, *p-value* = 0.01), RV (46.15%, *p-value* = 0.02), LA (44.93%, *p-value* = 0.06), and RA (39.49%, *p-value* = 0.02). Consistent trend is also observed in growth rate (~20%) and organ volume/bodyweight indices (~25%). On the contrary, no significant difference in aortic arch measurement is seen between *sl/sl* rat and the control group.

Conclusion
Despite the presence of normal morphology, significant cardiac growth retardation is detected in *sl/sl* rat, supporting the likely association between the cardiac anomalies and HSCR, at least in $ET_B^{-/-}$ subtype. Structural reduction is likely due to a combination of failure to thrive from enteric dysfunction, alterations to CaNCC colonization, and importantly coronary hypoperfusion from ET-1/ET_A-mediated hyper-vasoconstriction. Little correlation is detected between aortic arch development and *sl/sl* rat, supporting minor ET_B role in large vessels. Although further clinical study is warranted, $ET_B^{-/-}$ HSCR patients may likely require cardiac assessment in view of potential congenital cardiac defects.

Key Words: Hirschsprung disease, heart defects, Endothelin-B mutation, spotting-lethal rat.

1. Introduction

Endothelin B receptor (ET_B) is a G-protein-coupled heptahelical receptor sharing the same class as endothelin A receptor (ET_A). Both receptors are widely expressed with

interconnected functions, particularly in the cardiovascular system. Both ET_A and ET_B initiate downstream signalling through binding to endothelin. Endothelin are 21 amino-acids peptides categorized into three subclasses: ET-1, ET-2, and ET-3 (176). ET-3 is responsible for the proliferation of pluripotent neural crest cells (NCCs) through its interaction with ET_B to ensure normal intestinal development whereas ET-1 and ET-2 exert vascular functions through ET_A and ET_B binding.

Homozygous ET_B mutation is known to cause Hirschsprung's disease (HSCR), a well-described aganglionic intestinal disease affecting 1/5000 births globally but with an incidence up to 1/1370 births regionally (12). HSCR is generally treated with surgical resections; however, increasing understanding on HSCR and ET_B regulatory signalling suggests such treatments may not be sufficiently comprehensive. Recent studies suggested that multiple organ systems maybe be affected in syndromic HSCR patients (188, 537); up to 30% of HSCR patients are associated with abnormalities in the central nervous, gastrointestinal, genitourinary, endocrinological, immunological, and cardiovascular systems. Some of the HSCR-associated syndromes with cardiac abnormalities including Down's syndrome (up to 2-10% of HSCR cases), Di George syndrome, Haddad syndrome, Mowat-Wilson syndrome, Type IV Waardenburg syndrome (WS-IV), and McKusick-Kauffman syndrome (MKKS) (537, 581-583). Furthermore, conotruncal heart malformations such as atrial septal defect (ASD; 2.2%) and ventricular septal defect (VSD; 1.7%) are also noted in subpopulations of HSCR patients (21).

The pathogenesis of heart defects associated with HSCR and ET_B mutation may be partially stemmed from the migration failure of cardiac neural crest cell (CaNCC), a process

dictated predominantly by ET-1/ET_A signalling (230). Animals with ET_A mutation have been known to have high neonatal mortality with severe craniofacial and cardiac malformations (584, 585). Although ET_B mutation is not known to affect CaNCC directly, it has been reported to alter ET-1/ET_A signalling (381). Consequently, one can expect subtle cardiac changes to occur in $ET_B^{-/-}$ mutants.

Vascular dysfunction may predispose $ET_B^{-/-}$ mutant to suffer structural changes during development. ET_B's cardiovascular effects are bimodal, mediating both vasodilation and vasoconstriction through its binding with ET-1 (236, 586, 587), the principal endothelin isoform in the cardiovascular system. ET-1 is secreted by the vascular endothelial cells and endocardial cells of cardiomyocytes (214). The activation of ET-1/ET_B pathway leads to endothelial vasodilation through upregulation of nitric oxide (NO), prostacyclin, and endothelium-relaxing factor (EDRF); a balancing effect to the vasoconstriction mediated by ET-1/ET_A signalling in vascular smooth muscle cells (VSMC). Consequently, ET_B is likely to possess a beneficial role in myocardial circulation and thus end organ perfusion (189, 536, 588). By the same token, one can expect HSCR patients with homozygous $ET_B^{-/-}$ mutation to have impaired cardiovascular development and increased risks for hypertension and coronary artery disease due to uncontrolled ET-1/ET_A stimulation (589).

Although several microscopic and physiologic studies have been conducted to determine the functions and distribution of ET_B receptor, to the best of our knowledge, no macroscopic analyses have been completed to evaluate its effect on cardiac anatomy (188, 587, 590). We aim to complement prior studies through quantitative analysis on the cardiac changes of the spotting-lethal (*sl/sl*) rat, a naturally occurring $ET_B^{-/-}$ animal model of WS-IV,

with the phenotype of HSCR, hearing deficits, and white coat colour (413).

In order to acquire detailed yet structurally preserved anatomical information, we adopt X-ray micro-computed tomography (micro-CT) with modified tissue staining techniques (436). Micro-CT offers three-dimensional (3D) information with high resolution images comparable to the low powered 2D microscopy. In addition, improvement on imaging analysis software in recent years renders detection of subtle volumetric and dimensional changes in cardiac system possible.

In this study, we hypothesize the following:

1. $ET_B^{-/-}$ mutant may suffer minor body growth impairment at an early age.
2. Gross cardiac morphology may be preserved in $ET_B^{-/-}$ mutant.
3. Loss of ET_B function may be associated with reduced heart size, growth rate, and heart volume/bodyweight ratio.
4. Cardiac growth may be ET_B dose dependent.
5. Absence of functional ET_B has little effect on aortic arch growth.

2. Methods

2.1. Compliance with Ethical practice

All animal tissues used in this study were handled with care and strict compliance to ACT Health Human Research Ethics Committee (ACTH-HREC) and Australian National University Animal Experimentation Ethics Committee (ANU-AEEC), ethic approval project number A2011/67.

2.2. Rat culling and Method of euthanasia

All rat specimens used in this study were generated from crossbreeding between the heterozygous ($ET_B^{+/-}$) parents. This breeding colony was originally derived from a naturally occurring mutation and has been maintained in Australian National University (ANU) over the past 15 years.

Eleven neonatal rats with an average age of 88 hours were sacrificed. Individual rat's coat pattern, age, gender, and weight were recorded. These rats were over anaesthetized with 5% isoflurane for 15 minutes in modified gas chamber prior culling. These rats were culled via abdominal aortotomy following a midline laparotomy of 1 cm using scalpel and iris scissor. Five-millimetre tail-tip of each rat was resected and stored for subsequent genotyping.

2.3. Tissue preparation and staining protocols

Diffusion staining was performed in the following steps for successful micro-CT scanning. Firstly, midline thoracotomy of one centimetre was performed on rat carcass to facilitate tissue penetration of staining solution into the cardiac tissue. The thoracotomized bodies were immersed in 10% PBS solution for 30 minutes to wash out residual bodily fluid. This was followed by tissue fixation in 4% formalin solution for 24 hours. Next, formalin-fixed tissues were washed out with graded ethanol (EtOH) series: 20%, 50%, 70%, and 90% for 1 day each. Finally, tissue staining was completed in 1.5% iodine in 90% EtOH for a minimum of seven days prior to micro-CT scanning.

2.4. Image acquisition by micro-CT scanning

In this study, all rat samples were scanned using a commercial *in vivo* micro-CT scanner, Caliper Quantum FX. Additional quality assurance micro-CT scans were acquired using a custom-built *ex vivo* micro-CT system by ANU Applied Mathematical Department. The maximal resolution achievable by Caliper Quantum FX was 10 µm/voxel with an efficiency of 4.5 minutes per scan. The average dataset size was 256MB. The resultant images were stored as DICOM series and visualized using Drishti, an open-source software (453). The *ex vivo* micro-CT system built by ANU Applied Mathematical Department required at least fifteen hours of scanning time with additional eight hours of image-processing time via National Computational Infrastructure (NCI) services. The maximal resolution was 1 µm/voxel; magnification factor was limited by the physical size of the sample. The resultant images were stored as netCDF files and visualized with Drishti (453). Each dataset has an average size of 12 – 16 GB.

Due to the limited access to the *ex vivo* micro-CT scanners, all image data acquired by Caliper Quantum FX were filtered with non-local means (NLM) algorithms to improve image quality (559). Two sets of *ex vivo* micro-CT data were acquired for quality control to ensure sufficient anatomical details and image clarity in denoised *in vivo* micro-CT scans for quantitative analysis. Although not ideal*,* we found the image quality of NLM-processed *in vivo* micro-CT scans satisfactory for the purposes of this study.

2.5. Image segmentation and analysis

Acquired micro-CT data were first denoised using NLM algorithm to improve signal-to-noise ratios and image clarity (559). This code was implemented in a Linux operating system running on a setup of Intel (R) Core ™ i7-4770K CPU @3.5GHz with 32G of RAM and

Nvidia GeForce GTX Titan Black Kepler GK110 architecture.

Following the image filtering, micro-CT data were segmented semi-automatically through individual CT slices for selected organs using Drishti segmentation algorithms (453). To ensure accuracy, follow-up verification on image segmentation was performed one month after the initial processing: minimal variations were detected. The following cardiac organs were selected for quantitative measurements: whole heart, left atrium (LA), left ventricle (LV), right atrium (RA), right ventricle (RV), and ascending aortic arch (AA). Segmentation of the whole heart was first completed to determine potential gross cardiac defects in $ET_B^{-/-}$ mutants. The same process was repeated for each structure. The luminal width of AA was measured at the aortic orifice in axial view for standardize comparison. Three-dimensional (3D) volumetric measurements were completed following sub-segmentation of each structure through volume rendering.

To standardize comparison, the following anatomical definitions were adopted. The pulmonary circulatory inflow was defined by the superior and inferior vena cava orifices to right atrium; the outflow was defined by the pulmonary valve. The systemic circulatory inflow was defined by pulmonary vein orifices to the left atrium whereas the outflow was defined by the aortic valve. Both selections of left and right ventricles have included interventricular septal wall for better definition of organ boundary to standardize comparison. Lastly, for the comparison of AA, the boundary of AA was defined as the arterial vessel between the aortic valves to the first branching point, brachiocephalic artery.

2.6. H&E light microscopy

H&E light microscopy was completed for two of eleven rats following micro-CT scanning to assess anatomical accuracy provided by micro-CT scans. The following steps were performed. The iodine-stained hearts were sectioned longitudinally into 4mm thickness tissue-blocks and placed in cassettes. Contrast washout and dehydration were performed in 90% EtOH for 48 hours prior to paraffin embedment at 60°C. These tissue blocks were then sliced into 4 µm thick tissue-sheets with a microtome. Tissue-sheets were then laid in a water-bath of 5-6°C while being positioned onto pre-labelled glass slides. These slides were dried overnight at 37°C.

Progressive H&E staining was completed by placing the slides in alum-hematoxylin solutions until the appearance of dark red colour. Washing and 'bluing' with lithium carbonate solution were then performed. Lastly, washing and counter-staining with 0.5% eosin alcoholic solution were completed.

All H&E slides were reviewed with an Olympus IX71 microscope at 4x magnification.

2.7. Genotyping

After the completion of quantitative measurements, genotyping was performed. Three homozygous wild type ($ET_B^{+/+}$), three heterozygous ($ET_B^{+/-}$), and five homozygous spotting lethal (*sl/sl*; $ET_B^{-/-}$) rats were identified. The average ages of wild type, heterozygous, and homozygous mutant rats were 90.7 hours, 96 hours, and 83.2 hours respectively.

PCR genotyping was completed using the following protocols. Five-millimetres tail tips of the eleven rats were lysed with Proteinase K in lysis buffer, which consisted of 100mM

Tris pH 8, 5mM EDTA, 0.2% SDS, and 200mM NaCl in distilled water. The DNA was extracted via vortex heating and centrifuging to separate the DNA-containing supernatants from undigested materials. The supernatants were further vortexed and centrifuged to isolate the DNA pellets. The DNA pellets were then washed with 70% EtOH and dried. The DNA was then suspended and quantified using spectrophotometry. Next, PCR was completed with "Master-Mix" reagent, which included 10*PCR buffer Qiagen-contained $MgCl_2$, dNTP (10mM), Primer PS7 (33.3µM; 5'-CCA CTA AGA CCT CCT GGA CT-3'), Primer PS 15 (33.3µM; 5'-TCA CGA CTT AGA AAG CTA CAC T-3') and DNA polymerase (515). Afterward, this Master-Mix reagent was pipetted onto the PCR plates with the eleven rat DNAs. This was followed by PCR in Veriti 96-Well Thermal-Cycler. Finally, electrophoresis of fourteen DNA samples (eleven test-subject DNA and three controls: wild-type, heterozygote, and *sl/sl* rat) was run for one hour under the voltage setting of 100V and current setting of 55mA, with MassRuler (#SM1263, Fermentas) reference by the side. The resultant electrophoresis gel was visualized with Gel Documentation System DOC-Print VX5 (Vilber Lourmat).

2.8. Statistical Analysis

Based on the segregation analysis of colony data, *sl/sl* rat showed a strong autosomal recessive inheritance (*p-value* = 0.001) and high genetic penetrance (> 95% exhibits HSCR phenotype). Therefore, statistical comparison using the two-tail t-test was made between the *sl/sl* ($ET_B^{-/-}$) and the control group ($ET_B^{+/+}$ & $ET_B^{+/-}$) to determine the effect of ET_B on heart growth. The comparison was made in the following parameters: organ size, organ growth rate, and organ volume/bodyweight ratios. Albeit small, the latter two were made to further standardize the comparisons by accounting age and body size variations of individual rat. Additionally, these parameters provided estimating metrics for structural changes upon

developmental maturation.

The difference (%) between the control and *sl/sl* groups were calculated for each parameter. Additionally, the proportionality of individual cardiac substituent with respect to the whole heart (organ/heart ratio) were compared to explore potential regional effect. Lastly, data of respective wild types ($ET_B^{+/+}$) and heterozygotes ($ET_B^{+/-}$) were provided in the supplementary figures to illustrate possible gene-dose-dependent relationship. All statistical analysis was completed one month after the secondary verification review of image segmentation with the aid of GraphPad Prism version 8.0.0 for Windows, GraphPad Software, San Diego, California USA, www.graphpad.com.

3. Results

3.1. Reduced bodyweight and body growth rate in *sl/sl* rat

Based on our measurements of neonatal rats, ET_B mutation was associated with minor reductions in body size and body growth rate, at least at the age of eighty hours. As shown by Figure 1a, *sl/sl* ($ET_B^{-/-}$) rats have 16.32% smaller bodyweight than that of control group, *p-value* = 0.03. On the other hand, when standardized to rats' age, this difference was reduced to 3.53%, *p-value* = 0.577, as shown by Figure 1b. Although not shown, there was little difference in bodyweight and growth rate between the wild type ($ET_B^{+/+}$) and heterozygotes ($ET_B^{+/-}$), suggesting the absence of ET_B dose-dependent relationship.

3.2. *sl/sl* rat has a grossly normal cardiac morphology

Previous studies suggested disruptions in the endothelin system might lead to CaNCC migration failure and cause cardiac outflow tract defects (232). However, thorough reviews

of the eleven rat micro-CT scans did not reveal marked dysmorphology in cardiac constituents. As exemplified by the sectional micro-CT slices and H&E scan shown in Figure 2, *sl/sl* heart contained all the essential components of a normal heart: aorta, aortic semilunar valve, right and left atrium, right and left ventricles, intact interatrial and interventricular septum, and patent pulmonary vessels. Expectedly, cardiac anatomy of wild type and heterozygous rats shared the same features. This preliminary finding suggested ET_B may have little impact on CaNCC migration.

3.3. *sl/sl* rat has a significantly smaller heart (mm^3)

Following the morphological examinations, volumetric measurements were performed for quantitative comparison. Our data demonstrated homozygous ET_B mutation was associated with significant volumetric reductions in the heart and constituents.

As demonstrated by Figure 3, *sl/sl* rat has a significantly smaller heart than the control group, up to 38.7% reduction, *p-value* = 0.02. Similar changes were observed in the following constituents: LV (41.22%, *p-value* = 0.01), RV (46.15%, *p-value* = 0.02), LA (44.93%, *p-value* = 0.06), and RA (39.49%, *p-value* = 0.02). Volumetric measurement of AA also showed 22.00% reduction in *sl/sl* rats with respect to the control; however, this finding did not reach statistical significance, *p-value* = 0.25.

Although not reported by current literature, cardiac size may be positively correlated with ET_B gene copies. As shown by Supplementary Figure 1, wild type rat has the largest heart among the three genotypes; this was followed by the heterozygote in the middle and *sl/sl* rat in the last. Concordantly, LA, RA, LV and RV measurements of wild types were 42.76%

- 48.09% larger than those of *sl/sl* rats, whereas those of heterozygotes were only 34.71% - 44.71% larger.

Overall, we demonstrated neonatal *sl/sl* rats having approximately 40% smaller hearts with respect to the control group. These differences may widen with age until rats reach maturity.

3.4. *sl/sl* rat has significantly lower cardiac growth rates (mm^3/Hr)

ET_B mutation has a negative impact on cardiac growth rate. As shown by Figure 4, the growth rate of the whole heart in *sl/sl* rat was 23.70% lower than that of control group, *p-value* = 0.05. Significant reductions were also observed in the growth rates of LV (26.39%, *p-value* = 0.02) and RV (31.25%, *p-value* = 0.03). Although not reaching the statistical power, lower growth rates of LA (27.36%, *p-value* = 0.18), RA (23.42%, *p-value* = 0.10) and AA (9.28%, *p-value* = 0.51) were also detected in the *sl/sl* rats.

Further analysis showed stepwise decreases in organ growth rates with respect to functional copies of ET_B gene. As shown by Supplementary Figure 2, LA, RA, LV, and RV growth rates of heterozygous rats were 17.40% - 26.60% higher than those of *sl/sl* rats, whereas those of wild types were 29.43% - 35.91% higher. On the other hand, analyses on AA growth rates demonstrated no consistent correlations with ET_B dose.

Overall, an approximately 25% decrease in the growth rates of all heart constituents can be appreciated in neonatal *sl/sl* rats. This growth retardation may persist until age of maturation. Interestingly, this reduction was disproportionally larger than the 3.53%

reduction in bodyweight growth rate, suggesting an intrinsic effect of ET_B to the developing heart.

3.5. *sl/sl* rat has lower heart organ volume/bodyweight indices (mm^3/g)

Cardiac organ volume/bodyweight ratios demonstrated that the effect of ET_B mutation on heart structure was disproportionally larger than its effect on body size. As shown by Figure 5, *sl/sl* rat has smaller organ volume/bodyweight ratios than those of the control group in the following: whole heart (20.00%, *p-value* = 0.04), RA (20.79%, *p-value* = 0.05), LV (21.75%, *p-value* = 0.03), and RV (26.54%, *p-value* = 0.04). Although not achieving statistical significance, LA volume/bodyweight ratio of *sl/sl* rat was also lower by 25.75%, *p-value* = 0.13. Overall, homozygous ET_B mutation was associated with a disproportionally larger reduction in cardiac sizes with respect to changes in global body size. This was further supported by a stepwise decreasing pattern with reducing copies of functional ET_B gene, as illustrated by Supplementary Figure 3. On the other hand, little change was detected in AA measurements, with *sl/sl* rat having 5.17% larger AA than that of the control group, *p-value* = 0.70; this observation was consistent with ET_B's minor regulatory role on large vessel.

3.6. Uniform structural changes associated with ET_B mutation

Subtle variations in the structural changes of different heart components were detected in *sl/sl* rat. As shown by Figure 6, the differences in cardiac constituent/whole heart ratios were relatively uniform between *sl/sl* rat and the control group, suggesting the effect of ET_B mutation on the heart was likely global. Overall, these differences between the two groups were insignificant albeit a 5.81% reduction was detected in the RV/whole heart ratio of *sl/sl* rat.

4. Discussion

In this study, we demonstrated neonatal $ET_B^{-/-}$ HSCR model exhibits significant cardiac structural impairment. This was consistently illustrated through three parameters taken in *sl/sl* rat: up to 40% volumetric reductions in heart structures, 20% reduction in heart growth rate, and 25% reduction in organ volume/bodyweight indices. The causes for these cardiac growth restrictions likely include the following: global growth impairments due to enteric dysfunction; alterations in CaNCC development; vasodysregulation caused by the absence of ET_B.

Concurrent developmental anomalies occur in up to 30% of HSCR patients, five to eight percent of whom suffers congenital heart diseases (CHD) (591). While CHD occurs in only three percent of non-syndromic HSCR infants, the prevalence of CHD in chromosomal HSCR patients is remarkably high, ranging from 20% to 80%, with cardiac septal defects being the most common anomalies (581). Furthermore, regional paediatric data demonstrate that up to 48% of HSCR patients co-affected with Down's syndrome (HSCR/DS) have CHD (592); this high congruence suggest defects in cardiac and central nervous systems may be closely related in certain HSCR subtypes. Indeed, in addition to the cardiac structural abnormalities reported in this study, we have previously reported brain shrinkage (up to 20% reduction) in *sl/sl* rat despite preservation of normal organ morphology. Our findings suggest HSCR patients, at least in $ET_B^{-/-}$ variant, are likely to share subtle cardiac and neurological impairments. This also suggests that CHD incidence in HSCR is likely underestimated due to under-reporting of subtle cardiac anomalies.

Homozygous ET_B knock-out mutation ($ET_B^{-/-}$) causes WS-IV syndrome with prominent HSCR phenotypes. As previously mentioned, aberrant mutation in ET-3/ET_B signalling causes ENCC migration failure and thus ENS maldevelopment. This subsequently impairs the nutritional absorption in affected individuals (593). Consistently, a 16.53% decrease in bodyweight and a 3.42% decrease in body growth-rate are recorded in *sl/sl* rat, Figure 1. These bodily reductions likely contribute, at least partially, to the proportional shrinkage of the heart. Additionally, this growth retardation will likely worsen with age as the manifestation of enteric failure becomes progressively prominent.

Disruption in CaNCC migration may partially cause structural cardiac changes in *sl/sl* rat. Although limited literature is available to comment on the presence of direct linkage between ET-3/ET_B signalling on CaNCC migration, indirect alteration in ET-1/ET_A signalling through elevated ET-1 levels in $ET_B^{-/-}$ mutants has been suggested (381). CaNCC has been documented to colonize cardiac outflow tract (OFT) and pharyngeal arches during embryogenesis. This in turn facilitates the remodelling of pharyngeal arch arteries (PAAs), which gives rise to bilateral carotid arteries, segment of aortic arches, pulmonary artery, and ductus arteriosus (584). Consequently, removal of CaNCC during development causes inappropriate PAA regression and leads to type b interrupted aortic arch in mouse models (584). Furthermore, prior studies demonstrated that the presence of CaNCC promotes cardiac septation in mouse (594) and its absence leads to ventricular septal defects (VSDs) (585). Importantly, Clouthier et al (1998) demonstrated that mice with defective ET-1/ET_A signalling share features of velocardiofacial syndrome (230) like those of CaNCC migration failure. On the other hand, other than significant size shrinkage, *sl/sl* rat seems to exhibit a grossly normal heart; neither large vessel nor cardiac septal anomaly is detected. Although

prior lineage-tracing studies has not revealed the participation of CaNCC in the developments of myocardium and epicardium (595), biomarker studies using *Plxna2*, fate-mapping, and the finding of thin ventricular myocardium as a result of CaNCC gene knock-out studies (e.g. BMPR1A and PAX3) suggest CaNCC contributes to epicardial developments and ventricular myocardium (596-598). Concordantly, we found marked atrial and ventricular shrinkage in the heart of *sl/sl* rat, supporting subtle alterations in CaNCC pathway from ET-1/ET_A hyperstimulation may partially contribute to the myocardium maldevelopment.

Disruption in ET_B's vascular control may have partially contributed to the cardiac maldevelopment in *sl/sl* rat. ET_B is predominantly expressed in the vascular endothelium where it initiates vasodilation through binding with ET-1 and thus triggers decreased clearance of NO, prostacyclin, and EDRF. On the other hand, subtle ET_B presence has also been detected in VSMC, where activation by ET-1 causes vascular constriction; albeit this effect is minor in normal physiological state (189, 236, 536, 599). Nilsson et al (2008) illustrated ET_B's functional duality through stronger recordings of vasoconstrictive response in endothelium-denuded porcine coronary artery with Sarafotoxin 6c (600). This shows endothelial ET_B partially regulates baseline vasodilation and basal coronary perfusion, both of which are vital to the developing heart. Adding insult to injury, the absence of ET_B markedly reduces the clearance of ET-1 and thus increases ET-1 level by up to 6-folds in *sl/sl* rats (381). This is expected to cause elevated ET-1/ET_A stimulation and subsequent hyper-vasoconstriction of coronary artery. Consequently, coronary hypoperfusion worsens growth retardation of the heart, as shown by Figure 3 to 5 (601). Interestingly, the pattern of stepwise reduction in heart volume, growth rates, organ volume/bodyweight ratios correspond well with decreasing functional ET_B copies, as shown by Supplementary Figure 1

to 3. This pattern is also consistent with the inverse relationship between myocardial perfusion and the concentration of ET-1 perfusate to coronary artery (601). Furthermore, Figure 6 illustrates that reductions in ventricular myocardium is slightly more prominent than that of atrial myocardium, which may reflect variance in rat coronary arterial distribution; albeit this regional difference is very small.

Lastly, three-dimensional analyses made on aortic arch demonstrated no conclusive ET_B-dependent relationship, as shown by Figure 3 to 5. On the other hand, a subtle decrease in aortic luminal diameter is observed in *sl/sl* rat, as noted by Supplementary Table 1. This reflects the likely elevated basal vasoconstriction at the time of culling, likely mediated by elevated ET-1/ET_A signalling. This finding is consistent with prior reports that contractile control in large vessels is predominantly ET_A-mediated (586).

Overall, our result showed distinctive difference in cardiac growth between *sl/sl* and the control groups. The effect of ET_B on cardiogenesis is likely multifactorial rather than a pure manifestation of HSCR individual's poor growth (593). Although we cannot be certain on the exact pathogenesis of ET_B dysfunction leading to the cardiac reduction, in conjunction with prior studies, hypoperfusion from vascular dysregulation seems likely. Nevertheless, we acknowledge the possibility of growth impairment from enteric dysfunction and changes in CaNCC colonization to the developing heart, albeit these effects are likely minor if presented. Importantly, our finding provides a clue to the suspected cardiac impairment associated with HSCR, a traditionally thought surgical disease. Indeed, if this quantitative finding is translatable to human, HSCR patients are likely to suffer a significant cardiac structural reduction, ranging from 20% to 40%, and thereby increases risk for development of cardiac

failure, at least in the $ET_B^{-/-}$ subtype. Consequently, a wholistic management may be warranted.

Our findings suggest early screening for cardiovascular risk factors in individuals with HSCR may be beneficial, especially in those with $ET_B^{-/-}$ subtype. In conjunction to the known vascular dysfunction related to $ET_B^{-/-}$ mutation, significant structural compromise in the heart of animal model suggests a potential risk for cardiac dysfunction. Thus, a structural review using cardiac magnetic resonance imaging (MRI) followed by a baseline echocardiogram may be beneficial. Additionally, clinical uses of endothelin receptor antagonists should be with increasing caution given the potential adverse effect of ET_B inhibition.

5. Limitations

Although we have demonstrated significant structural defects in $ET_B^{-/-}$ HSCR animals, further studies are required. Firstly, we acknowledge the statistical power can be improved by higher sampling; this can be achieved by the availability of a more efficient image segmentation platform. Secondly, despite the image analysis was completed on a pre-set computing algorithm to minimize potential bias, future study should consider adopting additional operators and various software for verification of findings. Furthermore, functional assessments with echocardiograms may be beneficial in establishing the direct correlations between cardiac dysfunction and structural impairments. Lastly, clinical study using cardiac MRI can be beneficial in confirming cardiac defects in $ET_B^{-/-}$ HSCR patients and should be considered in future studies.

6. Conclusion

This study demonstrated a correlation between ET_B function and cardiac size in the *sl/sl* rat. The exact mechanism of action is unclear at this point but may well be due to a dysfunctional coronary artery tone. Preserved cardiac morphology and aortic arch dimensions suggest impaired CaNCC migration failure may play little role in HSCR. Nevertheless, the finding of significant cardiac size and growth impairment in $ET_B^{-/-}$ HSCR model is consistent with an elevated risk of congenital structural heart disease in $ET_B^{-/-}$ HSCR patients. It also raises the possibility that ET_B gene may have a role in the development of heart failure, coronary artery disease, and hypertension in the general population.

Chapter 6 Figures:

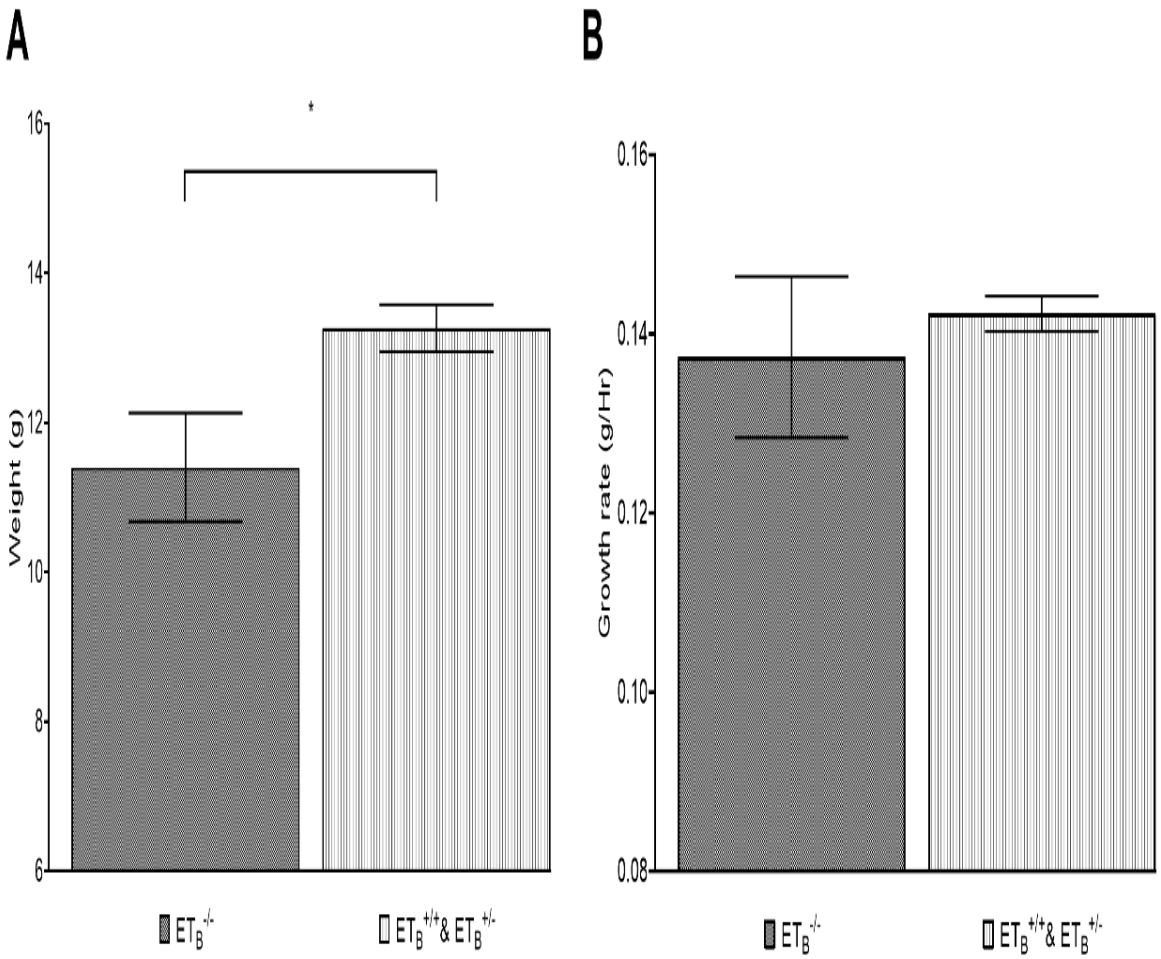

Figure 1: Decreases in bodyweight (A) and body-growth rates (B) in *sl/sl* rat.

**: statistically significant, p-value ≤ 0.05.*

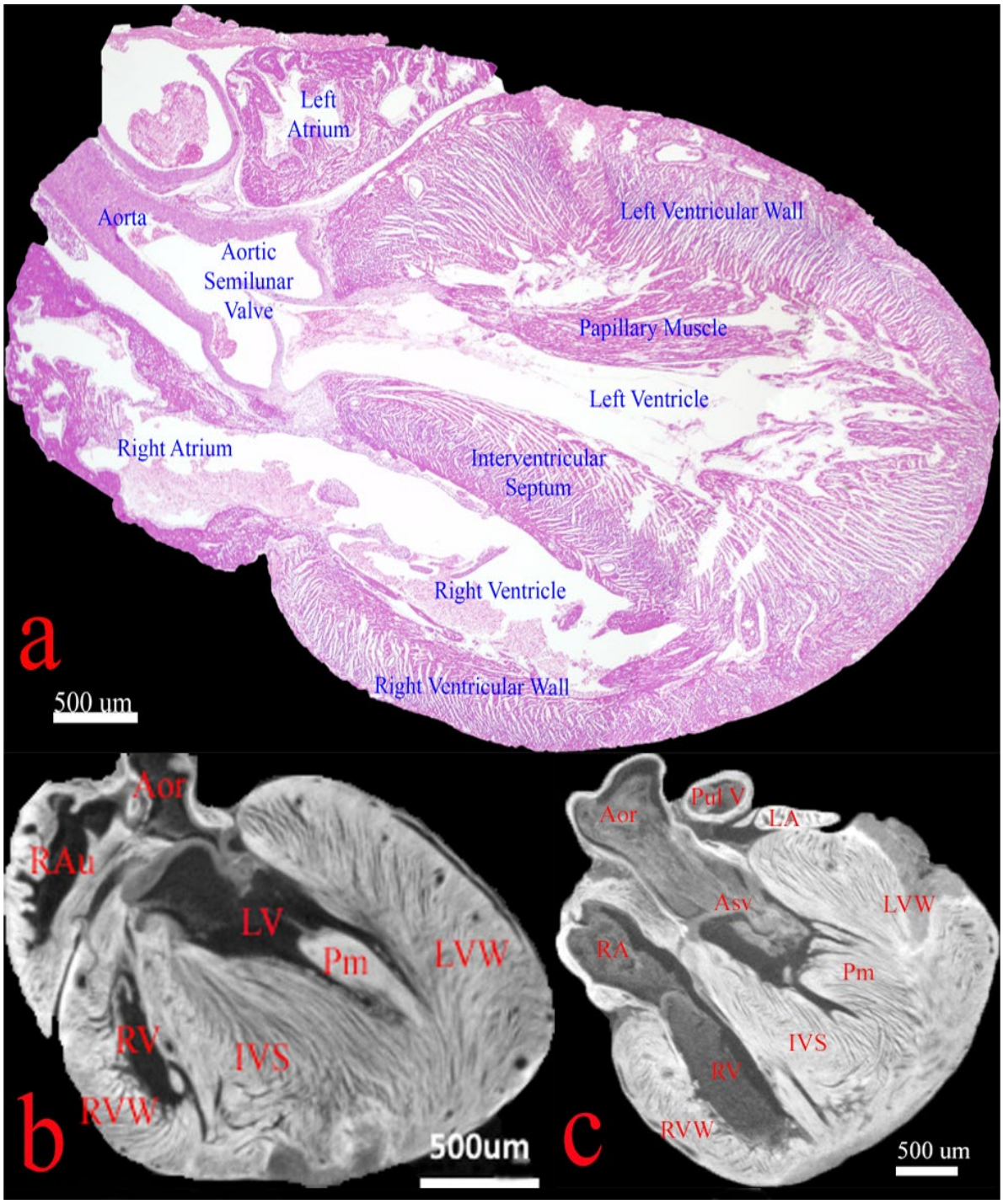

Figure 2: Grossly normal cardiac morphology and constituents in *sl/sl* rat.

Aor=Aorta; RAu=Right Auricle; RA=Right Atrium; RV=Right Ventricle; RVW=Right Ventricular Wall; IVS=Interventricular Septum; LA=Left Atrium; LV=Left Ventricle; LVW=Left Ventricular Wall; Pm=Papillary Muscle; Pul V=Pulmonary Vessel; Asv=Aortic semilunar valve.

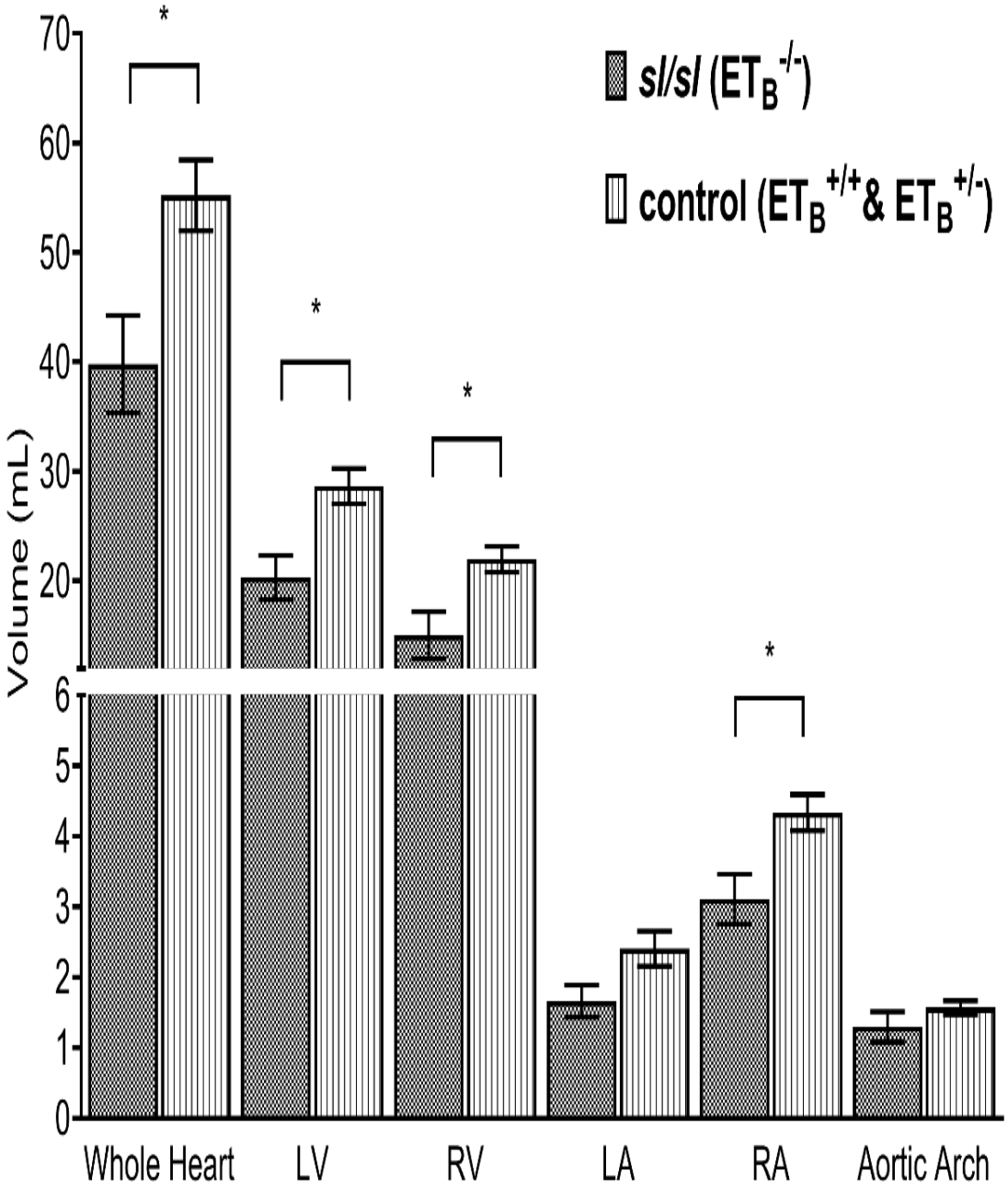

Figure 3: *sl/sl* rat has significantly smaller cardiac structures.

RA=Right Atrium; RV=Right Ventricle; LA=Left Atrium; LV=Left Ventricle.
**: statistically significant, p-value ≤ 0.05.*

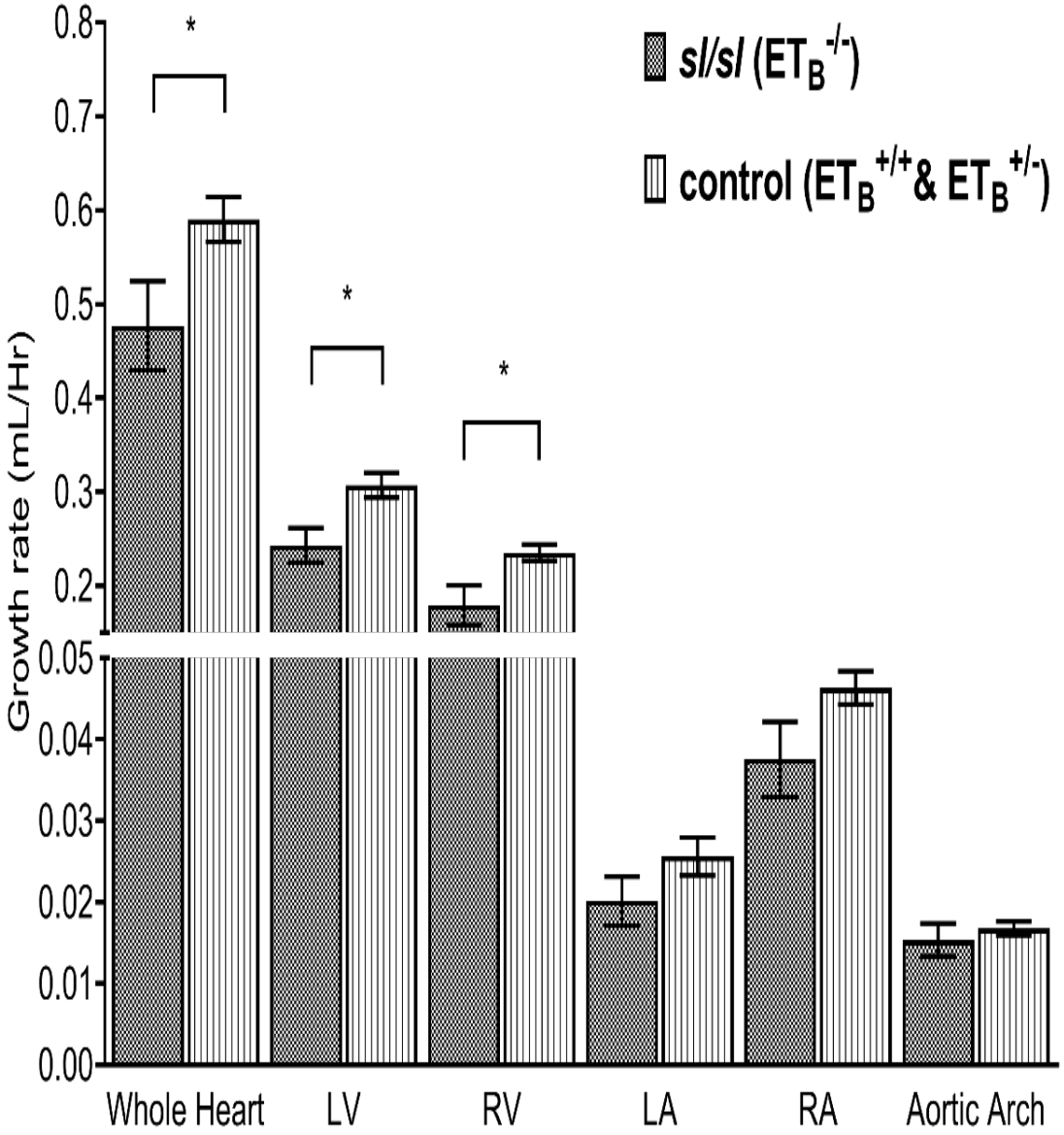

Figure 4: *sl/sl* rat has lower cardiac growth rates than the control group.

between the two groups in LV (0.24mm^3/Hr versus 0.31mm^3/Hr, *p-value* = 0.02) and RV (0.18mm^3/Hr versus 0.23mm^3/Hr, *p-value* = 0.03). Albeit not reaching statistical power, decreasing trend is also seen in LA (0.020mm^3/Hr versus 0.026mm^3/Hr, *p-value* = 0.18) and RA (0.038mm^3/Hr versus 0.046mm^3/Hr, *p-value* = 0.10). Aortic arch measurement shows little difference between the two groups: 0.015mm^3/Hr versus 0.017mm^3/Hr, *p-value* = 0.51.

RA=Right Atrium; RV=Right Ventricle; LA=Left Atrium; LV=Left Ventricle.
**: statistically significant, p-value $\leq$ 0.05.*

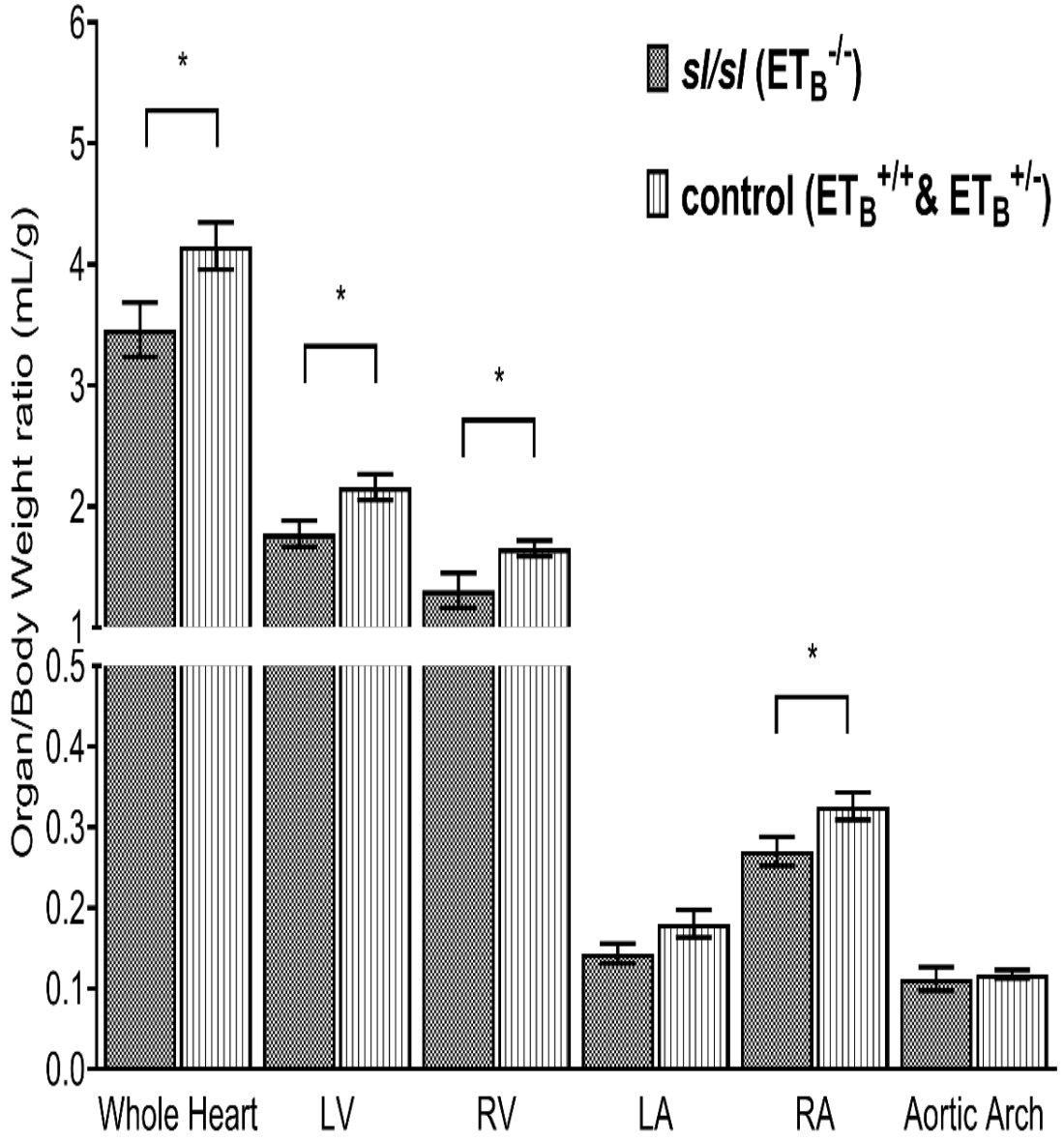

Figure 5: *sl/sl* rat has disproportionally larger reductions in its heart size with respect to its bodyweight.

RA=Right Atrium; RV=Right Ventricle; LA=Left Atrium; LV=Left Ventricle.
**: statistically significant in comparison to $ET_B^{-/-}$ group, $p \leq 0.05$.*

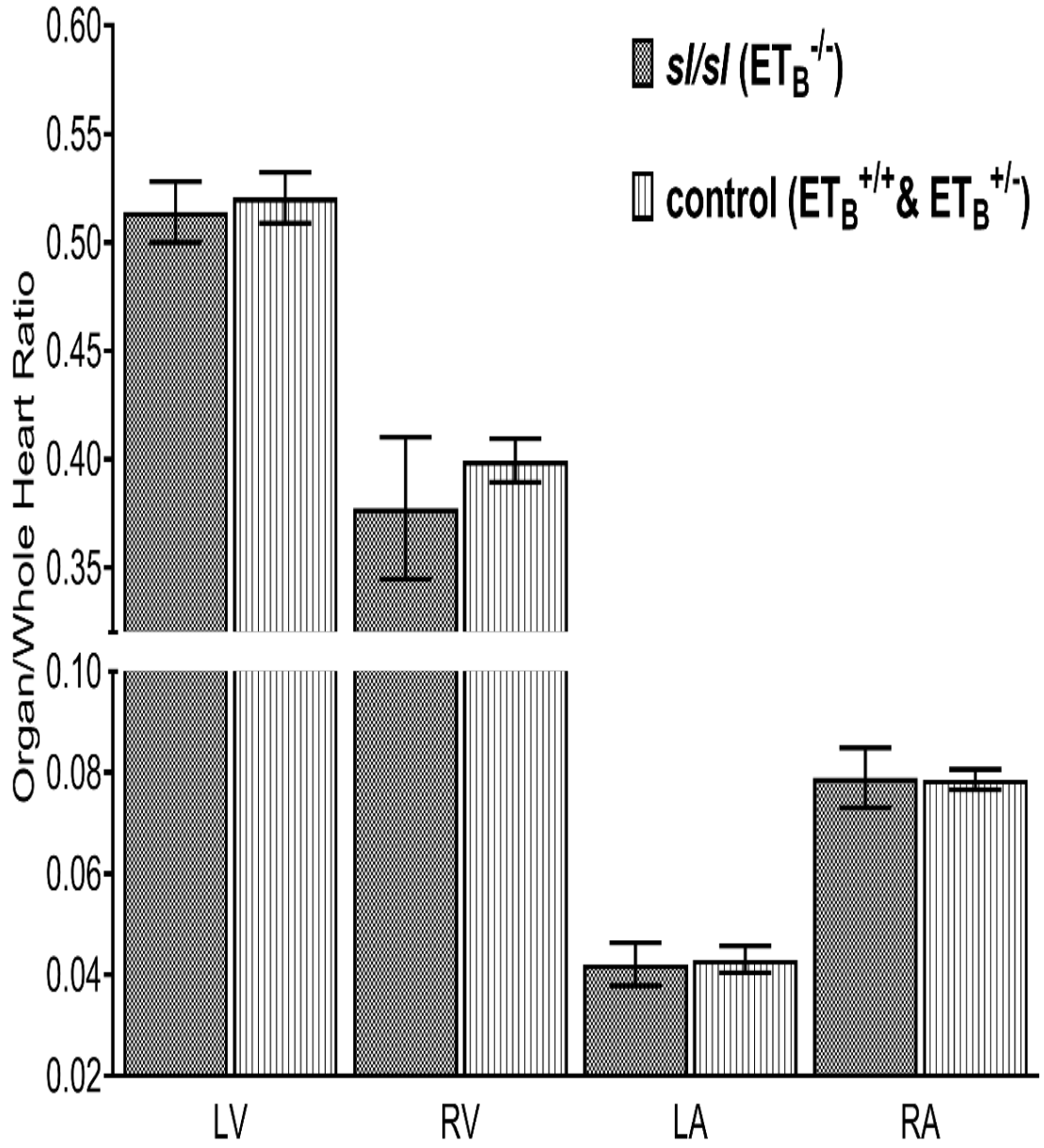

Figure 6: Cardiac shrinkage in *sl/sl* rat is relatively uniform across four major constituents.

Chapter 6 Supplementary Figures:

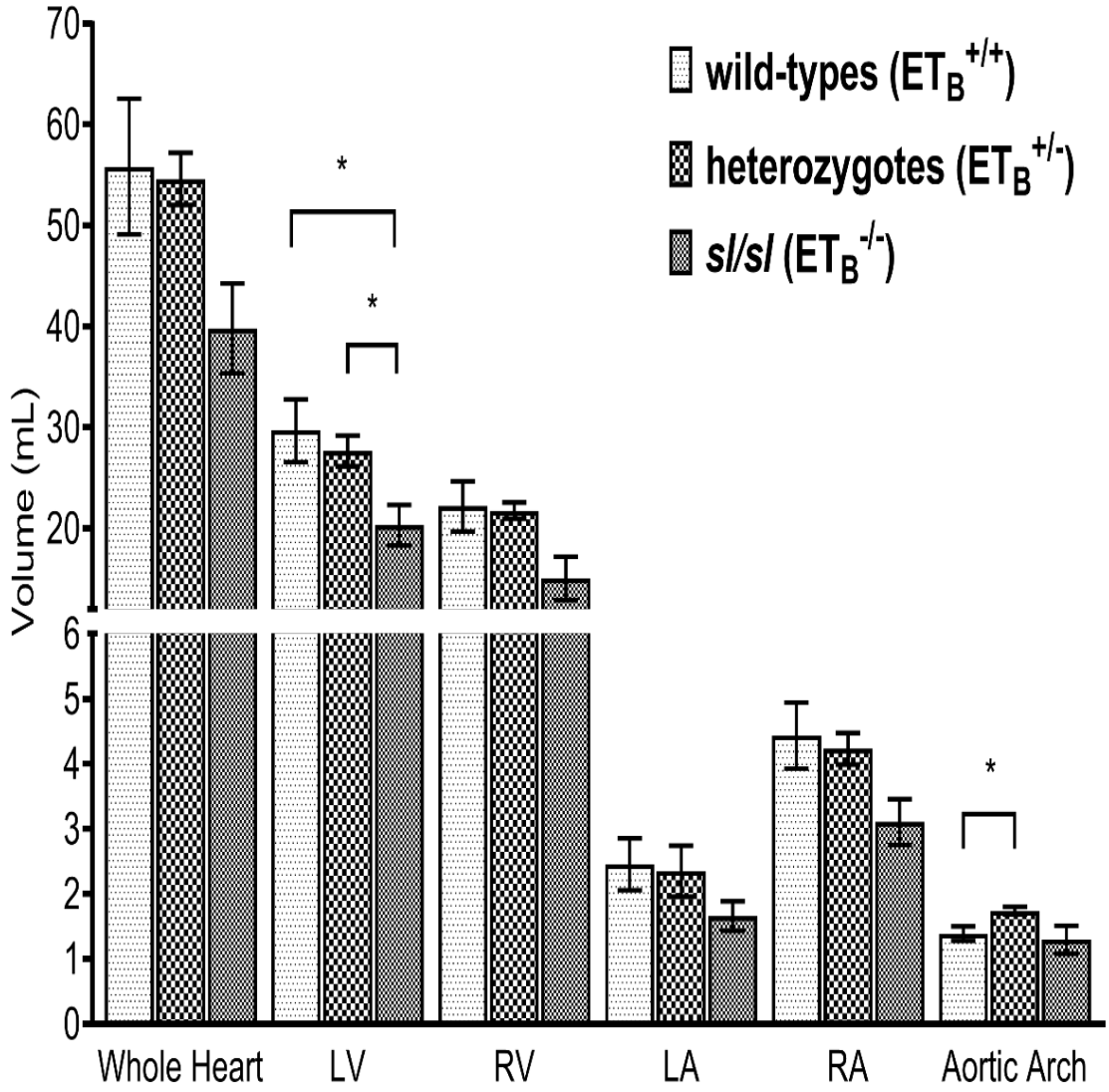

Supplementary Figure 1: Stepwise shrinkages are associated with decreasing functional ET_B.

RA=Right Atrium; RV=Right Ventricle; LA=Left Atrium; LV=Left Ventricle.
**: statistically significant in comparison to $ET_B^{-/-}$ group, $p \leq 0.05$.*

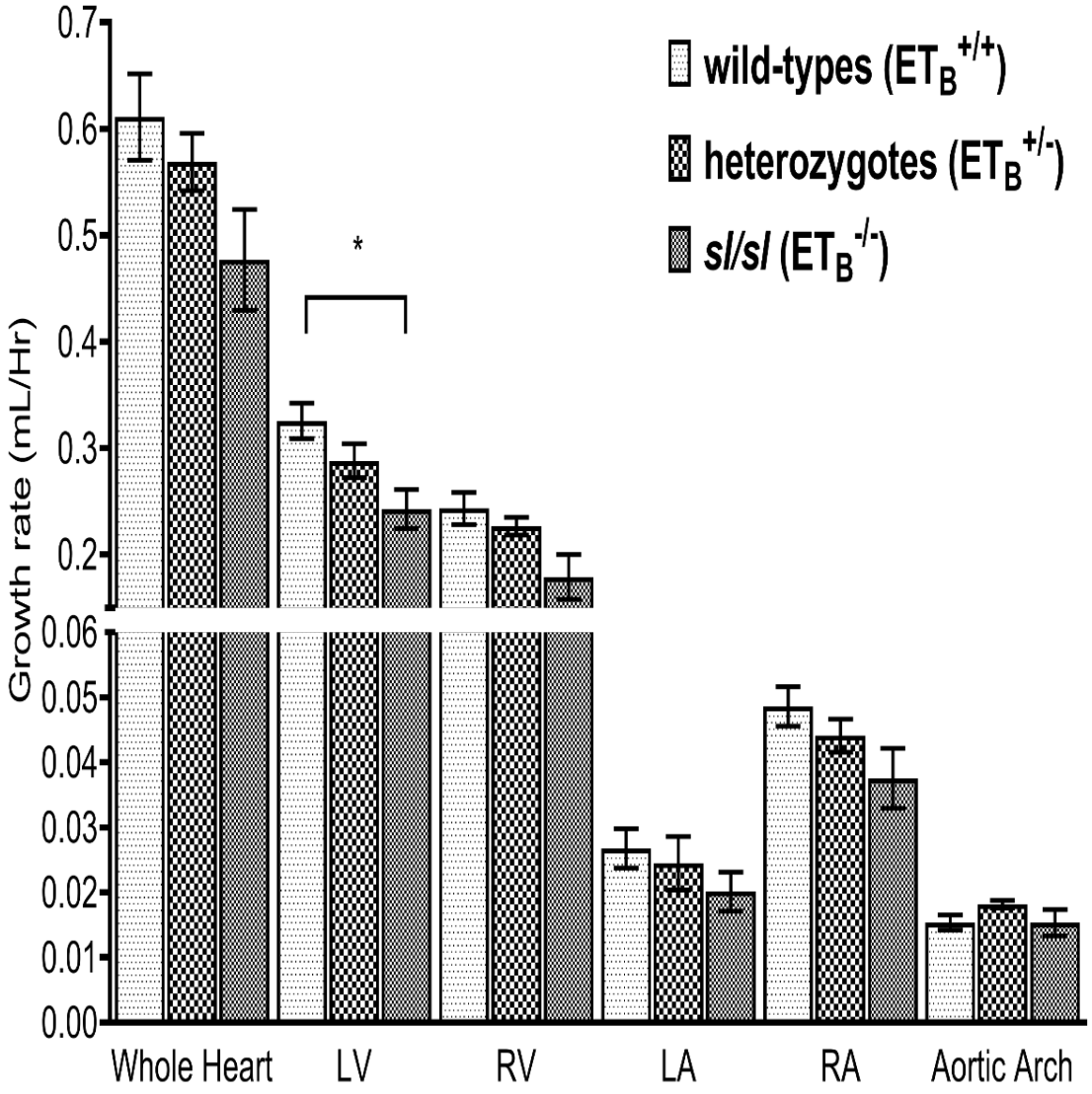

Supplementary Figure 2: Stepwise growth rate reduction is associated with decreasing functional ET_B.

RA=Right Atrium; RV=Right Ventricle; LA=Left Atrium; LV=Left Ventricle.
**: statistically significant in comparison to $ET_B^{-/-}$ group, $p \leq 0.05$.*

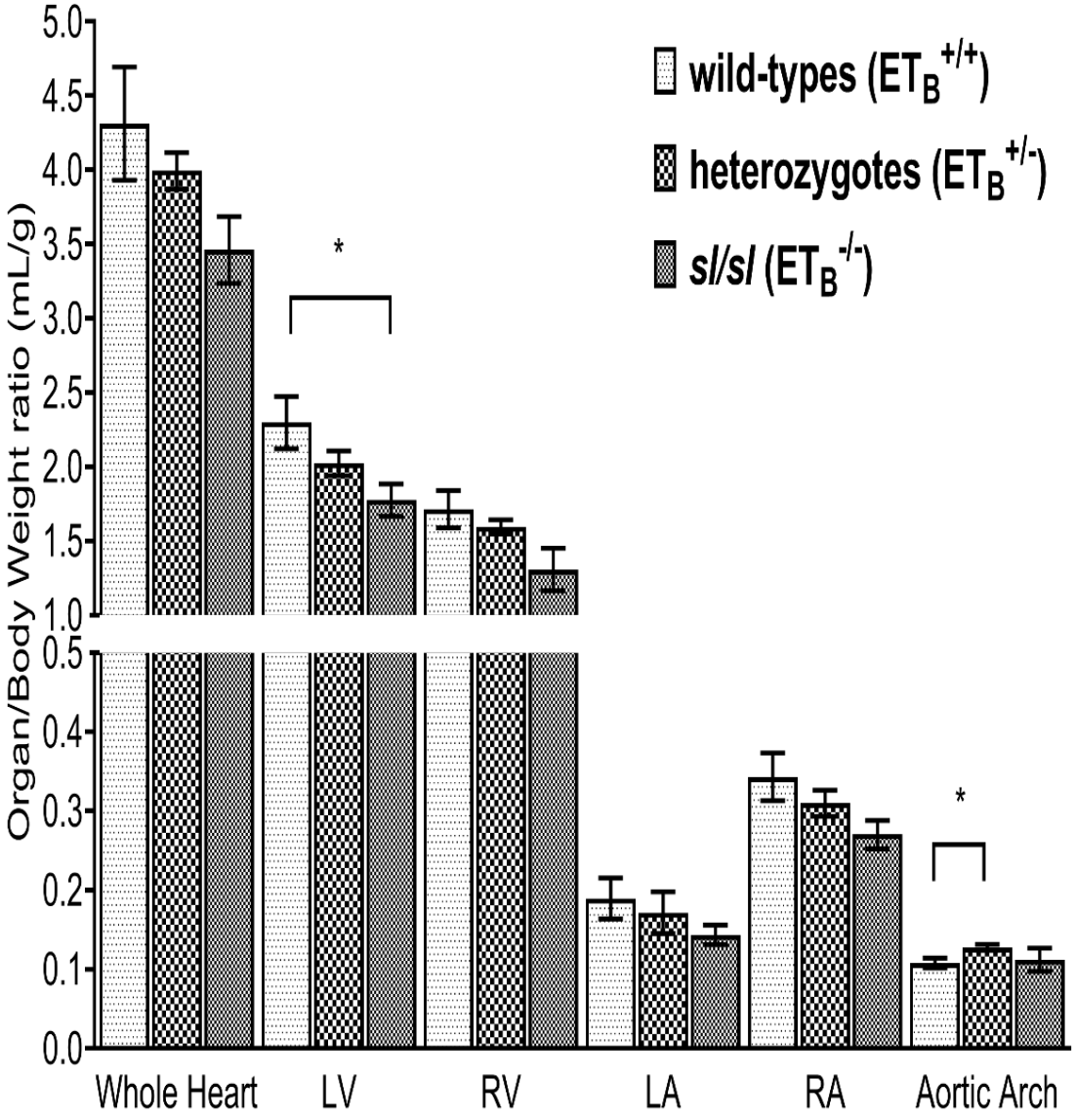

Supplementary Figure 3: stepwise reduction in organ/bodyweight ratio associated with decreasing copies of functional ET_B.

RA=Right Atrium; RV=Right Ventricle; LA=Left Atrium; LV=Left Ventricle.
**: statistically significant in comparison to $ET_B^{-/-}$ group, $p \leq 0.05$.*

Chapter 6 Supplementary Tables:

Dimensions	*sl/sl* ($ET_B^{-/-}$)	Control ($ET_B^{+/+}$ & $ET_B^{+/-}$)	Wildtypes ($ET_B^{+/+}$)	Heterozygotes ($ET_B^{+/-}$)
Aortic Arch (AA)				
AA luminal width (mm)	0.43	0.59	0.53	0.65
AA luminal width growth rate (mm/Hr)	0.0052	0.0063	0.0058	0.0068
AA luminal width/bodyweight (mm/g)	0.038	0.044	0.041	0.048

Supplementary Table 1: *sl/sl* rat has reduced luminal width of aortic arch when comparing to the control groups.

Two-dimensional measurement at the orifice of aortic valve showed *sl/sl* rat having a smaller intravascular width comparing to the control group. This trend persists when measurements are standardized to respective age and bodyweight, as shown by the comparison of width growth rate and width/bodyweight ratio, suggesting possible vasoconstrictions.

Chapter 7: Thesis Conclusion

This series of study demonstrates high-resolution soft-tissue imaging can be achieved by micro-CT scanning with modified protocols. Although the preparation processes involve sacrificing the animals for tissue staining and prolonged scanning, the resultant images offer excellent anatomical details with good soft-tissue contrast, a previous limiting factor for X-ray based imaging modality on biological studies. Furthermore, iodine-stained tissues retain the structural integrity and offers potential for future study, including traditional microscopy and immunohistochemistry. More importantly, through the use of image-analysis software, quantitative dimensional and volumetric analysis are possible.

Apart from devising a functional micro-CT imaging workflow for tissue study on postnatal animals, this series of study provides supporting evidence that $ET_B^{-/-}$ HSCR is likely a multi-organ disease with ET_B playing important roles in multi-organ development.

Endothelin B receptor regulates multiple signalling pathways and therefore acts as a major predisposing gene for HSCR. Traditionally, the effect of dysfunctional ET_B is thought to be restricted to the development of ENS and with little impact to the rest of the body, despite HSCR being a neurocristopathy. While many studies have suggested ET_B signalling pathways affect organogenesis, our study provides supporting quantitative evidence on the craniofacial, neural, and cardiac changes associated with HSCR and ET_B mutations. Indeed, structural analyses using high-definition micro-CT imaging on the animal model of $ET_B^{-/-}$ HSCR, *sl/sl* rat, demonstrates multi-organ impairments.

1. Basic parameters of $ET_B^{-/-}$ mutant, *sl/sl* rat

Our study reaffirms the basic genetic characteristics of *sl/sl* rat and quantifies penetrance in this model. Through retrospective analysis on the colony data of 864 offspring derived from crossbreeding between heterozygotes ($ET_B^{+/-}$), genetic makeup of the population follows closely to the expected 1:2:1 Mendelian inheritance ratio: $ET_B^{+/+}$ (n=203; 24%), $ET_B^{+/-}$ (n=398; 46%), and $ET_B^{-/-}$ (n=263; 30%), *p-value* = 0.001. Gender correlation reveals that there is slightly more male *sl/sl* rat. Additionally, high genetic penetrance is observed when correlating *sl/sl* phenotype with $ET_B^{-/-}$genotype. Over 95% of the *sl/sl* rats suffers colonic aganglionosis, only 1.9 % (normal bowel = 362; aganglionic = 7) of heterozygote and <1% (normal bowel = 156; aganglionic = 1) of wild type share similar phenotype. Little difference is observed between the latter two groups in terms of abnormal phenotypic incidences. These observations are consistent with HSCR in that *sl/sl* rat being a variably penetrant sex-modified autosomal recessive condition: a weak penetrance when heterozygous and strong penetrance when homozygous; a stronger penetrance on a male background and weaker on a female background. These characters correspond well with human HSCR. Therefore, despite HSCR being a multi-genetic neurocristopathy in general, *sl/sl* rat provided a clean animal model for studying the effect of ET_B and HSCR-associated manifestations.

Contrary to previous expectation, little growth impairment is observed in the neonatal stage. Based on our colony data of 864 offspring, little or no body-size reduction is detected in *sl/sl* rat for its first 48 hours of life. On the other hand, body-growth reduction becomes more apparent after the age of 7-days. This is consistent with growth being delayed by the developing starvation related to bowel obstruction from the HSCR. Therefore,

anatomical changes observed in neonatal animals <7 days of age are likely direct consequences of signalling disruption in target organs by ET_B mutation.

2. Craniofacial changes associated with HSCR model, *sl/sl* rat

Contrary to the initial reporting made by Hosoda et al (1994), we detect subtle craniofacial changes in *sl/sl* rats (354). Globally, *sl/sl* rats have approximately 5% reductions in craniofacial structures based on dimensional measurements. These changes share high resemblance with previously described "domestication syndrome" with distinctive features include flatter cranium, smaller oral orifice and dentition, shorter but wider nose, and subtle dystopia canthorum. Given the latter phenotype being the hallmark of PAX3-induced WS-I, its presence in ET_B-induced WS-IV model suggests a possible overlapping regulatory pathway between the two genes, at least in parts of craniofacial development. These findings support ET_B being a potential mediator in the neural crest cell alteration of domestication development.

While there is no direct signalling linkage documented between ET_B and cephalic neural crest cell (CNCC) migration, the observed changes may be explained by the indirect impact of ET_B on ET-1/ET_A pathway. Indeed, it has been determined that ET-1/ECE/ET_A regulates the migration of cephalic and vagal neural crest cell, which ultimately controls the craniofacial development. Consequently, disruption of this pathway results in severe dysmorphic features leading to mechanical asphyxia and thus perinatal death. These phenomena are seen in CATCH22 or velocardiofacial syndrome (230) as a result of hypostimulation of ET-1/ET_A signalling. On the other hand, ET_B-knockout reduces ET-1 clearance and removes the negative feedback on ET-1/ET_A signalling. Consequently, elevated

ET-1, up to 6-folds in *sl/sl* rat, can hyper-stimulate ET-1/ET_A signalling, an effect well illustrated by the elevation of blood pressure in $ET_B^{-/-}$ mutants or subjects treated with ET_B antagonists (378, 381). By the same reasoning, one can expect this hyperstimulation to modulate CNCC migration, leading to the subtle craniofacial changes observed in this series of study rather than the manifestations of full-blown CNCC migration failure.

Given similar pathogenesis are shared by *sl/sl* rat and $ET_B^{-/-}$ HSCR patients, this finding may be extrapolated in clinical setting. If so, it may be reasonable to suspect HSCR patients, at least $ET_B^{-/-}$ subtype, to have higher risks for obstructive sleep apnoea or dysphagia from nasal and oral passage malformations. Further correlation study on human scans is therefore warranted.

3. Structural changes in central nervous system of $ET_B^{-/-}$ HSCR model, *sl/sl* rat

Despite only subtle changes detected in its craniofacial morphology, significant changes in brain sizes and constituents are detected in *sl/sl* rat. Unlike HSCR-associated Mowat-Wilson syndrome, which has been suggested to exhibit agenesis of corpus callosum and hippocampus (562), micro-CT scans of *sl/sl* rat brain show the presence of all neural constituents. On the other hand, 20.33% volumetric reduction of the brain is detected in *sl/sl* rat when comparing with that of the control group. Similar pattern is observed in the measurements of the following constituents: cerebral cortex (24.60%, *p-value* = 0.02), caudate putamen (24.68%, *p-value* = 0.03), olfactory bulb (19.13%, *p-value* = 0.02), pituitary gland (30.08%, *p-value* = 0.02), medulla (21.05%, *p-value* = 0.11), and cerebellum (14.22%, *p-value* = 0.22). This decreasing trend continues to persist in the evaluations of organ growth rate and organ/bodyweight ratios; both indices show *sl/sl* mutant having disproportionally a

lower neural growth and brain proportions with respect to its body size. Furthermore, these changes are non-uniform and likely regional-dependent, consistent with elevation pattern of GDNF, a potent neurotrophic factor, triggered by $Ala^{1,3,11,15}$-ET-1, a ET_B-selective agonist (567). As a result, our study supports ET_B contributing to the CNS development, which is not explicitly stated previously.

Overall, our findings support homozygous knockout mutation of ET_B, one of the major causes of HSCR, exerting a negative impact on CNS development. While there are no reports commenting on the direct linkage between ET_B and neural induction during development, the observed neural growth impairment may be explained by several ET_B functions exerting indirect control. Firstly, ET_B activation by ET-1 mediates direct basal vasodilation by endothelium, which regulates blood supply to the growing central nervous system (CNS). Secondly, functional ET_B manages up to 80% of ET-1 degradation and exerts a negative feedback on the endothelial ECE-1 expression (387, 389); removal of ET_B thus causes marked ET-1 elevation and triggers hyperstimulation of ET-1/ET_A. Consequently, unchecked vasoconstriction in cerebral, meningeal, temporal and pial arteries reduces perfusion to the growing brain (319, 320). Moreover, ET-1/ET_B interaction can promote endothelial proliferation and angiogenesis (372), an important factor for the growing brain. Overall, we provide supporting macroscopic evidence showing impaired brain growth is associated with HSCR model, at least $ET_B^{-/-}$ subtype.

4. Cardiovascular changes detected in $ET_B^{-/-}$ HSCR model

As previously reported, endothelin system plays pivotal roles in the development of cardiovascular system and vasculature homeostasis. While majority of these studies are

focused on ET_A, we question ET_B's impact on the developing heart in a HSCR model. Unlike mutants with dysfunctional ET-1/ECE/ET_A signalling known to exhibit conotruncal malformations, with features include disrupted aortic arch, pulmonary atresia, and cardiac septal defects as seen in velocardiofacial syndrome (230), cardiac morphology in *sl/sl* rats appears to be normal on micro-CT scans. On the other hand, statistically significant volumetric size reductions are detected in the neonatal heart of *sl/sl* rat. Indeed, *sl/sl* group displays 38.70% volumetric reduction in heart, *p-value* = 0.02. Similar reductions are also observed in the following constituents: left atrium (44.93%, *p-value* = 0.06), left ventricle (41.22%, *p-value* = 0.01), right atrium (39.49%, *p-value* = 0.02), and right ventricle (46.15%, *p-value* = 0.02). This impairing relationship between ET_B mutation and the heart growth is supported by the growth rates comparison, with *sl/sl* rat having 23.42% to 31.25% reductions across all organs analysed. These findings imply heart size disparity may continue to worsen until animal reaches maturity. Furthermore, *sl/sl* rat has a reduction ranging from 20.00% to 27.36% in organ volume/body weight ratios, reflecting a disproportionally larger reduction in heart with respect to changes in its body size. Furthermore, this also demonstrates ET_B's impacts are likely organ specific or regional dependent. On the other hand, measurements made on aortic arch reveals no significant difference between the control and *sl/sl* groups.

Overall, our animal findings support the notion that HSCR patients are likely to exhibit structural cardiac growth impairment, at least in $ET_B^{-/-}$ individuals. The pathogenesis contributes to this impairment can be explained by the following. Firstly, potential alterations in ET-1/ET_A signalling from elevated ET-1 can cause changes in the colonization of cardiac outflow tract by cardiac neural crest cell (228). However, we suspect this effect to be minor given the absence of typical ventricular septal defect, aortic arch and pulmonary vasculature

malformations associated with cardiac NCC migration failure (584, 585). This is further supported by the little change seen in the aortic arch measurements. More importantly, reduced coronary perfusion to the growing heart from hyper-vasoconstriction likely plays a key role in retarding the heart growth. This hyper-vasoconstriction is due to a loss of endothelial ET_B-mediated basal vasodilation and elevated ET-1/ET_A stimulation in VSMC of coronary vessels (277, 375, 376).

5. Limitations of this study

We acknowledge there are several limitations in this series of studies. The intrinsic limitations of an animal study limit definitive statements on the clinical effect of ET_B mutation to be drawn; however, significant multi-organ changes detected in $ET_B^{-/-}$ animals nevertheless shed some light on its potential impact to human subjects. Further study on human subjects is therefore worthwhile. Secondly, the findings from this series of study can only be safely attributed to ET_B mutation despite polygenetic pathogenesis of HSCR shares many overlapping controls and thus clinical manifestations. Thirdly, in conjunction with significant structural impairments detected in $ET_B^{-/-}$ mutants, functional studies may be beneficial in terms of assessing cardiovascular and neurological capability. Fourthly, statistical power will benefit from a larger sample size; this can be achieved with the availability of efficient micro-CT scanners and image segmentation software.

6. Conclusion

In this series of study, we provide supporting evidence that HSCR, as a neurocristopathy, likely has multi-organ impairments, at least in $ET_B^{-/-}$ subtype. These manifestations are particularly evident in the neonatal brain and the heart of $ET_B^{-/-}$ model

animal, with modest changes in its craniofacial morphology. Although these results are based on *sl/sl* rat, these conclusions may be extrapolated to $ET_B^{-/-}$ HSCR patients. Additionally, we have found perfusion-dependent organs, such as brain and heart, are more likely to suffer growth retardations than the exoskeleton in $ET_B^{-/-}$ mutant, thus supporting reports on ET_B's beneficial vasodilatory role and negative feedback on ET_A signalling. Consequently, our findings suggest that HSCR patients, at least $ET_B^{-/-}$ subtype, maybe possess a higher risk for neural and cardiovascular diseases. Further clinical studies are required to confirm and elucidate clinical implications. Lastly, it may be worthwhile to incorporate wholistic approach for the managements of HSCR patient rather than a pure surgical solution.

Thesis References:

1. Turbeville S, Francis KM, Behm I, Chiu GR, Sanchez H, Morrison BA, et al. Prevalence and Incidence of Acute Myeloid Leukemia May be Higher Than Currently Accepted Estimates Among the ≥65 Year-Old Population in the United States. Blood. 2014;124(21):958-.
2. Leenders E, Sieber WK. Congenital megacolon observation by Frederick Ruysch--1691. Journal of pediatric surgery. 1970;5(1):1-3.
3. Skaba R. Historic milestones of Hirschsprung's disease (commemorating the 90th anniversary of Professor Harald Hirschsprung's death). Journal of pediatric surgery. 2007;42(1):249-51.
4. Whitehouse FR, Kernohan JW. Myenteric plexus in congenital megacolon; study of 11 cases. Archives of internal medicine (Chicago, Ill : 1908). 1948;82(1):75-111.
5. Bodian M, Stephens FD, Ward BC. Hirschsprung's disease and idiopathic megacolon. Lancet. 1949;1(6540):6-11.
6. Zuelzer WW, Wilson JL. Functional intestinal obstruction on a congenital neurogenic basis in infancy. American journal of diseases of children. 1948;75(1):40-64.
7. Swenson O. My early experience with Hirschsprung's disease. Journal of pediatric surgery.24(8):839-45.
8. Russell MB, Russell CA, Niebuhr E. An epidemiological study of Hirschsprung's disease and additional anomalies. Acta paediatrica (Oslo, Norway : 1992). 1994;83(1):68-71.
9. Skinner MA. Hirschsprung's disease. Current problems in surgery. 1996;33(5):389-460.
10. Goldberg EL. An epidemiological study of Hirschsprung's disease. International journal of epidemiology. 1984;13(4):479-85.
11. Rajab A, Freeman NV, Patton MA. Hirschsprung's disease in Oman. Journal of pediatric surgery. 1997;32(5):724-7.
12. Meza-Valencia BE, de Lorimier AJ, Person DA. Hirschsprung disease in the U.S. associated Pacific Islands: more common than expected. Hawaii medical journal. 2005;64(4):96-8, 100-1.
13. Singh SJ, Croaker GD, Manglick P, Wong CL, Athanasakos H, Elliott E, et al. Hirschsprung's disease: the Australian Paediatric Surveillance Unit's experience. Pediatric surgery international. 2003;19(4):247-50.
14. Reding R, de Ville de Goyet J, Gosseye S, Clapuyt P, Sokal E, Buts JP, et al. Hirschsprung's disease: a 20-year experience. Journal of pediatric surgery. 1997;32(8):1221-5.
15. C NF, Ricour C, Martelli H, Jacob SL, Pellerin D. Total colonic aganglionosis (with or without ileal involvement): a review of 27 cases. Journal of pediatric surgery. 1986;21(3):251-4.
16. Neilson IR, Yazbeck S. Ultrashort Hirschsprung's disease: myth or reality. Journal of pediatric surgery. 1990;25(11):1135-8.
17. Kapur RP. Practical pathology and genetics of Hirschsprung's disease. Seminars in pediatric surgery. 2009;18(4):212-23.
18. Gianino S, Grider JR, Cresswell J, Enomoto H, Heuckeroth RO. GDNF availability determines enteric neuron number by controlling precursor proliferation. Development. 2003;130(10):2187-98.
19. Stanchina L, Baral V, Robert F, Pingault V, Lemort N, Pachnis V, et al. Interactions between Sox10, Edn3 and Ednrb during enteric nervous system and melanocyte

development. Developmental biology. 2006;295(1):232-49.
20. Meier-Ruge W. Epidemiology of congenital innervation defects of the distal colon. Virchows Archiv A, Pathological anatomy and histopathology. 1992;420(2):171-7.
21. Spouge D, Baird PA. Hirschsprung disease in a large birth cohort. Teratology. 1985;32(2):171-7.
22. Garver KL, Law JC, Garver B. Hirschsprung disease: a genetic study. Clinical genetics. 1985;28(6):503-8.
23. Badner JA, Sieber WK, Garver KL, Chakravarti A. A genetic study of Hirschsprung disease. American journal of human genetics. 1990;46(3):568-80.
24. Ryan ET, Ecker JL, Christakis NA, Folkman J. Hirschsprung's disease: associated abnormalities and demography. Journal of pediatric surgery. 1992;27(1):76-81.
25. Ohgami N, Iida M, Yajima I, Tamura H, Ohgami K, Kato M. Hearing impairments caused by genetic and environmental factors. Environmental Health and Preventive Medicine. 2013;18(1):10-5.
26. Borst MJ, VanCamp JM, Peacock ML, Decker RA. Mutational analysis of multiple endocrine neoplasia type 2A associated with Hirschsprung's disease. Surgery. 1995;117(4):386-91.
27. Waardenburg PJ. A new syndrome combining developmental anomalies of the eyelids, eyebrows and nose root with pigmentary defects of the iris and head hair and with congenital deafness. American journal of human genetics. 1951;3(3):195-253.
28. Croaker GDH, Shi E, Simpson E, Cartmill T, Cass DT. Congenital central hypoventilation syndrome and Hirschsprung's disease. Archives of Disease in Childhood. 1998;78(4):316-22.
29. Goldberg RB, Shprintzen RJ. Hirschsprung megacolon and cleft palate in two sibs. Journal of craniofacial genetics and developmental biology. 1981;1(2):185-9.
30. Beales PL, Elcioglu N, Woolf AS, Parker D, Flinter FA. New criteria for improved diagnosis of Bardet-Biedl syndrome: results of a population survey. Journal of medical genetics. 1999;36(6):437-46.
31. Patterson K, Toomey KE, Chandra RS. Hirschsprung disease in a 46,XY phenotypic infant girl with Smith-Lemli-Opitz syndrome. The Journal of Pediatrics. 1983;103(3):425-7.
32. Makitie O, Kaitila I. Cartilage-hair hypoplasia--clinical manifestations in 108 Finnish patients. European journal of pediatrics. 1993;152(3):211-7.
33. Amiel J, Lyonnet S. Hirschsprung disease, associated syndromes, and genetics: a review. Journal of medical genetics. 2001;38(11):729-39.
34. Coran AG, Teitelbaum DH. Recent advances in the management of Hirschsprung's disease. American journal of surgery. 2000;180(5):382-7.
35. Holschneider AM, Meier-Ruge W, Ure BM. Hirschsprung's disease and allied disorders--a review. European journal of pediatric surgery : official journal of Austrian Association of Pediatric Surgery [et al] = Zeitschrift fur Kinderchirurgie. 1994;4(5):260-6.
36. Khan AR, Vujanic GM, Huddart S. The constipated child: how likely is Hirschsprung's disease? Pediatric surgery international. 2003;19(6):439-42.
37. Holland SK, Hessler RB, Reid-Nicholson MD, Ramalingam P, Lee JR. Utilization of peripherin and S-100 immunohistochemistry in the diagnosis of Hirschsprung disease. Modern pathology : an official journal of the United States and Canadian Academy of Pathology, Inc. 2010;23(9):1173-9.
38. Frager D, Medwid SW, Baer JW, Mollinelli B, Friedman M. CT of small-bowel obstruction: value in establishing the diagnosis and determining the degree and cause. AJR American journal of roentgenology. 1994;162(1):37-41.

39. Peyvasteh M, Askarpour S, Ostadian N, Moghimi M-R, Javaherizadeh H. DIAGNOSTIC ACCURACY OF BARIUM ENEMA FINDINGS IN HIRSCHSPRUNG'S DISEASE. Arquivos Brasileiros de Cirurgia Digestiva : ABCD. 2016;29(3):155-8.
40. Smith GHH, Cass D. Infantile Hirschsprung's disease — is a barium enema useful? Pediatric surgery international. 1991;6(4):318-21.
41. Nofech-Mozes Y, Rachmel A, Schonfeld T, Schwarz M, Steinberg R, Ashkenazi S. Difficulties in making the diagnosis of Hirschsprung disease in early infancy. Journal of paediatrics and child health. 2004;40(12):716-9.
42. Iwai N, Yanagihara J, Tokiwa K, Deguchi E, Perdzynski W, Takahashi T. Reliability of anorectal manometry in the diagnosis of Hirschsprung's disease. Zeitschrift fur Kinderchirurgie : organ der Deutschen, der Schweizerischen und der Osterreichischen Gesellschaft fur Kinderchirurgie = Surgery in infancy and childhood. 1988;43(6):405-7.
43. Hirsh EH, Hodges KS, Hersh T, McGarity WC. Anorectal manometry in the diagnosis of Hirschsprung's disease in adults. The American journal of gastroenterology. 1980;74(3):258-60.
44. Gad El-Hak NA, El-Hemaly MM, Negm EH, El-Hanafy EA, AbdEl Messeh MH, AbdEl Bary HH. Functional Outcome after Swenson's Operation for Hirshsprung's Disease. Saudi Journal of Gastroenterology : Official Journal of the Saudi Gastroenterology Association. 2010;16(1):30-4.
45. Pensabene L, Youssef NN, Griffiths JM, Di Lorenzo C. Colonic manometry in children with defecatory disorders. role in diagnosis and management. The American journal of gastroenterology. 2003;98(5):1052-7.
46. Martin MJ, Steele SR, Noel JM, Weichmann D, Azarow KS. Total colonic manometry as a guide for surgical management of functional colonic obstruction: Preliminary results. Journal of pediatric surgery. 2001;36(12):1757-63.
47. Andrassy RJ, Isaacs H, Weitzman JJ. Rectal suction biopsy for the diagnosis of Hirschsprung's disease. Annals of Surgery. 1981;193(4):419-24.
48. Kurer MH, Lawson JO, Pambakian H. Suction biopsy in Hirschsprung's disease. Arch Dis Child. 1986;61(1):83-4.
49. Tsuji S, Larabi Y. A modification of thiocholine-ferricyanide method of Karnovsky and Roots for localization of acetylcholinesterase activity without interference by Koelle's copper thiocholine iodide precipitate. Histochemistry. 1983;78(3):317-23.
50. Guinard-Samuel V, Bonnard A, De Lagausie P, Philippe-Chomette P, Alberti C, El Ghoneimi A, et al. Calretinin immunohistochemistry: a simple and efficient tool to diagnose Hirschsprung disease. Modern Pathology. 2009;22:1379.
51. Aldridge RT, Campbell PE. Ganglion cell distribution in the normal rectum and anal canal. A basis for the diagnosis of Hirschsprung's disease by anorectal biopsy. Journal of pediatric surgery. 1968;3(4):475-90.
52. Swenson O, Fisher JH, MacMahon HE. Rectal Biopsy as an Aid in the Diagnosis of Hirschsprung's Disease. New England Journal of Medicine. 1955;253(15):632-5.
53. Kiernan JA. Histological and histochemical methods : theory and practice. 3rd ed. Oxford [U.K.]: Butterworth-Heinemann; 1999. x, 502 p.
54. Karnovsky MJ, Roots L. A "DIRECT-COLORING" THIOCHOLINE METHOD FOR CHOLINESTERASES. The journal of histochemistry and cytochemistry : official journal of the Histochemistry Society. 1964;12:219-21.
55. Ikawa H, Kim SH, Hendren W, P KD. Acetylcholinesterase and manometry in the diagnosis of the constipated child. Archives of Surgery. 1986;121(4):435-8.

56. Lake BD, Puri P, Nixon HH, Claireaux AE. Hirschsprung's disease: an appraisal of histochemically demonstrated acetylcholinesterase activity in suction rectal biopsy specimens as an aid to diagnosis. Archives of pathology & laboratory medicine. 1978;102(5):244-7.
57. de Brito IA, Maksoud JG. Evolution with age of the acetylcholinesterase activity in rectal suction biopsy in Hirschsprung's disease. Journal of pediatric surgery. 1987;22(5):425-30.
58. Goto S, Ikeda K, Toyohara T. Histochemical confirmation of the acetylcholinesterase-activity in rectal suction biopsy from neonates with Hirschsprung's disease. Zeitschrift fur Kinderchirurgie : organ der Deutschen, der Schweizerischen und der Osterreichischen Gesellschaft fur Kinderchirurgie = Surgery in infancy and childhood. 1984;39(4):246-9.
59. Barshack I, Fridman E, Goldberg I, Chowers Y, Kopolovic J. The loss of calretinin expression indicates aganglionosis in Hirschsprung's disease. Journal of clinical pathology. 2004;57(7):712-6.
60. Baimbridge KG, Celio MR, Rogers JH. Calcium-binding proteins in the nervous system. Trends in neurosciences. 1992;15(8):303-8.
61. Kapur RP, Reed RC, Finn LS, Patterson K, Johanson J, Rutledge JC. Calretinin immunohistochemistry versus acetylcholinesterase histochemistry in the evaluation of suction rectal biopsies for Hirschsprung Disease. Pediatric and developmental pathology : the official journal of the Society for Pediatric Pathology and the Paediatric Pathology Society. 2009;12(1):6-15.
62. Hackam DJ, Superina RA, Pearl RH. Single-stage repair of Hirschsprung's disease: a comparison of 109 patients over 5 years. Journal of pediatric surgery. 1997;32(7):1028-31; discussion 31-2.
63. Ramesh JC, Ramanujam TM, Yik YI, Goh DW. Management of Hirschsprung's disease with reference to one-stage pull-through without colostomy. Journal of pediatric surgery. 1999;34(11):1691-4.
64. Sulkowski JP, Cooper JN, Congeni A, Pearson EG, Nwomeh BC, Doolin EJ, et al. Single-Stage Versus Multi-Stage Pull-Through for Hirschsprung's Disease: Practice Trends and Outcomes in Infants. Journal of pediatric surgery. 2014;49(11):1619-25.
65. Swenson O, Bill AH, Jr. Resection of rectum and rectosigmoid with preservation of the sphincter for benign spastic lesions producing megacolon; an experimental study. Surgery. 1948;24(2):212-20.
66. Duhamel B. A New Operation for the Treatment of Hirschsprung's Disease. Archives of Disease in Childhood. 1960;35(179):38-9.
67. Boley SJ. NEW MODIFICATION OF THE SURGICAL TREATMENT OF HIRSCHSPRUNG'S DISEASE. Surgery. 1964;56:1015-7.
68. Soave F. A NEW SURGICAL TECHNIQUE FOR TREATMENT OF HIRSCHSPRUNG'S DISEASE. Surgery. 1964;56:1007-14.
69. Bing X, Sun C, Wang Z, Su Y, Sun H, Wang L, et al. Transanal pullthrough Soave and Swenson techniques for pediatric patients with Hirschsprung disease. Medicine. 2017;96(10):e6209.
70. Chen Y, Nah SA, Laksmi NK, Ong CC, Chua JH, Jacobsen A, et al. Transanal endorectal pull-through versus transabdominal approach for Hirschsprung's disease: a systematic review and meta-analysis. Journal of pediatric surgery. 2013;48(3):642-51.
71. Mahajan JK, Rathod KK, Bawa M, Narasimhan KL. Transanal Swenson's operation for recto-sigmoid Hirschsprung's disease. African journal of paediatric surgery : AJPS.

2011;8(3):301-5.
72. Tannuri AC, Ferreira MA, Mathias AL, Tannuri U. Long-term results of the Duhamel technique are superior to those of the transanal pullthrough: A study of fecal continence and quality of life. Journal of pediatric surgery. 2017;52(3):449-53.
73. State D. Surgical treatment for idiopathic congenital megacolon (Hirschsprung's disease). Surgery, gynecology & obstetrics. 1952;95(2):201-12.
74. Rehbein F, Morger R, Kundert JG, Meier-Ruge W. Surgical problems in congenital megacolon (Hirschsprung's disease): A comparison of surgical technics. Journal of pediatric surgery. 1966;1(6):526-33.
75. Georgeson KE, Fuenfer MM, Hardin WD. Primary laparoscopic pull-through for Hirschsprung's disease in infants and children. Journal of pediatric surgery. 1995;30(7):1017-21; discussion 21-2.
76. Rintala RJ, Lindahl HG. Proctocolectomy and J-pouch ileo-anal anastomosis in children. Journal of pediatric surgery. 2002;37(1):66-70.
77. Wales PW. Surgical therapy for short bowel syndrome. Pediatric surgery international. 2004;20(9):647-57.
78. Wales PW, de Silva N, Langer JC, Fecteau A. Intermediate outcomes after serial transverse enteroplasty in children with short bowel syndrome. Journal of pediatric surgery. 2007;42(11):1804-10.
79. Sauvat F, Grimaldi C, Lacaille F, Ruemmele F, Dupic L, Bourdaud N, et al. Intestinal transplantation for total intestinal aganglionosis: a series of 12 consecutive children. Journal of pediatric surgery. 2008;43(10):1833-8.
80. Menezes M, Corbally M, Puri P. Long-term results of bowel function after treatment for Hirschsprung's disease: a 29-year review. Pediatric surgery international. 2006;22(12):987-90.
81. Marty TL, Seo T, Sullivan JJ, Matlak ME, Black RE, Johnson DG. Rectal irrigations for the prevention of postoperative enterocolitis in Hirschsprung's disease. Journal of pediatric surgery. 1995;30(5):652-4.
82. Gosain A, Frykman PK, Cowles RA, Horton J, Levitt M, Rothstein DH, et al. Guidelines for the diagnosis and management of Hirschsprung-associated enterocolitis. Pediatric surgery international. 2017;33(5):517-21.
83. Shen DH, Shi CR, Chen JJ, Yu SY, Wu Y, Yan WB. Detection of intestinal bifidobacteria and lactobacilli in patients with Hirschsprung's disease associated enterocolitis. World J Pediatr. 2009;5(3):201-5.
84. Wang X, Li Z, Xu Z, Wang Z, Feng J. Probiotics prevent Hirschsprung's disease-associated enterocolitis: a prospective multicenter randomized controlled trial. International journal of colorectal disease. 2015;30(1):105-10.
85. Frykman PK, Short SS. Hirschsprung-associated enterocolitis: prevention and therapy. Seminars in pediatric surgery. 2012;21(4):328-35.
86. Rintala RJ, Lindahl H. Sodium cromoglycate in the management of chronic or recurrent enterocolitis in patients with Hirschsprung's disease. Journal of pediatric surgery. 2001;36(7):1032-5.
87. Chumpitazi BP, Fishman SJ, Nurko S. Long-term clinical outcome after botulinum toxin injection in children with nonrelaxing internal anal sphincter. The American journal of gastroenterology. 2009;104(4):976-83.
88. Koivusalo AI, Pakarinen MP, Rintala RJ. Botox injection treatment for anal outlet obstruction in patients with internal anal sphincter achalasia and Hirschsprung's disease.

Pediatric surgery international. 2009;25(10):873-6.
89. Patrus B, Nasr A, Langer JC, Gerstle JT. Intrasphincteric botulinum toxin decreases the rate of hospitalization for postoperative obstructive symptoms in children with Hirschsprung disease. Journal of pediatric surgery. 2011;46(1):184-7.
90. Weber TR, Fortuna RS, Silen ML, Dillon PA. Reoperation for Hirschsprung's disease. Journal of pediatric surgery. 1999;34(1):153-6; discussion 6-7.
91. Heikkinen M, Lindahl H, Rintala RJ. Long-term outcome after internal sphincter myectomy for internal sphincter achalasia. Pediatric surgery international. 2005;21(2):84-7.
92. Blair GK, Murphy JJ, Fraser GC. Internal sphincterotomy in post-pull-through Hirschsprung's disease. Journal of pediatric surgery. 1996;31(6):843-5.
93. Young HM, Newgreen D. Enteric neural crest-derived cells: Origin, identification, migration, and differentiation. The Anatomical Record. 2001;262(1):1-15.
94. Heanue TA, Pachnis V. Enteric nervous system development and Hirschsprung's disease: advances in genetic and stem cell studies. Nature reviews Neuroscience. 2007;8(6):466-79.
95. Gershon MD. Genes and lineages in the formation of the enteric nervous system. Current opinion in neurobiology. 1997;7(1):101-9.
96. Sanders KM, Koh SD, Ward SM. INTERSTITIAL CELLS OF CAJAL AS PACEMAKERS IN THE GASTROINTESTINAL TRACT. Annual Review of Physiology. 2006;68(1):307-43.
97. Burns AJ, Pasricha PJ, Young HM. Enteric neural crest-derived cells and neural stem cells: biology and therapeutic potential. Neurogastroenterology and motility : the official journal of the European Gastrointestinal Motility Society. 2004;16 Suppl 1:3-7.
98. Kapur RP. Colonization of the murine hindgut by sacral crest-derived neural precursors: experimental support for an evolutionarily conserved model. Developmental biology. 2000;227(1):146-55.
99. Fu M, Lui VCH, Sham MH, Cheung ANY, Tam PKH. HOXB5 expression is spatially and temporarily regulated in human embryonic gut during neural crest cell colonization and differentiation of enteric neuroblasts. Developmental Dynamics. 2003;228(1):1-10.
100. Druckenbrod NR, Epstein ML. The pattern of neural crest advance in the cecum and colon. Developmental biology. 2005;287(1):125-33.
101. Druckenbrod NR, Epstein ML. Behavior of enteric neural crest-derived cells varies with respect to the migratory wavefront. Developmental Dynamics. 2007;236(1):84-92.
102. Nishiyama C, Uesaka T, Manabe T, Yonekura Y, Nagasawa T, Newgreen DF, et al. Trans-mesenteric neural crest cells are the principal source of the colonic enteric nervous system. Nature neuroscience. 2012;15(9):1211-8.
103. Barlow AJ, Dixon J, Dixon MJ, Trainor PA. Balancing neural crest cell intrinsic processes with those of the microenvironment in Tcof1 haploinsufficient mice enables complete enteric nervous system formation. Human Molecular Genetics. 2012;21(8):1782-93.
104. Attie T, Pelet A, Edery P, Eng C, Mulligan LM, Amiel J, et al. Diversity of RET proto-oncogene mutations in familial and sporadic Hirschsprung disease. Hum Mol Genet. 1995;4(8):1381-6.
105. Salomon R, Attié T, Pelet A, Bidaud C, Eng C, Amiel J, et al. Germline mutations of the RET ligand GDNF are not sufficient to cause hirschsprung disease. Nature Genetics. 1996;14(3):345-7.
106. Ivanchuk SM, Myers SM, Eng C, Mulligan LM. De novo mutation of GDNF, ligand for the RET/GDNFR-alpha receptor complex, in Hirschsprung disease. Hum Mol Genet. 1996;5(12):2023-6.

107. Doray B, Salomon R, Amiel J, Pelet A, Touraine R, Billaud M, et al. Mutation of the RET ligand, neurturin, supports multigenic inheritance in Hirschsprung disease. Hum Mol Genet. 1998;7(9):1449-52.
108. Pingault V, Bondurand N, Kuhlbrodt K, Goerich DE, Prehu MO, Puliti A, et al. SOX10 mutations in patients with Waardenburg-Hirschsprung disease. Nat Genet. 1998;18(2):171-3.
109. Parisi MA, Kapur RP. Genetics of Hirschsprung disease. Current opinion in pediatrics. 2000;12(6):610-7.
110. Hofstra RM, Valdenaire O, Arch E, Osinga J, Kroes H, Loffler BM, et al. A loss-of-function mutation in the endothelin-converting enzyme 1 (ECE-1) associated with Hirschsprung disease, cardiac defects, and autonomic dysfunction. American journal of human genetics. 1999;64(1):304-8.
111. Rosenthal A. The GDNF protein family: gene ablation studies reveal what they really do and how. Neuron. 1999;22(2):201-3.
112. Touraine RL, Attié-Bitach T, Manceau E, Korsch E, Sarda P, Pingault V, et al. Neurological Phenotype in Waardenburg Syndrome Type 4 Correlates with Novel SOX10 Truncating Mutations and Expression in Developing Brain. The American Journal of Human Genetics. 2000;66(5):1496-503.
113. Puffenberger EG, Hosoda K, Washington SS, Nakao K, deWit D, Yanagisawa M, et al. A missense mutation of the endothelin-B receptor gene in multigenic Hirschsprung's disease. Cell. 1994;79(7):1257-66.
114. Bidaud C, Salomon R, Van Camp G, Pelet A, Attie T, Eng C, et al. Endothelin-3 gene mutations in isolated and syndromic Hirschsprung disease. European journal of human genetics : EJHG. 1997;5(4):247-51.
115. Mowat DR, Croaker GD, Cass DT, Kerr BA, Chaitow J, Ades LC, et al. Hirschsprung disease, microcephaly, mental retardation, and characteristic facial features: delineation of a new syndrome and identification of a locus at chromosome 2q22-q23. Journal of medical genetics. 1998;35(8):617-23.
116. Brooks AS, Oostra BA, Hofstra RM. Studying the genetics of Hirschsprung's disease: unraveling an oligogenic disorder. Clinical genetics. 2005;67(1):6-14.
117. Eng C. RET proto-oncogene in the development of human cancer. Journal of clinical oncology : official journal of the American Society of Clinical Oncology. 1999;17(1):380-93.
118. Martucciello G, Thompson H, Mazzola C, Morando A, Bertagnon M, Negri F, et al. GDNF deficit in Hirschsprung's disease. Journal of pediatric surgery. 1998;33(1):99-102.
119. Bermingham N, Hillermann R, Gilmour F, Martin JE, Fisher EM. Human glial cell line-derived neurotrophic factor (GDNF) maps to chromosome 5. Human genetics. 1995;96(6):671-3.
120. Gorodinsky A, Zimonjic DB, Popescu NC, Milbrandt J. Assignment of the GDNF family receptor alpha-1 (GFRA1) to human chromosome band 10q26 by in situ hybridization. Cytogenetics and cell genetics. 1997;78(3-4):289-90.
121. Angrist M, Jing S, Bolk S, Bentley K, Nallasamy S, Halushka M, et al. Human GFRA1: cloning, mapping, genomic structure, and evaluation as a candidate gene for Hirschsprung disease susceptibility. Genomics. 1998;48(3):354-62.
122. Tansey MG, Baloh RH, Milbrandt J, Johnson EM, Jr. GFRalpha-mediated localization of RET to lipid rafts is required for effective downstream signaling, differentiation, and neuronal survival. Neuron. 2000;25(3):611-23.
123. Young HM, Hearn CJ, Farlie PG, Canty AJ, Thomas PQ, Newgreen DF. GDNF is a chemoattractant for enteric neural cells. Developmental biology. 2001;229(2):503-16.

124. Natarajan D, Marcos-Gutierrez C, Pachnis V, de Graaff E. Requirement of signalling by receptor tyrosine kinase RET for the directed migration of enteric nervous system progenitor cells during mammalian embryogenesis. Development. 2002;129(22):5151-60.
125. Pingault V, Puliti A, Prehu MO, Samadi A, Bondurand N, Goossens M. Human homology and candidate genes for the Dominant megacolon locus, a mouse model of Hirschsprung disease. Genomics. 1997;39(1):86-9.
126. Pingault V, Girard M, Bondurand N, Dorkins H, Van Maldergem L, Mowat D, et al. SOX10 mutations in chronic intestinal pseudo-obstruction suggest a complex physiopathological mechanism. Human genetics. 2002;111(2):198-206.
127. Touraine RL, Attie-Bitach T, Manceau E, Korsch E, Sarda P, Pingault V, et al. Neurological phenotype in Waardenburg syndrome type 4 correlates with novel SOX10 truncating mutations and expression in developing brain. American journal of human genetics. 2000;66(5):1496-503.
128. Bondurand N, Dastot-Le Moal F, Stanchina L, Collot N, Baral V, Marlin S, et al. Deletions at the SOX10 Gene Locus Cause Waardenburg Syndrome Types 2 and 4. The American Journal of Human Genetics. 2007;81(6):1169-85.
129. Kim J, Lo L, Dormand E, Anderson DJ. SOX10 maintains multipotency and inhibits neuronal differentiation of neural crest stem cells. Neuron. 2003;38(1):17-31.
130. Kapur RP. Early death of neural crest cells is responsible for total enteric aganglionosis in Sox10(Dom)/Sox10(Dom) mouse embryos. Pediatric and developmental pathology : the official journal of the Society for Pediatric Pathology and the Paediatric Pathology Society. 1999;2(6):559-69.
131. Mollaaghababa R, Pavan WJ. The importance of having your SOX on: role of SOX10 in the development of neural crest-derived melanocytes and glia. Oncogene. 2003;22(20):3024-34.
132. Bondurand N, Natarajan D, Barlow A, Thapar N, Pachnis V. Maintenance of mammalian enteric nervous system progenitors by SOX10 and endothelin 3 signalling. Development. 2006;133(10):2075-86.
133. Bowles J, Schepers G, Koopman P. Phylogeny of the SOX Family of Developmental Transcription Factors Based on Sequence and Structural Indicators. Developmental biology. 2000;227(2):239-55.
134. Wegner M. From head to toes: the multiple facets of Sox proteins. Nucleic Acids Research. 1999;27(6):1409-20.
135. Hong C-S, Saint-Jeannet J-P. Sox proteins and neural crest development. Seminars in Cell & Developmental Biology. 2005;16(6):694-703.
136. Potterf SB, Furumura M, Dunn KJ, Arnheiter H, Pavan WJ. Transcription factor hierarchy in Waardenburg syndrome: regulation of MITF expression by SOX10 and PAX3. Human genetics. 2000;107(1):1-6.
137. Bondurand N, Pingault V, Goerich DE, Lemort N, Sock E, Le Caignec C, et al. Interaction among SOX10, PAX3 and MITF, three genes altered in Waardenburg syndrome. Hum Mol Genet. 2000;9(13):1907-17.
138. Bondurand N, Girard M, Pingault V, Lemort N, Dubourg O, Goossens M. Human Connexin 32, a gap junction protein altered in the X-linked form of Charcot-Marie-Tooth disease, is directly regulated by the transcription factor SOX10. Hum Mol Genet. 2001;10(24):2783-95.
139. Lang D, Epstein JA. Sox10 and Pax3 physically interact to mediate activation of a conserved c-RET enhancer. Hum Mol Genet. 2003;12(8):937-45.

140. Ito Y, Wiese S, Funk N, Chittka A, Rossoll W, Bommel H, et al. Sox10 regulates ciliary neurotrophic factor gene expression in Schwann cells. Proceedings of the National Academy of Sciences of the United States of America. 2006;103(20):7871-6.
141. Zhu L, Lee HO, Jordan CS, Cantrell VA, Southard-Smith EM, Shin MK. Spatiotemporal regulation of endothelin receptor-B by SOX10 in neural crest-derived enteric neuron precursors. Nat Genet. 2004;36(7):732-7.
142. Pingault V, Ente D, Dastot-Le Moal F, Goossens M, Marlin S, Bondurand N. Review and update of mutations causing Waardenburg syndrome. Human mutation. 2010;31(4):391-406.
143. Rao VV, Loffler C, Hansmann I. The gene for the novel vasoactive peptide endothelin 3 (EDN3) is localized to human chromosome 20q13.2-qter. Genomics. 1991;10(3):840-1.
144. Arai H, Nakao K, Takaya K, Hosoda K, Ogawa Y, Nakanishi S, et al. The human endothelin-B receptor gene. Structural organization and chromosomal assignment. The Journal of biological chemistry. 1993;268(5):3463-70.
145. Matsuoka R, Sawamura T, Yamada K, Yoshida M, Furutani Y, Ikura T, et al. Human endothelin converting enzyme gene (ECE1) mapped to chromosomal region 1p36.1. Cytogenetics and cell genetics. 1996;72(4):322-4.
146. Wu TT, Tsai TW, Chu CT, Lee ZF, Hung CM, Su CC, et al. Low RET mutation frequency and polymorphism analysis of the RET and EDNRB genes in patients with Hirschsprung disease in Taiwan. J Hum Genet. 2005;50(4):168-74.
147. Garcia-Barcelo M, Sham MH, Lee WS, Lui VC, Chen BL, Wong KK, et al. Highly recurrent RET mutations and novel mutations in genes of the receptor tyrosine kinase and endothelin receptor B pathways in Chinese patients with sporadic Hirschsprung disease. Clin Chem. 2004;50(1):93-100.
148. Kim JH, Yoon KO, Kim H, Kim JK, Kim JW, Lee SK, et al. New variations of the EDNRB gene and its association with sporadic Hirschsprung's disease in Korea. Journal of pediatric surgery. 2006;41(10):1708-12.
149. Barlow A, de Graaff E, Pachnis V. Enteric nervous system progenitors are coordinately controlled by the G protein-coupled receptor EDNRB and the receptor tyrosine kinase RET. Neuron. 2003;40(5):905-16.
150. Nataf V, Amemiya A, Yanagisawa M, Le Douarin NM. The expression pattern of endothelin 3 in the avian embryo. Mechanisms of Development. 1998;73(2):217-20.
151. Baynash AG, Hosoda K, Giaid A, Richardson JA, Emoto N, Hammer RE, et al. Interaction of endothelin-3 with endothelin-B receptor is essential for development of epidermal melanocytes and enteric neurons. Cell. 1994;79(7):1277-85.
152. Mehta M, Sethi S, Pushker N, Bajaj MS, Ghose S. Delayed presentation of children with Waardenburg syndrome. Journal of pediatric ophthalmology and strabismus. 2010;47(6):382-3.
153. Read AP, Newton VE. Waardenburg syndrome. Journal of medical genetics. 1997;34(8):656-65.
154. da-Silva EO. Waardenburg I syndrome: a clinical and genetic study of two large Brazilian kindreds, and literature review. American journal of medical genetics. 1991;40(1):65-74.
155. Goodman RM, Lewithal I, Solomon A, Klein D. Upper limb involvement in the Klein-Waardenburg syndrome. American journal of medical genetics. 1982;11(4):425-33.
156. Sheffer R, Zlotogora J. Autosomal dominant inheritance of Klein-Waardenburg syndrome. American journal of medical genetics. 1992;42(3):320-2.
157. Hoth CF, Milunsky A, Lipsky N, Sheffer R, Clarren SK, Baldwin CT. Mutations in the

paired domain of the human PAX3 gene cause Klein-Waardenburg syndrome (WS-III) as well as Waardenburg syndrome type I (WS-I). American journal of human genetics. 1993;52(3):455-62.
158. Hughes AE, Newton VE, Liu XZ, Read AP. A gene for Waardenburg syndrome type 2 maps close to the human homologue of the microphthalmia gene at chromosome 3p12-p14.1. Nat Genet. 1994;7(4):509-12.
159. Syrris P, Carter ND, Patton MA. Novel nonsense mutation of the endothelin-B receptor gene in a family with Waardenburg-Hirschsprung disease. American journal of medical genetics. 1999;87(1):69-71.
160. Verheij JB, Kunze J, Osinga J, van Essen AJ, Hofstra RM. ABCD syndrome is caused by a homozygous mutation in the EDNRB gene. American journal of medical genetics. 2002;108(3):223-5.
161. Badner JA, Chakravarti A. Waardenburg syndrome and Hirschsprung disease: evidence for pleiotropic effects of a single dominant gene. American journal of medical genetics. 1990;35(1):100-4.
162. Edery P, Attie T, Amiel J, Pelet A, Eng C, Hofstra RM, et al. Mutation of the endothelin-3 gene in the Waardenburg-Hirschsprung disease (Shah-Waardenburg syndrome). Nat Genet. 1996;12(4):442-4.
163. Shamseldin HE, Rahbeeni Z, Alkuraya FS. Perturbation of the consensus activation site of endothelin-3 leads to Waardenburg syndrome type IV. American journal of medical genetics Part A. 2010;152a(7):1841-3.
164. Pingault V, Bondurand N, Lemort N, Sancandi M, Ceccherini I, Hugot JP, et al. A heterozygous endothelin 3 mutation in Waardenburg-Hirschsprung disease: is there a dosage effect of EDN3/EDNRB gene mutations on neurocristopathy phenotypes? Journal of medical genetics. 2001;38(3):205-9.
165. Southard-Smith EM, Angrist M, Ellison JS, Agarwala R, Baxevanis AD, Chakravarti A, et al. The Sox10(Dom) mouse: modeling the genetic variation of Waardenburg-Shah (WS4) syndrome. Genome research. 1999;9(3):215-25.
166. Yanagisawa M, Kurihara H, Kimura S, Tomobe Y, Kobayashi M, Mitsui Y, et al. A novel potent vasoconstrictor peptide produced by vascular endothelial cells. Nature. 1988;332(6163):411-5.
167. Inoue A, Yanagisawa M, Kimura S, Kasuya Y, Miyauchi T, Goto K, et al. The human endothelin family: three structurally and pharmacologically distinct isopeptides predicted by three separate genes. Proceedings of the National Academy of Sciences of the United States of America. 1989;86(8):2863-7.
168. Denault JB, Claing A, D'Orleans-Juste P, Sawamura T, Kido T, Masaki T, et al. Processing of proendothelin-1 by human furin convertase. FEBS letters. 1995;362(3):276-80.
169. Inoue A, Yanagisawa M, Takuwa Y, Mitsui Y, Kobayashi M, Masaki T. The human preproendothelin-1 gene. Complete nucleotide sequence and regulation of expression. The Journal of biological chemistry. 1989;264(25):14954-9.
170. Lee ME, Bloch KD, Clifford JA, Quertermous T. Functional analysis of the endothelin-1 gene promoter. Evidence for an endothelial cell-specific cis-acting sequence. The Journal of biological chemistry. 1990;265(18):10446-50.
171. Fabbrini MS, Valsasina B, Nitti G, Benatti L, Vitale A. The signal peptide of human preproendothelin-1. FEBS letters. 1991;286(1-2):91-4.
172. Barnes K, Turner AJ. The endothelin system and endothelin-converting enzyme in the brain: molecular and cellular studies. Neurochemical research. 1997;22(8):1033-40.

173. Webb DJ, Monge JC, Rabelink TJ, Yanagisawa M. Endothelin: new discoveries and rapid progress in the clinic. Trends in pharmacological sciences. 1998;19(1):5-8.
174. Kido T, Sawamura T, Masaki T. The processing pathway of endothelin-1 production. Journal of cardiovascular pharmacology. 1998;31 Suppl 1:S13-5.
175. Karne S, Jayawickreme CK, Lerner MR. Cloning and characterization of an endothelin-3 specific receptor (ETC receptor) from Xenopus laevis dermal melanophores. The Journal of biological chemistry. 1993;268(25):19126-33.
176. Kedzierski RM, Yanagisawa M. Endothelin system: the double-edged sword in health and disease. Annual review of pharmacology and toxicology. 2001;41:851-76.
177. Albertin G, Rossi GP, Majone F, Tiso N, Mattara A, Danieli GA, et al. Fine mapping of the human endothelin-converting enzyme gene by fluorescent in situ hybridization and radiation hybrids. Biochemical and biophysical research communications. 1996;221(3):682-7.
178. Xu D, Emoto N, Giaid A, Slaughter C, Kaw S, deWit D, et al. ECE-1: a membrane-bound metalloprotease that catalyzes the proteolytic activation of big endothelin-1. Cell. 1994;78(3):473-85.
179. Lorenzo MN, Khan RY, Wang Y, Tai SC, Chan GC, Cheung AH, et al. Human endothelin converting enzyme-2 (ECE2): characterization of mRNA species and chromosomal localization. Biochimica et biophysica acta. 2001;1522(1):46-52.
180. Warner TD, Schmidt HH, Kuk J, Mitchell JA, Murad F. Human brain contains a metalloprotease that converts big endothelin-1 to endothelin-1 and is inhibited by phosphoramidon and EDTA. British Journal of Pharmacology. 1992;106(3):505-6.
181. Emoto N, Yanagisawa M. Endothelin-converting enzyme-2 is a membrane-bound, phosphoramidon-sensitive metalloprotease with acidic pH optimum. The Journal of biological chemistry. 1995;270(25):15262-8.
182. Arinami T, Ishikawa M, Inoue A, Yanagisawa M, Masaki T, Yoshida MC, et al. Chromosomal assignments of the human endothelin family genes: the endothelin-1 gene (EDN1) to 6p23-p24, the endothelin-2 gene (EDN2) to 1p34, and the endothelin-3 gene (EDN3) to 20q13.2-q13.3. American journal of human genetics. 1991;48(5):990-6.
183. Kumagaye S, Kuroda H, Nakajima K, Watanabe TX, Kimura T, Masaki T, et al. Synthesis and disulfide structure determination of porcine endothelin: an endothelium-derived vasoconstricting peptide. International journal of peptide and protein research. 1988;32(6):519-26.
184. Huggins JP, Pelton JT, Miller RC. The structure and specificity of endothelin receptors: their importance in physiology and medicine. Pharmacology & therapeutics. 1993;59(1):55-123.
185. Kloog Y, Sokolovsky M. Similarities in mode and sites of action of sarafotoxins and endothelins. Trends in pharmacological sciences. 1989;10(6):212-4.
186. Bdolah A, Wollberg Z, Ambar I, Kloog Y, Sokolovsky M, Kochva E. Disturbances in the cardiovascular system caused by endothelin and sarafotoxin. Biochemical Pharmacology. 1989;38(19):3145-6.
187. Zigdon-Arad T, Bdolah A, Kochva E, Wollberg Z. Activity of sarafotoxin/endothelin peptides in the heart and brain of lower vertebrates. Toxicon. 1992;30(4):439-48.
188. Hua LL, Vedantham V, Barnes RM, Hu J, Robinson AS, Bressan M, et al. Specification of the mouse cardiac conduction system in the absence of Endothelin signaling. Developmental biology. 2014;393(2):245-54.
189. Hirata Y, Emori T, Eguchi S, Kanno K, Imai T, Ohta K, et al. Endothelin receptor subtype B mediates synthesis of nitric oxide by cultured bovine endothelial cells. The Journal of

clinical investigation. 1993;91(4):1367-73.
190. Arai H, Hori S, Aramori I, Ohkubo H, Nakanishi S. Cloning and expression of a cDNA encoding an endothelin receptor. Nature. 1990;348(6303):730-2.
191. Alexander SP, Benson HE, Faccenda E, Pawson AJ, Sharman JL, Spedding M, et al. The Concise Guide to PHARMACOLOGY 2013/14: G protein-coupled receptors. Br J Pharmacol. 2013;170(8):1459-581.
192. Russell FD, Molenaar P. The human heart endothelin system: ET-1 synthesis, storage, release and effect. Trends in pharmacological sciences. 2000;21(9):353-9.
193. Cernacek P, Stewart DJ, Monge JC, Rouleau JL. The endothelin system and its role in acute myocardial infarction. Canadian journal of physiology and pharmacology. 2003;81(6):598-606.
194. Black SM, Kumar S, Wiseman D, Ravi K, Wedgwood S, Ryzhov V, et al. Pediatric pulmonary hypertension: Roles of endothelin-1 and nitric oxide. Clinical hemorheology and microcirculation. 2007;37(1-2):111-20.
195. Bohm F, Pernow J. The importance of endothelin-1 for vascular dysfunction in cardiovascular disease. Cardiovascular research. 2007;76(1):8-18.
196. Kohan DE. Endothelins: renal tubule synthesis and actions. Clinical and experimental pharmacology & physiology. 1996;23(4):337-44.
197. Neuhofer W, Pittrow D. Role of endothelin and endothelin receptor antagonists in renal disease. Eur J Clin Invest. 2006;36 Suppl 3:78-88.
198. Schinelli S. Pharmacology and physiopathology of the brain endothelin system: an overview. Curr Med Chem. 2006;13(6):627-38.
199. Mortensen LH. Endothelin and the central and peripheral nervous systems: a decade of endothelin research. Clinical and experimental pharmacology & physiology. 1999;26(12):980-4.
200. MacCumber MW, Ross CA, Glaser BM, Snyder SH. Endothelin: visualization of mRNAs by in situ hybridization provides evidence for local action. Proceedings of the National Academy of Sciences of the United States of America. 1989;86(18):7285-9.
201. Huang SC. Endothelin receptors in gastrointestinal smooth muscle. Current protein & peptide science. 2005;6(6):547-57.
202. Lange M, Pagotto U, Renner U, Arzberger T, Oeckler R, Stalla GK. The role of endothelins in the regulation of pituitary function. Experimental and clinical endocrinology & diabetes : official journal, German Society of Endocrinology [and] German Diabetes Association. 2002;110(3):103-12.
203. Granger JP, Abram S, Stec D, Chandler D, LaMarca B. Endothelin, the kidney, and hypertension. Current hypertension reports. 2006;8(4):298-303.
204. Hinojosa-Laborde C, Lange DL. Endothelin regulation of adrenal function. Clinical and experimental pharmacology & physiology. 1999;26(12):995-9.
205. Mullol J, Picado C. Endothelin in nasal mucosa: role in nasal function and inflammation. Clinical and experimental allergy : journal of the British Society for Allergy and Clinical Immunology. 2000;30(2):172-7.
206. Mencarelli M, Pecorelli A, Carbotti P, Valacchi G, Grasso G, Muscettola M. Endothelin receptor A expression in human inflammatory cells. Regulatory peptides. 2009;158(1-3):1-5.
207. Mallat A, Lotersztajn S. Multiple hepatic functions of endothelin-1: physiopathological relevance. Journal of hepatology. 1996;25(3):405-13.
208. Cameron IT, Bacon CR, Collett GP, Davenport AP. Endothelin expression in the uterus. The Journal of steroid biochemistry and molecular biology. 1995;53(1-6):209-14.

209. Wolff K, Faxen M, Lunell NO, Nisell H, Lindblom B. Endothelin receptor type A and B gene expression in human nonpregnant, term pregnant, and preeclamptic uterus. American journal of obstetrics and gynecology. 1996;175(5):1295-300.
210. Meidan R, Levy N. The ovarian endothelin network: an evolving story. Trends in endocrinology and metabolism: TEM. 2007;18(10):379-85.
211. Lowenstein CJ, Morrell CN, Yamakuchi M. Regulation of Weibel-Palade body exocytosis. Trends in cardiovascular medicine. 2005;15(8):302-8.
212. Properzi G, Terenghi G, Gu X-H, Poccia G, Pasqua R, Francavilla S, et al. Early increase precedes a depletion of endothelin-1 but not of von Willebrand factor in cutaneous microvessels of diabetic patients. A quantitative immunohistochemical study. The Journal of Pathology. 1995;175(2):243-52.
213. Tonnessen T, Lunde PK, Giaid A, Sejersted OM, Christensen G. Pulmonary and cardiac expression of preproendothelin-1 mRNA are increased in heart failure after myocardial infarction in rats. Localization of preproendothelin-1 mRNA and endothelin peptide. Cardiovascular research. 1998;39(3):633-43.
214. Saetrum Opgaard O, Adner M, Peters TH, Xu CB, Stavenow L, Gulbenkian S, et al. Endocardial expression and functional characterization of endothelin-1. Mol Cell Biochem. 2001;224(1-2):151-8.
215. Kohan DE. Endothelin synthesis by rabbit renal tubule cells. The American journal of physiology. 1991;261(2 Pt 2):F221-6.
216. Barton M, Carmona R, Morawietz H, d'Uscio LV, Goettsch W, Hillen H, et al. Obesity Is Associated With Tissue-Specific Activation of Renal Angiotensin-Converting Enzyme In Vivo. Evidence for a Regulatory Role of Endothelin. 2000;35(1):329-36.
217. Yamauchi T, Ohnaka K, Takayanagi R, Umeda F, Nawata H. Enhanced secretion of endothelin-1 by elevated glucose levels from cultured bovine aortic endothelial cells. FEBS letters. 1990;267(1):16-8.
218. Malek A, Izumo S. Physiological fluid shear stress causes downregulation of endothelin-1 mRNA in bovine aortic endothelium. American Journal of Physiology-Cell Physiology. 1992;263(2):C389-C96.
219. Boulanger CM, Tanner FC, Béa ML, Hahn AW, Werner A, Lüscher TF. Oxidized low density lipoproteins induce mRNA expression and release of endothelin from human and porcine endothelium. Circulation Research. 1992;70(6):1191-7.
220. Matsuura A, Yamochi W, Hirata K-i, Kawashima S, Yokoyama M. Stimulatory Interaction Between Vascular Endothelial Growth Factor and Endothelin-1 on Each Gene Expression. Hypertension. 1998;32(1):89-95.
221. Emori T, Hirata Y, Ohta K, Shichiri M, Marumo F. Secretory mechanism of immunoreactive endothelin in cultured bovine endothelial cells. Biochemical and biophysical research communications. 1989;160(1):93-100.
222. Kurihara H, Yoshizumi M, Sugiyama T, Takaku F, Yanagisawa M, Masaki T, et al. Transforming growth factor-beta stimulates the expression of endothelin mRNA by vascular endothelial cells. Biochemical and biophysical research communications. 1989;159(3):1435-40.
223. Fujisaki H, Ito H, Hirata Y, Tanaka M, Hata M, Lin M, et al. Natriuretic peptides inhibit angiotensin II-induced proliferation of rat cardiac fibroblasts by blocking endothelin-1 gene expression. The Journal of clinical investigation. 1995;96(2):1059-65.
224. Wagner OF, Christ G, Wojta J, Vierhapper H, Parzer S, Nowotny PJ, et al. Polar secretion of endothelin-1 by cultured endothelial cells. The Journal of biological chemistry.

1992;267(23):16066-8.
225. Boulanger C, Luscher TF. Release of endothelin from the porcine aorta. Inhibition by endothelium-derived nitric oxide. The Journal of clinical investigation. 1990;85(2):587-90.
226. Stewart DJ, Cernacek P, Mohamed F, Blais D, Cianflone K, Monge JC. Role of cyclic nucleotides in the regulation of endothelin-1 production by human endothelial cells. American Journal of Physiology-Heart and Circulatory Physiology. 1994;266(3):H944-H51.
227. Battistini B, D'Orleans-Juste P, Sirois P. Endothelins: circulating plasma levels and presence in other biologic fluids. Laboratory investigation; a journal of technical methods and pathology. 1993;68(6):600-28.
228. Anggard E, Galton S, Rae G, Thomas R, McLoughlin L, de Nucci G, et al. The fate of radioiodinated endothelin-1 and endothelin-3 in the rat. Journal of cardiovascular pharmacology. 1989;13 Suppl 5:S46-9; discussion S74.
229. Abassi ZA, Tate JE, Golomb E, Keiser HR. Role of neutral endopeptidase in the metabolism of endothelin. Hypertension. 1992;20(1):89-95.
230. Clouthier DE, Hosoda K, Richardson JA, Williams SC, Yanagisawa H, Kuwaki T, et al. Cranial and cardiac neural crest defects in endothelin-A receptor-deficient mice. Development. 1998;125(5):813-24.
231. Kurihara Y, Kurihara H, Suzuki H, Kodama T, Maemura K, Nagai R, et al. Elevated blood pressure and craniofacial abnormalities in mice deficient in endothelin-1. Nature. 1994;368(6473):703-10.
232. Kurihara Y, Kurihara H, Oda H, Maemura K, Nagai R, Ishikawa T, et al. Aortic arch malformations and ventricular septal defect in mice deficient in endothelin-1. The Journal of clinical investigation. 1995;96(1):293-300.
233. Ruetten H, Thiemermann C. Endothelin-1 stimulates the biosynthesis of tumour necrosis factor in macrophages: ET-receptors, signal transduction and inhibition by dexamethasone. Journal of physiology and pharmacology : an official journal of the Polish Physiological Society. 1997;48(4):675-88.
234. Fujitani Y, Ninomiya H, Okada T, Urade Y, Masaki T. Suppression of endothelin-1-induced mitogenic responses of human aortic smooth muscle cells by interleukin-1 beta. The Journal of clinical investigation. 1995;95(6):2474-82.
235. Alonso D, Radomski MW. The Nitric Oxide-Endothelin-1 Connection. Heart Failure Reviews. 2003;8(1):107-15.
236. Seo B, Oemar BS, Siebenmann R, von Segesser L, Luscher TF. Both ETA and ETB receptors mediate contraction to endothelin-1 in human blood vessels. Circulation. 1994;89(3):1203-8.
237. Vuurmans TJL, Boer P, Koomans HA. Effects of Endothelin-1 and Endothelin-1 Receptor Blockade on Cardiac Output, Aortic Pressure, and Pulse Wave Velocity in Humans. Hypertension. 2003;41(6):1253-8.
238. Roux S, Breu V, Giller T, Neidhart W, Ramuz H, Coassolo P, et al. Ro 61–1790, a New Hydrosoluble Endothelin Antagonist: General Pharmacology and Effects on Experimental Cerebral Vasospasm. Journal of Pharmacology and Experimental Therapeutics. 1997;283(3):1110-8.
239. Ling GY, Cao WH, Onodera M, Ju KH, Kurihara H, Kurihara Y, et al. Renal sympathetic nerve activity in mice: comparison between mice and rats and between normal and endothelin-1 deficient mice. Brain research. 1998;808(2):238-49.
240. Nambi P, Wu HL, Pullen M, Aiyar N, Bryan H, Elliott J. Identification of endothelin receptor subtypes in rat kidney cortex using subtype-selective ligands. Molecular

pharmacology. 1992;42(2):336-9.
241. Alberts GF, Peifley KA, Johns A, Kleha JF, Winkles JA. Constitutive endothelin-1 overexpression promotes smooth muscle cell proliferation via an external autocrine loop. Journal of Biological Chemistry. 1994;269(13):10112-8.
242. Yang Z, Krasnici N, Lüscher TF. Endothelin-1 Potentiates Human Smooth Muscle Cell Growth to PDGF. Effects of ET_A and ET_B Receptor Blockade. 1999;100(1):5-8.
243. Peifley KA, Winkles JA. Angiotensin II and Endothelin-1 Increase Fibroblast Growth Factor-2 mRNA Expression in Vascular Smooth Muscle Cells. Biochemical and biophysical research communications. 1998;242(1):202-8.
244. Taylor DS, Cheng X, Pawlowski JE, Wallace AR, Ferrer P, Molloy CJ. Epiregulin is a potent vascular smooth muscle cell-derived mitogen induced by angiotensin II, endothelin-1, and thrombin. Proceedings of the National Academy of Sciences. 1999;96(4):1633-8.
245. Agui T, Xin X, Cai Y, Sakai T, Matsumoto K. Stimulation of interleukin-6 production by endothelin in rat bone marrow-derived stromal cells. Blood. 1994;84(8):2531-8.
246. Bernad A, Kopf M, Kulbacki R, Weich N, Koehler G, Gutierrez-Ramos JC. Interleukin-6 is required in vivo for the regulation of stem cells and committed progenitors of the hematopoietic system. Immunity. 1994;1(9):725-31.
247. Cho SW, Pirih FQ, Koh AJ, Michalski M, Eber MR, Ritchie K, et al. The soluble interleukin-6 receptor is a mediator of hematopoietic and skeletal actions of parathyroid hormone. The Journal of biological chemistry. 2013;288(10):6814-25.
248. Hofman FM, Chen P, Jeyaseelan R, Incardona F, Fisher M, Zidovetzki R. Endothelin-1 induces production of the neutrophil chemotactic factor interleukin-8 by human brain-derived endothelial cells. Blood. 1998;92(9):3064-72.
249. Bauters C, Asahara T, Zheng LP, Takeshita S, Bunting S, Ferrara N, et al. Site-specific therapeutic angiogenesis after systemic administration of vascular endothelial growth factor. Journal of vascular surgery. 1995;21(2):314-24; discussion 24-5.
250. Guo D, Jia Q, Song HY, Warren RS, Donner DB. Vascular endothelial cell growth factor promotes tyrosine phosphorylation of mediators of signal transduction that contain SH2 domains. Association with endothelial cell proliferation. The Journal of biological chemistry. 1995;270(12):6729-33.
251. Yoshizawa T, Shinmi O, Giaid A, Yanagisawa M, Gibson SJ, Kimura S, et al. Endothelin: a novel peptide in the posterior pituitary system. Science. 1990;247(4941):462-4.
252. Matsumoto H, Suzuki N, Onda H, Fujino M. Abundance of endothelin-3 in rat intestine, pituitary gland and brain. Biochemical and biophysical research communications. 1989;164(1):74-80.
253. Giaid A, Gibson SJ, Ibrahim BN, Legon S, Bloom SR, Yanagisawa M, et al. Endothelin 1, an endothelium-derived peptide, is expressed in neurons of the human spinal cord and dorsal root ganglia. Proceedings of the National Academy of Sciences of the United States of America. 1989;86(19):7634-8.
254. Lee ME, de la Monte SM, Ng SC, Bloch KD, Quertermous T. Expression of the potent vasoconstrictor endothelin in the human central nervous system. The Journal of clinical investigation. 1990;86(1):141-7.
255. Yoshizawa T, Kimura S, Kanazawa I, Uchiyama Y, Yanagisawa M, Masaki T. Endothelin localizes in the dorsal horn and acts on the spinal neurones: Possible involvement of dihydropyridine-sensitive calcium channels and substance P release. Neuroscience Letters. 1989;102(2):179-84.

256. Takahashi K, Ghatei MA, Jones PM, Murphy JK, Lam HC, O'Halloran DJ, et al. Endothelin in human brain and pituitary gland: comparison with rat. Journal of cardiovascular pharmacology. 1991;17 Suppl 7:S101-3.
257. Ando K, Hirata Y, Togashi K, Kawakami M, Marumo F. Endothelin-1- and endothelin-3-like immunoreactivity in human cerebrospinal fluid. Journal of cardiovascular pharmacology. 1991;17 Suppl 7:S434-6.
258. Kuwaki T, Koshiya N, Cao WH, Takahashi H, Terui N, Kumada M. Modulatory effects of endothelin-1 on central cardiovascular control in rats. The Japanese journal of physiology. 1990;40(6):827-41.
259. Kumada M, Cao W, Kuwaki T. Effect of endothelin on vasomotor and respiratory neurons in the rostral ventrolateral medulla in rats. Cellular and molecular neurobiology. 2003;23(4-5):691-707.
260. Cao WH, Kuwaki T, Unekawa M, Ling GY, Terui N, Kumada M. Action of endothelin-1 on vasomotor neurons in rat rostral ventrolateral medulla. Journal of cardiovascular pharmacology. 1993;22 Suppl 8:S196-8.
261. T K, Gy L, M O, T I, A N, Kh J, et al. ENDOTHELIN IN THE CENTRAL CONTROL OF CARDIOVASCULAR AND RESPIRATORY FUNCTIONS. Clinical and Experimental Pharmacology and Physiology. 1999;26(12):989-94.
262. Yamamoto T, Kimura T, Ota K, Shoji M, Inoue M, Sato K, et al. Central effects of endothelin-1 on vasopressin release, blood pressure, and renal solute excretion. The American journal of physiology. 1992;262(6 Pt 1):E856-62.
263. Kuwaki T, Cao WH, Kurihara Y, Kurihara H, Ling GY, Onodera M, et al. Impaired ventilatory responses to hypoxia and hypercapnia in mutant mice deficient in endothelin-1. American Journal of Physiology-Regulatory, Integrative and Comparative Physiology. 1996;270(6):R1279-R86.
264. Calogero AE, Raiti F, Nicolosi G, Burrello N, D'Agata R, Mantero F. Effects of endothelin-1 and endothelin-3 on rat hypothalamic corticotrophin-releasing hormone and pituitary ACTH release in vitro. The Journal of endocrinology. 1994;140(3):419-24.
265. Yasin S, Costa A, Navarra P, Pozzoli G, Kostoglou-Athanassiou I, Forsling M, et al. Endothelin-1 stimulates the in vitro release of neurohypophyseal hormones, but not corticotropin-releasing hormone, via ETA receptors. Neuroendocrinology. 1994;60(6):553-8.
266. Kanyicska B, Burris TP, Freeman ME. The Effects of Endothelins on the Secretion of Prolactin, Luteinizing Hormone, and Follicle-Stimulating Hormone Are Mediated by Different Guanine Nucleotide-Binding Proteins*. Endocrinology. 1991;129(5):2607-13.
267. Ehrenreich H, Anderson RW, Fox CH, Rieckmann P, Hoffman GS, Travis WD, et al. Endothelins, peptides with potent vasoactive properties, are produced by human macrophages. The Journal of experimental medicine. 1990;172(6):1741-8.
268. Chalmers GW, Little SA, Patel KR, Thomson NC. Endothelin-1-induced bronchoconstriction in asthma. American journal of respiratory and critical care medicine. 1997;156(2 Pt 1):382-8.
269. Adamicza A, Petak F, Asztalos T, Hantos Z. Effects of endothelin-1 on airway and parenchymal mechanics in guinea-pigs. The European respiratory journal. 1999;13(4):767-74.
270. Adamicza Á, Peták F, Asztalos T, Tiszlavicz L, Boros M, Hantos Z. Endothelin-1-induced airway and parenchymal mechanical responses in guinea-pigs: the roles of ETA and ETB receptors. European Respiratory Journal. 2001;17(5):975-81.
271. Barman SA, Pauly JR. Mechanism of action of endothelin-1 in the canine pulmonary circulation. Journal of Applied Physiology. 1995;79(6):2014-20.

272. Hasunuma K, Rodman DM, O'Brien RF, McMurtry IF. Endothelin 1 causes pulmonary vasodilation in rats. The American journal of physiology. 1990;259(1 Pt 2):H48-54.
273. Okada M, Yamashita C, Okada M, Okada K. Role of Endothelin-1 in Beagles With Dehydromonocrotaline-Induced Pulmonary Hypertension. Circulation. 1995;92(1):114-9.
274. Arvidsson K, Nemoto T, Mitsui Y, Ohashi S, Nakanishi H. The solution structure of human endothelin-2 a 1H-NMR and CD study. European journal of biochemistry. 1998;257(2):380-8.
275. Roubert P, Gillard V, Plas P, Chabrier PE, Braquet P. Binding characteristics of endothelin isoforms (ET-1, ET-2, and ET-3) in vascular smooth muscle cells. Journal of cardiovascular pharmacology. 1991;17 Suppl 7:S104-8.
276. Bacon CR, Davenport AP. Endothelin receptors in human coronary artery and aorta. Br J Pharmacol. 1996;117(5):986-92.
277. Maguire JJ, Davenport AP. ETA receptor-mediated constrictor responses to endothelin peptides in human blood vessels in vitro. Br J Pharmacol. 1995;115(1):191-7.
278. Ishida N, Tsujioka K, Tomoi M, Saida K, Mitsui Y. Differential activities of two distinct endothelin family peptides on ileum and coronary artery. FEBS letters. 1989;247(2):337-40.
279. Bloch KD, Hong CC, Eddy RL, Shows TB, Quertermous T. cDNA cloning and chromosomal assignment of the endothelin 2 gene: vasoactive intestinal contractor peptide is rat endothelin 2. Genomics. 1991;10(1):236-42.
280. Sundler F, Ekblad E, Grunditz T, Hakanson R, Uddman R. Vasoactive intestinal peptide in the peripheral nervous system. Annals of the New York Academy of Sciences. 1988;527:143-67.
281. Masuo Y, Ishikawa Y, Kozakai T, Uchide T, Komatsu Y, Saida K. Vasoactive intestinal contractor/endothelin-2 gene expression in the murine central nervous system. Biochemical and biophysical research communications. 2003;300(3):661-8.
282. Lin WW, Lee CY. Intestinal relaxation by endothelin isopeptides: involvement of Ca(2+)-activated K+ channels. European journal of pharmacology. 1992;219(3):355-60.
283. Douglas SA, Hiley CR. Endothelium-dependent vascular activities of endothelin-like peptides in the isolated superior mesenteric arterial bed of the rat. Br J Pharmacol. 1990;101(1):81-8.
284. Matsumoto H, Suzuki N, Kitada C, Fujino M. Endothelin family peptides in human plasma and urine: their molecular forms and concentrations. Peptides. 1994;15(3):505-10.
285. Howard PG, Plumpton C, Davenport AP. Anatomical localization and pharmacological activity of mature endothelins and their precursors in human vascular tissue. Journal of hypertension. 1992;10(11):1379-86.
286. Marciniak SJ, Plumpton C, Barker PJ, Huskisson NS, Davenport AP. Localization of immunoreactive endothelin and proendothelin in the human lung. Pulmonary pharmacology. 1992;5(3):175-82.
287. Plumpton C, Champeney R, Ashby MJ, Kuc RE, Davenport AP. Characterization of endothelin isoforms in human heart: endothelin-2 demonstrated. Journal of cardiovascular pharmacology. 1993;22 Suppl 8:S26-8.
288. Karet FE, Davenport AP. Localization of endothelin peptides in human kidney. Kidney international. 1996;49(2):382-7.
289. de la Monte SM, Quertermous T, Hong CC, Bloch KD. Regional and maturation-associated expression of endothelin 2 in rat gastrointestinal tract. The journal of histochemistry and cytochemistry : official journal of the Histochemistry Society. 1995;43(2):203-9.

290. Uchide T, Masuda H, Mitsui Y, Saida K. Gene expression of vasoactive intestinal contractor/endothelin-2 in ovary, uterus and embryo: comprehensive gene expression profiles of the endothelin ligand-receptor system revealed by semi-quantitative reverse transcription-polymerase chain reaction analysis in adult mouse tissues and during late embryonic development. Journal of molecular endocrinology. 1999;22(2):161-71.
291. Uchide T, Masuda H, Lee YS, Makiyama Y, Mitsui Y, Saida K. Fluctuating gene expression and localized cellular distribution of vasoactive intestinal contractor (VIC) in mouse uterus. The journal of histochemistry and cytochemistry : official journal of the Histochemistry Society. 2000;48(5):699-707.
292. Chang I, Bramall AN, Baynash AG, Rattner A, Rakheja D, Post M, et al. Endothelin-2 deficiency causes growth retardation, hypothermia, and emphysema in mice. The Journal of clinical investigation. 2013;123(6):2643-53.
293. Ko C, Gieske MC, Al-Alem L, Hahn Y, Su W, Gong MC, et al. Endothelin-2 in ovarian follicle rupture. Endocrinology. 2006;147(4):1770-9.
294. Palanisamy GS, Cheon YP, Kim J, Kannan A, Li Q, Sato M, et al. A novel pathway involving progesterone receptor, endothelin-2, and endothelin receptor B controls ovulation in mice. Molecular endocrinology (Baltimore, Md). 2006;20(11):2784-95.
295. Grimshaw MJ, Wilson JL, Balkwill FR. Endothelin-2 is a macrophage chemoattractant: implications for macrophage distribution in tumors. European journal of immunology. 2002;32(9):2393-400.
296. Grimshaw MJ, Naylor S, Balkwill FR. Endothelin-2 Is a Hypoxia-induced Autocrine Survival Factor for Breast Tumor Cells 1 Supported, in part, by Oxford BioMedica United Kingdom Ltd. (to M. J. G.). ¹. Molecular Cancer Therapeutics. 2002;1(14):1273-81.
297. Bloch KD, Eddy RL, Shows TB, Quertermous T. cDNA cloning and chromosomal assignment of the gene encoding endothelin 3. The Journal of biological chemistry. 1989;264(30):18156-61.
298. Sakurai T, Yanagisawa M, Takuwa Y, Miyazaki H, Kimura S, Goto K, et al. Cloning of a cDNA encoding a non-isopeptide-selective subtype of the endothelin receptor. Nature. 1990;348(6303):732-5.
299. Saida K, Mitsui Y, Ishida N. A novel peptide, vasoactive intestinal contractor, of a new (endothelin) peptide family. Molecular cloning, expression, and biological activity. The Journal of biological chemistry. 1989;264(25):14613-6.
300. Kurihara H, Kurihara Y, Nagai R, Yazaki Y. Endothelin and neural crest development. Cellular and molecular biology (Noisy-le-Grand, France). 1999;45(5):639-51.
301. D'Orleans-Juste P, Telemaque S, Claing A. Different pharmacological profiles of big-endothelin-3 and big-endothelin-1 in vivo and in vitro. Br J Pharmacol. 1991;104(2):440-4.
302. Shiba R, Sakurai T, Yamada G, Morimoto H, Saito A, Masaki T, et al. Cloning and expression of rat preproendothelin-3 cDNA. Biochemical and biophysical research communications. 1992;186(1):588-94.
303. O'Reilly G, Charnock-Jones DS, Davenport AP, Cameron IT, Smith SK. Presence of messenger ribonucleic acid for endothelin-1, endothelin-2, and endothelin-3 in human endometrium and a change in the ratio of ETA and ETB receptor subtype across the menstrual cycle. The Journal of clinical endocrinology and metabolism. 1992;75(6):1545-9.
304. Miyauchi Y, Sakai S, Maeda S, Shimojo N, Watanabe S, Honma S, et al. Increased plasma levels of big-endothelin-2 and big-endothelin-3 in patients with end-stage renal disease. Life sciences. 2012;91(13-14):729-32.

305. Nagy N, Goldstein AM. Endothelin-3 regulates neural crest cell proliferation and differentiation in the hindgut enteric nervous system. Developmental biology. 2006;293(1):203-17.
306. Kuwaki T, Koshiya N, Takahashi H, Terui N, Kumada M. Modulatory effects of rat endothelin on central cardiovascular control in rats. The Japanese journal of physiology. 1990;40(1):97-116.
307. Kanyicska B, Burris TP, Freeman ME. Endothelin-3 inhibits prolactin and stimulates LH, FSH and TSH secretion from pituitary cell culture. Biochemical and biophysical research communications. 1991;174(1):338-43.
308. Zhu B, Herbert J. Behavioural, autonomic and endocrine responses associated with c-fos expression in the forebrain and brainstem after intracerebroventricular infusions of endothelins. Neuroscience. 1996;71(4):1049-62.
309. Samson WK, Skala K, Steven Huang FL, Gluntz S, Alexander B, Gómez-Sánchez CE. Central nervous system action of endothelin-3 to inhibit water drinking in the rat. Brain research. 1991;539(2):347-51.
310. Goto K, Kasuya Y, Matsuki N, Takuwa Y, Kurihara H, Ishikawa T, et al. Endothelin activates the dihydropyridine-sensitive, voltage-dependent Ca2+ channel in vascular smooth muscle. Proceedings of the National Academy of Sciences of the United States of America. 1989;86(10):3915-8.
311. Douglas SA, Ohlstein EH. Signal transduction mechanisms mediating the vascular actions of endothelin. Journal of vascular research. 1997;34(3):152-64.
312. Ruiz-Opazo N, Hirayama K, Akimoto K, Herrera VL. Molecular characterization of a dual endothelin-1/Angiotensin II receptor. Molecular medicine (Cambridge, Mass). 1998;4(2):96-108.
313. Lecoin L, Sakurai T, Ngo MT, Abe Y, Yanagisawa M, Le Douarin NM. Cloning and characterization of a novel endothelin receptor subtype in the avian class. Proceedings of the National Academy of Sciences of the United States of America. 1998;95(6):3024-9.
314. Regard JB, Sato IT, Coughlin SR. Anatomical profiling of G protein-coupled receptor expression. Cell. 2008;135(3):561-71.
315. Lipa JE, Neligan PC, Perreault TM, Baribeau J, Levine RH, Knowlton RJ, et al. Vasoconstrictor effect of endothelin-1 in human skin: role of ETA and ETB receptors. The American journal of physiology. 1999;276(2 Pt 2):H359-67.
316. Maguire JJ, Davenport AP. Endothelin receptors and their antagonists. Seminars in nephrology. 2015;35(2):125-36.
317. Morton AJ, Davenport AP. Cerebellar neurons and glia respond differentially to endothelins and sarafotoxin S6b. Brain research. 1992;581(2):299-306.
318. Harland SP, Kuc RE, Pickard JD, Davenport AP. Characterization of endothelin receptors in human brain cortex, gliomas, and meningiomas. Journal of cardiovascular pharmacology. 1995;26 Suppl 3:S408-11.
319. Adner M, Jansen I, Edvinsson L. Endothelin-A receptors mediate contraction in human cerebral, meningeal and temporal arteries. Journal of the autonomic nervous system. 1994;49 Suppl:S117-21.
320. Hardebo JE, Kahrstrom J, Owman C, Salford LG. Endothelin is a potent constrictor of human intracranial arteries and veins. Blood vessels. 1989;26(5):249-53.
321. Johansson S, Povlsen GK, Edvinsson L. Expressional changes in cerebrovascular receptors after experimental transient forebrain ischemia. PloS one. 2012;7(7):e41852.
322. Larsen CC, Povlsen GK, Rasmussen MN, Edvinsson L. Improvement in neurological

outcome and abolition of cerebrovascular endothelin B and 5-hydroxytryptamine 1B receptor upregulation through mitogen-activated protein kinase kinase 1/2 inhibition after subarachnoid hemorrhage in rats. Journal of neurosurgery. 2011;114(4):1143-53.
323. Kelly-Cobbs AI, Harris AK, Elgebaly MM, Li W, Sachidanandam K, Portik-Dobos V, et al. Endothelial endothelin B receptor-mediated prevention of cerebrovascular remodeling is attenuated in diabetes because of up-regulation of smooth muscle endothelin receptors. The Journal of pharmacology and experimental therapeutics. 2011;337(1):9-15.
324. Bax WA, Bruinvels AT, van Suylen RJ, Saxena PR, Hoyer D. Endothelin receptors in the human coronary artery, ventricle and atrium. A quantitative autoradiographic analysis. Naunyn-Schmiedeberg's archives of pharmacology. 1993;348(4):403-10.
325. Sakai S, Miyauchi T, Kobayashi M, Yamaguchi I, Goto K, Sugishita Y. Inhibition of myocardial endothelin pathway improves long-term survival in heart failure. Nature. 1996;384:353.
326. MacCarthy PA, Grocott-Mason R, Prendergast BD, Shah AM. Contrasting inotropic effects of endogenous endothelin in the normal and failing human heart: studies with an intracoronary ET(A) receptor antagonist. Circulation. 2000;101(2):142-7.
327. Molenaar P, O'Reilly G, Sharkey A, Kuc RE, Harding DP, Plumpton C, et al. Characterization and localization of endothelin receptor subtypes in the human atrioventricular conducting system and myocardium. Circ Res. 1993;72(3):526-38.
328. Kuc RE, Carlebur M, Maguire JJ, Yang P, Long L, Toshner M, et al. Modulation of endothelin receptors in the failing right ventricle of the heart and vasculature of the lung in human pulmonary arterial hypertension. Life sciences. 2014;118(2):391-6.
329. Zolk O, Quattek J, Sitzler G, Schrader T, Nickenig G, Schnabel P, et al. Expression of endothelin-1, endothelin-converting enzyme, and endothelin receptors in chronic heart failure. Circulation. 1999;99(16):2118-23.
330. Dagassan PH, Breu V, Clozel M, Kunzli A, Vogt P, Turina M, et al. Up-regulation of endothelin-B receptors in atherosclerotic human coronary arteries. Journal of cardiovascular pharmacology. 1996;27(1):147-53.
331. Batra VK, McNeill JR, Xu Y, Wilson TW, Gopalakrishnan V. ETB receptors on aortic smooth muscle cells of spontaneously hypertensive rats. The American journal of physiology. 1993;264(2 Pt 1):C479-84.
332. Wackenfors A, Emilson M, Ingemansson R, Hortobagyi T, Szok D, Tajti J, et al. Ischemic heart disease induces upregulation of endothelin receptor mRNA in human coronary arteries. European journal of pharmacology. 2004;484(1):103-9.
333. Henry PJ, Rigby PJ, Self GJ, Preuss JM, Goldie RG. Relationship between endothelin-1 binding site densities and constrictor activities in human and animal airway smooth muscle. Br J Pharmacol. 1990;100(4):786-92.
334. Taylor TA, Gariepy CE, Pollock DM, Pollock JS. Gender differences in ET and NOS systems in ETB receptor-deficient rats: effect of a high salt diet. Hypertension. 2003;41(3 Pt 2):657-62.
335. Knott PG, D'Aprile AC, Henry PJ, Hay DW, Goldie RG. Receptors for endothelin-1 in asthmatic human peripheral lung. Br J Pharmacol. 1995;114(1):1-3.
336. Hall SM, Davie N, Klein N, Haworth SG. Endothelin receptor expression in idiopathic pulmonary arterial hypertension: effect of bosentan and epoprostenol treatment. European Respiratory Journal. 2011;38(4):851-60.
337. Chow LH, Subramanian S, Nuovo GJ, Miller F, Nord EP. Endothelin receptor mRNA expression in renal medulla identified by in situ RT-PCR. The American journal of physiology.

1995;269(3 Pt 2):F449-57.
338. Terada Y, Tomita K, Nonoguchi H, Marumo F. Different localization of two types of endothelin receptor mRNA in microdissected rat nephron segments using reverse transcription and polymerase chain reaction assay. The Journal of clinical investigation. 1992;90(1):107-12.
339. Davenport AP, Maguire JJ. Endothelin. Handbook of experimental pharmacology. 2006(176 Pt 1):295-329.
340. Rubin LJ, Badesch DB, Barst RJ, Galie N, Black CM, Keogh A, et al. Bosentan therapy for pulmonary arterial hypertension. The New England journal of medicine. 2002;346(12):896-903.
341. Weber C, Schmitt R, Birnboeck H, Hopfgartner G, van Marle SP, Peeters PAM, et al. Pharmacokinetics and pharmacodynamics of the endothelin-receptor antagonist bosentan in healthy human subjects. Clinical Pharmacology & Therapeutics. 1996;60(2):124-37.
342. Kalra PR, Moon JC, Coats AJ. Do results of the ENABLE (Endothelin Antagonist Bosentan for Lowering Cardiac Events in Heart Failure) study spell the end for non-selective endothelin antagonism in heart failure? International journal of cardiology. 2002;85(2-3):195-7.
343. Kiowski W, Sutsch G, Hunziker P, Muller P, Kim J, Oechslin E, et al. Evidence for endothelin-1-mediated vasoconstriction in severe chronic heart failure. Lancet. 1995;346(8977):732-6.
344. McMurray JJ, Teerlink JR, Cotter G, Bourge RC, Cleland JG, Jondeau G, et al. Effects of tezosentan on symptoms and clinical outcomes in patients with acute heart failure: the VERITAS randomized controlled trials. Jama. 2007;298(17):2009-19.
345. Urbanowicz W, Sogni P, Moreau R, Tazi KA, Barriere E, Poirel O, et al. Tezosentan, an endothelin receptor antagonist, limits liver injury in endotoxin challenged cirrhotic rats. Gut. 2004;53(12):1844-9.
346. Pulido T, Adzerikho I, Channick RN, Delcroix M, Galiè N, Ghofrani H-A, et al. Macitentan and Morbidity and Mortality in Pulmonary Arterial Hypertension. New England Journal of Medicine. 2013;369(9):809-18.
347. Adachi M, Yang YY, Furuichi Y, Miyamoto C. Cloning and characterization of cDNA encoding human A-type endothelin receptor. Biochemical and biophysical research communications. 1991;180(3):1265-72.
348. Cyr C, Huebner K, Druck T, Kris R. Cloning and chromosomal localization of a human endothelin ETA receptor. Biochemical and biophysical research communications. 1991;181(1):184-90.
349. Lin HY, Kaji EH, Winkel GK, Ives HE, Lodish HF. Cloning and functional expression of a vascular smooth muscle endothelin 1 receptor. Proceedings of the National Academy of Sciences of the United States of America. 1991;88(8):3185-9.
350. Isberg V, Vroling B, van der Kant R, Li K, Vriend G, Gloriam D. GPCRDB: an information system for G protein-coupled receptors. Nucleic Acids Res. 2014;42(Database issue):D422-5.
351. Horstmeyer A, Cramer H, Sauer T, Muller-Esterl W, Schroeder C. Palmitoylation of endothelin receptor A. Differential modulation of signal transduction activity by post-translational modification. The Journal of biological chemistry. 1996;271(34):20811-9.
352. Cramer H, Muller-Esterl W, Schroeder C. Subtype-specific desensitization of human endothelin ETA and ETB receptors reflects differential receptor phosphorylation. Biochemistry. 1997;36(43):13325-32.
353. Freedman NJ, Ament AS, Oppermann M, Stoffel RH, Exum ST, Lefkowitz RJ.

Phosphorylation and desensitization of human endothelin A and B receptors. Evidence for G protein-coupled receptor kinase specificity. The Journal of biological chemistry. 1997;272(28):17734-43.
354. Hosoda K, Hammer RE, Richardson JA, Baynash AG, Cheung JC, Giaid A, et al. Targeted and natural (piebald-lethal) mutations of endothelin-B receptor gene produce megacolon associated with spotted coat color in mice. Cell. 1994;79(7):1267-76.
355. Verhaar MC, Strachan FE, Newby DE, Cruden NL, Koomans HA, Rabelink TJ, et al. Endothelin-A receptor antagonist-mediated vasodilatation is attenuated by inhibition of nitric oxide synthesis and by endothelin-B receptor blockade. Circulation. 1998;97(8):752-6.
356. Montanari A, Biggi A, Carra N, Fasoli E, Calzolari M, Corsini F, et al. Endothelin-A blockade attenuates systemic and renal hemodynamic effects of L-NAME in humans. Hypertension. 2000;35(1 Pt 2):518-23.
357. Haynes WG, Webb DJ. Contribution of endogenous generation of endothelin-1 to basal vascular tone. Lancet. 1994;344(8926):852-4.
358. Maguire JJ, Kuc RE, O'Reilly G, Davenport AP. Vasoconstrictor endothelin receptors characterized in human renal artery and vein in vitro. Br J Pharmacol. 1994;113(1):49-54.
359. Masaki T. Possible role of endothelin in endothelial regulation of vascular tone. Annual review of pharmacology and toxicology. 1995;35:235-55.
360. Givertz MM, Colucci WS, LeJemtel TH, Gottlieb SS, Hare JM, Slawsky MT, et al. Acute endothelin A receptor blockade causes selective pulmonary vasodilation in patients with chronic heart failure. Circulation. 2000;101(25):2922-7.
361. Lavelle A, Sugrue R, Lawler G, Mulligan N, Kelleher B, Murphy DM, et al. Sitaxentan-induced hepatic failure in two patients with pulmonary arterial hypertension. European Respiratory Journal. 2009;34(3):770-1.
362. Vizza CD, Fedele F, Pezzuto B, Rubin LJ. Safety and efficacy evaluation of ambrisentan in pulmonary hypertension. Expert opinion on drug safety. 2012;11(6):1003-11.
363. Nelson JB, Fizazi K, Miller K, Higano C, Moul JW, Akaza H, et al. Phase 3, randomized, placebo-controlled study of zibotentan (ZD4054) in patients with castration-resistant prostate cancer metastatic to bone. Cancer. 2012;118(22):5709-18.
364. Chiappori AA, Haura E, Rodriguez FA, Boulware D, Kapoor R, Neuger AM, et al. Phase I/II study of atrasentan, an endothelin A receptor antagonist, in combination with paclitaxel and carboplatin as first-line therapy in advanced non-small cell lung cancer. Clinical cancer research : an official journal of the American Association for Cancer Research. 2008;14(5):1464-9.
365. de Zeeuw D, Coll B, Andress D, Brennan JJ, Tang H, Houser M, et al. The endothelin antagonist atrasentan lowers residual albuminuria in patients with type 2 diabetic nephropathy. Journal of the American Society of Nephrology : JASN. 2014;25(5):1083-93.
366. Mann JFE, Green D, Jamerson K, Ruilope LM, Kuranoff SJ, Littke T, et al. Avosentan for overt diabetic nephropathy. Journal of the American Society of Nephrology : JASN. 2010;21(3):527-35.
367. Baltatu OC, Zaugg CE, Schumacher C, Louie P, Campos LA, Bader M. Avosentan is protective in hypertensive nephropathy at doses not causing fluid retention. Pharmacological Research. 2014;80:9-13.
368. Cai Y, Yamada T, Xin X, Agui T, Matsumoto K. Mapping of the genes for rat endothelin receptor type A (ETAR) and type B (ETBR) to chromosomes 19 and 15 respectively. Animal genetics. 1995;26(1):39-41.
369. Okamoto Y, Ninomiya H, Tanioka M, Sakamoto A, Miwa S, Masaki T. Palmitoylation of

human endothelinB. Its critical role in G protein coupling and a differential requirement for the cytoplasmic tail by G protein subtypes. The Journal of biological chemistry. 1997;272(34):21589-96.
370. Stannard C, Lehenkari P, Godovac-Zimmermann J. Functional Diversity of Endothelin Pathways in Human Lung Fibroblasts May Be Based on Structural Diversity of the Endothelin Receptors. Biochemistry. 2003;42(47):13909-18.
371. Cramer H, Schmenger K, Heinrich K, Horstmeyer A, Boning H, Breit A, et al. Coupling of endothelin receptors to the ERK/MAP kinase pathway. Roles of palmitoylation and G(alpha)q. European journal of biochemistry. 2001;268(20):5449-59.
372. Shichiri M, Kato H, Marumo F, Hirata Y. Endothelin-1 as an autocrine/paracrine apoptosis survival factor for endothelial cells. Hypertension. 1997;30(5):1198-203.
373. White DG, Cannon TR, Garratt H, Mundin JW, Sumner MJ, Watts IS. Endothelin ETA and ETB receptors mediate vascular smooth-muscle contraction. Journal of cardiovascular pharmacology. 1993;22 Suppl 8:S144-8.
374. Wright CE, Fozard JR. Regional vasodilation is a prominent feature of the haemodynamic response to endothelin in anaesthetized, spontaneously hypertensive rats. European journal of pharmacology. 1988;155(1):201-3.
375. Berti F, Rossoni G, Della Bella D, Villa LM, Buschi A, Trento F, et al. Nitric oxide and prostacyclin influence coronary vasomotor tone in perfused rabbit heart and modulate endothelin-1 activity. Journal of cardiovascular pharmacology. 1993;22(2):321-6.
376. Filep JG, Foldes-Filep E, Rousseau A, Sirois P, Fournier A. Vascular responses to endothelin-1 following inhibition of nitric oxide synthesis in the conscious rat. Br J Pharmacol. 1993;110(3):1213-21.
377. Ohuchi T, Kuwaki T, Ling GY, Dewit D, Ju KH, Onodera M, et al. Elevation of blood pressure by genetic and pharmacological disruption of the ETB receptor in mice. The American journal of physiology. 1999;276(4):R1071-7.
378. Love MP, Ferro CJ, Haynes WG, Plumpton C, Davenport AP, Webb DJ, et al. Endothelin receptor antagonism in patients with chronic heart failure. Cardiovascular research. 2000;47(1):166-72.
379. Bohm F, Pernow J, Lindstrom J, Ahlborg G. ETA receptors mediate vasoconstriction, whereas ETB receptors clear endothelin-1 in the splanchnic and renal circulation of healthy men. Clinical science (London, England : 1979). 2003;104(2):143-51.
380. Fukuroda T, Fujikawa T, Ozaki S, Ishikawa K, Yano M, Nishikibe M. Clearance of circulating endothelin-1 by ETB receptors in rats. Biochemical and biophysical research communications. 1994;199(3):1461-5.
381. Gariepy CE, Ohuchi T, Williams SC, Richardson JA, Yanagisawa M. Salt-sensitive hypertension in endothelin-B receptor-deficient rats. The Journal of clinical investigation. 2000;105(7):925-33.
382. Stewart DJ, Levy RD, Cernacek P, Langleben D. Increased plasma endothelin-1 in pulmonary hypertension: marker or mediator of disease? Annals of internal medicine. 1991;114(6):464-9.
383. Saito Y, Kazuwa N, Shirakami G, Mukoyama M, Arai H, Hosoda K, et al. Endothelin in patients with chronic renal failure. Journal of cardiovascular pharmacology. 1991;17 Suppl 7:S437-9.
384. Gandhi CR, Kang Y, De Wolf A, Madariaga J, Aggarwal S, Scott V, et al. Altered endothelin homeostasis in patients undergoing liver transplantation. 1996;2(5):362-9.
385. Sutsch G, Kiowski W, Yan XW, Hunziker P, Christen S, Strobel W, et al. Short-term oral

endothelin-receptor antagonist therapy in conventionally treated patients with symptomatic severe chronic heart failure. Circulation. 1998;98(21):2262-8.
386. Kelland NF, Kuc RE, McLean DL, Azfer A, Bagnall AJ, Gray GA, et al. Endothelial cell-specific ETB receptor knockout: autoradiographic and histological characterisation and crucial role in the clearance of endothelin-1. Canadian journal of physiology and pharmacology. 2010;88(6):644-51.
387. Bremnes T, Paasche JD, Mehlum A, Sandberg C, Bremnes B, Attramadal H. Regulation and intracellular trafficking pathways of the endothelin receptors. The Journal of biological chemistry. 2000;275(23):17596-604.
388. Johnström P, Fryer TD, Richards HK, Harris NG, Barret O, Clark JC, et al. Positron emission tomography using 18F-labelled endothelin-1 reveals prevention of binding to cardiac receptors owing to tissue-specific clearance by ET B receptors in vivo. British journal of pharmacology. 2005;144(1):115-22.
389. Naomi S, Iwaoka T, Disashi T, Inoue J, Kanesaka Y, Tokunaga H, et al. Endothelin-1 inhibits endothelin-converting enzyme-1 expression in cultured rat pulmonary endothelial cells. Circulation. 1998;97(3):234-6.
390. Masaoka H, Suzuki R, Hirata Y, Emori T, Marumo F, Hirakawa K. Raised plasma endothelin in aneurysmal subarachnoid haemorrhage. Lancet. 1989;2(8676):1402.
391. Zimmermann M. Endothelin in cerebral vasospasm. Clinical and experimental results. Journal of neurosurgical sciences. 1997;41(2):139-51.
392. Mitani H, Takimoto M, Bandoh T, Kimura M. Increases of vascular endothelin-converting enzyme activity and endothelin-1 level on atherosclerotic lesions in hyperlipidemic rabbits. European journal of pharmacology. 2000;387(3):313-9.
393. Kowala MC, Rose PM, Stein PD, Goller N, Recce R, Beyer S, et al. Selective blockade of the endothelin subtype A receptor decreases early atherosclerosis in hamsters fed cholesterol. The American journal of pathology. 1995;146(4):819-26.
394. Stewart DJ, Kubac G, Costello KB, Cernacek P. Increased plasma endothelin-1 in the early hours of acute myocardial infarction. Journal of the American College of Cardiology. 1991;18(1):38-43.
395. Grover GJ, Dzwonczyk S, Parham CS. The endothelin-1 receptor antagonist BQ-123 reduces infarct size in a canine model of coronary occlusion and reperfusion. Cardiovascular research. 1993;27(9):1613-8.
396. Wendel M, Knels L, Kummer W, Koch T. Distribution of endothelin receptor subtypes ETA and ETB in the rat kidney. The journal of histochemistry and cytochemistry : official journal of the Histochemistry Society. 2006;54(11):1193-203.
397. Pollock DM, Opgenorth TJ. ETA receptor-mediated responses to endothelin-1 and big endothelin-1 in the rat kidney. Br J Pharmacol. 1994;111(3):729-32.
398. Edwards RM, Stack EJ, Pullen M, Nambi P. Endothelin inhibits vasopressin action in rat inner medullary collecting duct via the ETB receptor. The Journal of pharmacology and experimental therapeutics. 1993;267(3):1028-33.
399. Williams DL, Jr., Jones KL, Pettibone DJ, Lis EV, Clineschmidt BV. Sarafotoxin S6c: an agonist which distinguishes between endothelin receptor subtypes. Biochemical and biophysical research communications. 1991;175(2):556-61.
400. Das B, Sarkar C, Shankar PR. Pretreatment with sarafotoxin 6c prior to coronary occlusion protects against infarction and arrhythmias via cardiomyocyte mitochondrial K(ATP) channel activation in the intact rabbit heart during ischemia/reperfusion. Cardiovascular drugs and therapy. 2007;21(4):243-51.

401. Takai M, Umemura I, Yamasaki K, Watakabe T, Fujitani Y, Oda K, et al. A potent and specific agonist, Suc-[Glu9,Ala11,15]-endothelin-1(8-21), IRL 1620, for the ETB receptor. Biochemical and biophysical research communications. 1992;184(2):953-9.
402. Briyal S, Nguyen C, Leonard M, Gulati A. Stimulation of endothelin B receptors by IRL-1620 decreases the progression of Alzheimer's disease. Neuroscience. 2015;301:1-11.
403. Ihara M, Saeki T, Fukuroda T, Kimura S, Ozaki S, Patel AC, et al. A novel radioligand [125I]BQ-3020 selective for endothelin (ETB) receptors. Life sciences. 1992;51(6):Pl47-52.
404. Karet FE, Kuc RE, Davenport AP. Novel ligands BQ123 and BQ3020 characterize endothelin receptor subtypes ETA and ETB in human kidney. Kidney international. 1993;44(1):36-42.
405. Nambi P, Pullen M. [125I]-BQ3020, a potent ETB-selective agonist, displays species differences in its binding characteristics. Neuropeptides. 1995;28(3):191-6.
406. Kim R, Chiorean EG, Amin M, Rocha-Lima CMS, Gandhi J, Harris WP, et al. Phase 2 study of combination SPI-1620 with docetaxel as second-line advanced biliary tract cancer treatment. British Journal Of Cancer. 2017;117:189.
407. Ishikawa K, Ihara M, Noguchi K, Mase T, Mino N, Saeki T, et al. Biochemical and pharmacological profile of a potent and selective endothelin B-receptor antagonist, BQ-788. Proceedings of the National Academy of Sciences. 1994;91(11):4892-6.
408. Okada M, Nishikibe M. BQ-788, a selective endothelin ET(B) receptor antagonist. Cardiovascular drug reviews. 2002;20(1):53-66.
409. Früh T, Saika H, Svensson L, Pitterna T, Sakaki J, Okada T, et al. IRL 2500: A potent ETB selective endothelin antagonist. Bioorganic & Medicinal Chemistry Letters. 1996;6(19):2323-8.
410. Webb RL, Navarrete AE, Ksander GM. Effects of the ETB-selective antagonist IRL 2500 in conscious spontaneously hypertensive and Wistar-Kyoto rats. Journal of cardiovascular pharmacology. 1995;26 Suppl 3:S389-92.
411. Tanaka T, Tsukuda E, Nozawa M, Nonaka H, Ohno T, Kase H, et al. RES-701-1, a novel, potent, endothelin type B receptor-selective antagonist of microbial origin. Molecular pharmacology. 1994;45(4):724-30.
412. Hocher B, Dembowski C, Slowinski T, Friese ST, Schwarz A, Siren AL, et al. Impaired sodium excretion, decreased glomerular filtration rate and elevated blood pressure in endothelin receptor type B deficient rats. Journal of molecular medicine (Berlin, Germany). 2001;78(11):633-41.
413. Gariepy CE, Cass DT, Yanagisawa M. Null mutation of endothelin receptor type B gene in spotting lethal rats causes aganglionic megacolon and white coat color. Proceedings of the National Academy of Sciences of the United States of America. 1996;93(2):867-72.
414. Matsushima Y, Shinkai Y, Kobayashi Y, Sakamoto M, Kunieda T, Tachibana M. A mouse model of Waardenburg syndrome type 4 with a new spontaneous mutation of the endothelin-B receptor gene. Mammalian genome : official journal of the International Mammalian Genome Society. 2002;13(1):30-5.
415. Dembowski C, Hofmann P, Koch T, Kamrowski-Kruck H, Riedesel H, Krammer H-J, et al. Phenotype, intestinal morphology, and survival of homozygous and heterozygous endothelin B receptor–deficient (spotting lethal) rats. Journal of pediatric surgery. 2000;35(3):480-8.
416. Elisa T, Antonio P, Giuseppe P, Alessandro B, Giuseppe A, Federico C, et al. Endothelin Receptors Expressed by Immune Cells Are Involved in Modulation of Inflammation and in Fibrosis: Relevance to the Pathogenesis of Systemic Sclerosis. 2015;2015:147616.
417. Kak AC, Slaney M, IEEE Engineering in Medicine and Biology Society. Principles of

computerized tomographic imaging. New York: IEEE Press; 1988. x, 329 p.
418. Feldkamp LA, Davis LC, Kress JW. Practical cone-beam algorithm. J Opt Soc Am A. 1984;1(6):612-9.
419. FLANNERY BP, DECKMAN HW, ROBERGE WG, D'AMICO KL. Three-Dimensional X-ray Microtomography. Science. 1987;237(4821):1439-44.
420. Kinney JH, Johnson QC, Nichols MC, Bonse U, Saroyan RA, Nusshardt R, et al. X-ray microtomography on beamline X at SSRL. Review of Scientific Instruments. 1989;60(7):2471-4.
421. Natterer F, Ritman EL. Past and future directions in x-ray computed tomography (CT). International Journal of Imaging Systems and Technology. 2002;12(4):175-87.
422. Burghardt AJ, Link TM, Majumdar S. High-resolution computed tomography for clinical imaging of bone microarchitecture. Clinical orthopaedics and related research. 2011;469(8):2179-93.
423. Mather ML, Morgan SP, White LJ, Tai H, Kockenberger W, Howdle SM, et al. Image-based characterization of foamed polymeric tissue scaffolds. Biomedical materials. 2008;3(1):015011.
424. Nakagaki S, Iijima M, Handa K, Koike T, Yasuda Y, Saito T, et al. Micro-CT and histologic analyses of bone surrounding immediately loaded miniscrew implants: comparing compression and tension loading. Dental materials journal. 2014;33(2):196-202.
425. Peyrin F. Evaluation of bone scaffolds by micro-CT. Osteoporosis international : a journal established as result of cooperation between the European Foundation for Osteoporosis and the National Osteoporosis Foundation of the USA. 2011;22(6):2043-8.
426. Oliveira MF, Lima I, Borghi L, Lopes RT. X-ray microtomography application in pore space reservoir rock. Applied radiation and isotopes : including data, instrumentation and methods for use in agriculture, industry and medicine. 2012;70(7):1376-8.
427. Wirkner CS, Richter S. Improvement of microanatomical research by combining corrosion casts with MicroCT and 3D reconstruction, exemplified in the circulatory organs of the woodlouse. Microscopy research and technique. 2004;64(3):250-4.
428. Wirkner CS, Prendini L. Comparative morphology of the hemolymph vascular system in scorpions--a survey using corrosion casting, MicroCT, and 3D-reconstruction. Journal of morphology. 2007;268(5):401-13.
429. Ribi W, Senden TJ, Sakellariou A, Limaye A, Zhang S. Imaging honey bee brain anatomy with micro-X-ray-computed tomography. Journal of neuroscience methods. 2008;171(1):93-7.
430. Mizutani R, Takeuchi A, Hara T, Uesugi K, Suzuki Y. Computed tomography imaging of the neuronal structure of Drosophila brain. Journal of synchrotron radiation. 2007;14(Pt 3):282-7.
431. Metscher BD. MicroCT for developmental biology: a versatile tool for high-contrast 3D imaging at histological resolutions. Developmental dynamics : an official publication of the American Association of Anatomists. 2009;238(3):632-40.
432. Howard CV, Reed M. Unbiased stereology three-dimensional measurement in microscopy. 2nd ed. Abingdon, Oxon: BIOS Scientific Publishers; 2005. 277 S. p.
433. Mouton PR, Ebrary. Principles and practices of unbiased stereology an introduction for bioscientists. Baltimore: Johns Hopkins University Press; 2002. electronic text. p.
434. Renghini C, Komlev V, Fiori F, Verne E, Baino F, Vitale-Brovarone C. Micro-CT studies on 3-D bioactive glass-ceramic scaffolds for bone regeneration. Acta biomaterialia. 2009;5(4):1328-37.

435. Chen K-C, Arad A, Song Z-M, Croaker D. High-definition neural visualization of rodent brain using micro-CT scanning and non-local-means processing. BMC Med Imaging. 2018;18(1):38-.
436. Chen KC AA, Song ZM, Croaker DG. High-Definition Heart Visualization using Micro-CT Scanning on Experimental Rats. J Clin Exp Cardiolog. 2018;9(606).
437. Bradley RS, McNeil A, Withers PJ. An examination of phase retrieval algorithms as applied to phase contrast tomography using laboratory sources. Proc Spie. 2010;7804.
438. Wilkins SW, Gureyev TE, Gao D, Pogany A, Stevenson AW. Phase-contrast imaging using polychromatic hard X-rays. Nature. 1996;384(6607):335-8.
439. Schambach SJ, Bag S, Schilling L, Groden C, Brockmann MA. Application of micro-CT in small animal imaging. Methods. 2010;50(1):2-13.
440. Roth H, Neubrand T, Mayer T, editors. Improved inspection of miniaturised interconnections by digital X-ray inspection and computed tomography. Electronics Packaging Technology Conference (EPTC), 2010 12th; 2010 8-10 Dec. 2010.
441. Weninger WJ, Geyer SH, Mohun TJ, Rasskin-Gutman D, Matsui T, Ribeiro I, et al. High-resolution episcopic microscopy: a rapid technique for high detailed 3D analysis of gene activity in the context of tissue architecture and morphology. Anatomy and embryology. 2006;211(3):213-21.
442. Sharpe J, Ahlgren U, Perry P, Hill B, Ross A, Hecksher-Sørensen J, et al. Optical Projection Tomography as a Tool for 3D Microscopy and Gene Expression Studies. Science. 2002;296(5567):541-5.
443. Dhenain M, Ruffins SW, Jacobs RE. Three-Dimensional Digital Mouse Atlas Using High-Resolution MRI. Developmental biology. 2001;232(2):458-70.
444. Turnbull DH, Mori S. MRI in mouse developmental biology. NMR in biomedicine. 2007;20(3):265-74.
445. Smithpeter CL, Dunn AK, Welch AJ, Richards-Kortum R. Penetration depth limits of in vivo confocal reflectance imaging. Applied optics. 1998;37(13):2749-54.
446. Weninger WJ, Geyer SH. Episcopic 3D Imaging Methods: Tools for Researching Gene Function. Current genomics. 2008;9(4):282-9.
447. Alanentalo T, Loren CE, Larefalk A, Sharpe J, Holmberg D, Ahlgren U. High-resolution three-dimensional imaging of islet-infiltrate interactions based on optical projection tomography assessments of the intact adult mouse pancreas. Journal of biomedical optics. 2008;13(5):054070.
448. Ruffins SW, Martin M, Keough L, Truong S, Fraser SE, Jacobs RE, et al. Digital three-dimensional atlas of quail development using high-resolution MRI. TheScientificWorldJournal. 2007;7:592-604.
449. Wong MD, Spring S, Henkelman RM. Structural stabilization of tissue for embryo phenotyping using micro-CT with iodine staining. PloS one. 2013;8(12):e84321.
450. Missbach-Guentner J, Hunia J, Alves F. Tumor blood vessel visualization. The International journal of developmental biology. 2011;55(4-5):535-46.
451. Metscher BD. MicroCT for comparative morphology: simple staining methods allow high-contrast 3D imaging of diverse non-mineralized animal tissues. BMC physiology. 2009;9:11.
452. Pauwels E, Van Loo D, Cornillie P, Brabant L, Van Hoorebeke L. An exploratory study of contrast agents for soft tissue visualization by means of high resolution X-ray computed tomography imaging. Journal of microscopy. 2013;250(1):21-31.
453. Limaye A. Drishti, A volume exploration and Presentation Tool. Developments in X-

Ray Tomography VIII; 17 October 20122012.
454. Schindelin J, Rueden CT, Hiner MC, Eliceiri KW. The ImageJ ecosystem: An open platform for biomedical image analysis. Molecular Reproduction and Development. 2015;82(7-8):518-29.
455. Buades A, Coll B, Morel JM, editors. A non-local algorithm for image denoising. 2005 IEEE Computer Society Conference on Computer Vision and Pattern Recognition (CVPR'05); 2005 20-25 June 2005.
456. Schindelin J, Arganda-Carreras I, Frise E, Kaynig V, Longair M, Pietzsch T, et al. Fiji: an open-source platform for biological-image analysis. Nat Meth. 2012;9(7):676-82.
457. Coupe P, Yger P, Prima S, Hellier P, Kervrann C, Barillot C. An optimized blockwise nonlocal means denoising filter for 3-D magnetic resonance images. IEEE Trans Med Imaging. 2008;27(4):425-41.
458. Denic A, Macura SI, Mishra P, Gamez JD, Rodriguez M, Pirko I. MRI in Rodent Models of Brain Disorders. Neurotherapeutics : the journal of the American Society for Experimental NeuroTherapeutics. 2011;8(1):3-18.
459. Gabbay-Benziv R, Reece EA, Wang F, Bar-Shir A, Harman C, Turan OM, et al. A step-wise approach for analysis of the mouse embryonic heart using 17.6 Tesla MRI. Magnetic resonance imaging. 2017;35:46-53.
460. Stauber M, Muller R. Micro-computed tomography: a method for the non-destructive evaluation of the three-dimensional structure of biological specimens. Methods in molecular biology. 2008;455:273-92.
461. Pardridge WM. Introduction to the blood-brain barrier methodology, biology, and pathology. Cambridge etc.: Cambridge University Press; 1998. XIV, 486 S. p.
462. Neuwelt EA. Mechanisms of disease: the blood-brain barrier. Neurosurgery. 2004;54(1):131-40; discussion 41-2.
463. Cotton FA, Cotton FA. Advanced inorganic chemistry. 6th / ed. New York: Wiley; 1999. xv, 1355 p.
464. Everett M, Miller W. The role of phosphotungstic and phosphomolybdic acids in connective tissue staining I. Histochemical studies. Histochem J. 1974;6(1):25-34.
465. Gignac PM, Kley NJ. Iodine-enhanced micro-CT imaging: methodological refinements for the study of the soft-tissue anatomy of post-embryonic vertebrates. Journal of experimental zoology Part B, Molecular and developmental evolution. 2014;322(3):166-76.
466. Wells AF. Structural inorganic chemistry. 5th ed. Oxford: Clarendon Press; 1984. 1 v. p.
467. Johnson GA, Ali-Sharief A, Badea A, Brandenburg J, Cofer G, Fubara B, et al. High-throughput morphologic phenotyping of the mouse brain with magnetic resonance histology. NeuroImage. 2007;37(1):82-9.
468. Kerwin J, Scott M, Sharpe J, Puelles L, Robson SC, Martinez-de-la-Torre M, et al. 3 dimensional modelling of early human brain development using optical projection tomography. BMC neuroscience. 2004;5:27.
469. Jacobs RE, Papan C, Ruffins S, Tyszka JM, Fraser SE. MRI: volumetric imaging for vital imaging and atlas construction. Nature reviews Molecular cell biology. 2003;Suppl:SS10-6.
470. de Crespigny A, Bou-Reslan H, Nishimura MC, Phillips H, Carano RA, D'Arceuil HE. 3D micro-CT imaging of the postmortem brain. Journal of neuroscience methods. 2008;171(2):207-13.
471. Degenhardt K, Wright AC, Horng D, Padmanabhan A, Epstein JA. Rapid 3D phenotyping of cardiovascular development in mouse embryos by micro-CT with iodine staining. Circulation Cardiovascular imaging. 2010;3(3):314-22.

472. Ehling J, Theek B, Gremse F, Baetke S, Mockel D, Maynard J, et al. Micro-CT imaging of tumor angiogenesis: quantitative measures describing micromorphology and vascularization. The American journal of pathology. 2014;184(2):431-41.
473. Razavi H, Dusch MN, Zarafshar SY, Taylor CA, Feinstein JA. A method for quantitative characterization of growth in the 3-D structure of rat pulmonary arteries. Microvascular research. 2012;83(2):146-53.
474. Wong MD, Dorr AE, Walls JR, Lerch JP, Henkelman RM. A novel 3D mouse embryo atlas based on micro-CT. Development. 2012;139(17):3248-56.
475. Arce GR. Weighted Median Filters. Nonlinear Signal Processing: John Wiley & Sons, Inc.; 2005. p. 139-250.
476. Arias-Castro E, Donoho DL. Does median filtering truly preserve edges better than linear filtering? 2009:1172-206.
477. Huang T, Yang G, Tang G. A fast two-dimensional median filtering algorithm. IEEE Transactions on Acoustics, Speech, and Signal Processing. 1979;27(1):13-8.
478. Gerig G, Kubler O, Kikinis R, Jolesz FA. Nonlinear anisotropic filtering of MRI data. IEEE Trans Med Imaging. 1992;11(2):221-32.
479. Sheppard AP, Sok RM, Averdunk H. Techniques for image enhancement and segmentation of tomographic images of porous materials. Physica A: Statistical Mechanics and its Applications. 2004;339(1–2):145-51.
480. Chambolle A. An Algorithm for Total Variation Minimization and Applications. Journal of Mathematical Imaging and Vision. 2004;20(1):89-97.
481. Little MA, Jones NS. Sparse Bayesian Step-Filtering for High-Throughput Analysis of Molecular Machine Dynamics. Int Conf Acoust Spee. 2010:4162-5.
482. Rudin LI, Osher S, Fatemi E. Nonlinear total variation based noise removal algorithms. Physica D: Nonlinear Phenomena. 1992;60(1):259-68.
483. Dabov K, Foi A, Katkovnik V, Egiazarian K, editors. BM3D Image Denoising with Shape-Adaptive Principal Component Analysis. SPARS'09 - Signal Processing with Adaptive Sparse Structured Representations; 2009 2009-04-06; Saint Malo, Francehttps://hal.inria.fr/inria-00369582/document
https://hal.inria.fr/inria-00369582/file/33.pdf.
484. Danielyan A, Katkovnik V, Egiazarian K. BM3D Frames and Variational Image Deblurring. IEEE Transactions on Image Processing. 2012;21(4):1715-28.
485. Bradley RS, McNeil A, Withers PJ, editors. An examination of phase retrieval algorithms as applied to phase contrast tomography using laboratory sources2010.
486. Roth H, Neubrand T, Mayer T, editors. Improved inspection of miniaturised interconnections by digital X-ray inspection and computed tomography. 2010 12th Electronics Packaging Technology Conference; 2010 8-10 Dec. 2010.
487. Limaye A, editor Drishti: a volume exploration and presentation tool2012.
488. Genin L, Champagnat F, Le Besnerais G. Background first- and second-order modeling for point target detection. Applied optics. 2012;51(31):7701-13.
489. Bertrand A, Pasquier A, Petiet A, Wiggins C, Kraska A, Joseph-Mathurin N, et al. Micro-MRI study of cerebral aging: ex vivo detection of hippocampal subfield reorganization, microhemorrhages and amyloid plaques in mouse lemur primates. PloS one. 2013;8(2):e56593.
490. Anversa P, Beghi C, Kikkawa Y, Olivetti G. Myocardial infarction in rats. Infarct size, myocyte hypertrophy, and capillary growth. Circ Res. 1986;58(1):26-37.
491. Chen TL, Zhu GL, He XL, Wang JA, Wang Y, Qi GA. Short-term pretreatment with

atorvastatin attenuates left ventricular dysfunction, reduces infarct size and apoptosis in acute myocardial infarction rats. International journal of clinical and experimental medicine. 2014;7(12):4799-808.
492. Johns HE, Cunningham JR. The physics of radiology. 4th ed. Springfield, Ill.: Thomas; 1983. xix, 796 p.
493. Bushberg JT. The essential physics of medical imaging. 3rd ed. Philadelphia: Wolters Kluwer Health/Lippincott Williams & Wilkins; 2012. xii, 1030 p.
494. Chemical Rubber Company. Handbook of chemistry and physics. Cleveland, Ohio: Chemical Rubber.
495. Quintarelli G, Zito R, Cifonelli JA. On phosphotungstic acid staining. I. The journal of histochemistry and cytochemistry : official journal of the Histochemistry Society. 1971;19(11):641-7.
496. Hubbell JH. Photon mass attenuation and mass energy-absorption coefficients for H, C, N, O, Ar, and seven mixtures from 0.1 keV to 20 MeV. Radiation research. 1977;70(1):58-81.
497. Hollas JM. Modern spectroscopy. 4th ed. Chichester ; Hoboken, NJ: J. Wiley; 2004. xxvii, 452 p.
498. Wolken JJ. Euglena; an experimental organism for biochemical and biophysical studies. 2d ed. [New York]: Appleton-Century-Crofts; 1967. xiii, 204 p.
499. Cheng W, Au DK, Knowles CH, Anand P, Tam PK. Hirschsprung's disease: a more generalised neuropathy? Journal of pediatric surgery. 2001;36(2):296-300.
500. Sayed M, al-Alaiyan S. Agenesis of corpus callosum, hypertrophic pyloric stenosis and Hirschsprung disease: coincidence or common etiology? Neuropediatrics. 1996;27(4):204-6.
501. Staiano A, Santoro L, De Marco R, Miele E, Fiorillo F, Auricchio A, et al. Autonomic dysfunction in children with Hirschsprung's disease. Dig Dis Sci. 1999;44(5):960-5.
502. Amiel J, Sproat-Emison E, Garcia-Barcelo M, Lantieri F, Burzynski G, Borrego S, et al. Hirschsprung disease, associated syndromes and genetics: a review. Journal of medical genetics. 2008;45(1):1-14.
503. Croaker GDH. A Cook's tour around Hirschsprung's disease. Current Paediatrics. 2006;16(3):182-91.
504. Kontges G, Lumsden A. Rhombencephalic neural crest segmentation is preserved throughout craniofacial ontogeny. Development. 1996;122(10):3229-42.
505. Yanagisawa H, Yanagisawa M, Kapur RP, Richardson JA, Williams SC, Clouthier DE, et al. Dual genetic pathways of endothelin-mediated intercellular signaling revealed by targeted disruption of endothelin converting enzyme-1 gene. Development. 1998;125(5):825-36.
506. Milunsky JM. Waardenburg Syndrome Type I. In: Adam MP, Ardinger HH, Pagon RA, Wallace SE, Bean LJH, Stephens K, et al., editors. GeneReviews((R)). Seattle (WA): University of Washington, Seattle
University of Washington, Seattle. GeneReviews is a registered trademark of the University of Washington, Seattle. All rights reserved.; 1993.
507. On the 150(th) Anniversary of Darwin's Submission of One of his "Five Great Books", The Variation of Animals and Plants Under Domestication, to his publisher John Murray. Alzheimers Dement. 2016;12(1):1.
508. Wilkins AS, Wrangham RW, Fitch WT. The “Domestication Syndrome” in Mammals: A Unified Explanation Based on Neural Crest Cell Behavior and Genetics. Genetics. 2014;197(3):795-808.
509. Clutton-Brock J, Clutton-Brock J, Natural History Museum (London England). A natural

history of domesticated mammals. 2nd ed. Cambridge, U.K. ; New York, NY, USA
London ;: Cambridge University Press ;
Natural History Museum; 1999. viii, 238 p. p.
510. Zeuner FE. A history of domesticated animals. London: Hitchinson; 1963. 560p p.
511. Tassabehji M, Newton VE, Read AP. Waardenburg syndrome type 2 caused by mutations in the human microphthalmia (MITF) gene. Nat Genet. 1994;8(3):251-5.
512. Antonellis A, Bennett WR, Menheniott TR, Prasad AB, Lee-Lin SQ, Program NCS, et al. Deletion of long-range sequences at Sox10 compromises developmental expression in a mouse model of Waardenburg-Shah (WS4) syndrome. Hum Mol Genet. 2006;15(2):259-71.
513. Arnold S, Pelet A, Amiel J, Borrego S, Hofstra R, Tam P, et al. Interaction between a chromosome 10 RET enhancer and chromosome 21 in the Down syndrome-Hirschsprung disease association. Human mutation. 2009;30(5):771-5.
514. Johnstrom P, Fryer TD, Richards HK, Harris NG, Barret O, Clark JC, et al. Positron emission tomography using 18F-labelled endothelin-1 reveals prevention of binding to cardiac receptors owing to tissue-specific clearance by ET B receptors in vivo. Br J Pharmacol. 2005;144(1):115-22.
515. Brennan A, Dean CH, Zhang AL, Cass DT, Mirsky R, Jessen KR. Endothelins Control the Timing of Schwann Cell Generation in Vitro and in Vivo. Developmental biology. 2000;227(2):545-57.
516. Barrett RL, Harris EF. Anabolic steroids and craniofacial growth in the rat. Angle Orthod. 1993;63(4):289-98.
517. Goto S, Fujita Y, Hotta M, Sugiyama A, Maki K. Influence of differences in the hardness and calcium content of diets on the growth of craniofacial bone in rats. Angle Orthod. 2015;85(6):969-79.
518. Tsai CY, Yang LY, Chen KT, Chiu WC. The influence of masticatory hypofunction on developing rat craniofacial structure. Int J Oral Maxillofac Surg. 2010;39(6):593-8.
519. Ulgen M, Baran S, Kaya H, Karadede I. The influence of the masticatory hypofunction on the craniofacial growth and development in rats. Am J Orthod Dentofacial Orthop. 1997;111(2):189-98.
520. Issa S, Bondurand N, Faubert E, Poisson S, Lecerf L, Nitschke P, et al. EDNRB mutations cause Waardenburg syndrome type II in the heterozygous state. Human mutation. 2017;38(5):581-93.
521. Kim HY. Statistical notes for clinical researchers: Evaluation of measurement error 2: Dahlberg's error, Bland-Altman method, and Kappa coefficient. Restor Dent Endod. 2013;38(3):182-5.
522. Addison WHF, Appleton JL. The structure and growth of the incisor teeth of the albino rat. Journal of morphology. 1915;26(1):43-96.
523. Griffith JQ, Farris EJ. rat in laboratory investigation. 1949.
524. Pierpont JW, St Jacques D, Seaver LH, Erickson RP. A family with unusual Waardenburg syndrome type I (WSI), cleft lip (palate), and Hirschsprung disease is not linked to PAX 3. Clinical genetics. 1995;47(3):139-43.
525. Tachibana M, Kobayashi Y, Matsushima Y. Mouse models for four types of Waardenburg syndrome. Pigment cell research. 2003;16(5):448-54.
526. Miller JP, German RZ. Protein Malnutrition Affects the Growth Trajectories of the Craniofacial Skeleton in Rats. The Journal of Nutrition. 1999;129(11):2061-9.
527. Zhang YB, Hu J, Zhang J, Zhou X, Li X, Gu C, et al. Genome-wide association study identifies multiple susceptibility loci for craniofacial microsomia. Nat Commun.

2016;7:10605.
528. Brunoni D, Joffe R, Farah LMS, Cunha AJB. Hirschsprung megacolon, cleft lip and palate, mental retardation and minor congenital malformations. Journal of Clinical Dysmorphology. 1983;1:20-2.
529. Hurst JA, Markiewicz M, Kumar D, Brett EM. Unknown syndrome: Hirschsprung's disease, microcephaly, and iris coloboma: a new syndrome of defective neuronal migration. Journal of medical genetics. 1988;25(7):494-7.
530. Slavikova T, Zabojnikova L, Babala J, Varga I. An embryological point of view on associated congenital anomalies of children with Hirschsprung disease. Bratislavske lekarske listy. 2015;116(11):640-7.
531. Greally MT. Shprintzen-Goldberg Syndrome. In: Adam MP, Ardinger HH, Pagon RA, Wallace SE, Bean LJH, Mefford HC, et al., editors. GeneReviews(R). Seattle (WA)1993.
532. Garavelli L, Donadio A, Zanacca C, Banchini G, Della Giustina E, Bertani G, et al. Hirschsprung disease, mental retardation, characteristic facial features, and mutation in the gene ZFHX1B (SIP1): confirmation of the Mowat-Wilson syndrome. American journal of medical genetics Part A. 2003;116A(4):385-8.
533. Kumar AR, Steinbacher D. Advances in the Treatment of Syndromic Midface Hypoplasia Using Monobloc and Facial Bipartition Distraction Osteogenesis. Seminars in Plastic Surgery. 2014;28(4):179-83.
534. Leonard MG, Gulati A. Endothelin B receptor agonist, IRL-1620, enhances angiogenesis and neurogenesis following cerebral ischemia in rats. Brain research. 2013;1528:28-41.
535. Leonard MG, Prazad P, Puppala B, Gulati A. Selective Endothelin-B Receptor Stimulation Increases Vascular Endothelial Growth Factor in the Rat Brain during Postnatal Development. Drug research. 2015;65(11):607-13.
536. Namiki A, Hirata Y, Ishikawa M, Moroi M, Aikawa J, Machii K. Endothelin-1- and endothelin-3-induced vasorelaxation via common generation of endothelium-derived nitric oxide. Life sciences. 1992;50(10):677-82.
537. Ida-Eto M, Ohgami N, Iida M, Yajima I, Kumasaka MY, Takaiwa K, et al. Partial requirement of endothelin receptor B in spiral ganglion neurons for postnatal development of hearing. The Journal of biological chemistry. 2011;286(34):29621-6.
538. Haddad GG, Mazza NM, Defendini R, Blanc WA, Driscoll JM, Epstein MA, et al. Congenital failure of automatic control of ventilation, gastrointestinal motility and heart rate. Medicine (Baltimore). 1978;57(6):517-26.
539. Kusafuka T, Wang Y, Puri P. Novel mutations of the endothelin-B receptor gene in isolated patients with Hirschsprung's disease. Hum Mol Genet. 1996;5(3):347-9.
540. Gariepy CE, Williams SC, Richardson JA, Hammer RE, Yanagisawa M. Transgenic expression of the endothelin-B receptor prevents congenital intestinal aganglionosis in a rat model of Hirschsprung disease. The Journal of clinical investigation. 1998;102(6):1092-101.
541. Kohzuki M, Chai SY, Paxinos G, Karavas A, Casley DJ, Johnston CI, et al. Localization and characterization of endothelin receptor binding sites in the rat brain visualized by in vitro autoradiography. Neuroscience. 1991;42(1):245-60.
542. Webber KM, Pennefather JN, Head GA, van den Buuse M. Endothelin induces dopamine release from rat striatum via endothelin-B receptors. Neuroscience. 1998;86(4):1173-80.
543. Shibata S, Niwa M, Himeno A, Gana NG, Shigematsu K, Matsumoto M, et al. The endothelin ETA receptor exists in the caudal solitary tract nucleus of the rat brain. Cellular

and molecular neurobiology. 1997;17(1):151-6.
544. Fernandez-Durango R, de Juan JA, Zimman H, Moya FJ, Garcia de la Coba M, Fernandez-Cruz A. Identification of endothelin receptor subtype (ETB) in human cerebral cortex using subtype-selective ligands. Journal of neurochemistry. 1994;62(4):1482-8.
545. Giaid A, Gibson SJ, Herrero MT, Gentleman S, Legon S, Yanagisawa M, et al. Topographical localisation of endothelin mRNA and peptide immunoreactivity in neurones of the human brain. Histochemistry. 1991;95(3):303-14.
546. Salvatore S, Vingolo EM. Endothelin-1 role in human eye: a review. J Ophthalmol. 2010;2010:354645.
547. Uchida Y, Ninomiya H, Saotome M, Nomura A, Ohtsuka M, Yanagisawa M, et al. Endothelin, a novel vasoconstrictor peptide, as potent bronchoconstrictor. European journal of pharmacology. 1988;154(2):227-8.
548. Yuen TJ, Johnson KR, Miron VE, Zhao C, Quandt J, Harrisingh MC, et al. Identification of endothelin 2 as an inflammatory factor that promotes central nervous system remyelination. Brain. 2013;136(Pt 4):1035-47.
549. Swire M, Kotelevtsev Y, Webb DJ, Lyons DA, ffrench-Constant C. Endothelin signalling mediates experience-dependent myelination in the CNS. eLife. 2019;8:e49493.
550. Vidovic M, Chen MM, Lu QY, Kalloniatis KF, Martin BM, Tan AH, et al. Deficiency in endothelin receptor B reduces proliferation of neuronal progenitors and increases apoptosis in postnatal rat cerebellum. Cellular and molecular neurobiology. 2008;28(8):1129-38.
551. Ehrenreich H, Nau TR, Dembowski C, Hasselblatt M, Barth M, Hahn A, et al. Endothelin b receptor deficiency is associated with an increased rate of neuronal apoptosis in the dentate gyrus. Neuroscience. 2000;95(4):993-1001.
552. Xie D, Croaker GD, Li J, Song ZM. Reduced cell proliferation and increased apoptosis in the hippocampal formation in a rat model of Hirschsprung's disease. Brain research. 2016;1642:79-86.
553. Back SA, Tuohy TM, Chen H, Wallingford N, Craig A, Struve J, et al. Hyaluronan accumulates in demyelinated lesions and inhibits oligodendrocyte progenitor maturation. Nature medicine. 2005;11(9):966-72.
554. Hammond TR, McEllin B, Morton PD, Raymond M, Dupree J, Gallo V. Endothelin-B Receptor Activation in Astrocytes Regulates the Rate of Oligodendrocyte Regeneration during Remyelination. Cell reports. 2015;13(10):2090-7.
555. Gadea A, Schinelli S, Gallo V. Endothelin-1 Regulates Astrocyte Proliferation and Reactive Gliosis via a JNK/c-Jun Signaling Pathway. 2008;28(10):2394-408.
556. Grell AS, Thigarajah R, Edvinsson L, Samraj AK. Regulatory mechanism of endothelin receptor B in the cerebral arteries after focal cerebral ischemia. PloS one. 2014;9(12):e113624.
557. Spray S, Johansson SE. Enhanced contractility of intraparenchymal arterioles after global cerebral ischaemia in rat - new insights into the development of delayed cerebral hypoperfusion. 2017;220(4):417-31.
558. Garavelli L, Ivanovski I, Caraffi SG, Santodirocco D, Pollazzon M, Cordelli DM, et al. Neuroimaging findings in Mowat–Wilson syndrome: a study of 54 patients. Genetics in Medicine. 2017;19(6):691-700.
559. Buades A, Coll B, Morel J-M. A Non-Local Algorithm for Image Denoising. Proceedings of the 2005 IEEE Computer Society Conference on Computer Vision and Pattern Recognition (CVPR'05) - Volume 2 - Volume 02. 1069066: IEEE Computer Society; 2005. p. 60-5.
560. Stoll C, Dott B, Alembik Y, Roth MP. Associated congenital anomalies among cases

with Down syndrome. Eur J Med Genet. 2015;58(12):674-80.
561. Van de Putte T, Maruhashi M, Francis A, Nelles L, Kondoh H, Huylebroeck D, et al. Mice lacking ZFHX1B, the gene that codes for Smad-interacting protein-1, reveal a role for multiple neural crest cell defects in the etiology of Hirschsprung disease-mental retardation syndrome. American journal of human genetics. 2003;72(2):465-70.
562. Paz JA, Kim CA, Goossens M, Giurgea I, Marques-Dias MJ. Mowat-Wilson syndrome: neurological and molecular study in seven patients. Arquivos de neuro-psiquiatria. 2015;73(1):12-7.
563. Boardman JP, Syrris P, Holder SE, Robertson NJ, Carter N, Lakhoo K. A novel mutation in the endothelin B receptor gene in a patient with Shah-Waardenburg syndrome and Down syndrome. Journal of medical genetics. 2001;38(9):646-7.
564. Ambar I, Kloog Y, Kochva E, Wollberg Z, Bdolah A, Oron U, et al. Characterization and localization of a novel neuroreceptor for the peptide sarafotoxin. Biochemical and biophysical research communications. 1988;157(3):1104-10.
565. Tsaur ML, Wan YC, Lai FP, Cheng HF. Expression of B-type endothelin receptor gene during neural development. FEBS letters. 1997;417(2):208-12.
566. Naidoo V, Naidoo S, Mahabeer R, Raidoo DM. Cellular distribution of the endothelin system in the human brain. J Chem Neuroanat. 2004;27(2):87-98.
567. Koyama Y, Tsujikawa K, Matsuda T, Baba A. Intracerebroventricular administration of an endothelin ETB receptor agonist increases expressions of GDNF and BDNF in rat brain. Eur J Neurosci. 2003;18(4):887-94.
568. Feger GI, Schilling L, Ehrenreich H, Wahl M. Endothelium-dependent relaxation counteracting the contractile action of endothelin-1 is partly due to ETB receptor activation. Research in experimental medicine Zeitschrift fur die gesamte experimentelle Medizin einschliesslich experimenteller Chirurgie. 1997;196(6):327-37.
569. Johansson SE, Larsen SS, Povlsen GK, Edvinsson L. Early MEK1/2 inhibition after global cerebral ischemia in rats reduces brain damage and improves outcome by preventing delayed vasoconstrictor receptor upregulation. PloS one. 2014;9(3):e92417.
570. McDougall ARA, Wiradjaja V, Azhan A, Li A, Hale N, Wlodek ME, et al. Intrauterine Growth Restriction Alters the Postnatal Development of the Rat Cerebellum. Developmental neuroscience. 2017;39(1-4):215-27.
571. Sun Y, Zhang X, Chen Z, Xu M, Ou M. Reduction of Uterine Perfusion Pressure Induced Redistribution of Endothelin Receptor Type-B Between the Intima and Media Contributes to the Pathogenesis of Pregnancy-Induced Hypertension. Cellular physiology and biochemistry : international journal of experimental cellular physiology, biochemistry, and pharmacology. 2017;44(5):1715-25.
572. Nishikawa K, Ayukawa K, Hara Y, Wada K, Aoki S. Endothelin/endothelin-B receptor signals regulate ventricle-directed interkinetic nuclear migration of cerebral cortical neural progenitors. Neurochemistry international. 2011;58(3):261-72.
573. Koyama Y, Nagae R, Tokuyama S, Tanaka K. I.c.v administration of an endothelin ET(B) receptor agonist stimulates vascular endothelial growth factor-A production and activates vascular endothelial growth factor receptors in rat brain. Neuroscience. 2011;192:689-98.
574. Ansar S, Eftekhari S, Waldsee R, Nilsson E, Nilsson O, Saveland H, et al. MAPK signaling pathway regulates cerebrovascular receptor expression in human cerebral arteries. BMC neuroscience. 2013;14:12.
575. DeLong MR, Wichmann T. Circuits and circuit disorders of the basal ganglia. Arch Neurol. 2007;64(1):20-4.

576. Gilbert CD, Sigman M. Brain states: top-down influences in sensory processing. Neuron. 2007;54(5):677-96.
577. Gozal D. Congenital central hypoventilation syndrome: an update. Pediatric pulmonology. 1998;26(4):273-82.
578. Verdy M, Weber AM, Roy CC, Morin CL, Cadotte M, Brochu P. Hirschsprung's disease in a family with multiple endocrine neoplasia type 2. Journal of pediatric gastroenterology and nutrition. 1982;1(4):603-7.
579. Peretz H, Luboshitsky R, Baron E, Biton A, Gershoni R, Usher S, et al. Cys 618 Arg mutation in the RET proto-oncogene associated with familial medullary thyroid carcinoma and maternally transmitted Hirschsprung's disease suggesting a role for imprinting. Human mutation. 1997;10(2):155-9.
580. Romeo G, Ceccherini I, Celli J, Priolo M, Betsos N, Bonardi G, et al. Association of multiple endocrine neoplasia type 2 and Hirschsprung disease. Journal of internal medicine. 1998;243(6):515-20.
581. Duess JW, Puri P. Syndromic Hirschsprung's disease and associated congenital heart disease: a systematic review. Pediatric surgery international. 2015;31(8):781-5.
582. Sandoval RL, Zaconeta CM, Margotto PR, Cardoso MT, Franca EM, Medina CT, et al. Congenital central hypoventilation syndrome associated with Hirschsprung's Disease: case report and literature review. Rev Paul Pediatr. 2016;34(3):374-8.
583. Davenport M, Taitz LS, Dickson JA. The Kaufman-McKusick syndrome: another association. Journal of pediatric surgery. 1989;24(11):1192-4.
584. Kirby ML, Gale TF, Stewart DE. Neural crest cells contribute to normal aorticopulmonary septation. Science. 1983;220(4601):1059-61.
585. Porras D, Brown CB. Temporal-spatial ablation of neural crest in the mouse results in cardiovascular defects. Developmental dynamics : an official publication of the American Association of Anatomists. 2008;237(1):153-62.
586. Bacon CR, Cary NR, Davenport AP. Endothelin peptide and receptors in human atherosclerotic coronary artery and aorta. Circ Res. 1996;79(4):794-801.
587. Pollock DM, Portik-Dobos V, Procter C, Gariepy CE, Yanagisawa M. Arterial pressure response to endothelin-1 and sarafotoxin 6c in rescued endothelin-B-deficient rats. Journal of cardiovascular pharmacology. 2000;36(5 Suppl 1):S82-5.
588. de Nucci G, Thomas R, D'Orleans-Juste P, Antunes E, Walder C, Warner TD, et al. Pressor effects of circulating endothelin are limited by its removal in the pulmonary circulation and by the release of prostacyclin and endothelium-derived relaxing factor. Proceedings of the National Academy of Sciences of the United States of America. 1988;85(24):9797-800.
589. Kelland NF, Webb DJ. Clinical trials of endothelin antagonists in heart failure: publication is good for the public health. Heart (British Cardiac Society). 2007;93(1):2-4.
590. Skovsted GF, Kruse LS, Larsen R, Pedersen AF, Trautner S, Sheykhzade M, et al. Heart ischaemia-reperfusion induces local up-regulation of vasoconstrictor endothelin ETB receptors in rat coronary arteries downstream of occlusion. Br J Pharmacol. 2014;171(11):2726-38.
591. Pini Prato A, Rossi V, Mosconi M, Holm C, Lantieri F, Griseri P, et al. A prospective observational study of associated anomalies in Hirschsprung's disease. Orphanet journal of rare diseases. 2013;8:184.
592. Croaker GDH. Clinical and Molecular Biological Studies in Hirschsprung's Disease [Doctoral thesis, University of Sydney, Sydney, Australia]. University of Sydney: University of

Sydney. ; 2002.
593. Dembowski C, Hofmann P, Koch T, Kamrowski-Kruck H, Riedesel H, Krammer HJ, et al. Phenotype, intestinal morphology, and survival of homozygous and heterozygous endothelin B receptor--deficient (spotting lethal) rats. Journal of pediatric surgery. 2000;35(3):480-8.
594. Webb S, Qayyum SR, Anderson RH, Lamers WH, Richardson MK. Septation and separation within the outflow tract of the developing heart. Journal of anatomy. 2003;202(4):327-42.
595. Jiang X, Rowitch DH, Soriano P, McMahon AP, Sucov HM. Fate of the mammalian cardiac neural crest. Development. 2000;127(8):1607-16.
596. Brown CB, Feiner L, Lu MM, Li J, Ma X, Webber AL, et al. PlexinA2 and semaphorin signaling during cardiac neural crest development. Development. 2001;128(16):3071-80.
597. Engleka KA, Gitler AD, Zhang M, Zhou DD, High FA, Epstein JA. Insertion of Cre into the Pax3 locus creates a new allele of Splotch and identifies unexpected Pax3 derivatives. Developmental biology. 2005;280(2):396-406.
598. Stottmann RW, Choi M, Mishina Y, Meyers EN, Klingensmith J. BMP receptor IA is required in mammalian neural crest cells for development of the cardiac outflow tract and ventricular myocardium. Development. 2004;131(9):2205-18.
599. Tirapelli CR, Casolari DA, Yogi A, Montezano AC, Tostes RC, Legros E, et al. Functional characterization and expression of endothelin receptors in rat carotid artery: involvement of nitric oxide, a vasodilator prostanoid and the opening of K+ channels in ETB-induced relaxation. Br J Pharmacol. 2005;146(6):903-12.
600. Nilsson D, Wackenfors A, Gustafsson L, Ugander M, Paulsson P, Ingemansson R, et al. Endothelin receptor-mediated vasodilatation: effects of organ culture. European journal of pharmacology. 2008;579(1-3):233-40.
601. Domenech R, Macho P, Gonzalez R, Huidobro-Toro JP. Effect of endothelin on total and regional coronary resistance and on myocardial contractility. European journal of pharmacology. 1991;192(3):409-16.